UNIVERSIDADE TÉCNICA DE LISBOA

INSTITUTO SUPERIOR TÉCNICO

Reconstruction methods and tests of the AMS RICH detector

Sensitivity to light isotope measurements and dark matter searches

Rui Miguel Faísca Rodrigues Pereira

(Licenciado)

Dissertação para obtenção do Grau de Doutor em Física

Orientador: Doutor Fernando José de Carvalho Barão

Júri

Presidente: Presidente do Conselho Científico do IST

Vogais: Doutor Jorge Venceslau Comprido Dias de Deus
Doutor Jorge Casaus Armentano
Doutor Mário João Martins Pimenta
Doutor Fernando José de Carvalho Barão
Doutor Bernardo António Neto Gomes Baptista Tomé
Doutor Laurent Yves Marie Derôme

Setembro de 2010

Resumo

O Espectrómetro Magnético Alfa (AMS), cuja versão final AMS-02 será instalada na Estação Espacial Internacional em 2011 por um mínimo de 3 anos, é um detector projectado para medir os espectros de raios cósmicos carregados com energias até à região do TeV e com capacidade de detecção de fotões de alta energia até algumas centenas de GeV. Está equipado com diversos subsistemas, um dos quais é um detector RICH de focagem aproximada com um radiador dual (aerogel+NaF) que fornece medidas fiáveis de velocidade e carga.

Um protótipo do RICH foi construído, sendo sujeito a vários testes entre 2002 e 2003. Um método para reconstrução de carga a partir de sinais de cintiladores é descrito e os seus resultados para dados de teste de feixe são apresentados. O procedimento para determinação da produção de luz de sete amostras de aerogel a partir de dados de teste de feixe, conducente à escolha do radiador final, é apresentado detalhadamente.

Em 2008 o detector AMS-02 foi montado no CERN sem o seu magneto e exposto ao fluxo natural de raios cósmicos. Os resultados obtidos para a produção de luz do aerogel do RICH são apresentados e comparados com resultados de simulações e da extrapolação dos resultados do protótipo.

Estudos complementares foram efectuados no quadro das simulações de AMS. Métodos de reconstrução de eventos de AMS sem informação do detector de traços são apresentados. As capacidades do detector para separação de massa são avaliadas para os canais de isótopos leves (H, He, Be) e $\overline{\mathrm{D}}/\overline{\mathrm{p}}$, e as suas implicações para a física de raios cósmicos são brevemente discutidas.

Palavras-chave: RICH/AMS, Ângulo de Čerenkov, Reconstrução de Carga com Cintiladores, Avaliação da Produção de Luz em Aerogel, Reconstrução Autónoma, Separação de Massa.

Abstract

The Alpha Magnetic Spectrometer (AMS), whose final version AMS-02 is to be installed on the International Space Station in 2011 for at least 3 years, is a detector designed to measure charged cosmic-ray spectra with energies up to the TeV region and with high energy photon detection capability up to a few hundred GeV. It is equipped with several subsystems, one of which is a proximity focusing RICH detector with a dual radiator (aerogel+NaF) that provides reliable measurements for velocity and charge.

A RICH prototype was built and underwent several tests between 2002 and 2003. A method for charge reconstruction from scintillator signals is described and its results for beam test data are presented. The procedure for the determination of the light yield of seven aerogel samples from beam test data, leading to the choice of the final radiator, is presented in detail.

In 2008 the AMS-02 detector was assembled at CERN without its magnet and exposed to the natural cosmic-ray flux. Results obtained for the light yield of the RICH aerogel are presented and compared with results from simulations and from the extrapolation of prototype results.

Complementary studies were performed in the framework of AMS simulations. Methods for reconstruction of AMS events without information from the Tracker are presented. Detector capabilities for mass separation are evaluated for the light isotope (H, He, Be) and $\overline{\mathrm{D}}/\overline{\mathrm{p}}$ channels, and their implications for cosmic-ray physics are briefly discussed.

Keywords: RICH/AMS, Čerenkov angle, Scintillator Charge Reconstruction, Aerogel Light Yield Evaluation, Standalone Reconstruction, Mass Separation.

Acknowledgements

This work is dedicated to my family, and in particular to my parents and my brother João, for their love, support and encouragement, in good times and in bad times, during all these years.

I would like to thank my thesis director, Professor Fernando Barão, for his guidance and support.

I thank Professor Mário Pimenta for accepting me at LIP and for his guidance in my initial work with AMS.

I first heard of AMS from Professor João Seixas. He was also present at a number of other occasions along my academic path. A special acknowledgement is due to him.

I would like to thank all members of LIP-Lisbon for the good work environment and for their help on many occasions.

A very special thanks to Luísa Arruda who, sitting at the next desk and also working in AMS, was forced to answer countless questions and help with all sorts of problems big and small, not to mention having to endure the not-so-rare occasions when I was in a bad mood.

Thanks to João Borges who for a few years, including the early days of this work, was the third AMS element in our office and therefore shared with Luísa the burden of having to interact with me on a daily basis. Thank you also to Pedro Mendes Jorge, the newcomer to our office, who is now sharing that burden from a non-AMS point of view.

I would like to thank Patrícia Gonçalves for helping me with her AMS knowledge.

I thank David Maurin for sharing with us his knowledge of cosmic rays, as well as his good mood.

Being part of an international team, I was present at many meetings, both formal and informal, that were extremely important for this work. I would like to thank the members of the AMS and RICH collaborations and in particular Jorge Casaus, Carlos Delgado, Javier Berdugo, Michel Buénerd, Vitaly Choutko, Francesca Giovacchini and Mariusz Sapinski for information exchanges.

I thank the LPSC team and in particular Michel Buénerd, Mariane Mangin-Brinet, Yoann Sallaz-Damaz and Maxime Loth for their guidance during my stay in Grenoble.

I thank Vitaly Choutko for his guidance in my stay at CERN, and Francesca Giovacchini for the useful discussions during that stay. I thank my LIP colleagues, in particular Alberto Palma, António Morais, João Gentil, Marcelo Jordão and Nuno Anjos, for the good atmosphere in our dinner meetings at CERN.

Thank you to the LIP computing staff for their help dealing with computers, those dangerous and unpredictable entities, hoping that I did not take too much advantage of the strategic placement of my office just next to theirs.

Thank you to the LIP secretariat for their flawless assistance with travelling plans and other bureaucratic details.

This work was supported by a doctoral degree grant from Portugal's Foundation for Science and Technology (Fundação para a Ciência e a Tecnologia — FCT).

Contents

List of Figures

List of Tables

Introduction

The work presented in this thesis was conducted at the Lisbon centre of LIP — Laboratório de Instrumentação e Física Experimental de Partículas, in the framework of the Portuguese collaboration in the AMS experiment, under the supervision of the head of the Portuguese group, Professor Fernando Barão. It included a two-week stay at the Laboratoire de Physique Subatomique et de Cosmologie (LPSC) in Grenoble, France, in November-December 2005, and a one-month stay at CERN in July-August 2008, as well as several shorter visits to CIEMAT (Madrid), CERN and LPSC for collaboration meetings.

This thesis is divided in four parts with a total of ten chapters.

Part I, corresponding to the first two chapters, introduces the main physics themes related to the content of this thesis. In Chapter 1 an introduction to cosmic rays and to the physical conditions associated to their propagation and detection is made. Chapter 2 focuses on the problem of dark matter, its detection and composition, and its relation with supersymmetric models.

In Part II, composed of Chapters 3 and 4, a description of AMS and the RICH subdetector is made. Chapter 3 introduces the AMS experiment and its two flight detectors: the prototype AMS-01 flown in 1998 and the final detector AMS-02 currently undergoing the final tests before being placed on the International Space Station in 2011. The AMS full software chain is also presented. Chapter 4 describes the AMS-02 RICH detector, the standalone RICH simulation and the RICH velocity and charge reconstruction algorithm developed at LIP.

Part III comprises Chapters 5 to 9, corresponding to studies performed on the reconstruction of particle properties and tests of the RICH detector. The AMS RICH prototype, and the tests performed with it between 2002 and 2003, are introduced in Chapter 5. In Chapter 6 the development of a method for charge reconstruction with scintillators in the framework of the RICH prototype tests is described, allowing for the calibration and validation of RICH charge reconstruction. Chapter 7 presents the studies performed on light yield evaluation for the aerogel samples tested with the RICH prototype, which led to the selection of the radiator material to be used in AMS-02. Chapter 8 describes the analysis of the AMS-02 RICH performance and of the reconstruction quality using cosmic data collected with the AMS-02 detector in 2008, after its first assembly with no magnet, and in 2009, with the superconducting magnet present, including results for aerogel light yield which are compared with simulation results and also with an extrapolation of prototype values obtained in Chapter 7. Chapter 9 introduces novel methods for reconstruction of particle velocity and direction without information from the AMS Tracker (developed from the standard LIP event reconstruction), one based solely on information from the RICH detector and others based on combined information from the RICH and Time-of-Flight detectors and describes the results obtained from the application of these methods to simulated events and to cosmic data from 2008.

Finally, Part IV corresponds to Chapter 10, where studies on mass separation capabilities of the AMS-02 RICH detector, and its implications on the physics of cosmic-ray production and propagation, are presented. The cases discussed are those of $\overline{\mathrm{D}}/\overline{\mathrm{p}}$, where a possible dark matter signal may be detected, and the light isotope ratios D/p, ^{3}He/^{4}He, and ^{10}Be/^{9}Be.

The conclusions of this work are then summarized.

Part I

Physics introduction

Chapter 1

Cosmic rays

1.1 The atomic picture of matter

The possibility of matter being made of discrete entities ("atoms") was considered since Antiquity. However, such idea could not be put to the test before the development of modern experimental sciences. It was only in the early 19^{th} century that the modern atomic picture of matter emerged from the work of authors such as John Dalton and Amedeo Avogadro, leading to the familiar classification of chemical substances as atoms and molecules. During the following century, the scientific community gradually accepted the atomic hypothesis as experimental evidence increased. Albert Einstein's 1905 explanation [1] of Brownian motion (first observed by Robert Brown in 1827 [2]) in terms of collisions of individual molecules helped to settle the question of the existence of atoms.

At the same time, indications of a subatomic structure of matter had already begun to appear. X-rays were discovered by Wilhelm Röntgen in 1895 [3]. In 1896 Henri Becquerel discovered radioactivity [4] and in 1897 J. J. Thomson discovered the first subatomic particle, the electron [5]. The following decades would see the development of a new description of atoms and their structure based on quantum mechanics.

1.2 The discovery of cosmic rays

The existence of a radiation flux coming from space was not immediately apparent due to the radioactivity of the Earth itself. It was only when measurements of radiation-induced ionization failed to show the expected decrease with altitude beyond the first few hundred metres that a possible extraterrestrial source was investigated. Cosmic rays were finally identified by Victor F. Hess, who performed several balloon experiments between 1911 and 1913 showing that the radiation flux increased with altitude. These included observations performed at night and during a solar eclipse which showed no decrease in cosmic radiation, indicating that the Sun was not the main source of cosmic rays [6].

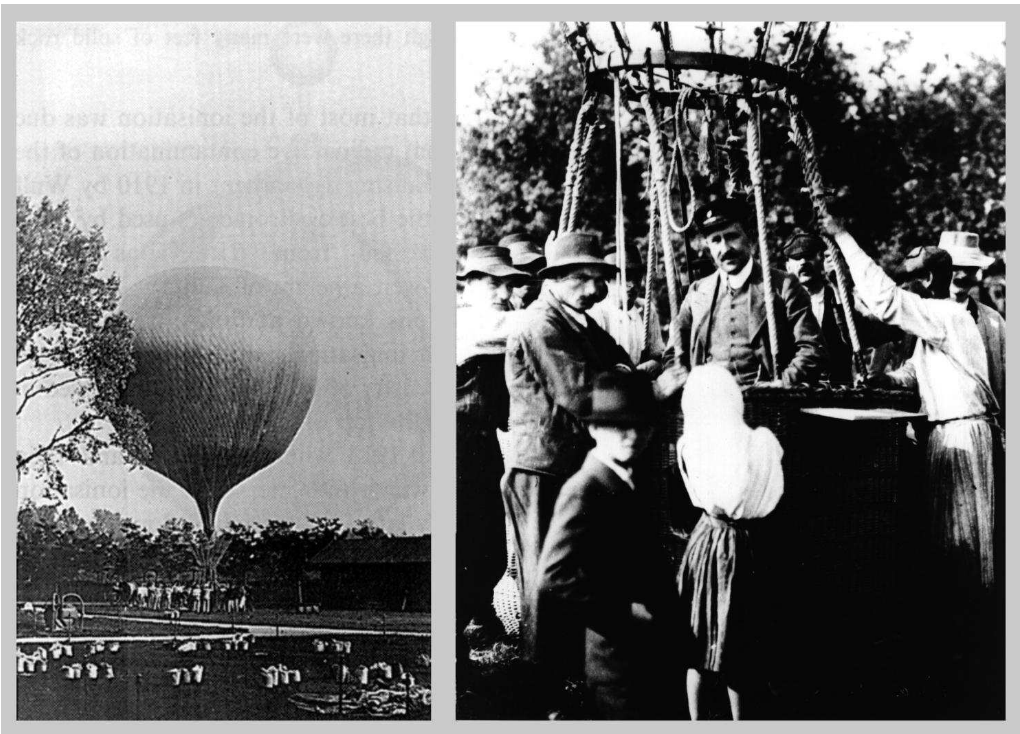

Figure 1.1: *Victor Hess and the balloon where the observations that led to the discovery of cosmic rays were performed* [7].

Initially, it was assumed that the extraterrestrial radiation would consist of γ-rays [8]. The designation "cosmic rays", coined by Robert A. Millikan in the 1920s [8, 9], reflects this historical assumption. The first serious challenge to that scenario came in 1927 from Jacob Clay, who measured a small variation in the cosmic-ray flux as function of geographical latitude [8]. In 1929 Walter Bothe and Werner Kolhörster interpreted then-existing results as indicating the presence of charged particles in cosmic rays [10]. During the 1930s the corpuscular nature of cosmic rays gained acceptance as new results were obtained, namely the discovery of the positron in cosmic rays by Carl D. Anderson in 1932 [11, 12] (leading to a short-lived role of the positron as candidate to main cosmic-ray constituent [8]) and the measurement of an east-west asymmetry explainable only by the predominance of positively charged particles in the cosmic-ray flux [13]. Around 1940 it had been established that protons were the main constituent of primary cosmic rays [14].

1.3 Cosmic-ray spectrum

In the past century, studies of cosmic rays progressed from simple detection to a detailed knowledge of their composition and energy distribution using sophisticated particle detectors.

Progress on cosmic ray studies was initially driven by fundamental physics research, but other scientific areas were gradually involved. Radiocarbon dating is based on the production of ^{14}C nuclei in the upper atmosphere from interactions between atmospheric ^{14}N and neutrons originating from cosmic-ray interactions [15]. Biological effects of cosmic radiation [16], and shielding mechanisms to reduce exposure [17], are being studied as part of the research effort on future manned missions in the Solar System. Effects of cosmic rays on electronic equipment must be taken into consideration in all space missions [18]. Even at the Earth's surface, cosmic rays are starting to become a significant hazard due to the miniaturization of electronic circuits [19]. Possible effects of cosmic rays on the Earth's climate, in particular through an effect on the planet's cloud cover, are also being considered [20].

1.3.1 Energy distribution of cosmic rays

Cosmic rays reaching the Earth's vicinity have a wide range of energies. The most energetic particles found in cosmic rays have energies above 10^{19} eV, greatly exceeding the highest values ever reached in purposely-built accelerators. By comparison, CERN's Large Hadron Collider beams currently (September 2010) hold the record for highest man-made particle energy, having reached 3.5 TeV (3.5×10^{12} eV) in

March 2010 [21], and are expected to reach 7 TeV in a few years [22].

The most remarkable feature in the cosmic-ray spectrum is its almost perfectly exponential reduction in flux with energy, that is, $\Phi \propto E^{-\alpha}$, which covers approximately 10 orders of magnitude in energy (from $\sim 10^9$ eV to $\sim 10^{19}$ eV) and 30 orders of magnitude in flux (Fig. 1.2). Some changes of slope occur in that range: the *knee*, between 10^{15} and 10^{16} eV, where the spectral index α changes from ~ 2.7 to ~ 3.1, the *second knee*, between 10^{17} and 10^{18} eV, where the spectral index increases again to ~ 3.3, and the *ankle*, between 10^{18} and 10^{19} eV, where the spectral index returns to ~ 2.7.

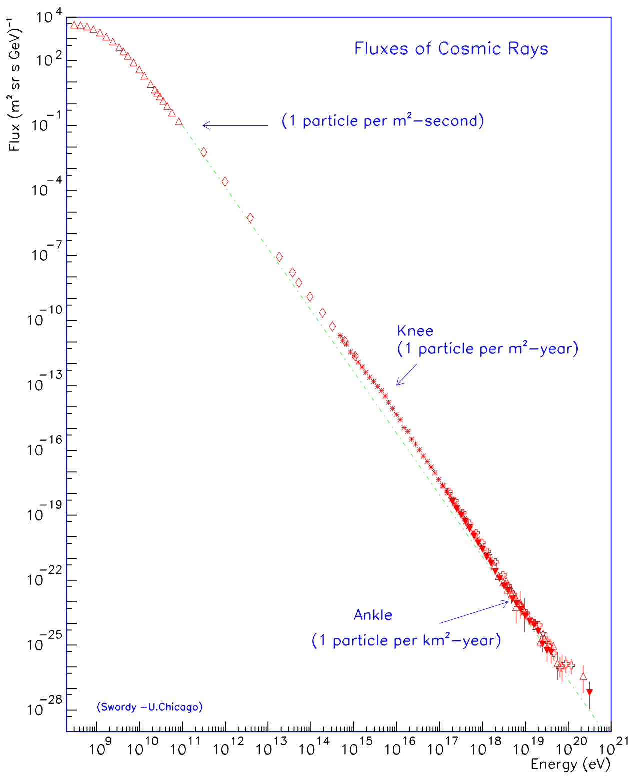

Figure 1.2: *The flux of cosmic rays as function of energy, compiled by S. Swordy* [23].

The shape of the cosmic-ray spectrum beyond 10^{19} eV is a major subject of current research. For energies beyond $\sim 5 \times 10^{19}$ eV the cosmic-ray flux is expected to be suppressed due to interactions between protons (the main component of cosmic rays) and cosmic microwave background (CMB) photons reaching the centre-of-mass energy needed to produce a Δ^+ resonance (approximately 1232 MeV [24]). This phenomenon is known as the GZK (Greisen-Zatsepin-Kuzmin) cutoff [25, 26]. The earliest results for this energy region, obtained by the AGASA experiment [27], did not show the expected reduction in the number of events. However, more recent data from HiRes [28, 29] and Auger [30, 31] do not confirm the AGASA claim and instead display a drop in the statistics as expected from the GZK cutoff [24].

1.3.2 Composition of cosmic rays

It is now known that the incident flux of particles at the top of the Earth's atmosphere consists essentially of nuclear matter in the form of protons ($\sim 90\%$ of all cosmic rays), α particles, that is, ^{4}He nuclei ($\sim 10\%$), and heavier nuclei ($\sim 1\%$). The abundance of elements with $Z \lesssim 30$ in cosmic rays is quite similar to that found in the Solar System, but rare elements tend to have higher abundances in cosmic rays, as shown in Fig. 1.4. This is clearly seen for Z = 21-25 and in particular for Z = 3-5 (Li, Be, B) where cosmic-ray abundances are many orders of magnitude higher [33].

Differences observed between Solar System and cosmic-ray abundances are believed to be mainly due to interactions that cosmic-ray nuclei undergo before reaching Earth. Cosmic rays are classified as *primary*, those that are accelerated at the source, and *secondary*, those that are the produced in interactions between primaries and interstellar gas[1]. Primary nuclei correspond to protons and to those nuclei produced in the Big Bang nucleosynthesis (mainly ^{4}He) or in stars (e.g. C, O, Ne, Fe). Secondaries include Li, Be and B [24]. The fractions of primary nuclei are nearly constant in the energy range from a few GeV to hundreds of TeV (Fig. 1.5). The ratio of secondary to primary nuclei decreases with energy [24].

Other charged particles present in cosmic rays include electrons ($\sim 1\%$), positrons ($\sim 10^{-3}$), and antiprotons ($\sim 10^{-4}$), as shown in Fig. 1.3.

[1]The designations primary and secondary are also used with a different meaning in the context of atmospheric interactions of cosmic rays, as mentioned in Section 1.4.

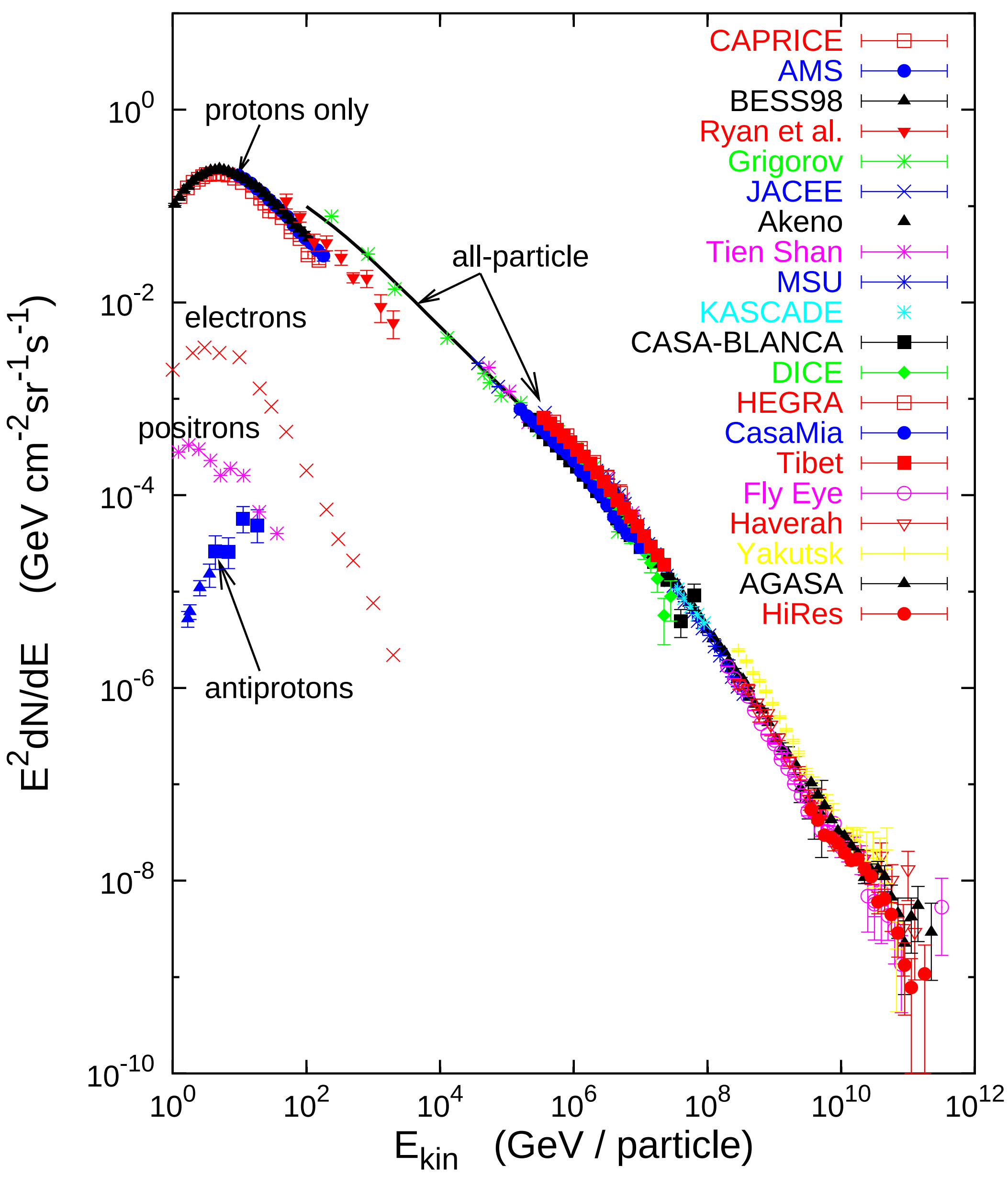

Figure 1.3: *The flux of cosmic rays as function of energy for different particle types, compiled by T. K. Gaisser. From Ref.* [32].

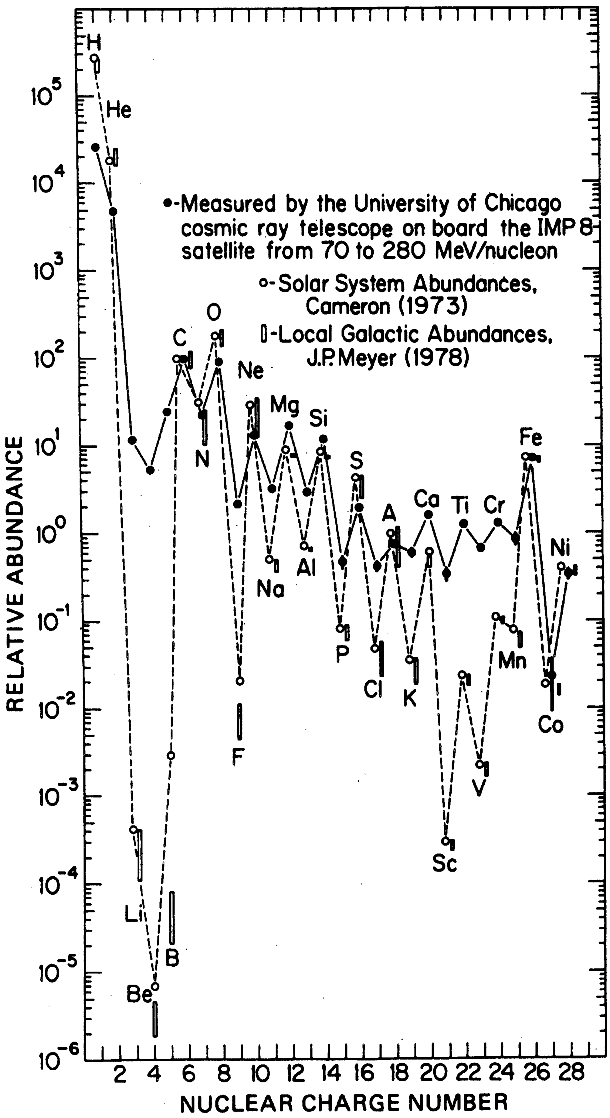

Figure 1.4: *Comparison of elemental abundances in cosmic rays (filled dots) with Solar System abundances (open dots) and local galactic abundances (open boxes). From Ref.* [34].

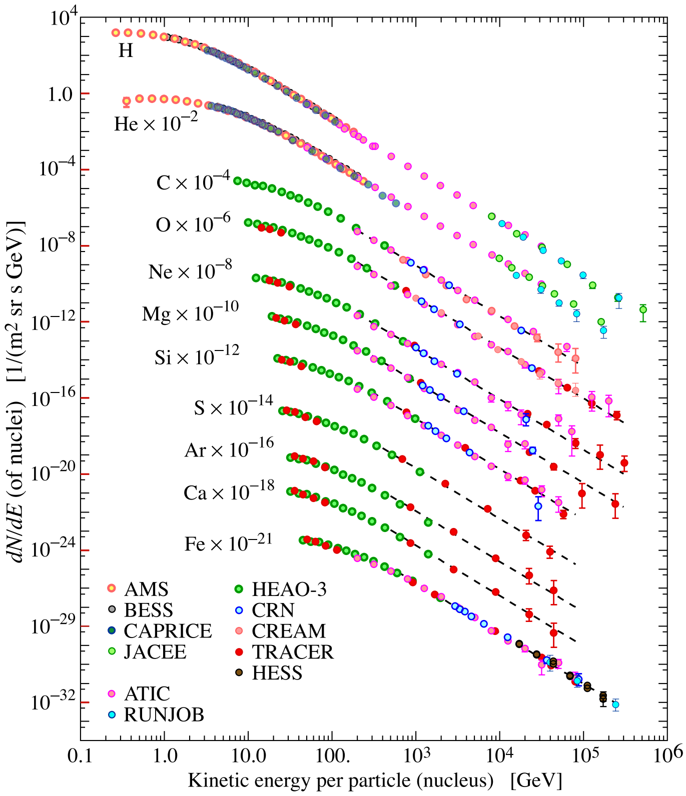

Figure 1.5: *Energy spectrum for major nuclear components of primary cosmic radiation. From Ref.* [24].

1.3.3 Solar modulation

Space inside the Solar System is not empty. There is a plasma, made of a mixture of ions and electrons, that is constantly flowing from the Sun. This flux, originating from the solar corona, is termed *solar wind* [35].

Fluxes at the low-energy end of the cosmic-ray spectrum are subject to significant variations due to interactions with solar wind. This effect, known as solar modulation, may be approximated to that of a modulation by a heliocentric electric field, the "force-field approximation" [36, 37]. Solar modulation has an intensity that is related to solar activity.

Sunspots are the most visible effect of solar activity on the appearance of the Sun, and have been regularly observed by astronomers since the early 17$^{\text{th}}$ century [38]. Solar activity follows a cycle with an average duration of approximately 11 years, as discovered by Samuel H. Schwabe in 1843 from sunspot data (Fig. 1.6).

The solar cycle is in fact a magnetic cycle, as shown by George E. Hale in the beginning of the 20th century [39]. The magnetic polarity of sunspots is reversed from one cycle to the next, meaning that the complete cycle is actually 2×11 years [39]. However, since magnetic polarity is not important in most contexts, the term cycle continues to be used for the 11-year period.

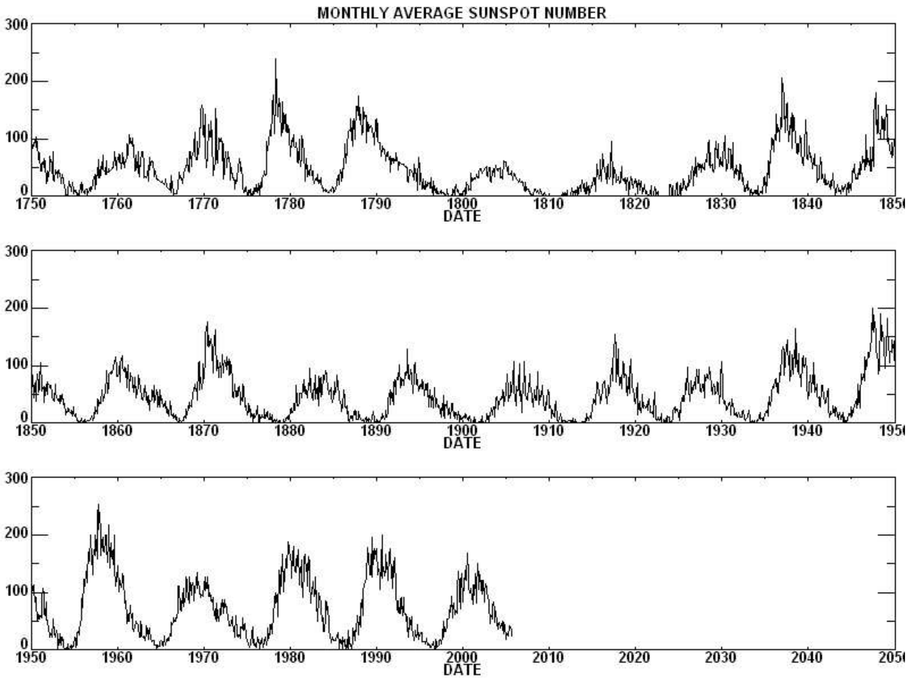

Figure 1.6: *Monthly average sunspot number since 1749* [40].

There are significant fluctuations in the solar cycle period around the 11-year average, with durations between 9 and 14 years having been recorded in the last few centuries [38]. The intensity of solar cycles is also quite variable. Between 1645 and 1715 solar activity was extremely low, with few visible sunspots. This period is known as Maunder minimum [41]. In contrast, since the middle of the 20th century the sun has been very active. Indirect estimates of historical solar activity obtained from Earth data show that the current level is high when compared to the typical values of the last 9300 years [42].

At the time of writing (September 2010) solar activity is leaving the minimum phase of its 11-year cycle and is expected to increase rapidly towards the next solar maximum, estimated to occur in 2013. The most recent predictions indicate that this will likely be the lowest maximum in a century (Fig. 1.7) [43].

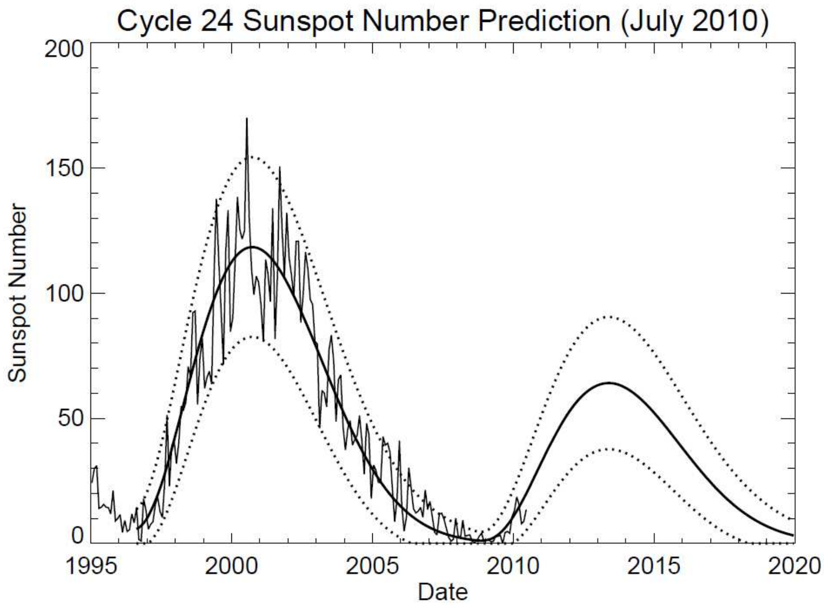

Figure 1.7: *Sunspot number during the last solar cycle and July 2010 prediction for next cycle from the NASA/Marshall Space Flight Center* [43].

1.3.4 Geomagnetic effects

The Earth possesses a magnetic field, which is approximately dipolar, generated mainly by the rotation of its conducting, fluid outer core. The intensity of the Earth's magnetic field at the planet's surface ranges from 30 μT to 60 μT, approximately. Charged particles approaching Earth have their trajectories changed by the planet's magnetic field, and will also in turn influence the shape of the magnetic field itself. The Earth's magnetosphere is the result of interactions between solar wind and the planet's magnetic field.

Cosmic-ray particles reaching the Earth's vicinity, having already been modulated by solar effects in their paths through the Solar System, will then interact with the magnetosphere. This interaction means that the detectable cosmic-ray flux is function of geographical location and of altitude. In particular, there is a geomagnetic cutoff in particle rigidity R ($R = p/Z$) that is more important at lower latitudes (Fig. 1.8).

The geomagnetic cutoff is not absolute, however: the fraction of detectable particles does not increase from 0 to 1 at the cutoff but instead, around the cutoff value, a rigidity range (the cosmic ray penumbra) exists where a complex dependence on

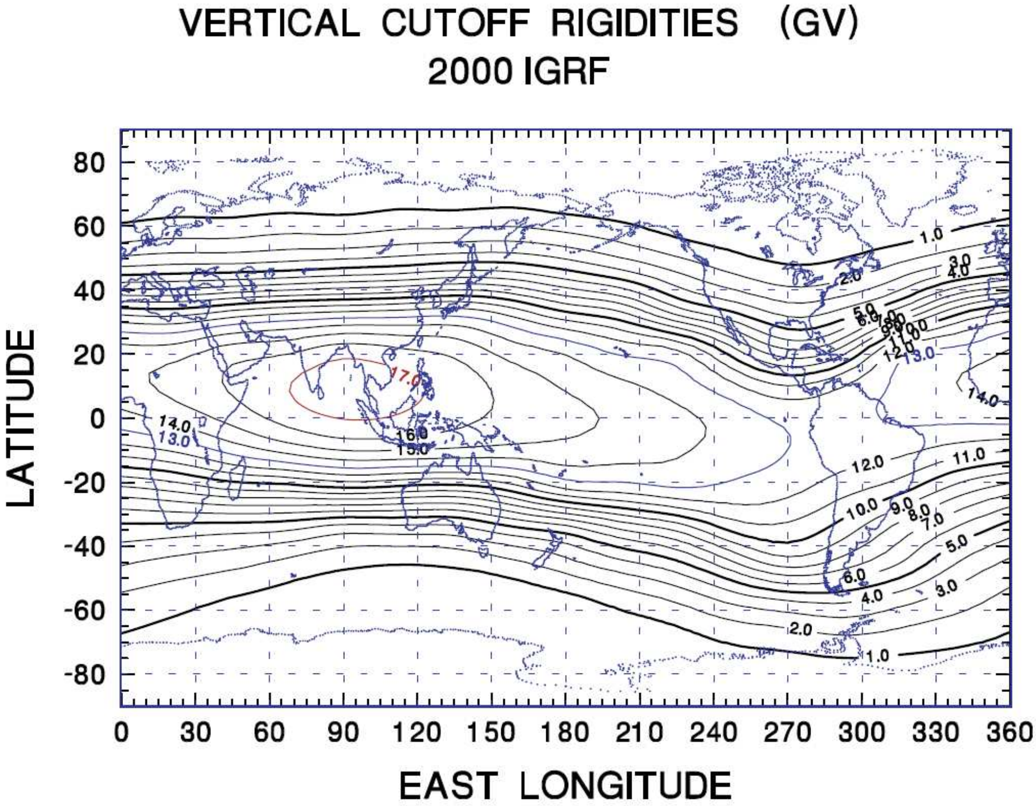

Figure 1.8: *Vertical cutoff rigidity contours at the ground for Epoch 2000 obtained using the International Geomagnetic Reference Field (IGRF) model* [44]. *From Ref.* [45].

both rigidity and particle orientation (including the previously mentioned east-west asymmetry) is seen [46].

Calculating geomagnetic effects requires a large amount of computing power since it becomes necessary to determine the trajectories of many individual particles. Variations in the Earth's magnetic field, such as secular changes and short-term effects in response to solar activity, mean that its characteristics, including cutoff rigidities, are also a function of time [46].

1.4 Cosmic rays at the Earth

The interstellar distances traversed by cosmic-ray particles mean that only stable and very long-lived ($t_{1/2} \gtrsim 10^6$ yr) particles and nuclei are present in the flux that reaches the Earth's vicinity. However, this changes rapidly as cosmic-ray particles enter the atmosphere and undergo significant interactions, leading to a very different spectrum at the ground. The charged cosmic radiation arriving at sea level consists essentially of muons, as shown in Fig. 1.9.

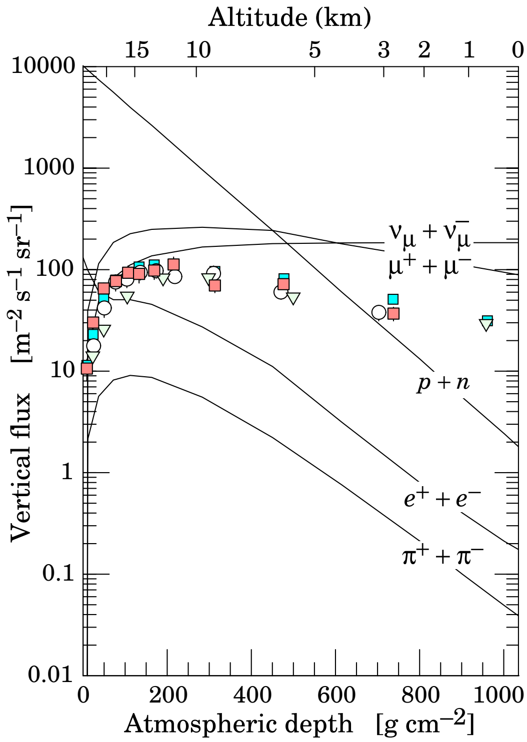

Figure 1.9: *Estimated vertical fluxes of cosmic rays in the atmosphere with $E > 1$ GeV. The points show measurements of negative muons with $E_\mu > 1$ GeV. From Ref.* [24].

In the case of cosmic rays with high energies, the number of interactions generated from a single primary particle may be so high that a cascade of interactions occurs and a *cosmic-ray shower* is formed [47]. Showers produced by particles at the high end of the cosmic-ray spectrum include billions of particles spread over a surface area of several km^2. An example of a simulated air shower produced by a proton is shown in Fig. 1.10.

Muons are the overwhelming component ($\sim$ 99%) of charged cosmic radiation collected at sea level, but many other particles are present [24]. Historically, cosmic-ray studies played a major role in particle discovery: the positron (as previously mentioned), the muon [50, 51, 52, 53], charged pions [54] and kaons [55] were all discovered in cosmic rays before being produced in man-made experiments.

Methods used in the detection of charged cosmic-ray particles are similar to those

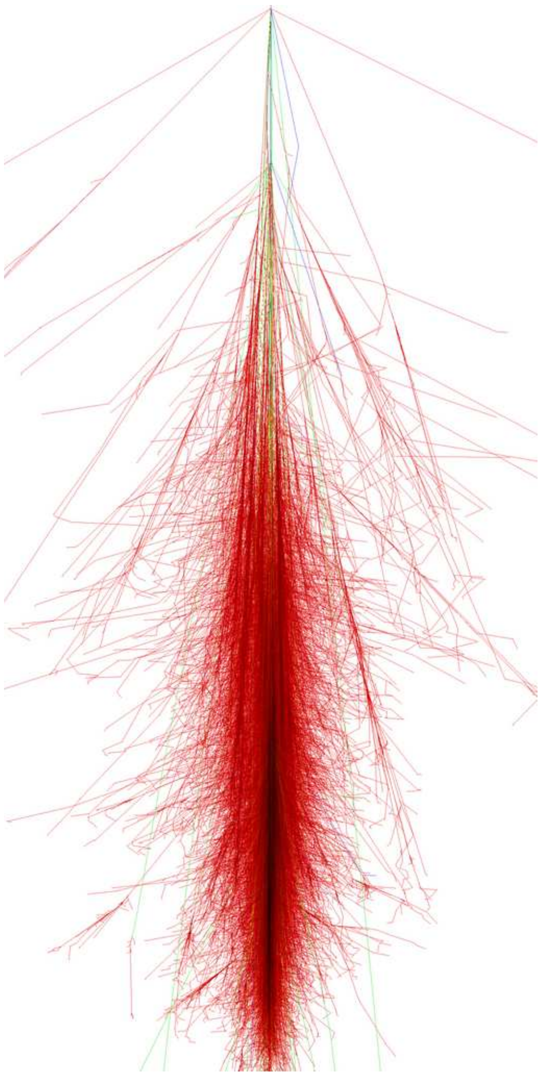

Figure 1.10: *Image of a simulated air shower produced by a vertical 1 TeV proton interacting at an altitude of 30 km, produced using the CORSIKA package* [48]. *Compiled by F. Schmidt* [49].

used to study other high-energy particles, and usually rely on their electromagnetic and nuclear interactions. The highest-energy cosmic ray particles may be indirectly detected by measuring the particle showers they generate in the Earth's atmosphere (a method used e.g. in the Pierre Auger Observatory [56]) while for particles with lower energies the measurement of the original (primary) cosmic-ray particle fluxes[2] is only possible through direct particle detection above the atmosphere, that is, in high-altitude balloon (e.g. BESS-Polar [57]) or space experiments. The AMS detectors, and AMS-02 in particular, use a combination of several detection techniques to measure the cosmic-ray flux in space, as will be described in Chapter 3. The AMS-02 RICH detector, which is a central subject in this work, is described in detail in Chapter 4.

1.5 Origin of cosmic rays

Despite cosmic rays having been discovered almost a century ago, their origin is still a subject of current research. In particular, no generally accepted mechanism has been found to explain the existence of the most energetic cosmic-ray particles.

The elemental and isotopic composition of cosmic rays has shown that they originate from outside the Solar System. Supernova remnants are viewed as the likely source of cosmic rays in our Galaxy. It is generally accepted that galactic cosmic rays are accelerated through the interaction of charged particles with large-scale magnetic fields [58], a mechanism proposed by Enrico Fermi in 1949 [59]. The Fermi mechanism operates in strong shock fronts powered by supernova explosions and propagating from the corresponding supernova remnant into the interstellar medium [58]. The maximum energy to which a particle may be accelerated through this process is related to the properties of the supernova event and proportional to the particle's charge. The current knowledge of supernova physics indicates that this

[2] Particles reaching the top of the atmosphere are referred to as *primary* particles, while those produced in the atmosphere from cosmic-ray interactions are called *secondary* particles. It is an unfortunate coincidence that the particles called primary in this sense are themselves subdivided in primary and secondary according to the processes in which they are produced before reaching Earth, as mentioned in Subsection 1.3.2, but such dual usage of these terms is widespread in literature.

energy cutoff should be roughly at $E_{max} \approx Z \cdot 10^{15}$ eV [58]. The unfolding of results obtained from the KASCADE experiment in H, He, CNO and Fe is consistent with $E_{max} \simeq Z \cdot 3 \times 10^{15}$ eV [32].

The cutoff described above occurs at the energy region corresponding to the knee of the cosmic-ray spectrum, but the steepening observed after the knee is much smaller than it would be if no other mechanisms existed for generating cosmic rays. Therefore, the particle flux beyond $\sim 10^{17}$ eV remains unexplained [32].

Particles at the high end of the cosmic-ray spectrum ($\sim 10^{19}$ eV) are thought to be extragalactic. Different explanations for their origin, including jets from active galactic nuclei [32], and even new physics (e.g. decay of topological defects), have been suggested. For these energies it becomes possible to search directly for sources using the particle's incoming direction since the deflection due to magnetic fields becomes small even for intergalactic distances. This kind of search recently had its first significant result: a correlation of ultra-high energy cosmic rays with astronomical sources (active galactic nuclei) was reported in 2007 by the Pierre Auger collaboration [60]. However, an update on these results including additional data collected between 2007 and 2009 shows a weaker correlation [61].

It has been predicted, in the context of studies on the dark matter problem [62], that the primary cosmic ray flux may include a small component originating from the annihilation of dark matter particles, which would be easier to observe in antimatter channels (see e.g. [63, 64]). Dark matter will be discussed in Chapter 2. The specific subject of dark matter signals in cosmic rays, and the possibility of detecting such signals in AMS-02, will be addressed in Chapter 10.

The propagation of cosmic rays from their sources to Earth is also a major subject of active research. It is generally believed that most sources of Galactic cosmic rays are near the Galactic disc, following a radial distribution [65]. The differences between the elemental and isotopic abundances found in the cosmic ray flux and those measured for distant astronomical bodies through spectroscopy are essentially attributable to propagation in the interstellar medium. A detailed knowledge of cosmic-ray abundances is therefore very important for the development of realistic propagation scenarios.

The energy distribution observed for cosmic rays is the result not only of acceleration at the source but also of propagation details. It is usually assumed that at the source all elements have energy distributions with an identical spectral index [58]. Subsequent interactions with the interstellar medium depend on the specific properties of each particle, leading to some differences in spectra observed at Earth. In particular, the spectral index is expected to become slightly lower for heavier elements, a result that is in agreement with observations: $\alpha = 2.71 \pm 0.02$ for protons and $\alpha = 2.59 \pm 0.06$ for iron ($Z = 26$) [66].

Diffusion effects due to Galactic magnetic fields are believed to play a major part in the propagation of cosmic rays, leading to the essentially isotropic flux that is detected at the Solar System [65]. Only at extreme energies ($\sim 10^{19}$ eV) there is a possibility of detecting anisotropies, as previously mentioned. Convection due to Galactic winds may also play a role in propagation [65].

1.6 Conclusions

A century after their discovery, cosmic rays are still a major territory of active research. Behind the almost perfect power law of their global distribution lies a vast amount of information that may be used to improve the knowledge of astrophysical processes, and, due to modulation effects, also of solar physics and geomagnetism. Open issues in fundamental physics, such as dark matter, may also profit from valuable contributions from cosmic ray studies.

The progress in the determination of cosmic ray spectra led to the development of more detailed models for their production and propagation to explain the observed features.

Despite the flux of cosmic rays at the Solar System being isotropic, the presence of many types of particles, generated by different processes and each having a specific energy spectrum, means that cosmic rays are an extremely valuable source of information, even for hitherto unobserved phenomena such as dark matter annihilation.

A detailed knowledge of radiation in space, and of cosmic rays in particular, is important not only in itself but also because of the effects of solar and cosmic radiation in human activities, both in space and on Earth.

Chapter 2

Dark matter and supersymmetry

Astronomical observations have been part of human culture for millennia. However, the evaluation of the true dimensions of outer space is a comparatively recent accomplishment.

The Copernican revolution and the development of the telescope led to a rough determination of the size of planetary orbits in the Solar System, and also of the speed of light, before the end of the 17$^{\text{th}}$ century. Interstellar distances posed a bigger challenge: the first parallax measurements of distances to nearby stars were only obtained in the 1830s, although earlier guesses based on the assumption of stars having a brightness similar to that of the Sun had already given an idea of the distance scales involved [67].

2.1 Universal expansion and the Big Bang model

Before the 20$^{\text{th}}$ century, the general view among astronomers was that of an eternal, infinite Universe, with significant change happening only on local scales. Some authors had already considered problems posed this scenario, however. That was the case of Olbers' paradox, which indicated that an infinite, uniform Universe with an infinite age could not be dark if the inverse square law for light propagation was still valid on cosmic scales. The exclusively attractive nature of (Newtonian) gravity, on the other hand, meant that considering a large but finite extension of stars surrounded by a void would in turn lead the problem of the eventual gravitational collapse of such a configuration in a finite time [68].

It was only in the early 20$^{\text{th}}$ century that certain types of "nebulae" observed by astronomers since the Renaissance were unambiguously identified as large star systems similar to the Milky Way. Detailed studies of these objects, now called galaxies, soon followed, leading to Edwin P. Hubble's discovery of an approximately linear relationship between apparent distance (as evaluated from luminosity) and redshift and its interpretation in terms of an expanding Universe [69].

The development of General Relativity by Albert Einstein in the late 1900s and 1910s [70] was an essential step in the move towards a new perspective on the Universe: for the first time a mathematical framework existed to describe the evolution of the Universe as a whole. Initially, Einstein himself introduced a parameter in his equations (the *cosmological constant*) to obtain the static Universe he thought would be correct [71], but soon afterwards it was realized that such adjustment was not satisfactory since the solution obtained was unstable. The cosmological constant, later abandoned by Einstein [72], prevented him from predicting the expansion of the Universe that would be discovered by Hubble a decade later (ironically, the cosmological constant would return in a different context long after Einstein's death). In the meantime, General Relativity had become the basis for the development of modern cosmology. Even before Hubble's discovery of universal expansion, the development of what would later be called Big Bang model had already begun with the work of Alexander Friedmann and Georges Lemaître [72].

Data supporting the Big Bang model were progressively collected during the second half of the 20$^{\text{th}}$ century. Primordial abundances of light isotopes (i.e. the abundances that existed before stars were formed), and in particular the large fraction of ^{4}He ($\simeq 24\%$ by mass) [73], were measured and explained as the result of Big Bang nucleosynthesis. In 1965, the discovery of the cosmic microwave background (CMB) radiation by Arno Penzias and Robert Wilson [74] provided perhaps the most important confirmation for the Big Bang scenario.

One major question that arose from the Big Bang model was that of the long-term result of the ongoing cosmic expansion: will it continue forever or will it reverse at some moment, leading to a final collapse in the distant future, i.e., a Big Crunch? To answer this question the contents of the Universe have to be evaluated with enough precision. In particular, the value of the density parameter Ω must be known. Its value is given by $\Omega = \frac{8\pi G\rho}{3H^2}$, where ρ is the energy density of the Universe and H is the Hubble parameter (with H_0, Hubble's "constant", being its present-day value). It may also be written as $\Omega = \rho/\rho_c$, where $\rho_c = \frac{3H^2}{8\pi G}$ is the critical density.

In the absence of vacuum energy (such as a cosmological constant), the Universe would continue to expand if $\Omega \leq 1$, and would recollapse if $\Omega > 1$. Vacuum energy changes this picture, however, as will be mentioned in the following section.

2.2 The dark matter problem

2.2.1 Origins of the dark matter problem

In 1933, Fritz Zwicky was the first author to mention a clear discrepancy between visible mass and radial velocities after studying eight galaxies in the Coma cluster [75, 76]. Later, strong evidence for dark matter came from galactic rotation curves. In 1939 Horace W. Babcock measured the rotation of the Andromeda galaxy, Milky Way's largest neighbour, and found that outer regions had a higher velocity than what should be expected from the luminous matter content in the galaxy [77].

However, insufficient data and uncertainties in astronomical parameters, such as the value of Hubble's constant H_0 which relates redshift and distance, limited progress in the following decades. It was only in the 1970s that the discrepancy between visible matter and the observed gravitational interactions was acknowledged as a central subject in astrophysics [78, 79, 80]. In addition, the development of inflationary cosmology in the 1980s pointed towards a flat Universe scenario ($\Omega = 1$) [81] while the observation of luminous matter showed $\Omega_{lum} \ll 1$ [82]. Two competing explanations were put forward for this discrepancy:

- *Dark matter*: there is a large amount of matter in the Universe which is not detectable except for its gravitational effect.
- *Modified gravity*: on large scales such as those of galaxies and galaxy clusters, the behaviour of gravitation departs from what is predicted by General Relativity.

In recent decades dark matter gradually became the generally accepted explanation [62], although some researchers continue to pursue the modified gravity approach [83].

Variants of the dark matter scenario were developed between the 1970s and 1990s, many of which explained the invisible mass exclusively in terms of some form of baryonic matter, e.g., MACHOs (MAssive Compact Halo Objects) [84]. Some models used neutrinos, known to be very abundant in the Universe, as the primary dark matter component assuming they had a non-zero mass (which had not yet been proven at the time) [85]. Other models predicted the existence of new kinds of particles (such as Weakly Interacting Massive Particles, WIMPs) [85]. Mixed scenarios with different kinds of dark matter constituents were also considered.

2.2.2 Observational evidence for non-baryonic dark matter

Observational cosmology made great progress in the last two decades. Results from different experiments dramatically improved the knowledge of cosmological parameters, finally leading to reliable conclusions with respect to the long-term result of universal expansion. One of the results of such progress was the establishment of dark matter as a major component of the present-day Universe.

Advances in the observation of supernovae at different redshifts led in 1998 to the unexpected discovery of an acceleration in the expansion of the Universe [86, 87, 88]. This acceleration may be interpreted as the effect of a vacuum energy density, called *dark energy*, a term coined in 1998 by Michael S. Turner [89]. This vacuum energy appears to be similar to Einstein's cosmological constant, that is, it is constant in time and in space, or at least varies very slowly [90]. It is currently the largest fraction of the Universe's total energy density, as detailed below.

The detection of fluctuations in CMB radiation was first reported in 1992 from data obtained by the Cosmic Background Explorer (COBE) satellite [92]. Precision measurements of the CMB spectrum and its fluctuations made in the last decade by the WMAP (Wilkinson Microwave Anisotropy Probe) satellite (Fig. 2.1), together with other observations (such as those of high-redshift supernovae [93] and Baryon Acoustic Oscillations (BAO) [94]), led to what is now called the Λ-CDM model or concordance model. According to this model, the Universe is flat ($\Omega = 1$) and its energy density is distributed (according to the most recent available data [95]) as

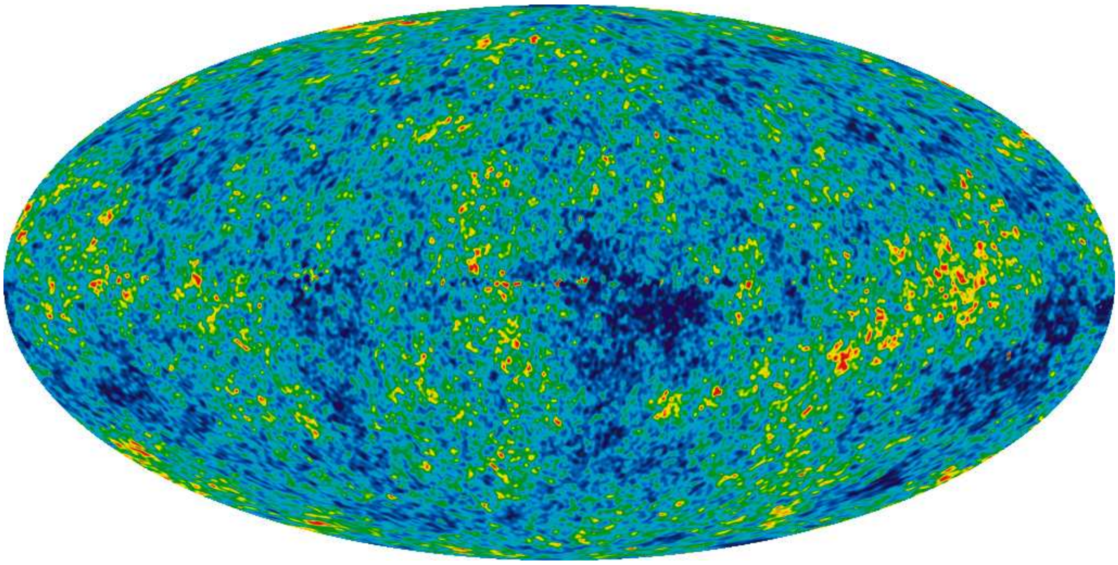

Figure 2.1: *Map of cosmic microwave background fluctuations obtained from seven years of WMAP data. From the WMAP webpage* [91].

follows:

- **Dark energy**: $\Omega_\Lambda = 0.728^{+0.015}_{-0.016}$
- **Dark matter (non-baryonic)**: $\Omega_c = 0.227 \pm 0.014$
- **Baryons**: $\Omega_b = 0.0456 \pm 0.0016$

Detailed measurements of the abundances of the lightest isotopes, essentially produced during the Big Bang nucleosynthesis, firmly placed the density of baryonic matter Ω_b in the $0.04 - 0.05$ range as indicated above (Fig. 2.2). This is significantly higher than the total visible matter content in galaxies [96], meaning that baryonic dark matter *does* exist. On the other hand, this value is much lower than the estimated total matter density $\Omega_m \simeq 0.27$, leading to the conclusion that over 80% of the Universe's matter content is not only dark but also non-baryonic, that is, *non-baryonic dark matter*.

In the past neutrinos were major dark matter candidates, but the three known neutrino types (ν_e, ν_μ, ν_τ) have now been excluded as dominant constituents of dark matter since they would necessarily be "hot", i.e. relativistic due to their low masses. The limit from direct measurements of beta decay for the mass of the electron neutrino is $m(\nu_e) < 2$ eV (95% C.L.) [98], a limit that is expected to

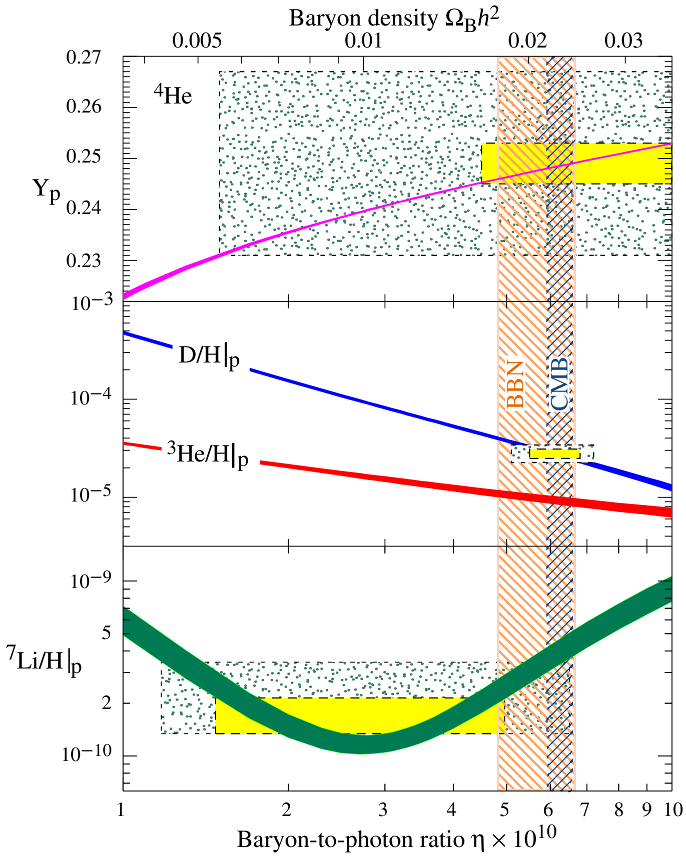

Figure 2.2: *Abundances of light isotopes as predicted by the standard model of big-bang nucleosynthesis (BBN). Bands show 95% confidence level range. Boxes indicate observed abundances (smaller: 2σ statistical errors, larger: 2σ statistical+systematic). Vertical bands indicate the CMB measure of baryon density and BBN concordance range. From Ref.* [24]. *The current value for h is* 0.705 ± 0.013 [97], *which gives* $h^2 \simeq 0.5$.

improve by an order of magnitude with the upcoming KATRIN experiment which will start collecting data in 2012 [99]. On the other hand, the differences in squared masses obtained from oscillation experiments [98]:

$$\Delta m^2_{12} = 8.0^{+0.4}_{-0.3} \times 10^{-5}\ \mathrm{eV}^2$$
$$1.9 \times 10^{-3}\ \mathrm{eV}^2 < \Delta m^2_{23} < 3.0 \times 10^{-3}\ \mathrm{eV}^2$$

are small enough to imply that the limit obtained for $m(\nu_e)$ applies to all three masses. The limit inferred from cosmological observations for the sum of the three neutrino masses is stricter: $\sum m_i < 0.67$ eV (95% C.L.) [97].

In addition to the clear discrepancy that is found when estimates for total and baryonic matter are obtained from different methods (that is, $\Omega_m > \Omega_b$), important indications for the existence of non-baryonic dark matter have also been collected from the observation of specific astronomical bodies. Rotation curves in galaxies have already been mentioned. Other methods used to evaluate the distribution of non-luminous matter include observations of graviational lensing and the study of hot gas in clusters, which can only be gravitationally bound if the cluster mass is large enough [100].

One specific case that has been identified in recent years is that of galaxy cluster 1E0657-56, the so-called “bullet cluster”. According to observations, the visible matter in this cluster is concentrated in a central region, but the total matter distribution inferred from gravitational lensing is quite different, with two independent concentrations, one on each side of the visible matter. This has been interpreted as the result of a collision between two clusters, where the visible matter in each cluster (which is obviously baryonic) interacted in such a way that friction produced a single central concentration, while the two dark matter concentrations, which are virtually non-interacting except through gravitational effects, passed through each other and continued their trajectories without significant friction [100].

Several direct detection experiments are searching for non-baryonic particles, and in particular for those that fit the promising WIMP description (such kind of particles is also predicted by supersymmetric models, as described later in this chapter). For the expected range of WIMP masses (10 GeV to 10 TeV) and velocities (hundreds of km/s, similar to relative star velocities and to the velocity at which the

Solar System is orbiting the Galactic centre) it is expected that WIMPs will interact through elastic scattering on nuclei with typical recoil energies of 1 to 100 keV [24]. Due to the expected low rates for such events (at most one event per day and per kg of material), the search for such interactions must be performed in very low-background environments, such as underground facilities using low radioactivity materials [24], similar to those used for neutrino experiments.

However, while dark matter studies based on astronomical observations have yielded major results in the last two decades, the same has not occurred in the area of direct detection. Until now, no undisputed evidence of a dark matter signal was reported by any of the different experiments in this field.

During the last decade, one of the collaborations involved in this search, the DAMA project (DAMA/Nai and DAMA/LIBRA experiments) has been reporting a periodic signal that is interpreted by the DAMA collaboration as being due to dark matter detection [101]. Oscillations in the DAMA signal are compatible with the period (one year) and the phase (peak at June 2) that would be expected from variations in dark matter annihilation rates due to the Earth's trajectory as it orbits the Sun while moving in the Galaxy along with the rest of the Solar System.

However, the DAMA signal has not been accepted as evidence for dark matter. Negative results reported by other direct detection experiments are incompatible with DAMA in a typical WIMP scenario, meaning that either the DAMA signal is due to a WIMP with unexpected properties or it is not due to dark matter detection but instead to some other effect [102]. This issue should be settled in the next few years, as DAMA continues to collect data and other experiments become increasingly sensitive.

2.3 Supersymmetry as a possible solution to the dark matter problem

The Standard Model (SM) of particle physics is now well established. All particles predicted by the SM have now been discovered, with the exception of the Higgs boson which is expected to be discovered at CERN's Large Hadron Collider. Table 2.1 list the elementary particles included in the Standard Model.

STANDARD MODEL PARTICLES

	Particle	Mass (GeV/c^2)	electric charge	spin
Quarks	u	$(1.5 \text{ to } 3.3) \times 10^{-3}$	$+2/3$	$1/2$
	d	$(3.5 \text{ to } 6.0) \times 10^{-3}$	$-1/3$	$1/2$
	c	$1.27^{+0.07}_{-0.11}$	$+2/3$	$1/2$
	s	$0.104^{+0.026}_{-0.034}$	$-1/3$	$1/2$
	t	171.2 ± 2.1	$+2/3$	$1/2$
	b	$4.20^{+0.17}_{-0.07}$	$-1/3$	$1/2$
Leptons	e^-	5.110×10^{-4}	-1	$1/2$
	ν_e	$< 2 \times 10^{-6}$	0	$1/2$
	μ^-	0.1057	-1	$1/2$
	ν_μ	$< 2 \times 10^{-6}$	0	$1/2$
	τ^-	1.777	-1	$1/2$
	ν_τ	$< 2 \times 10^{-6}$	0	$1/2$
Gauge bosons	γ	0	0	1
	$W^\pm$	80.4	± 1	1
	Z^0	91.2	0	1
	g	0	0	1
Higgs boson	H^0	114 to 158 or 175 to 185 (95% C.L.)	0	0

Table 2.1: *List of Standard Model particles. Each quark and lepton has an antiparticle which is not listed. Data on particle masses are from Ref.* [24]*. The mass limits for H^0 include the results of Tevatron collaborations announced in July 2010* [103].

Until now, the only departure observed from the expected SM properties is in the case of neutrino masses, which are predicted to be zero in the SM. The discovery of neutrino oscillations indicates that neutrinos have small masses although, as previously mentioned, their values have not been directly measured until now.

Since none of the Standard Model particles appear to be a good candidate to the role of main dark matter constituent, research is now focused on a number of unobserved particles whose existence is predicted by different models.

Supersymmetry (SUSY) [104], which has been developed since the 1970s, is a very promising extension of the Standard Model that gradually became a major subject of research. Supersymmetry predicts that each of the elementary particles in the SM will have a "superpartner" with a spin differing by 1/2, that is, each boson will have a fermion superpartner and vice-versa. In addition, in supersymmetric models the Higgs sector must be expanded. In the Minimal Supersymmetric Model (MSSM), instead of a single Higgs boson H^0, there are three neutral Higgs particles, h^0, H^0 and A^0, and a pair of charged particles $H^\pm$ [105].

Some superpartners will mix. In particular, the superpartners of the neutral electroweak bosons (γ and Z^0) and neutral Higgs bosons h^0 and H^0 mix and give rise to four *neutralinos* ($\tilde{\chi}_1^0$, $\tilde{\chi}_2^0$, $\tilde{\chi}_3^0$, $\tilde{\chi}_4^0$), while the superpartners of $W^\pm$ and $H^\pm$ mix to form two *charginos* ($\tilde{\chi}_1^\pm$, $\tilde{\chi}_2^\pm$).

Table 2.2 lists the supersymmetric partners predicted by SUSY.

There are important theoretical motivations for SUSY, namely the unification of the three gauge couplings at high energy in a way that is not possible in the Standard Model [24]. If supersymmetry does exist it must be broken, since unbroken SUSY would imply that the masses of SM particles and of their superpartners would be the same, which is clearly not the case [24]. Theoretical considerations suggest that, if it exists, SUSY will likely be found at the TeV scale [24], possibly within the reach of the LHC.

2.3.1 The lightest neutralino as a dark matter candidate

If supersymmetry exists, it is generally expected that the multiplicative quantum number R, known as *R-parity* and defined as

$$R = (-1)^{3B+L+2S}$$

SUPERSYMMETRIC PARTNERS

	Particle	electric charge	spin
Squarks	$\tilde{u}$, $\tilde{c}$, $\tilde{t}$	$+2/3$	0
	$\tilde{d}$, $\tilde{s}$, $\tilde{b}$	$-1/3$	0
Sleptons	$\tilde{e}^-$, $\tilde{\mu}^-$, $\tilde{\tau}^-$	-1	0
	$\tilde{\nu}_e$, $\tilde{\nu}_\mu$, $\tilde{\nu}_\tau$	0	0
Gluinos	$\tilde{g}$	0	1/2
Neutralinos	$\tilde{\chi}_1^0$, $\tilde{\chi}_2^0$, $\tilde{\chi}_3^0$, $\tilde{\chi}_4^0$	0	1/2
Charginos	$\tilde{\chi}_1^\pm$, $\tilde{\chi}_2^\pm$	± 1	1/2

Table 2.2: *List of superpartners predicted by supersymmetry. Each squark and slepton has an antiparticle which is not listed. Neutralinos and charginos are mass eigenstates corresponding to mixtures of superpartners (see main text for details).*

where B is the baryon number, L is the lepton number and S in the spin, will be conserved [106].

The conservation of R-parity means that the decay of any supersymmetric particle will necessarily produce at least one other supersymmetric particle, leading to the lightest supersymmetric particle (LSP) being stable. In most SUSY scenarios this particle is the lightest of the four neutralinos. The lightest neutralino $\tilde{\chi}_1^0$ — hereafter simply referred to as "neutralino" — is expected to have a mass of the order of a few hundred GeV. Observation of the Universe's large scale structure indicates that dark matter is non-relativistic, that is, "cold". The neutralino fits this description and therefore arises as a dark matter candidate of the WIMP kind.

2.3.2 Supersymmetry signals on the cosmic-ray spectrum

Even if neutralinos exist in large numbers, as required to comprise the known dark matter density, they will not be easily detectable by direct means since, apart from their gravitational influence, they only interact via the weak nuclear force [107], meaning that like neutrinos they can cross astronomical bodies such as stars or planets without interacting.

However, indirect signals of neutralino presence might be detected in cosmic rays. The neutralino is its own antiparticle, and neutralino annihilation ($\tilde{\chi}_1^0\tilde{\chi}_1^0 \rightarrow ...$) will occur, particularly in regions of space with a high density of these particles, e.g. galactic halos.

The products of neutralino annihilation will have a composition and energy spectrum different from those found in ordinary cosmic rays. Identical numbers of particles and antiparticles will be produced, with a significant fraction having low energies due to kinematical reasons.

In general, antimatter channels are better suited for this kind of search due to the much lower number of antiparticles compared to particles in the global cosmic flux. Promising channels for indirect neutralino detection include positrons, antiprotons and antideuterons [64]. Further discussion on the antideuteron case will be presented in Chapter 10.

2.4 Conclusions

Dark matter is well established as a major component of our Universe, but its composition remains a mystery. It is now certain that most dark matter is not made of any of the currently known types of particles. A number of experiments are underway aiming at the direct detection of dark matter particles but no conclusive evidence has been found yet.

Among dark matter candidates, WIMPs, with masses around the order of the TeV, are particularly promising since they fit the cold dark matter scenario inferred from astronomical observations and at the same time are a consequence (in the form of neutralinos) of well-motivated supersymmetric extensions of the Standard Model.

If supersymmetry exists and neutralinos are the main component of dark matter, the spectrum of cosmic rays should include a component due to neutralino annihilation. Such component must be disentangled from a large background of conventional events. Antimatter channels (positrons, antiprotons, antideuterons) are the most promising for this kind of study.

Part II

Experimental setup

Chapter 3

The AMS experiment

3.1 Detection of cosmic rays in space

Cosmic rays interact strongly with the Earth's atmosphere. The probability of a charged cosmic-ray particle reaching sea level without interacting is virtually zero. This fact has led to the development of experiments for the detection of cosmic rays at the highest possible altitude.

The usage of balloons for cosmic-ray detection has a long tradition going back to the original discovery of the phenonenon by Victor Hess. Valuable information has been collected from number of balloon experiments, usually flown at very high altitudes (tens of km) in polar regions where the effect of the geomagnetic cutoff is lower.

However, balloon experiments are limited by three severe constraints. One is a maximum altitude of $\sim$ 40 km, which implies that a non-negligible atmosphere (at least a few g/cm^2) is always present above the detector. Another constraint is related to the mass of the detector and consequently to its size: the experimental apparatus has to be light enough to be lifted to a very high altitude. Finally, the duration of the experiment is also limited: the longest balloon flights on record did not exceed a few weeks.

Given the limitations of the balloon approach, taking the detection of cosmic rays to outer space appears to be a natural next step. Space provides a nearly perfect vacuum even at low Earth orbits, keeping undesired particle interactions at a very low level. Mass limits are a significant constraint for any space experiment, but existing launchers are able to put several tonnes in orbit. In addition, a space experiment may operate for a number of years in a stable orbit, providing the time needed for collecting a very large statistics of events, making possible a detailed study not only of the major components of cosmic rays but also of less abundant particles.

The concept of a charged cosmic-ray spectrometer in space was developed in recent years by two collaborations, AMS, which plans to place a large detector at the International Space Station, and PAMELA [108], a smaller satellite-based experiment which is operating since 2006.

3.2 The AMS collaboration

AMS (Alpha Magnetic Spectrometer) is a broad international collaboration involving many hundreds of researchers from 56 institutes in 16 countries [109]. The original proposal for the experiment [110] was approved by the United States Department of Energy in April 1995.

The collaboration's goal of taking a particle spectrometer to space was achieved in two stages: a test flight with a simplified detector aboard the Space Shuttle, which took place in 1998, and a second mission aboard the International Space Station, now scheduled to start in 2011 and expected to last for several years.

3.3 First phase: AMS-01

The AMS concept was initially put to test through the construction of a preliminary detector, AMS-01, which was flown aboard U.S. Space Shuttle Discovery in June 1998.

The AMS-01 detector

The AMS-01 detector was a simplified version of the final spectrometer AMS-02. It included a permanent Nd-Fe-B magnet, a Time-of-Flight (TOF) detector with four layers, a silicon Tracker with six planes, an Aerogel Threshold Counter (ATC) and Anti-Coincidence Counters (ACC). A schematic view of the AMS-01 detector is shown in Fig. 3.1.

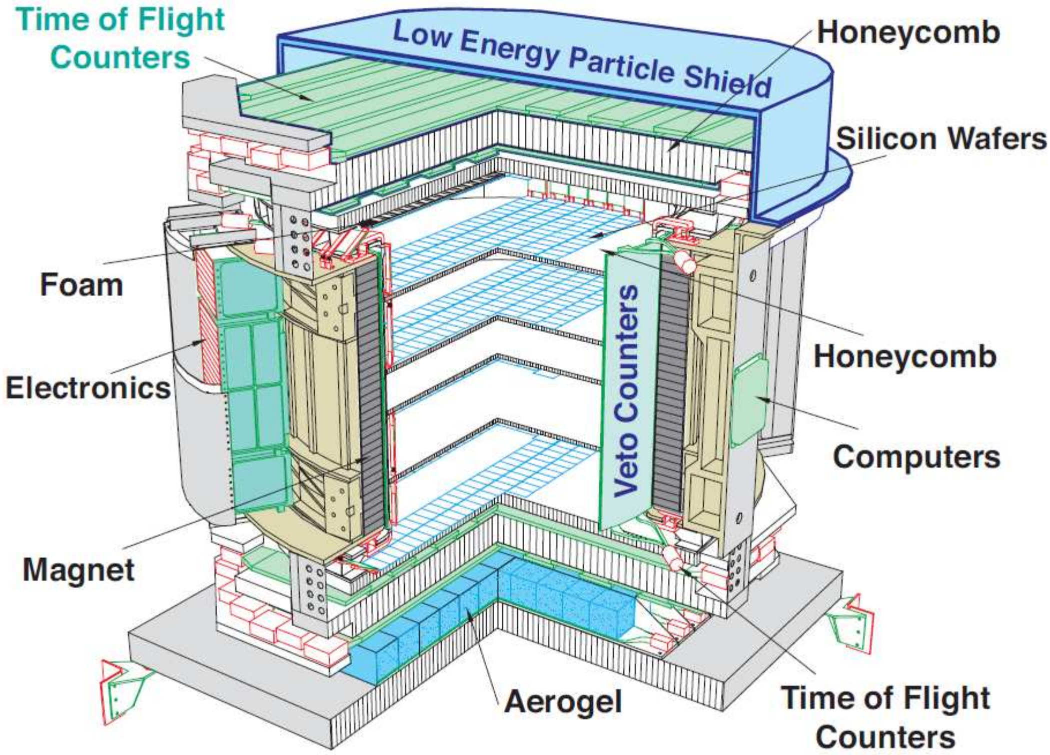

Figure 3.1: *Schematic view of the AMS-01 detector. From Ref.* [111].

The June 1998 test flight

AMS-01 was flown aboard U.S. Space Shuttle Discovery in the STS-91 mission [112], which took place between June 2 and June 12, 1998. This flight included a four-day docking with the Russian space station Mir (from June 4 to June 8) in what was the ninth and last Shuttle-Mir docking mission.

During this flight the shuttle's orbit had an inclination of 51.7° and the geodetic altitude ranged from 320 km to 390 km. Approximately 100 hours of data were taken outside the Mir docking period at zenith angles of 0° (upwards), 20°, 45° and 180° (downwards). In addition, data were taken during the Mir docking period at zenith angles varying between 40° and 145°.

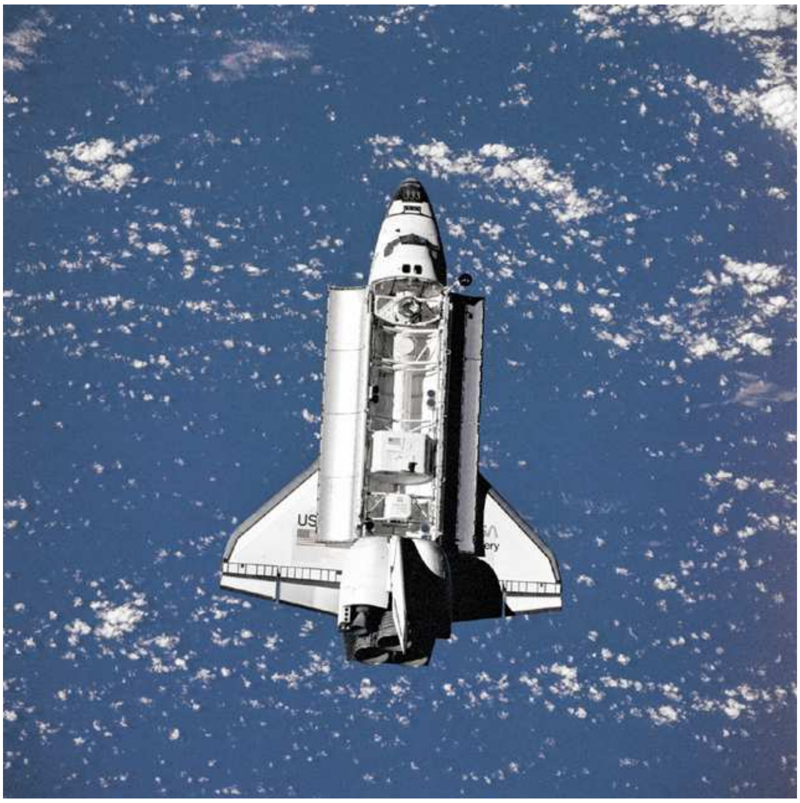

Figure 3.2: *The AMS-01 detector aboard U.S. Space Shuttle Discovery in 1998, as seen from the Russian space station Mir* [113].

AMS-01 results

The 1998 flight of AMS-01 was successful. In addition to proving the feasibility of the AMS concept, significant results were obtained regarding the cosmic-ray spectrum. In particular, the upper limit on the presence of antimatter in cosmic rays was improved to $\overline{\mathrm{He}}/\mathrm{He} < 1.1 \times 10^{-6}$ [114]. The proton spectrum was measured with high precision, and important results were obtained for other species [114].

A full report on the results obtained with the AMS-01 detector may be found in Ref. [114]. Additional results of AMS-01 may be found in Refs. [115, 116, 117, 118, 119, 120, 121].

3.4 Second phase: AMS-02

The final detector, AMS-02, is expected to be mounted on a U.S. Space Shuttle to be flown to the International Space Station (ISS) where it will acquire data for a long period, with a minimum duration of 3 to 5 years being expected.

At the time of writing, AMS-02 is expected to be flown aboard the Space Shuttle Endeavour in mission STS-134, scheduled to take off on February 26, 2011 [122]. This is expected to be the last mission of the U. S. Space Shuttle program, although the possibility of an additional mission is currently being evaluated.

The AMS-02 detector

AMS-02 is a particle detector designed to study the cosmic-ray flux by direct detection of particles above the Earth's atmosphere using state-of-the-art particle identification techniques. The detector was originally designed to be equipped with a superconducting magnet cooled by superfluid helium, but on April 18, 2010, a decision was made to replace the superconducting magnet with the permanent magnet used in the AMS-01 Space Shuttle flight [123].

The spectrometer is composed of several subdetectors: a Transition Radiation Detector (TRD), a Time-of-Flight (TOF) detector, a Silicon Tracker, Anticoincidence Counters (ACC), a Ring Imaging Čerenkov (RICH) detector and an Electromagnetic Calorimeter (ECAL). Fig. 3.3 shows a schematic view of the full AMS-02 detector.

The main components of AMS-02 are described below.

The permanent magnet

The AMS permanent magnet was used in the AMS-01 test flight and, following the April 2010 decision, is also being used in AMS-02, replacing the superconducting magnet. A schematic diagram of the AMS permanent magnet is shown in Fig. 3.4.

The permanent magnet is made from 64 high-grade Nd-Fe-B sectors, with each sector being composed of 100 blocks. The configuration used, shown in Fig. 3.5, produces a magnetic field of 0.15 T with negligible dipole moment. The bending power obtained is $BL^2 = 0.15$ Tm^2 [111].

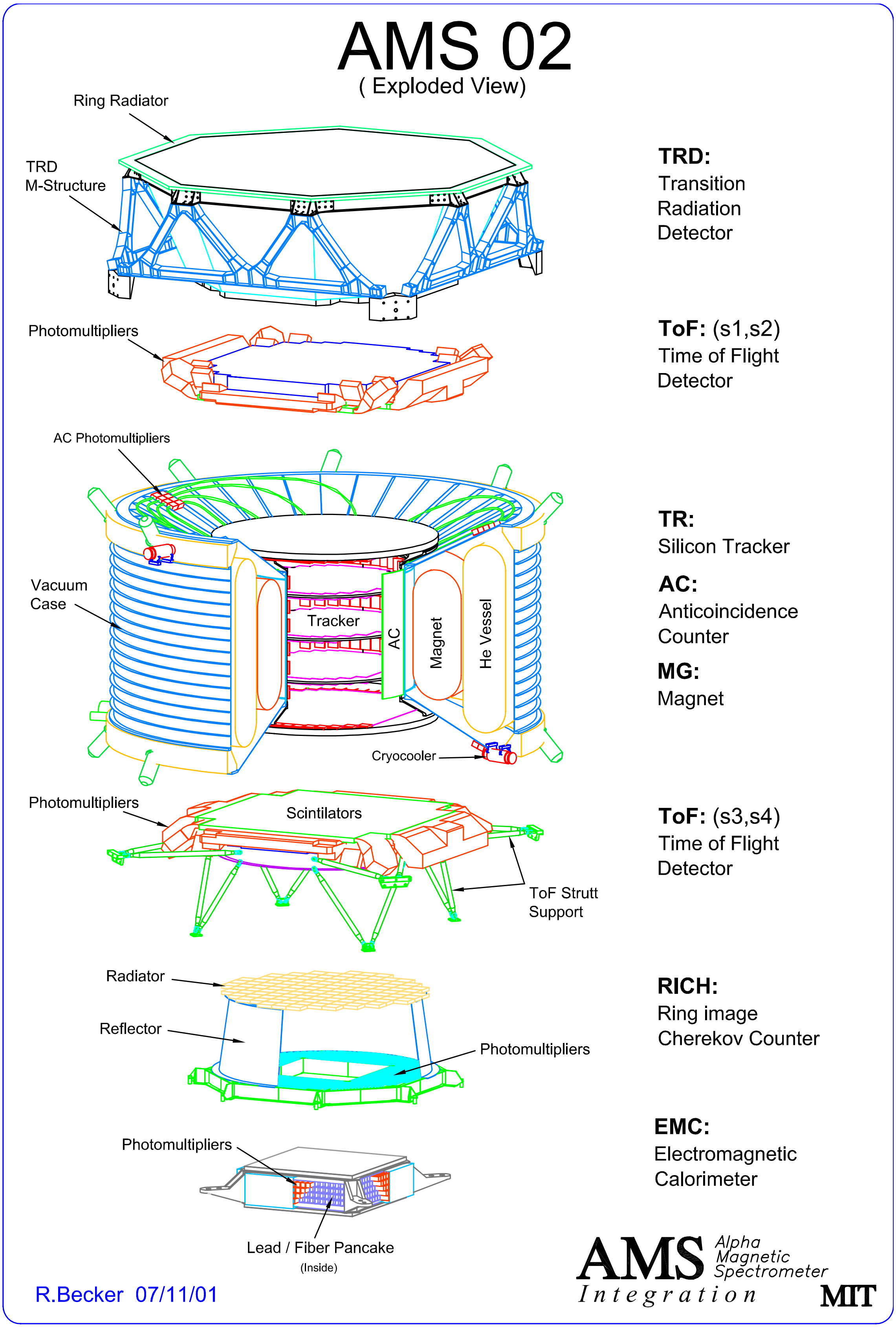

Figure 3.3: *Exploded view of the AMS-02 detector* [124]*. The Tracker planes are shown in the original configuration used until April 2010.*

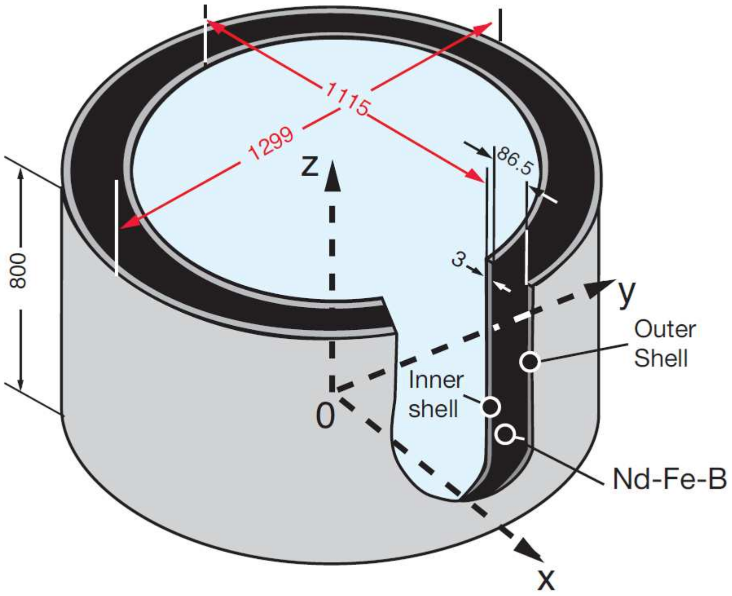

Figure 3.4: *The AMS permanent magnet. From Ref.* [111].

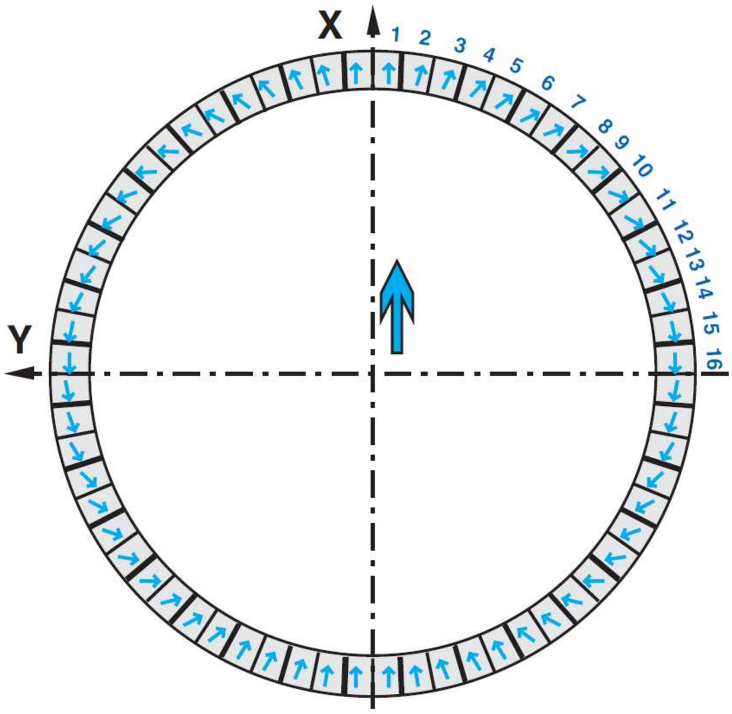

Figure 3.5: *Magnetic field orientation of the AMS permanent magnet. From Ref.* [111].

The superconducting magnet

Prior to the decision on the magnet change described above, the bending power needed for particle identification in AMS-02 was provided by a superconducting magnet (Fig. 3.6) with a field $B = 0.860$ T and a bending power $BL^2 = 0.862$ Tm^2 [111].

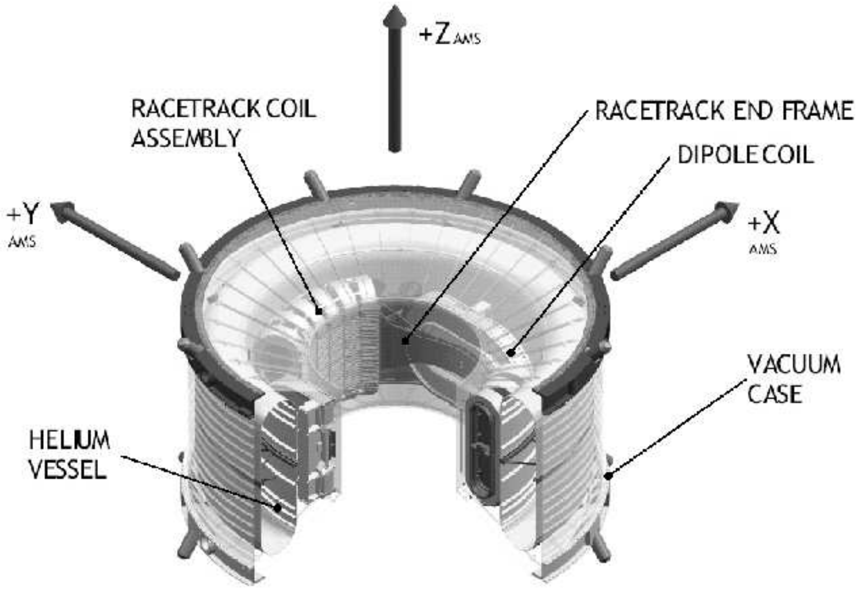

Figure 3.6: *The AMS-02 superconducting magnet.*

The AMS-02 superconducting magnet has a total of 14 superconducting coils (Fig. 3.7). The two large coils generate the magnetic dipole field perpendicular to the experiment axis, while the 12 flux return coils control the stray field and also contribute to the dipole field.

The current in the superconducting magnet is carried by niobium-titanium (NbTi) filaments developed specifically for this experiment by ETH Zürich. This material is superconducting at temperatures below 4 K.

The magnet cooling system uses superfluid liquid helium. Liquid helium becomes a superfluid below 2.17 K, and the system operates at 1.8 K. The helium vessel is a toroidal tank made of aluminium with a volume of 2500 ℓ.

The magnet was planned to be launched at operating temperature but with no field.

The superconducting magnet was used in tests performed with the full AMS-02

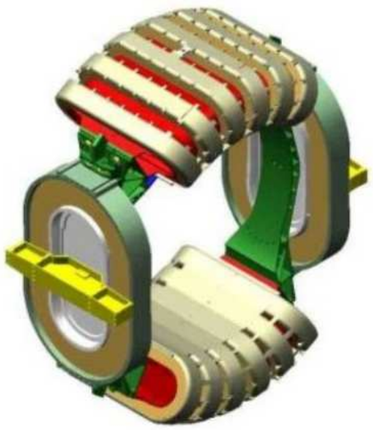

Figure 3.7: *The AMS superconducting magnet coils.*

detector during 2009, including the December 2009 cosmic tests used in the long-term light yield stability studies of Chapter 8, and also in tests performed in the first months of 2010.

The Transition Radiation Detector (TRD)

The Transition Radiation Detector (TRD) of AMS-02 is placed at the top of the detector, therefore being the first subdetector that a typical cosmic-ray particle will cross.

Transition radiation is the electromagnetic radiation emitted when charged particles cross the boundary between two media with different dielectric properties. Since the probability of a particle emitting a photon at one such boundary is very small, a multilayer structure is used in the TRD. The transition radiation is proportional to the particle's Lorentz factor $\gamma = \frac{1}{1-\sqrt{v^2/c^2}} = E/m$. Since the emission of this radiation has a threshold of $\gamma \approx 500$, protons and other nuclei will have a much lower probability of emitting transition radiation than electrons and positrons. Such difference provides an important method for p/e discrimination at energies of tens to hundreds of GeV.

The AMS-02 TRD consists of 328 modules, each having a fleece radiator with a thickness of 20 mm and straw tube proportional wire chambers filled with a

Xe/CO_2 (80%:20%) mixture (Fig. 3.8) to detect the transition photons produced. The modules are arranged in 20 layers supported by an octagonal pyramidal structure (Fig. 3.9).

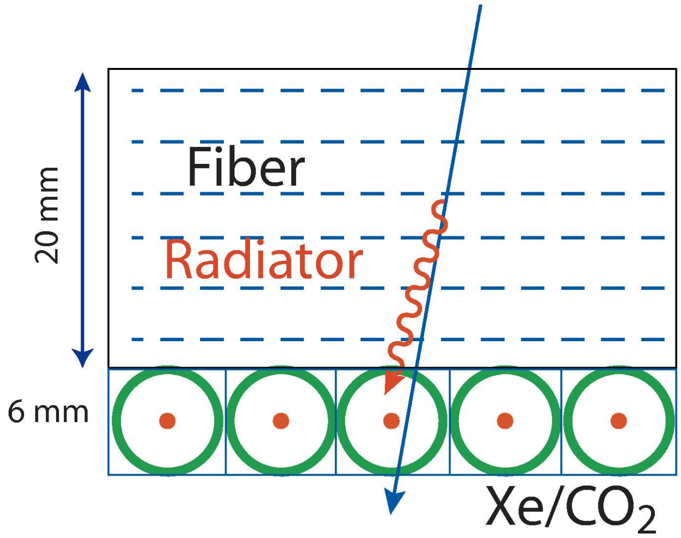

Figure 3.8: *Schematic view of a TRD module.*

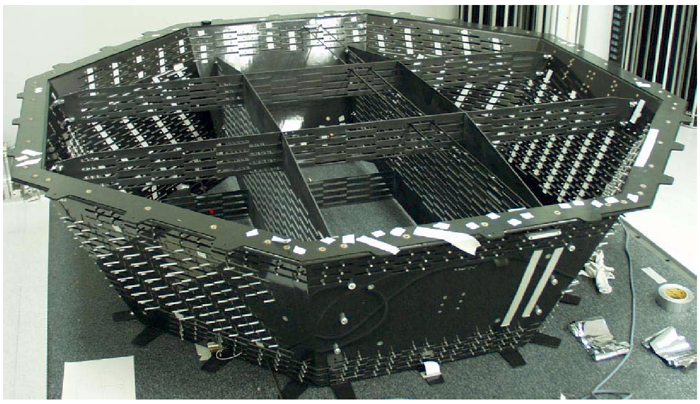

Figure 3.9: *The AMS-02 TRD support structure.*

The Time-Of-Flight (TOF) detector

The AMS-02 Time-Of-Flight (TOF) is expected not only to make velocity measurements but also to provide the fast trigger for charged particles and also converted photons.

The TOF system consists of two parts, the upper and lower TOF, separated by a distance of 1 m. It has a total of four planes, two for the upper TOF and two for the lower TOF (Fig. 3.10). Each plane is roughly circular, with a sensitive area of 1.2 m^2 divided in scintillator paddles 12 cm wide with an overlap of 0.5 cm between paddles. The quality of measurements is improved by having perpendicular paddle orientations in each of the two pairs of planes.

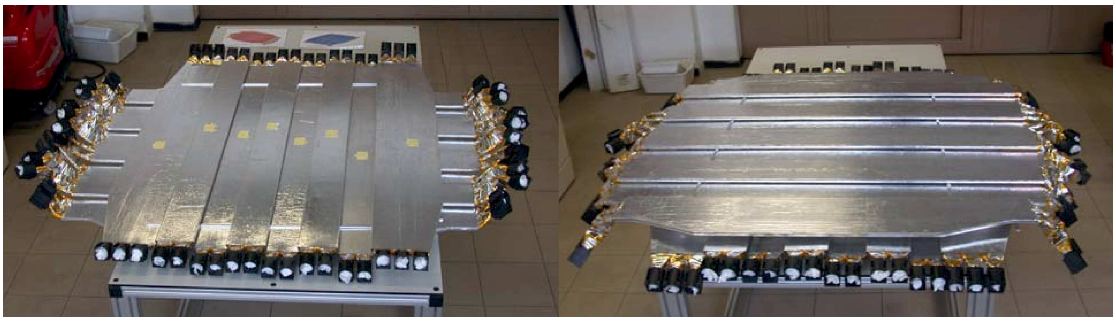

Figure 3.10: *The AMS-02 TOF during an assembly test (Left: upper TOF, Right: lower TOF).*

The expected time resolution of the AMS-02 TOF is ~ 130 ps, giving a velocity resolution $\sigma_\beta = 3\%$ for protons. In addition, the energy loss of charged particles in measured with enough accuracy to allow for charge identification up to $Z \simeq 20$.

The Silicon Tracker

The Silicon Tracker is placed at the centre of the AMS-02 detector. In its original layout (used in all simulation and real data studies presented in this thesis), the tracking system is made of eight layers of double-sided silicon microstrips. The layers are arranged in five tracker planes, with the three inner planes having ladders on both sides and the two outer planes only having a ladder on one side.

At the time of the decision on the replacement of the AMS-02 magnet, it was decided to make a small change in the Tracker layout with the goal of partially compensating for the loss in bending power. This change affected each end of the

Tracker. Instead of having all Tracker layers placed between the upper and lower TOF planes, as shown in Fig. 3.3, the upper layer, which was just below the upper TOF, was moved to the top of the TRD, while the lower layer, placed just above the lower TOF, became smaller and part of its material was included in a new ninth layer which was placed between the RICH and ECAL detectors.

Tracker planes have approximately the same dimensions of TOF planes. One of the inner Tracker planes is shown in Fig. 3.11.

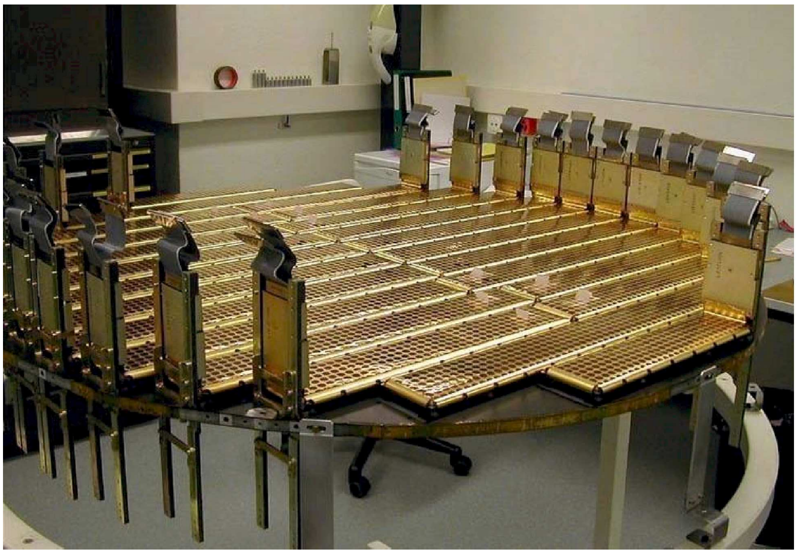

Figure 3.11: *Inner plane of the AMS-02 Tracker.*

In its original layout, the AMS-02 Tracker is expected to perform measurements of particle positions with a precision of $\sim 10\ \mu$m along the bending plane (yOz) and $\sim 30\ \mu$m on the transverse direction. For the same layout, particle rigidity should be measured with a precision of 2% at a few GV, with rigidities measurable up to the TV region.

Like the TOF, the Tracker will be able to measure particle charge from energy deposition. It is expected that such measurement will be possible up to $Z \simeq 26$.

The Anti-Coincidence Counters (ACC)

The Anti-Coincidence Counters (ACC) of AMS-02 are placed inside the inner bore of the detector's magnet. Their purpose is to detect particles entering the Tracker laterally, outside the main acceptance, which may create signals in the detector leading to bad event reconstructions. There are a total of 16 scintillator panels placed vertically around the central detector region, as shown in Fig. 3.12.

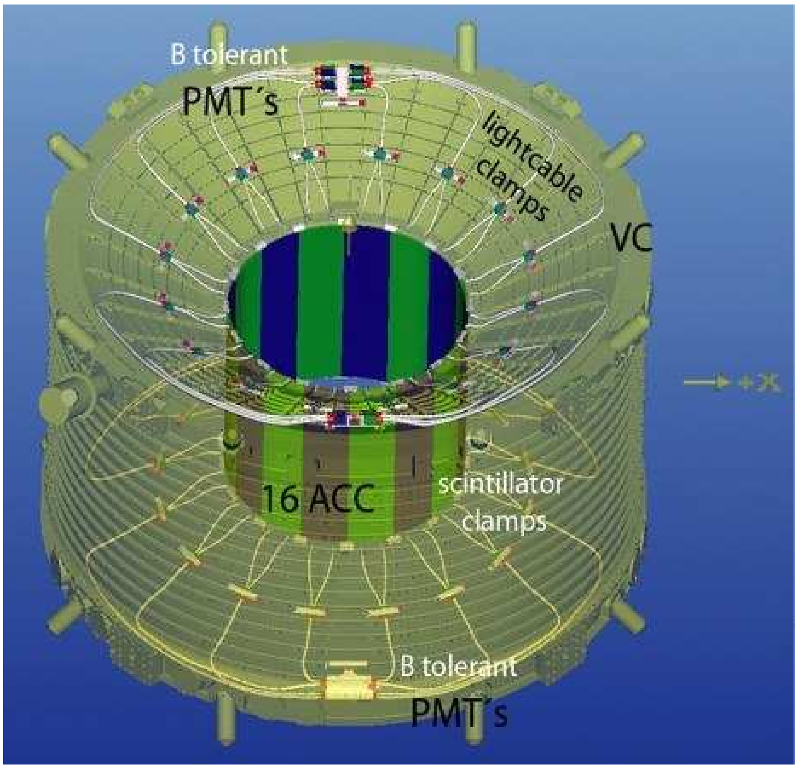

Figure 3.12: *The AMS-02 system of Anti-Coincidence Counters.*

The Ring Imaging Čerenkov (RICH) detector

The Ring Imaging Čerenkov (RICH) detector of AMS-02 is a proximity focusing detector with a dual radiator composed of silica aerogel with $n = 1.05$ and sodium fluoride (NaF) with $n = 1.33$. It is placed immediately below the lower TOF and above the ECAL detector. This subdetector will be discussed in detail in the next chapter.

The Electromagnetic Calorimeter (ECAL)

The Electromagnetic Calorimeter (ECAL) was included in AMS-02 to provide the detector with gamma-ray detection capabilities. It is placed at the bottom of the detector, below the RICH. A wide energy range, from GeV up to TeV, will be detectable.

The ECAL is a fine-grained lead-scintillating fibre sampling calorimeter with an active area of 648×648 mm^2 and a thickness of 166.5 mm. It is made of superlayers made of 1 mm lead foils interleaved with scintillating fibres with a diameter of 1 mm and glued together with epoxy Fig. 3.13. This design allows for precise 3-dimensional imaging of longitudinal and lateral shower development.

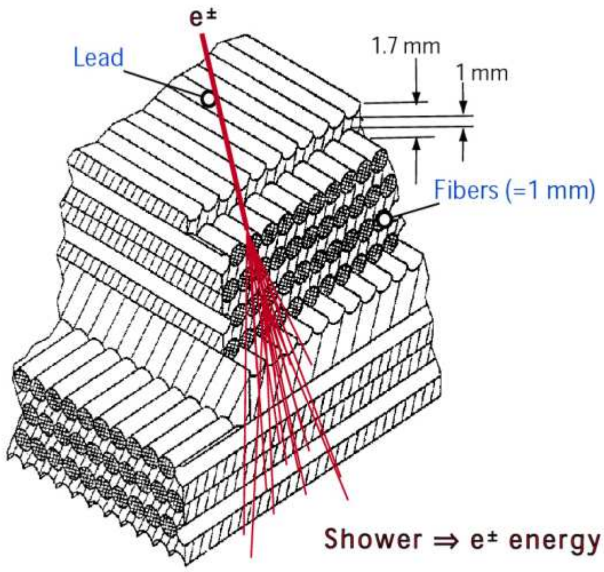

Figure 3.13: *Structure of the AMS-02 ECAL system.*

Photons may be detected in two ways: either by the direct measurement of a photon interaction in the ECAL or through the identification of a particle-antiparticle pair produced in the material of a previous subdetector.

The AMICA Star Tracker

The AMS-02 star tracker, termed AMICA (Astro Mapper for Instrument Check of Attitude), is attached to the Silicon Tracker structure. Its purpose is to provide measurement of the detector's orientation to allow for the identification of γ-ray sources. Such identification is not necessary in the case of charged particles, since their trajectories are far from being straight lines, and therefore they do not point to their sources.

The AMICA instrument consists of a pair of small optical telescopes mounted on either side of the Silicon Tracker. It will be able to provide a real-time 3D trans-formation of the AMS mechanical x-y-z frame to sky coordinates with a precision better than 20 arcseconds at rates up to 20 Hz.

Detector assembly

The assembly of the AMS-02 detector took place at the AMS experimental hall located in building 867 of CERN's Prévessin site near Geneva.

The detector was assembled for the first time, without magnet, in the beginning of 2008 (Fig. 3.14). Following a series of tests, including the acquisition of cosmic-ray events (see Chapter 8), the detector was disassembled again, since it would not possible to add the magnet directly to the assembled detector.

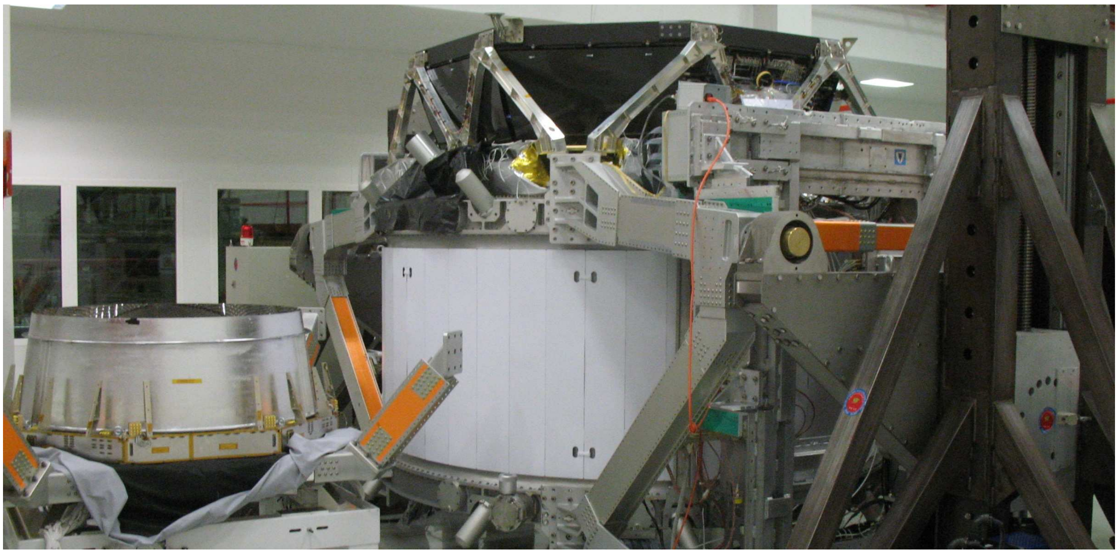

Figure 3.14: *The AMS-02 detector during its first assembly at CERN in February 2008. The RICH mirror and detection matrix are on the left.* [125]

The AMS-02 superconducting magnet arrived at the CERN assembly site in December 2008 (Fig. 3.15). The second assembly of the detector, including this magnet, took place during 2009. AMS-02 underwent a beam test at CERN's SPS in February 2010 before being shipped to ESTEC where it underwent additional testing. Immediately after the end of the ESTEC test campaign it was decided (on April 18, 2010) to replace the superconducting magnet in AMS-02 with the permanent magnet used in AMS-01. This decision was motivated by the results of the thermal/vacuum testing at ESTEC, which indicated that the superconducting magnet would only be able to operate for approximately 20 months [123]. Minor changes were also decided on the configuration of the Silicon Tracker, as previously mentioned, to improve its measurement of the particle's trajectory and therefore compensate the loss in measument accuracy derived from the reduction in the magnetic field intensity [123]. Such decision implied a delay of a few months in the AMS schedule. The magnet swap took place in June 2010 [123]. A final beam test took place at CERN during August 2010.

Following the last tests, AMS-02 flew on August 26, 2010 aboard a United States Airforce C-5M Super Galaxy [123] to NASA's Kennedy Space Center where it will be mounted on the Space Shuttle and fly to the International Space Station.

Figure 3.15: *Arrival of the AMS-02 superconducting magnet at the AMS experimental hall on December 18, 2008.* [126]

AMS-02 in space

The AMS-02 detector will be carried by a U.S. Space Shuttle to the International Space Station where it will be mounted and is expected to collect data for several years.

The required power (2 kW) will be provided by the ISS's electrical system.

Fig. 3.16 shows an artistic impression of the detector installed on the International Space Station.

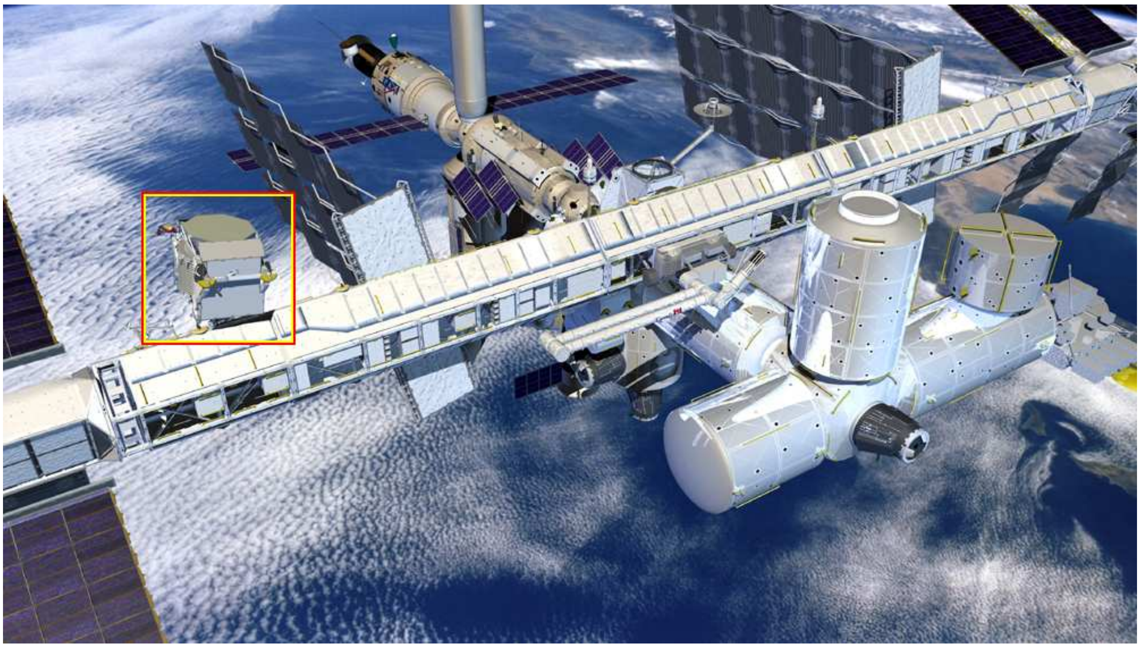

Figure 3.16: *Artistic impression of AMS-02 on the International Space Station* [124].

Goals of AMS-02

The AMS experiment has three main goals: a detailed measurement of the cosmic-ray spectrum, the search for possible cosmological antimatter, and the search for indirect dark matter signals. In addition, is Electromagnetic Calorimeter will allow AMS to collect data on γ-rays.

Measurement of the cosmic-ray spectrum

The long exposure time and large acceptance (~ 0.5 m^2·sr) of AMS-02 will enable it to collect an unprecedented statistics of more than 10^{10} events, leading to detailed energy spectra of different particles.

Charge identification will be possible up to the iron region ($Z = 26$). Mass separation was expected to be attainable for the lightest elements (up to $Z = 4$) prior to the decision on the magnet replacement, which may have some effect on the detector's capabilities for this task.

Search for cosmological antimatter

The origin of the matter-antimatter asymmetry is one of the unsolved problems in standard cosmology. It is generally assumed that the Universe had similar amounts of matter and antimatter in its earliest stages. However, our visible Universe shows no signs of such symmetry: either (a) some process acting differently on matter and antimatter created today's asymmetry, or (b) matter and antimatter were segregated and what is observed corresponds to a local variation, the Universe as a whole having domains of matter like ours but also domains of antimatter.

The absence of significant signals of matter-antimatter annihilation means that, if antimatter domains exist, they are at least tens of Mpc away from us. But, due to the low particle density of intergalactic space, it is conceivable that antiparticles from those very distant domains could arrive on Earth in small quantities. Production of nuclear antimatter with $Z > 1$ from ordinary matter is so unlikely that the unambiguous detection of a single anti-helium nucleus would be a signal of the existence of antimatter domains in the Universe. Anti-carbon would be a clear signal of the existence of anti-stars.

With its unprecedented statistics, AMS-02 has a unique chance of finding one of those elusive antinuclei, or at least greatly improving the existing limits on their abundance.

Search for indirect dark matter signals

As described in Chapter 2, it is likely that interactions involving the yet undiscovered non-baryonic dark matter constituents will make a small contribution to the global cosmic-ray flux observed at Earth, especially in the case of antiparticles. The AMS experiment, with its very high statistics and excellent particle identification capabilities, will be in a good position to identify that contribution. A study on the AMS capabilities for the detection of a dark matter signal was performed in the context of this thesis and is presented in Chapter 10.

3.5 The AMS-02 software chain

A full-scale detector simulation and offline reconstruction software was developed in the framework of the AMS-02 collaboration. The main code was written in the C++ language with physical processes being simulated using the GEANT toolkit [127, 128, 129]. Event simulation and offline event reconstruction are incorporated into a single software package. Results of event reconstruction and analysis are stored in ROOT format [130].

Reconstruction algorithms, written in C++ and Fortran, were developed by several groups (including the LIP Lisbon group) participating in the AMS collaboration.

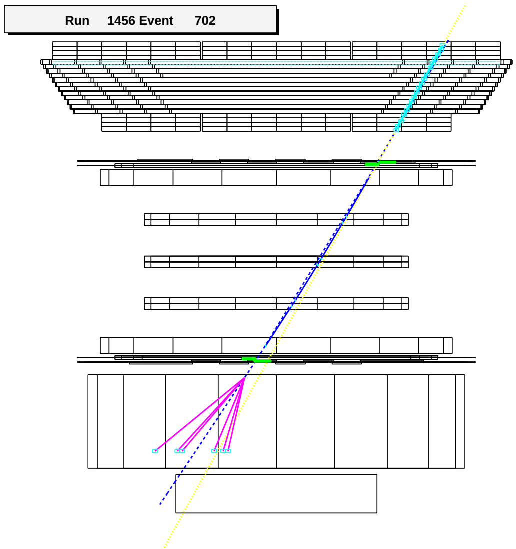

Figure 3.17: *A simulated proton event as seen in the AMS-02 display.*

The LIP contribution to the AMS software chain included RICH reconstruction algorithms for particle velocity and charge with and without particle data from outside the RICH. Most algorithms had initially been developed and tested in the framework of the standalone RICH simulation. A detailed description of the standard LIP velocity and charge reconstruction algorithms, which are based on Tracker data and were used for event reconstruction in part of the work presented in this thesis (Chapters 7, 8 and 10), may be found in Ref. [131]. In the context of the present work, the aforementioned algorithms were used as a base from which new reconstruction algorithms independent of Tracker data were developed. These new algorithms are presented in detail in Chapter 9.

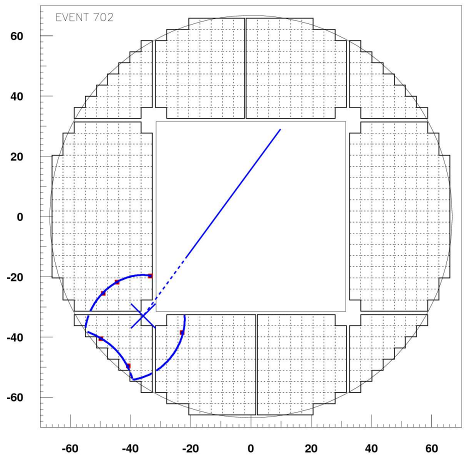

Figure 3.18: *The same event of Fig. 3.17 as seen in the RICH display developed at LIP.*

Part of the simulation work presented in this thesis was performed using the AMS simulation software, as indicated in the corresponding sections.

3.6 Conclusions

The AMS collaboration has demonstrated the feasibility of the AMS project. A simplified detector, AMS-01, was built and flown successfully aboard the Space Shuttle in 1998. The final detector AMS-02 is now fully assembled and has been thoroughly tested. It is now ready to be taken to Kennedy Space Center from where it will be launched to the International Space Station aboard Space Shuttle Endeavour in February 2011.

In conjunction with the development of the AMS detectors, the AMS software chain was developed. The AMS software includes a detailed simulation of the detector and offline event reconstruction for both simulated and real events. Part of the work performed in the context of this thesis used this software.

The AMS-02 detector will operate at the ISS for several years, collecting an unprecedented statistics of cosmic-ray data. Such volume of information will greatly improve the knowledge of the cosmic ray spectrum, and in particular of its less abundant components, which will provide new insights on the unsolved problems of dark matter and of cosmological antimatter.

Chapter 4

The AMS-02 RICH detector

One of the subdetectors in AMS-02 is a Ring Imaging Čerenkov (RICH) detector. This kind of detector reconstructs the velocity and trajectory of a charged particle emitting Čerenkov radiation by detecting the ring pattern formed as that radiation incides on a detection surface.

The concept of what is now called RICH detector was first proposed in 1977 by Jacques Séguinot and Tom Ypsilantis [132]. However, the acroynm RICH was subsequently coined by Tord Ekelöf.

4.1 The Čerenkov effect

Čerenkov radiation is produced by charged particles crossing a dielectric medium where the speed of light is lower than the speed of the charged particle, that is, if the medium has refractive index n, Čerenkov emission will occur if

$$v > \frac{c}{n}$$

and photons will be emitted at a Čerenkov angle θ_c (with respect to the particle's trajectory) which is given by

$$\cos\theta_c = \frac{1}{\beta n}$$

This phenomenon was first characterized in 1934 by Sergey Vavilov and Pavel Čerenkov. The explanation for this effect was later presented by Ilya Frank and Igor Tamm in the framework of classical electrodynamics.

The minimum velocity may be translated into a condition in energy. A particle with mass m will emit Čerenkov radiation if its energy E satisfies the condition

$$E > m\frac{n}{\sqrt{n^2-1}}$$

The number of radiated photons per unit of length and energy if given by the expression

$$\frac{d^2N}{dx\ dE} = \frac{2\pi\alpha}{hc}\ Z^2\ sin^2\theta_c = \frac{2\pi\alpha}{hc}\ Z^2\ \left(1-\frac{1}{\beta^2 n^2}\right)$$

This means that the number of photons is proportional to the distance traversed by the particle in the radiator and to the square of the particle charge. In addition, photon emission increases with both β and n.

Čerenkov radiation is polarized, its electric polarization vector lying on the plane defined by the charged particle and photon directions.

4.2 The AMS-02 RICH layout

The AMS-02 RICH detector (Fig. 4.1) has a conical shape with a simple basic layout consisting of a radiator plane at the top, a detection plane at the bottom, and a lateral mirror surrounding the volume between the two planes to avoid the loss of light on the sides. There is a large hole in the detection plane due to presence of the AMS-02 ECAL.

Charged particles will typically enter the RICH by crossing the radiator plane, generating a Čerenkov cone that may be detected as a ring produced by its intersection with the detection plane. Part of the ring will appear reflected in the case of Čerenkov cones intersecting the lateral mirror.

Patterns must be reconstructed from the individual hit signals collected in the bottom plane. In the case of high charges, the ring pattern will be clearly visible. For typical events, however, this will not be the case, since most particles crossing the RICH will be single-charged. For such particles, when the efficiency of the detection

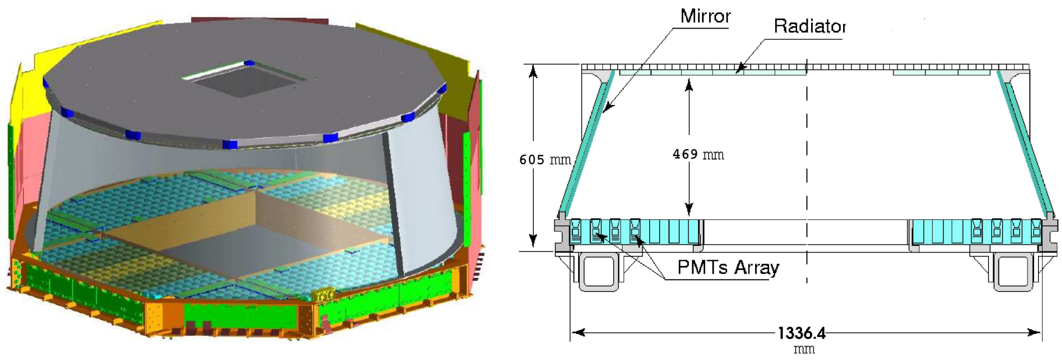

(a) (b)

Figure 4.1: *Schematic views of the AMS-02 RICH detector. (a) Perspective view, with the NaF square (top) and the ECAL hole (bottom square) clearly visible. (b) Side view with detector dimensions.*

matrix is taken into consideration, the expected number of visible hits will be of the order of 10 for a full ring produced in aerogel by a particle with $\beta = 1$. Detailed studies on the number of hits observed in RICH events are presented in Chapters 7 and 8 of this thesis.

4.3 Radiators

The RICH radiator plane (Fig. 4.2) contains two different radiators: a central square of sodium fluoride (NaF), with a thickness of 5 mm and a refractive index $n = 1.334$, covering $\sim 10\%$ of the RICH acceptance, and silica aerogel with $n = 1.05$ and a thickness of 25 mm covering the remainder of the top surface.

Silica aerogel

The medium used as main radiator of the AMS RICH is a silica (SiO_2) aerogel, produced by the Boreskov Institute of Catalysis in Novosibirsk, Russia [133], with a refractive index $n = 1.05$ and a clarity of approximately $C = 0.0061\ \mu\text{m}^4\ \text{cm}^{-1}$ on average. A total of 92 aerogel tiles, with a thickness of 2.5 cm, are included in the detector: 60 square tiles (11.4×11.4 cm) and 32 smaller tiles, shaped like truncated

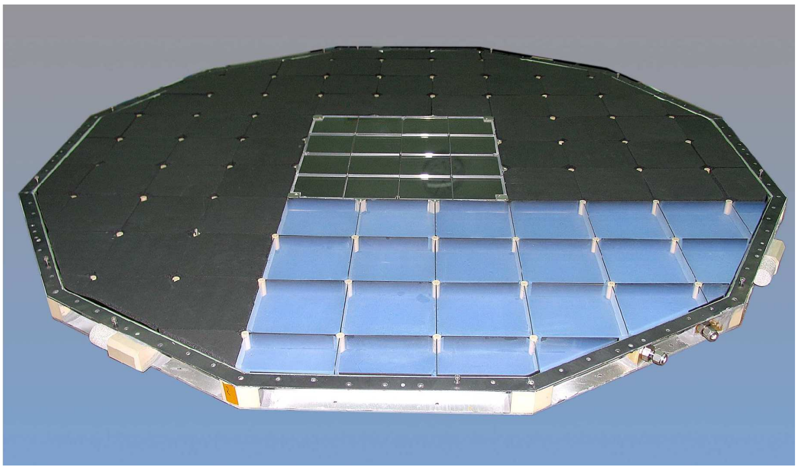

Figure 4.2: *RICH radiator container with the 16 NaF tiles and 23 of 92 aerogel tiles assembled.*

squares, in the edges of the radiator plane. An aerogel tile is shown in Fig. 4.3.

Figure 4.3: *An aerogel tile.*

Slight variations exist in individual tile properties. The fluctuations in the refractive index are at the level of 10^{-3}. Tile clarity has a fluctuation of about 5% around the average value. Tile thicknesses have a fluctuation at the level of 1%. A detailed discussion of variations in RICH tile properties and their consequences on Čerenkov light yield is presented as part of the RICH light yield studies in Subsection 8.2.2.

Sodium fluoride (NaF)

The central part of the RICH radiator is made of 16 square tiles of sodium fluoride (NaF) with a refractive index $n = 1.334$. All NaF tiles are identical, having a side length of 8.6 cm and a thickness of 0.5 cm.

The presence of the NaF radiator serves the dual purpose of allowing the detection of particles in the large velocity range between the NaF and aerogel radiation thresholds ($\beta = 0.75 - 0.95$) and of generating larger Čerenkov rings for central particles, which might escape detection if their trajectories pointed towards the ECAL hole (the maximum possible Čerenkov angle, corresponding to $\beta = 1$, is 17.8° in aerogel and 41.4° in NaF).

4.4 Reflector

To increase light collection in the AMS RICH, a lateral mirror (Fig. 4.4) surrounding the expansion volume has been included.

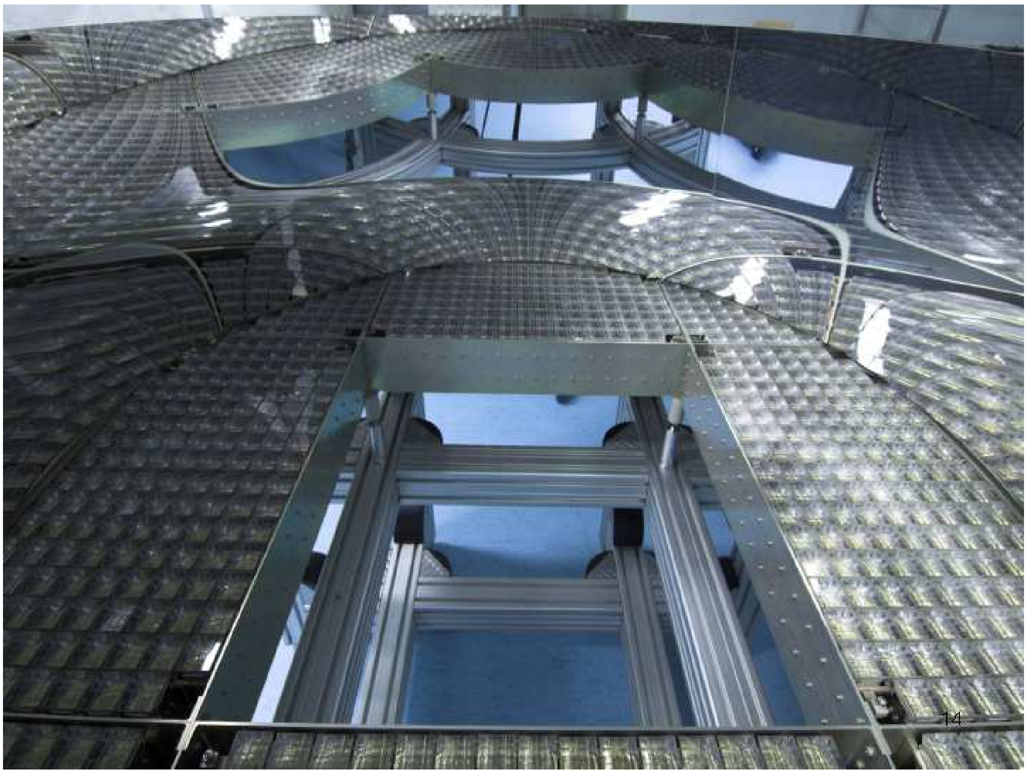

Figure 4.4: *The RICH mirror and detection matrix during the RICH detector assembly at CIEMAT in 2007.*

The lateral mirror has a conical shape, with an upper radius of 60 cm and a lower radius of 67 cm. It consists of a carbon fibre reinforced composite substrate with a multilayer coating made of aluminium (100 nm) and silica (SiO_2) (300 nm) vacuum-deposited in the inner surface. The full mirror is made of three segments, each covering 120° of the RICH contour.

The expected reflectivity for the RICH mirror was 85%. Results of reflectivity measurements confirm that the design goals have been fulfilled (Fig. 4.5).

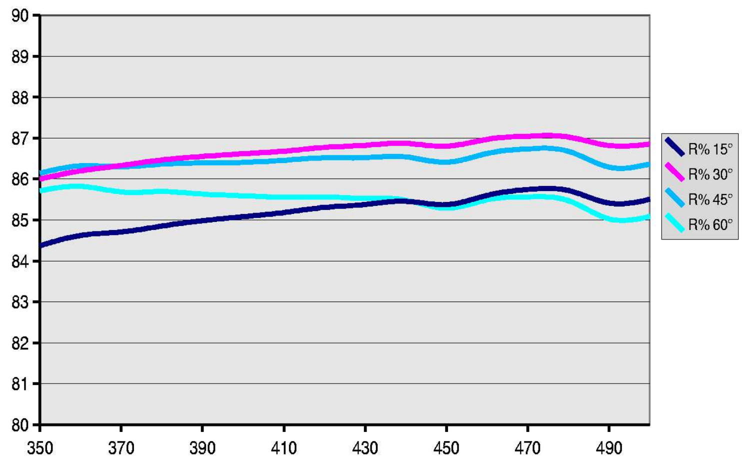

Figure 4.5: *Results obtained for the reflectivity (in %) of the RICH mirror as function of photon wavelength (in nm) for different incidence angles.*

4.5 Detection matrix

The detection matrix of the AMS RICH consists of 680 unit cells (Fig. 4.6), each including a photomultiplier attached to a light guide and front-end electronics, placed around the central hole. The matrix is divided into eight segments, four rectangular and four triangular, as shown in Fig. 4.7.

Photomultipliers

The photomultiplier tube (PMT) model used in the AMS-02 RICH is the 4×4 multianode Hamamatsu R7600-M16, shown in Fig. 4.8(a). Its quantum efficiency as function of photon wavelength is shown in Fig. 4.8(b).

Light guides

To increase the efficiency of light collection, each photomultiplier is coupled to a pyramidal light guide with a base area of 34×34 mm. Each light guide consists

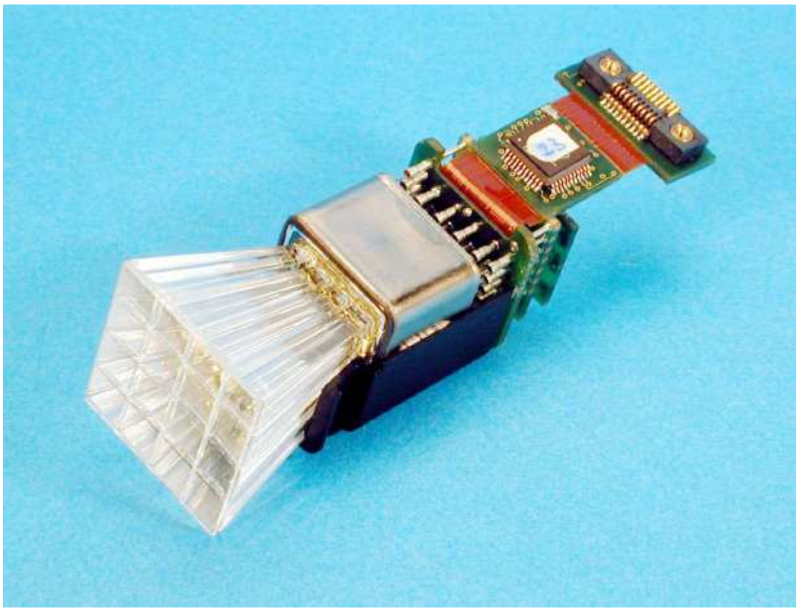

Figure 4.6: *A RICH detection cell. Left to right: light guide, photomultiplier and front-end electronics. Part of the housing cell is visible at the bottom.*

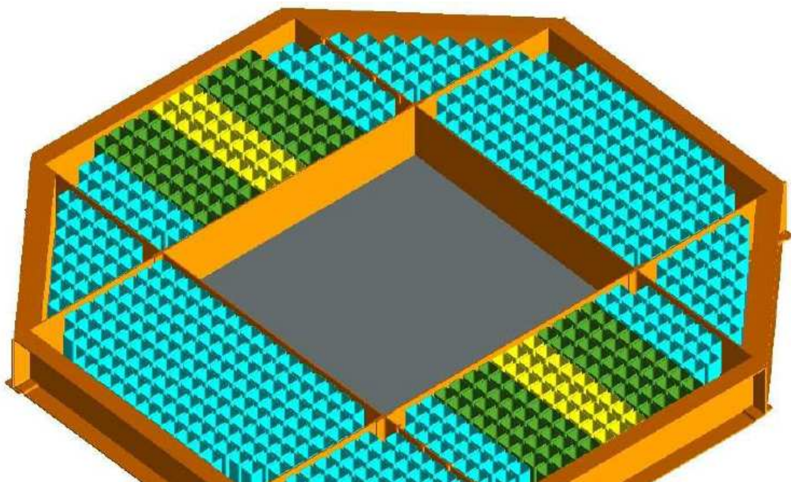

Figure 4.7: *The RICH detection matrix. Brown lines show its division in eight grids, four triangular and four rectangular. Cells are coloured according to their magnetic shielding thickness: central yellow band = 1.2 mm, green bands = 1.0 mm, cyan regions = 0.8 mm.*

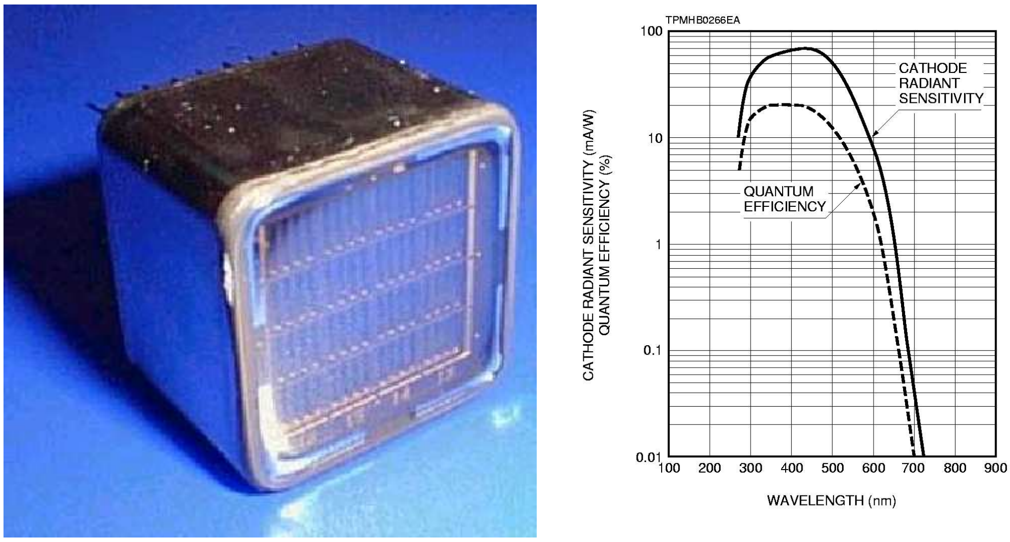

(a) (b)

Figure 4.8: *(a) The Hamamatsu R7600-M16 photomultiplier. (b) Quantum efficiency as function of wavelength for this PMT model.*

of 16 light pipes, one for each pixel, glued together. The light pipe material is the acrylic plastic Diakon LG-703 from Lucite International.

Since photomultipliers are spaced at intervals of 37 mm, there are gaps 3 mm wide between light guides where photons are not detected. The fraction of active area in the detection matrix is therefore $(34/37)^2 = 0.844$.

Magnetic shielding

Since the electronic components of detection matrix are sensitive to magnetic fields, the detection cells are shielded (Fig. 4.9). The thickness of the shielding varies between 0.8 and 1.2 mm depending on cell position, as shown in Fig. 4.7, since some regions of the matrix are expected to experience stronger magnetic fields than others.

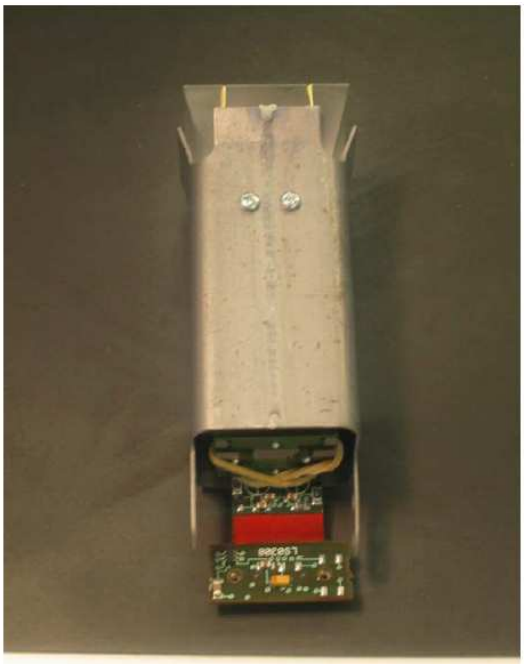

Figure 4.9: *A RICH detection cell surrounded by its magnetic shielding.*

4.6 Detector assembly

The assembly of the RICH detector took place at CIEMAT in Madrid, Spain between 2006 and 2007. Images of the RICH matrix and mirror during the detector assembly are shown in Fig. 4.10.

Several tests were performed on the RICH components. The characterization of individual aerogel tiles took place at LPSC in Grenoble, France. Thermal and vacuum testing of RICH grids was performed at CIEMAT. Testing and characterization of individual unit cells also took place at CIEMAT. Vibration tests were performed on a full rectangular grid at INTA in Madrid. Magnetic field tests were performed at CERN and at LCMI in Grenoble. A vibration test was performed on the radiator container (with all NaF tiles and a quarter of aerogel tiles) at SERMS in Terni, Italy. Figure 4.11 shows images of some of these tests.

The fully assembled RICH detector was moved to CERN in January 2008 for integration with the other components of AMS-02 (Fig. 4.12).

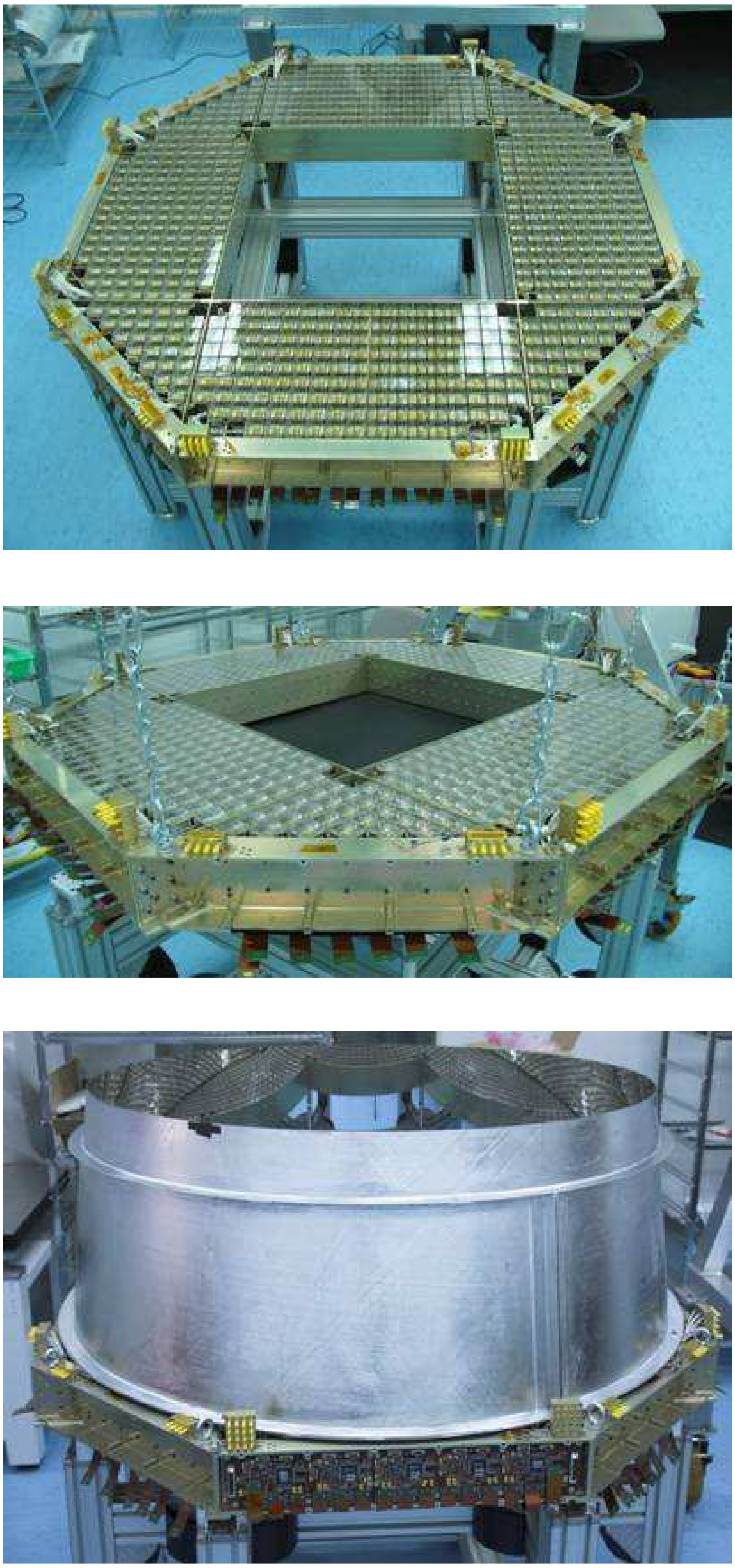

Figure 4.10: *Images of the AMS-02 RICH matrix and mirror during the detector assembly at CIEMAT.*

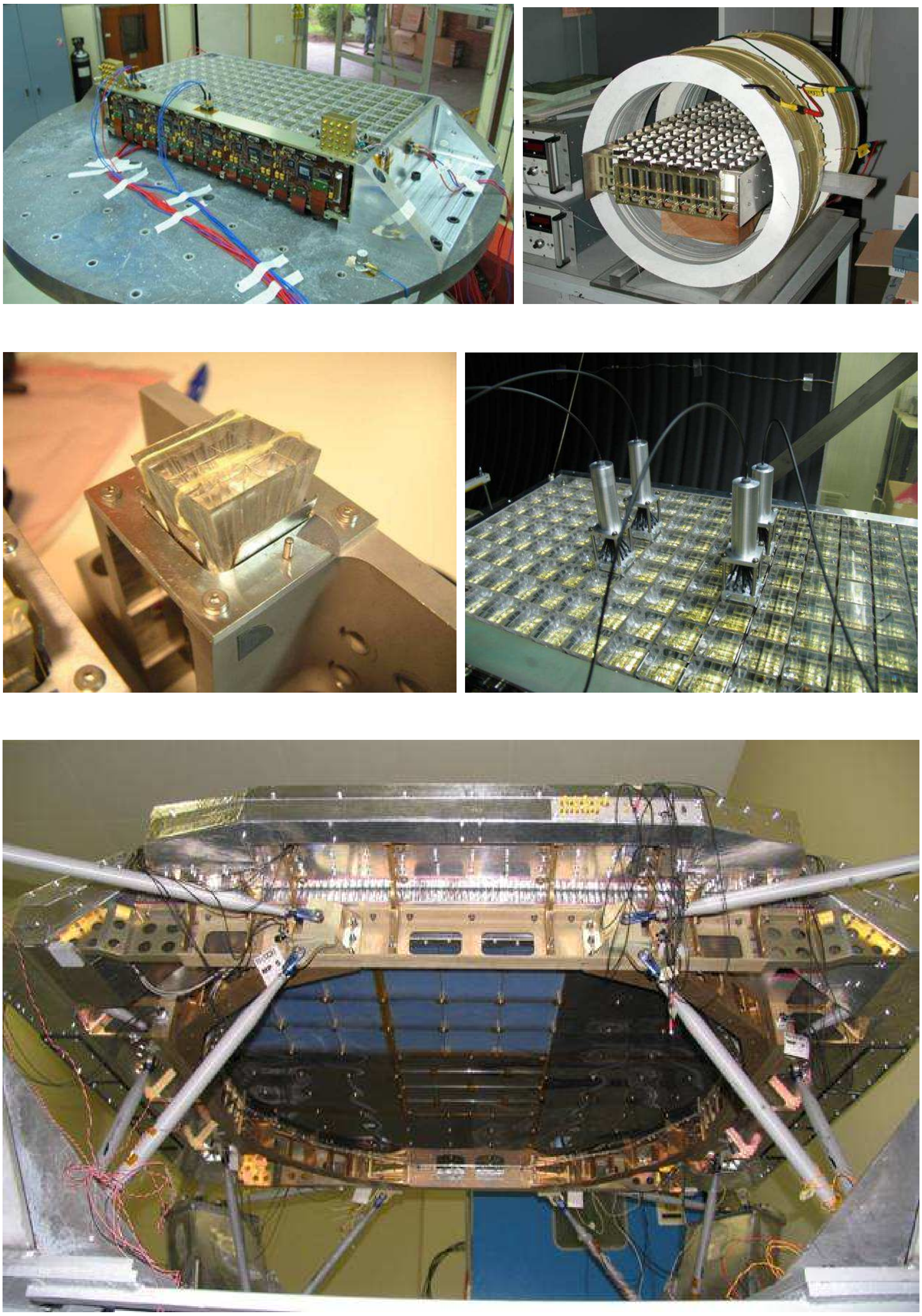

Figure 4.11: *Images of some of the tests performed on the RICH components. Top left: Grid vibration test at INTA. Top right: Grid magnetic field test. Centre left: Unit cell during vibration test. Centre right: Unit cell characterization at CIEMAT. Bottom: Test of radiator container (with lower TOF) at SERMS.*

Figure 4.12: *The RICH detector (without the radiator plane) at CERN in January 2008.*

4.7 Detector simulation

In addition to the full AMS simulation mentioned in Section 3.5, a standalone simulation of the RICH detector has been developed by the CIEMAT and LIP members of the AMS collaboration. This simulation, programmed in C++ and Fortran and using the GEANT toolkit, provides a lighter tool for event simulation and analysis in RICH-centered studies. This software package incorporates the RICH reconstruction algorithms developed by the CIEMAT and LIP groups.

In the RICH simulation, only this specific subdetector is described in detail. The uncertainy of the AMS track (which is the main external information needed to performed a good RICH reconstruction) is reproduced by smearing the simulated track.

Part of the simulation work presented in this thesis was performed using this software package, as indicated in the corresponding sections.

4.8 Event reconstruction

In the AMS-02 RICH detector, the velocity and charge of crossing particles are determined from the Čerenkov photon ring reconstruction. In the present work, ring reconstruction was performed using the standard LIP reconstruction algorithms described in Ref. [131] (except in the case of the studies with new algorithms described in Chapter 9). From event to event, different photon patterns can be obtained depending on particle velocity, impact point and direction. The determination of the radiated photons' aperture angle (θ_c), after the pattern reconstruction, allows to derive the particle's velocity, $\beta = \frac{1}{n\cos\theta_c}$. On the other hand, the particle's charge derives from the signal associated to the photon ring (N_{pe}), according to $Z^2 \propto \frac{N_{pe}}{\varepsilon}\frac{1}{\sin^2\theta_c}$ where ε is an overall efficiency factor that includes both the ring acceptance and the photon detection efficiency (absorption and scattering effects included).

Apart from the Čerenkov ring, charged particles also produce a signal in the region where they reach the detection matrix, due to the acrylic light guide crossing. This signal is concentrated in a few pixels and is much stronger than the one from ring hits. It is not considered for standard ring reconstructions, although it may be useful in some situations (e.g. reconstructions that do not rely on Tracker data, as mentioned in Chapter 9).

The AMS goals on mass separation for light isotope identification up to beryllium and charge separation up to iron ($Z = 26$) impose severe constraints on the RICH design and monitoring. A velocity accuracy of $\sim 10^{-3}$ for singly charged particles is aimed. At least three hits in the Čerenkov ring are necessary for a reliable event reconstruction due to the presence of noisy hits from aerogel scattered photons or photomultiplier dark current. The more hits (and photoelectrons) are present in the ring the better is the accuracy of the velocity measurement as stated by the expression:

$$\frac{\Delta\beta}{\beta} = \frac{\tan\theta_c \Delta\theta_c}{Z\sqrt{N_{(Z=1)}}}$$

where θ_c is the Čerenkov angle and $N_{(Z=1)}$ is the number of photoelectrons observed for $Z = 1$ particles. The single hit Čerenkov angle uncertainty ($\Delta\theta_c$) depends on the detector pixel size and radiator's thickness and chromaticity.

The quality of charge measurement depends on the number of Čerenkov photons detected. Uncertainties on individual charge measurements arise from statistical fluctuations on the collected signal and photomultiplier amplification ($\sigma_{pe} \sim 0.5$-0.6), and systematic effects from variations on radiator tiles (thickness, optical properties), mirror reflectivity and readout matrix (photomultiplier gain, detection cell efficiency):

$$\Delta Z = \frac{1}{2}\sqrt{\frac{1+\sigma_{pe}^2}{N_{(Z=1)}} + Z^2 \left(\frac{\Delta N}{N}\right)^2_{syst}}$$

The statistical uncertainty, dominant in the low charge region, does not depend on the charge as the Čerenkov signal increases with Z^2. On the other hand, it depends on the number of photoelectrons ($N_{(Z=1)}$) expected for singly charged particles. Systematic errors in light yield estimation become dominant at high charges and have to be limited in order to fulfill the requirement of charge separation up to iron [131]. For instance, requiring a charge error (ΔZ) lower than 0.3 charge units as a criterion for charge separation on iron region and assuming a statistical error ~ 0.2 (corresponds to $N_{(Z=1)} \sim 8$), an upper limit for the systematic uncertainty of $\sim 1.5\%$ is obtained.

Therefore, the higher is the aerogel light yield the better will be the uncertainty on the velocity and charge determination. In addition, the reconstruction efficiency increases with light yield.

The quality of event reconstruction in the RICH detector is a central subject in this work. Studies performed on this subject, based on the LIP reconstruction algorithms, are presented in Chapters 7 (for the RICH prototype) and 8 (for the final RICH detector in AMS-02). Further studies on the possibility of reconstructing RICH events without information from the Tracker are presented in Chapter 9.

4.9 Conclusions

A Ring Imaging Čerenkov detector (RICH) was built for the AMS-02 experiment. This detector has a dual radiator configuration with a large surface of silica aerogel ($n = 1.05$) and a central region of sodium fluoride which increases the detector's geometrical acceptance and range of detectable particle velocities. Light collection is improved by a conical mirror surrounding the expansion volume.

Detailed tests were successfully performed on the detector's components. In January 2008 the RICH was delivered to CERN and incorporated into the full AMS-02 detector.

A standalone simulation of the RICH detector was developed by the CIEMAT and LIP groups as a lighter counterpart to the full AMS software chain. The RICH software package includes reconstruction algorithms and has been used in several studies, including part of those presented in this thesis.

The RICH detector was designed to perform accurate measurements of particle velocity ($\Delta\beta/\beta \sim 10^{-3}$ for $Z = 1$) and to discriminate individual charges up to the iron region. These quality measurements will be essential for event reconstruction in AMS-02.

Part III

Reconstruction methods and RICH tests

Chapter 5

RICH prototype

The research effort leading to the final AMS-02 RICH detector included the construction of a RICH prototype. Between 2002 and 2003, this prototype underwent several tests: a cosmic-ray test at ISN (now LPSC) in Grenoble between July and September 2002 and two in-beam tests at CERN in October 2002 and October 2003.

5.1 RICH prototype setup

The AMS RICH prototype, shown in Fig. 5.1, was built to reproduce part of a sector in the final RICH detection matrix to be included in AMS-02. However, there were some differences between the prototype and flight matrix layouts in addition to their different sizes.

The detection matrix of the AMS RICH prototype consisted of 96 Hamamatsu R7600-M16 photomultipliers (identical to the ones in the final detector), each with 4×4 pixels, coupled to solid light guides. The PMT pitch was 31 mm instead of the final detector's 37 mm. The light guides used in the prototype were slightly smaller, with the same height of the flight ones (30 mm) but a top side length of 31 mm instead of 34 mm. This meant that the prototype matrix did not have dead spaces between light guides. The material used in the prototype light guides was an acrylic plastic from Saint-Gobain (Bicron BC-800), which was less transparent than the material used in the final light guides. The prototype light guide foil was also made of Bicron BC-800, less transparent than the final material (Hesa-Glas).

No fixed radiator was included in the prototype. Instead, different radiator

Figure 5.1: *The AMS RICH prototype.*

samples (NaF and several types of silica aerogel) were placed in front of the detection matrix as needed. In most cases a single tile was used at the time; however, in some runs of the cosmic-ray test three aerogel tiles were present simultaneously [134].

A Hesa-Glas foil with a thickness of 1 mm is present under the aerogel tiles in the final radiator configuration. Most prototype runs had no similar foil placed under the radiator tiles, but a Plexiglas foil with a thickness of 0.75 mm was present for some runs in both the cosmic-ray test and the 2002 in-beam test.

During parts of the 2003 beam test a mirror segment corresponding to a 30° sector (1/12 of total) was added to the RICH prototype. This mirror segment was 22 cm high and 29.5 cm wide. The mirror coating was made of silicon monoxide (SiO). The reflectivity of this mirror segment has been evaluated from data to be $(75.1 \pm 0.2)\%$ [131], which is in agreement with the manufacturer's measurements.

The main differences between the prototype setup and the final detector configuration are summarized in Table 5.1.

	Item	Prototype	Flight
Matrix layout	Number of PMTs	96	680
	Light guide pitch	31 mm	37 mm
	Pixel size	7.75 mm	8.5 mm
	Active area	100%	84.4%
Radiator	Radiator tiles	1 NaF or 1 aerogel or 3 aerogel	92 aerogel (n=1.05) + 16 NaF
	Radiator foil	none or Plexiglas	Hesa-Glas
Mirror	Mirror coverage	none or 30°	360°
	Mirror coating	SiO	SiO_2
Light guides	Light guide foil	Bicron BC-800	Hesa-Glas
	Light guide material	Bicron BC-800	Diakon LG-703

Table 5.1: *Differences between the RICH prototype and flight detectors.*

5.2 The 2002 cosmic-ray test

The test of the AMS prototype using cosmic muons took place at the Institut de Sciences Nucléaires (ISN)[1] in Grenoble, France, between July 26 and September 13, 2002.

Four radiator samples were used in this test: one NaF sample with a thickness of 5 mm, one aerogel sample with $n = 1.02$ from the Boreskov Institute of Catalysis in Novosibirsk [133] and two aerogel samples from Matsushita Electric Works[2] [135] with refractive indices 1.03 and 1.05.

The RICH prototype matrix was placed horizontally, with radiator samples being placed above it at a distance of 75 mm for NaF runs and either 326.5 mm or 416.5 mm for aerogel runs. The setup used in this test is shown in Fig. 5.2.

A total of 1×10^6 events were collected using the three aerogel samples and the NaF sample. NaF events corresponded to approximately 1/10 of the total statistics collected [134].

[1]In 2003 ISN was renamed Laboratoire de Physique Subatomique et de Cosmologie (LPSC).
[2]In 2008 Matsushita Electric Works, Ltd. was renamed Panasonic Electric Works Co., Ltd..

Figure 5.2: *The AMS RICH prototype during the 2002 cosmic-ray test.*

5.3 Beam tests: 2002, 2003

The October 2002 beam test

The first of the two in-beam tests undergone by the RICH prototype took place at CERN in experimental hall H8 between October 15 and October 19, 2002 using a beam of secondary ion fragments. The primary beam, provided by CERN's Super Proton Synchrotron (SPS), was composed of lead ($Z = 82$) ions with a momentum of 20 GeV/c/nucleon and incided on a beryllium ($Z = 4$) target to produce the secondary beam.

Test beam settings were varied between runs. Selections performed included ion beams with a momentum of 20 GeV/c/nucleon and mass-to-charge ratio $A/Z = 1.5$, 2 and 2.25 and also proton beams with momenta of 5, 7, 9, 11, 13, 15, 20 and 30 GeV/c. A total of 5×10^6 events were collected during this test [136].

Five aerogel samples were tested, three of them from Matsushita with refractive indices 1.03 (two samples) and 1.05, and other two from the Boreskov Institute of Catalysis with refractive indices 1.03 and 1.04. One NaF sample was also tested.

Since the test beam was horizontal, the RICH prototype matrix was placed in a vertical position perpendicular to the beam, with radiator samples crossing the beam path. The distance from radiator to detection matrix was 75 mm in the case of NaF runs, and between 375 mm and 417.4 mm in aerogel runs.

In addition to the RICH prototype, other subdetector parts of the AMS spectrometer were also present [137, 138].

The October 2003 beam test

The second in-beam test with the RICH prototype, also using a secondary ion beam, had a setup which was very similar to the one used in the first in-beam test. It was again performed at CERN's experimental hall H8 using an SPS beam, taking place between October 22 and October 31, 2003. The primary beam was composed of indium ($Z = 49$) ions with a momentum of 158 GeV/c/nucleon and incided on a lead target, producing secondary fragments that essentially kept the same momentum per nucleon of the primary ions.

A selection of certain isotopes and charges was performed through A/Z beam settings. The values $A/Z = 2$, 2.25 and 2.35 were used. In addition, a few runs used secondary protons with 5, 7, 9, 11, 13 and 15 GeV/c. A total of 11×10^6 events were collected during this test [136].

Detectors present included, in addition to the RICH, a Silicon Tracker, a Čerenkov counter (present only in part of the runs) and two organic scintillators. The full apparatus used in the 2003 test is shown in Fig. 5.3.

Secondary beam particles were forced to successively cross the following detectors:

a) Silicon Tracker

b) Scintillator 2

c) Čerenkov counter (when present)

d) Scintillator 1

e) RICH prototype

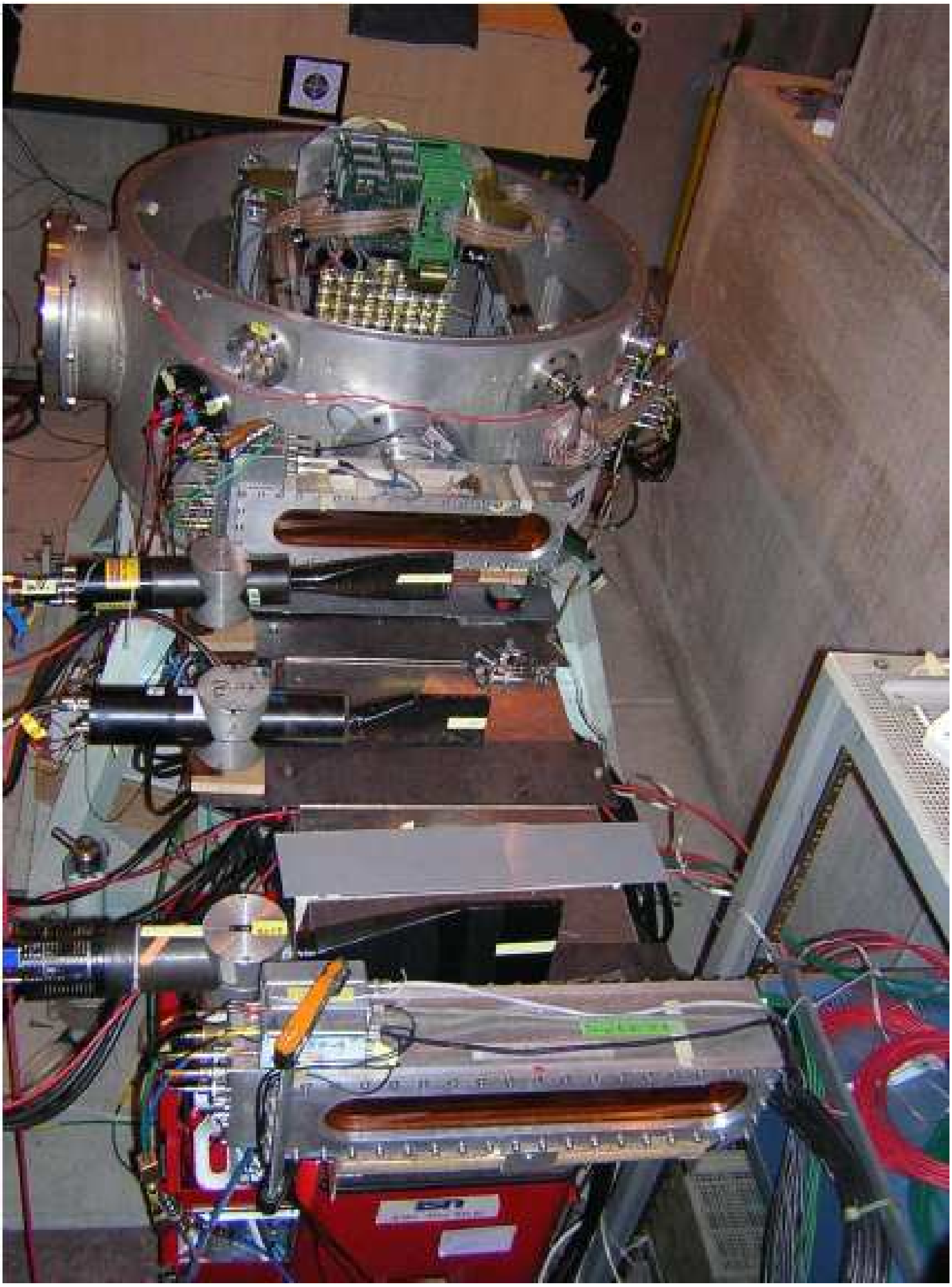

Figure 5.3: *Experimental setup for the 2003 beam test at CERN. The RICH prototype is at the top of the image.*

Three aerogel samples were tested, one of which (with $n = 1.03$, from the Boreskov Institute of Catalysis) had already been used in the 2002 test. The other two samples had a refractive index 1.03 from Matsushita and a refractive index 1.05 from the Boreskov Institute.

The prototype mirror segment, corresponding to a 30° sector, was present during part of the test.

The RICH prototype matrix was again placed in a vertical position perpendicular to the beam, with radiator samples intersecting the beam path. The distance from radiator to detection matrix was 78 mm in the case of NaF runs, and between 330 mm and 432 mm in aerogel runs.

In some runs, the prototype (radiator plus detection matrix) was rotated to have a non-perpendicular beam incidence. Inclinations of 5°, 10°, 15° and 20° were used.

5.4 Conclusions

A prototype of the AMS RICH was built for detailed studies on the capabilities of the full detector. Some differences existed between the components used in the prototype and those included in the final detector. Extensive testing was performed with this prototype in the years 2002 and 2003, including the acquisition of cosmic muons and two dedicated beam tests in conjunction with other detectors. Valuable data were collected, giving an important contribution for the subsequent work on the RICH.

Chapter 6

Charge reconstruction with scintillators

Two organic scintillators were present during the in-beam tests performed at CERN in 2002 and 2003, described in the previous chapter in Section 5.3. One of the purposes of their inclusion was to provide the trigger for the RICH prototype, since charged particles crossing each scintillator generate light that was collected by photomultipliers coupled to them.

Scintillator signals can provide more information, however. In general, for a given scintillator operating under constant conditions, the signal generated by a charged particle will be function of the particle's velocity, charge and trajectory. In the case of the 2003 test, excluding the few proton runs, all beam particles had $\beta \simeq 1$ and a similar momentum per nucleon ($p = 158$ GeV/c/nucleon). Trajectories were also virtually identical. The scintillator signal was therefore expected to be function of the particle's charge only. Studies were performed to develop a method for charge measurement using scintillator data from the 2003 test.

6.1 The scintillator signal

For each of the scintillators, Scintillator 1 (SC1) and Scintillator 2 (SC2)[1], a numerical reading was obtained from the digitization of anode signal of the photomultiplier connected to it. These were 12-bit readings, meaning that for each particle SC1 and SC2 provided an integer value between 0 and 4095. Fig. 6.1 shows the distribution of scintillator signals for one data run.

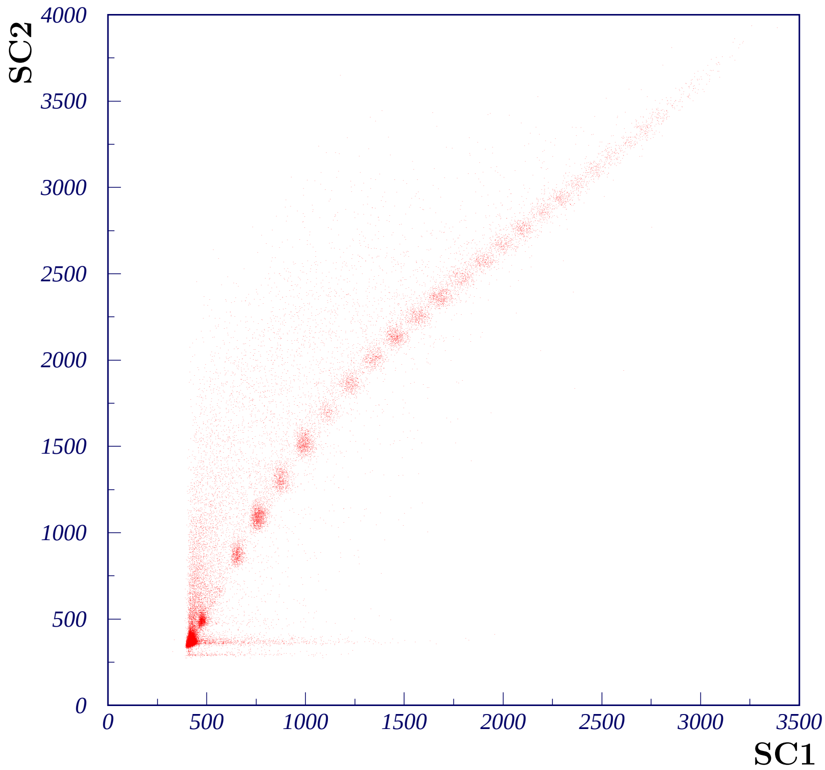

Figure 6.1: *Scatter plot of ADC measurement pairs for run 510. Spots corresponding to individual charges up to $Z \sim 20$ are clearly visible.*

The repeated use of this procedure for a large number of events allowed the creation of a signal spectrum showing the frequency distribution of the digital signal. In a stable setup, the detected signal was expected to be closely related to the beam

[1]The scintillator numbering used here corresponds to the convention adopted in the AMS tests. In reality, beam particles crossed Scintillator 2 before crossing Scintillator 1, as mentioned in Section 5.3.

particle's charge. The resolution obtained with this setup was appropriate to allow for a good charge separation.

6.2 Discrete charges as a calibration tool

In principle, scintillator response to charged particles with the same velocity is expected to be proportional to the square of the particle charge. However, for high charges, saturation effects occur and the observed signal follows a non-linear law that clearly departs from the expected behaviour on Z^2.

The fact that ion charge is always a multiple of the elementary charge e means that, provided that the correlation between charge and signal is accurate enough, the signal distribution for a large sample of events will show clear peaks corresponding to successive integer charges.

Such peaks were observed in data runs of this beam test, in both SC1 and SC2. They could thus be used to obtain an estimate for ion charge. Data from ion runs, each with about 10^5 events, provided visible peaks up to the region of $Z \sim$ 15-20. The typical ratio between peak width (σ) and the distance between consecutive peaks was ~ 0.2 for low charges.

At least one charge peak must be positively identified with a certain charge Z in order to know the atomic numbers for the set of all peaks. It was observed that for small charges (up to $Z \simeq 6$), the signal follows the Z^2 law accurately. Therefore, the distances between successive peaks follow an arithmetic progression. Additionally, for beam runs with $A/Z = 2$ the beryllium ($Z = 4$) peak is absent, since this is the only light element that does not have a stable isotope with an equal number of protons and neutrons. The unmistakable, wider gap seen in charge spectra identifies its neighbouring peaks as $Z = 3$ (lithium) and $Z = 5$ (boron).

The calibration procedure involves several stages, as described below.

6.3 First evaluation of peak positions

The first step in the calibration procedure is calculating peak values for each scintillator. To achieve this, Gaussian fits were performed for most visible peaks. For the last peaks, low statistics makes Gaussian fits unusable, therefore approximate values for peak centre were taken from direct observation of the signal distribution. A linear extrapolation was used to estimate peak positions for the region where they are no longer visible.

A list of reference values was therefore compiled for each scintillator, relating particle charge and anode readings, e.g., using superscripts a for SC1 and b for SC2:

$$
\begin{array}{ll}
X_0^a = 374 & X_0^b = 283 \\
X_1^a = 385 & X_1^b = 299 \\
X_2^a = 418 & X_2^b = 372 \\
X_3^a = 473 & X_3^b = 494 \\
X_4^a = 546 & X_4^b = 674 \\
X_5^a = 637 & X_5^b = 876 \\
\quad\ldots & \quad\ldots
\end{array}
$$

Values X_0^a and X_0^b correspond to pedestal values. The Z^2 law for low charges may be expressed by $X_n^i \simeq X_0^i + k_i n^2$ $(i = a, b)$, for $n \lesssim 6$.

6.4 Charge estimation from peak data

The charge estimates Z_1, Z_2 corresponding to scintillator anode readings S_1, S_2 are given by

$$
\begin{aligned}
Z_1 &= I_1 + \tfrac{S_1 - X_{I_1}^a}{X_{I_1+1}^a - X_{I_1}^a} \\
Z_2 &= I_2 + \tfrac{S_2 - X_{I_2}^b}{X_{I_2+1}^b - X_{I_2}^b}
\end{aligned}
$$

where I_1, I_2 are the highest integer values for which $S_1 > X_{I_1}^a$ and $S_2 > X_{I_2}^b$, respectively.

For each event, this process gives a provisional charge estimate for each scintillator. An average value is given by $Z = (Z_1 + Z_2)/2$.

6.5 Calibration refinements

6.5.1 Charge compatibility

Provisional values Z_1 and Z_2 are not necessarily consistent between them at higher charges beyond visible peaks. Even at lower charges some fine tuning may be still required. Cross-checks must therefore be performed. This was achieved by plotting the distribution of $\Delta Z = Z_1 - Z_2$ for several narrow bands of Z: [0.0,2.0], [2.0,4.0], [4.0,6.0], ...

For each ΔZ distribution a clear peak is visible at a given displacement D. If the estimates for Z_1 and Z_2 are compatible then $D = 0$.

The tails in the ΔZ distribution are expected to be non-symmetric due to the existence of events where ion fragmentation occured between the first and second scintillator measurements. In those events a higher charge was measured in the first scintillator crossed by the particles (SC2) than in the second one (SC1). Therefore $Z_1 < Z_2$, increasing the tail for negative values of ΔZ. This effect was clearly observed in many distributions.

To make charge measurements Z_1 and Z_2 compatible only one of the calibrations has to be changed. Positive values of D mean there is an underestimation of Z_2 with respect to Z_1, while negative values of D are the consequence of a relative overestimation of Z_2. Therefore SC1 was chosen as reference and the calibration values for SC2 were changed according to the following expressions, in which $(X_{new})^b_{I_2}$ are the new values and $(X_{old})^b_{I_2}$ are the old ones, and each displacement D is divided into an integer part U and a decimal part d for which $D = U + d$, $U \in \mathbb{Z}$, $d \in [0, 1[$:

$$(X_{new})^b_{I_2} = (X_{old})^b_{I_2-U} - d\left[(X_{old})^b_{I_2-U} - (X_{old})^b_{I_2-U-1}\right]$$

For small corrections ($|\,D\,| < 1$), this expression may be written as:

$$\begin{aligned}
(X_{new})^b_{I_2} &= (X_{old})^b_{I_2} - D\left[(X_{old})^b_{I_2+1} - (X_{old})^b_{I_2}\right] \qquad && (-1 < D < 0) \\
(X_{new})^b_{I_2} &= (X_{old})^b_{I_2} - D\left[(X_{old})^b_{I_2} - (X_{old})^b_{I_2-1}\right] \qquad && (0 < D < 1)
\end{aligned}$$

After this procedure is completed results for Z_1 and Z_2 should be fully compatible. All distributions for ΔZ at various Z should peak at zero. However, small deviations may still be found due to errors in some previous measurements of D. If this is the case, the procedure should be repeated until such errors are negligible.

When full compatibility is achieved, clear peaks should be visible in the Z distribution up to the $Z \sim 20$-30 region, but those peaks will not necessarily fall in integral values, meaning that a global rescaling of the calibration functions is needed to complete the process.

6.5.2 Final rescaling

The corrections described above will now be applied once more, but this time data on both scintillators should be corrected. For each integer charge, displacements $D = U + d$ (as above) are now given by $D = Z_{true} - Z_{peak}$, and the corrections to apply are:

$$(X_{new})^a_{I_1} = (X_{old})^a_{I_1-U} - d\,[(X_{old})^a_{I_1-U} - (X_{old})^a_{I_1-U-1}]$$
$$(X_{new})^b_{I_2} = (X_{old})^b_{I_2-U} - d\,[(X_{old})^b_{I_2-U} - (X_{old})^b_{I_2-U-1}]$$

A charge distribution may be obtained using values of Z for all events in a given run. In this new distribution peak definition is improved with respect to the previous Z_1 and Z_2 and a greater number of peaks is visible, typically up to $Z \sim 26$ (iron), the definition of further peaks being limited by the extremely low statistics for heavier elements.

For values of Z beyond the last visible peak a linear law is assumed, the value of the slope being the one measured for the region between the last two visible peaks.

6.6 Calibration results

As expected, calibration parameters for a given scintillator were completely modified after any change in the anode voltage (e.g., SC1 between runs 575 and 579). However, a smaller yet still significant difference was observed even between consecutive runs for which no setup parameters were apparently changed. This instability was larger in SC1 than in SC2. In the case of SC1, using the previous run's calibration data could mean a difference in the charge estimate of as much as 1.

The inspection of charge measurements during a given run showed no visible change, meaning the cause of these relatively small changes should be found in some effect that occured between runs.

A faster way of calibrating consecutive runs with such small variations is to use the final calibration from a previous run as starting point and proceed directly to the ΔZ distributions.

The scintillator calibration procedure was successfully applied to anode readings in the following 45 runs: 506, 510, 511, 513, 514, 515, 516, 517, 518, 519, 520, 525, 526, 527, 529, 530, 531, 532, 533, 538, 539, 540, 542, 543, 544, 545, 546, 575, 579, 580, 581, 583, 584, 585, 586, 587, 588, 589, 590, 591, 599, 607, 612, 613, 614.

Runs up to 599 corresponded to a beam selection of $A/Z = 2$. The last four runs had a selection of $A/Z = 9/4$.

Run 575 showed a unique feature in the ADC measurements for SC2: charges smaller than 2 gave very high readings, close to the maximum for the 12-bit ADC, while for higher charges a truncated spectrum was seen. Analysis of these data eventually showed that the readings were ordinary ones but had been shifted. The usual spectrum was recovered when values modulo $4096 = 2^{12}$ were used. The simplest way to perform this correction is to subtract 4096 from the high values. The pedestal value and low charge values may therefore be interpreted as negative, the exact figures being in this case $X_0^b = -52$ for pedestal and $X_1^b = -34$ for Z=1. For the case Z=2 the value is already positive: $X_2^b = 18$.

The full calibration tables obtained for the two scintillators are presented in Appendix A.

6.7 Scintillator response models

6.7.1 Z^2 law

A naive approach to the problem of scintillator response would suggest that the scintillator signal should be proportional to the square of the particle's charge. In practice, scintillator readings always have a pedestal term, meaning that the expected behaviour would be

$$f(Z) = a + bZ^2$$

This law only describes scintillator response for small charges. In the case of the 2003 test, it is a good model up to $Z \simeq 5$. For higher charges, saturation effects become very significant. Fig. 6.2 shows this effect for one run.

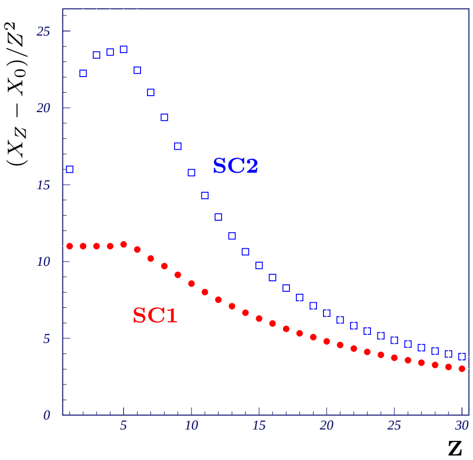

Figure 6.2: *Evolution of $(X_Z - X_0)/Z^2$ for both scintillators in run 510 according to the calibration obtained. This quantity should be independent of Z if no saturation occurred.*

6.7.2 Birks model, original version

In the approach first proposed by Birks in 1951 to describe the effect of saturation [139], the scintillator reading is expected to follow the law

$$f(Z) = a + \frac{bZ^2}{1+cZ^2}$$

Using this expression to fit the 2003 results, it was verified that a good fit was obtained when its domain was restricted to $Z \lesssim 15$. However, the extension of the fit to higher Z was not very successful, because the Birks formula is not able to describe the approximately linear increase of the scintillator signal at $Z \gtrsim 15$.

6.7.3 Birks model, modified by Chou

In 1952 Chou proposed the introduction of an additional term in the Birks formula [140]. Translating this change into the scintillator law, the following expression is obtained:

$$f(Z) = a + \frac{bZ^2}{1+cZ^2+dZ^4}$$

Results obtained using this fit are presented in the next section.

6.7.4 Birks model, modified with inverse tangent

Another version of the Birks model [141] introduces an inverse tangent function in the expression of signal dependence on Z:

$$f(Z) = a + \frac{bZ^2}{1 + c \times \arctan(dZ^2/c)}$$

Results obtained using this fit are also presented in the next section.

6.8 Comparison of experimental data with scintillator models

To evaluate the accuracy of models for scintillator response, the results obtained for scintillator calibration were fitted with two different models:

- Model 1: Birks-Chou model (see 6.7.3).
- Model 2: Birks model with inverse tangent (see 6.7.4).

To account for the different accuracy in the determination of points for the different values of Z, the following expression was used to obtain progressive error bars:

$$\Delta(X_Z^a) = 0.5 \oplus (10^{Z/30} \times 0.02\sqrt{X_Z^a - X_0^a})$$

The fixed term ensures a minimum error bar for all points, since peak positions were determined only to the nearest integer, while the second term accounts for the variation in total statistics. The factor $10^{Z/30}$ corresponds to the effect of total statistics falling exponentially by a factor 10 for each 15 elements (which is roughly the effect seen in test beam runs), while the expression under the square root gives the uncertainty growth expected for increasing signals. The factor 0.02 was chosen as appropriate to give a moderate progression in relative errors.

A reasonable agreement was obtained, with similar errors for both fits. An example of fit results for one run, using all points up to $Z = 30$, is shown in Fig. 6.3. The corresponding differences between fit results and calibration points is shown in Fig. 6.4. Fit results for the same run, taking into account points up to $Z = 20$ only, are shown in Fig. 6.5. The corresponding evolution in fit deviations is shown in Fig. 6.6.

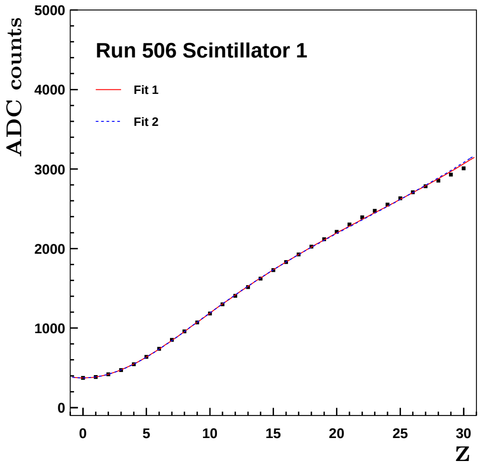

(a)

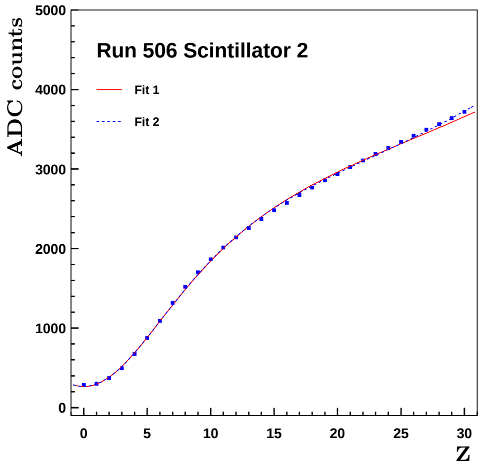

(b)

Figure 6.3: *Fit results for run 506 using* $Z = 0$-30 *as the fit range.*

The evolution of scintillator response in the $Z = 0$-30 range was globally matched by both formulae (Fig. 6.3). In the case of the fit for the $Z = 0$-20 range (Fig. 6.5), a good match was obtained for those values but the extrapolation towards $Z > 20$ showed a strong disagreement. One feature in the Birks-Chou fit result shows clearly that even this description of scintillator response is not fully adequate: parameters c and d in this model are expected to be positive since they come from saturation effects which will reduce the scintillator signal, but when the fitting procedure is applied the parameter d usually takes negative values. This means that the Birks-Chou expression cannot be regarded as more than a generic three-parameter fit, and its coefficients must be taken as simple parameters with no direct physical significance.

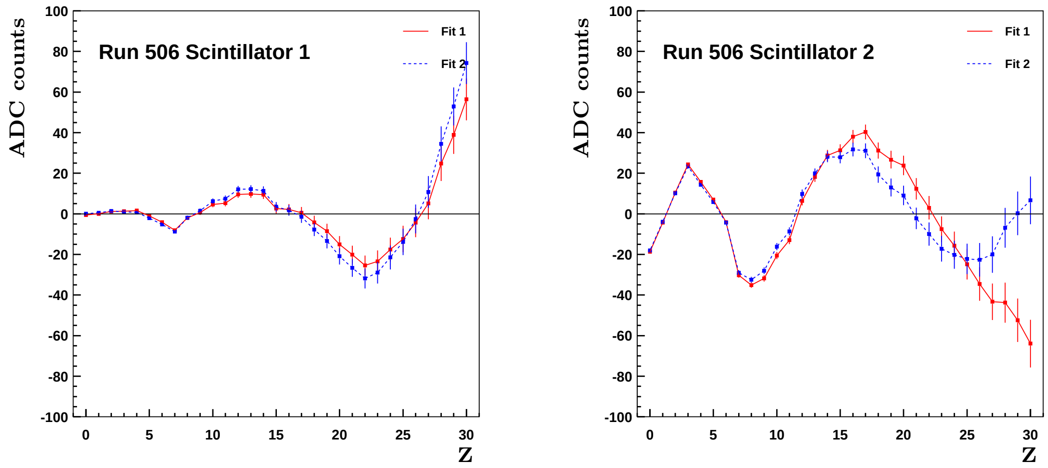

(a) (b)

Figure 6.4: *Fit deviations (in ADC counts) from calibration results for run 506 using* $Z = 0$-30 *as the fit range.*

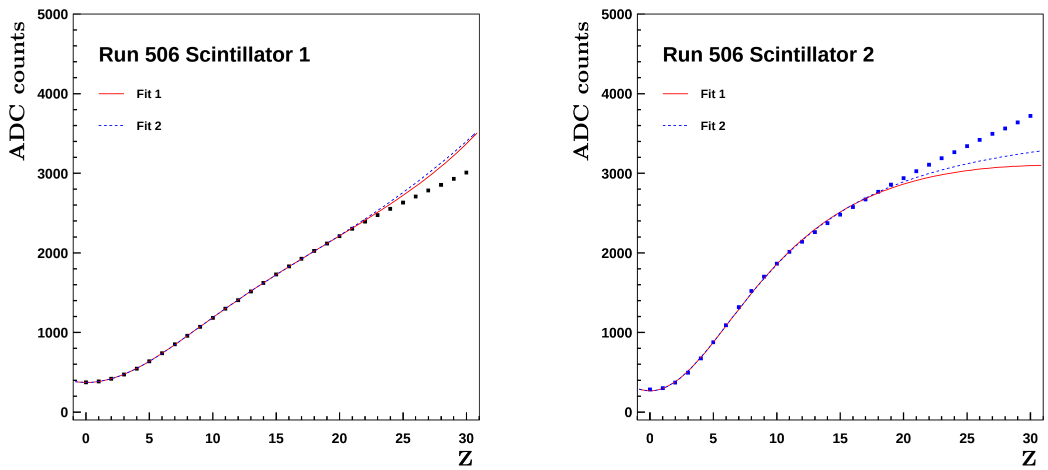

(a) (b)

Figure 6.5: *Fit results for run 506 using* $Z = 0$-20 *as the fit range.*

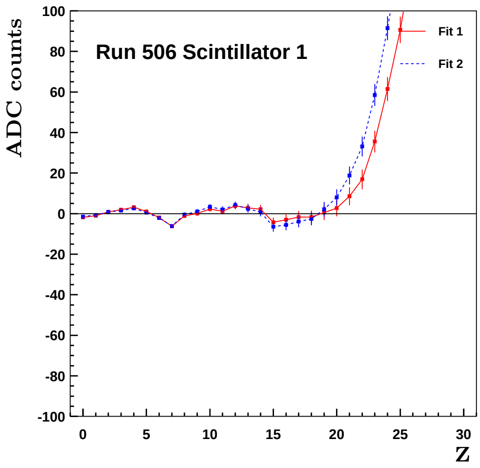

(a)

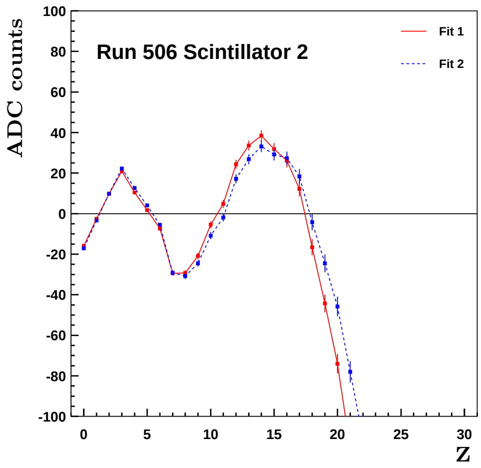

(b)

Figure 6.6: *Fit deviations (in ADC counts) from calibration results for run 506 using $Z = $0-20 as the fit range.*

In general, the quality of the fits is not sufficient for the fitted curves to be used instead of the original calibration results. Fit deviations frequently reach tens of ADC counts, as seen in Figs. 6.4 and 6.6, especially in cases where non-linearities in scintillator response are more important. Such deviations translate into changes in reconstructed Z of several tenths of charge units, similar to the scintillator charge resolution.

6.9 Data selection and multi-run distributions

The presence of two independent scintillators was important in the calibration refinements for high charges. In addition, the difference between results from the two scintillators provides a natural test of the measurement's robustness.

If Z_1 and Z_2 are the charge measurements provided by the scintillators SC1 and SC2, and the charge difference ΔZ is defined as $\Delta Z = |Z_1 - Z_2|$, a quality cut for charge compatibility may be established: $\Delta Z < 0.5$.

The application of this cut clearly improved the charge distribution. Figure 6.7 shows the reconstructed charge distribution for the same event before and after appyling the quality cut.

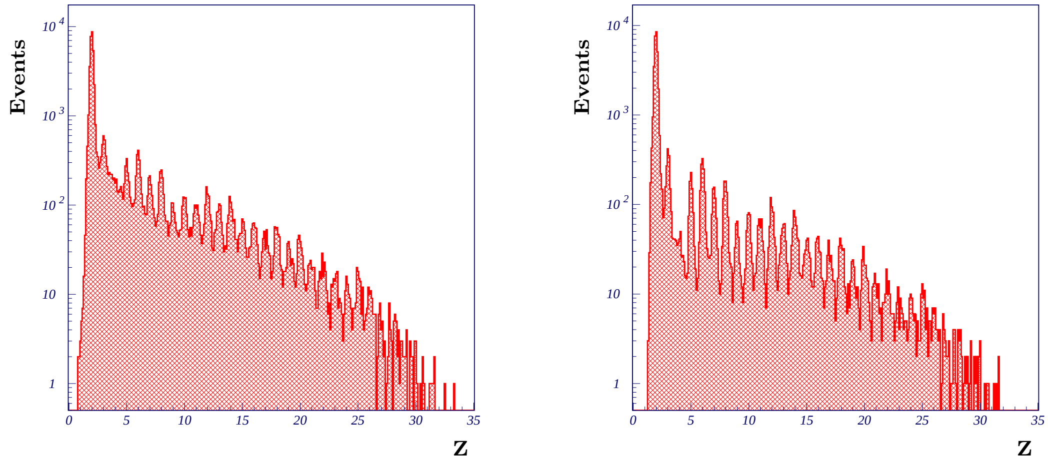

(a) (b)

Figure 6.7: *Distribution of reconstructed charges obtained for run 510: (a) all events, (b) after compatibility selection ($\Delta Z < 0.5$).*

Results from different runs may be added to obtain increased statistics. Figure 6.8 shows the charge distributions before and after the quality cut for a set of 27 runs with $A/Z = 2$. The original charge distribution corresponds to a total of 1.7×10^6 events, of which 78% pass the quality cut. Details of the refined distribution are shown in Fig. 6.9. Charge peaks are visible up to $Z \simeq 30$.

The charge resolution obtained with scintillators of a few tenths of charge units, ranging from $\simeq 0.15$ for the lightest elements to $\simeq 0.35$ for iron, as shown in Fig. 6.10. It is likely that a few more charges beyond $Z = 30$ might be discriminated if the corresponding nuclei were present in the beam in higher numbers.

The results presented in this chapter have been applied in the context of the LIP analysis of the AMS RICH prototype data. An excellent agreement was found between the scintillator charge measurement presented here and the charge measurement obtained from the Čerenkov ring signal [131], as shown in Fig. 6.11.

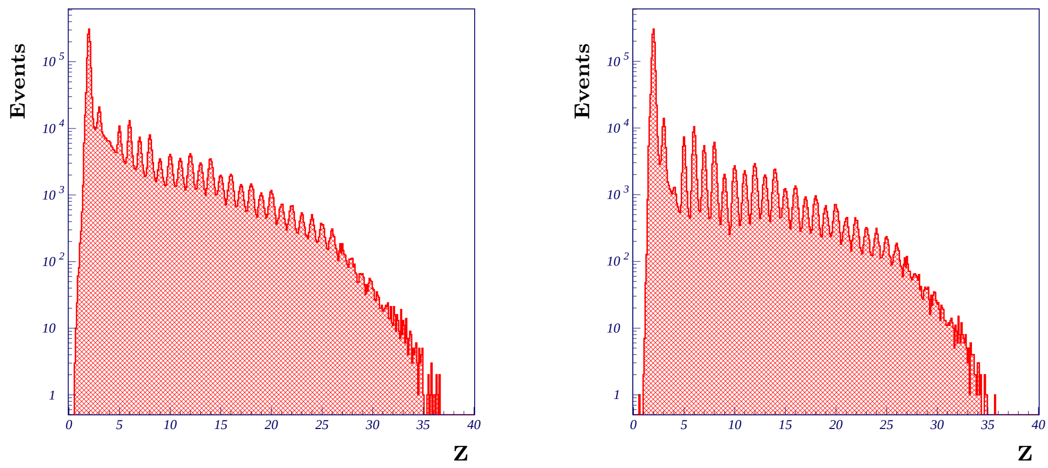

(a) (b)

Figure 6.8: *Distribution of reconstructed charges obtained for a total of 27 runs (all with $A/Z = 2$): (a) all events, (b) after compatibility selection ($\Delta Z < 0.5$).*

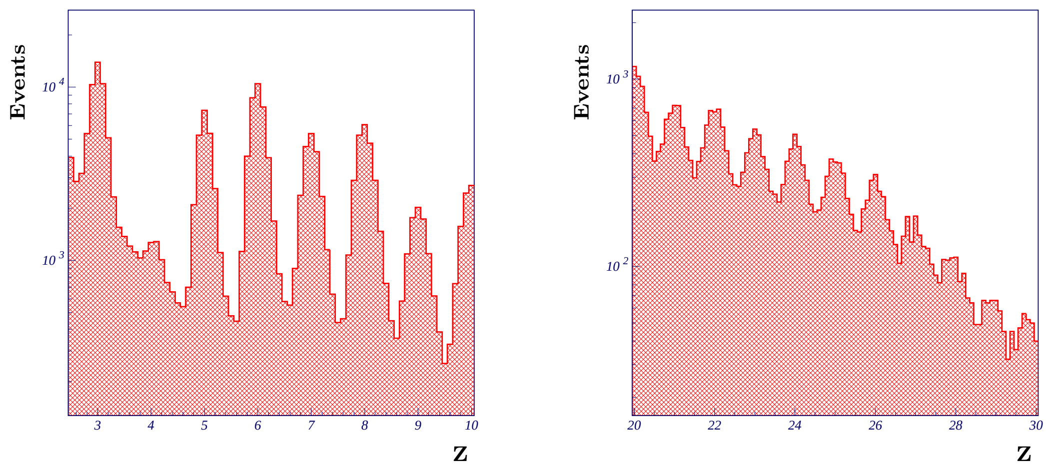

(a) (b)

Figure 6.9: *Two details of Fig. 6.8(b): (a) Low Z region showing a small Be peak due to contamination from ions with $A/Z \neq 2$; (b) High Z region displaying clear charge peaks up to $Z \simeq 30$.*

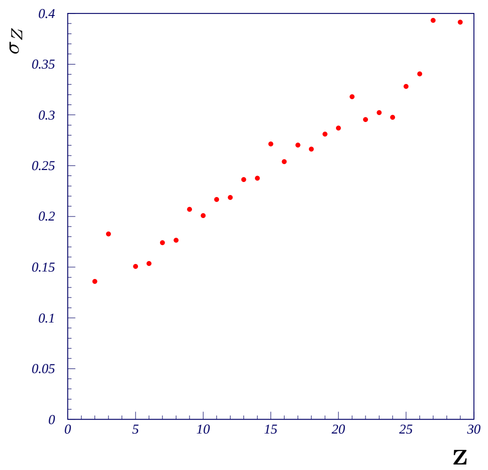

Figure 6.10: *Scintillator charge resolution as function of Z, evaluated from peak widths given by Gaussian fits to the global charge distribution of a total of 27 runs with $A/Z = 2$ after compatibility selection.*

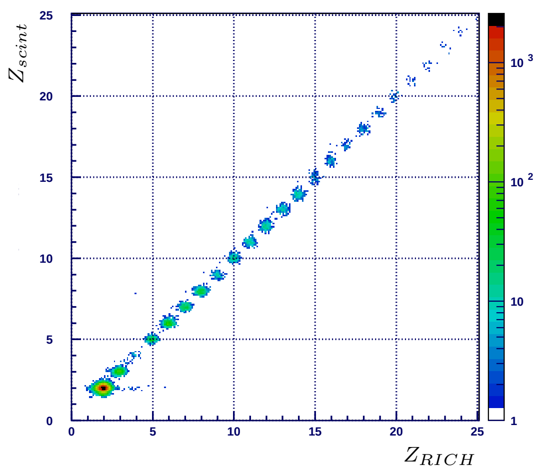

Figure 6.11: *Comparison of charge measurements obtained from scintillators and from the RICH prototype in the 2003 beam test. (from Ref. [131])*

6.10 Conclusions

Scintillator anode readings provided reliable, independent measurements of ion charge in the October 2003 beam test of the AMS prototype. These results may be used to evaluate the quality of other charge measurements, including the one provided by Čerenkov ring reconstruction in the RICH detector.

Scintillator calibration was applied successfully to a total of 45 runs with $A/Z = 2$ and $A/Z = 9/4$. Charge identification was possible up to the region of iron ($Z \simeq 30$), this upper limit coming from the low number of counts at higher charges.

Results obtained were compared to existing models of scintillator response. The best results were obtained for the Birks-Chou model and the Birks model with inverse tangent. In general, however, an accurate fit across all charges is not possible, and large differences in scintillator response for different conditions make fit parameters unpredictable. This means that none of the fits considered can replace evaluations for each individual run and scintillator using peaks in charge distribution.

Chapter 7

Aerogel light yield evaluation in prototype beam tests

This chapter summarizes the procedure and results of the light yield characterization studies based on the data collected during the in-beam tests performed at CERN in 2002 and 2003 using the AMS RICH prototype [136]. Detailed descriptions of the RICH prototype and of the in-beam tests can be found in Chapter 5.

Simulated data samples played an important role in this study. These simulations were performed using the standalone RICH simulation code described in Section 4.7.

7.1 Aerogel samples

A total of seven aerogel samples from two manufacturers were tested at different beam energies during the 2002 and 2003 campaigns.

In the 2002 beam test five aerogel samples were tested, three of them from Matsushita (MEC) with refractive indices 1.03 (two samples) and 1.05, and other two from the Boreskov Institute of Catalysis (CIN) with refractive indices 1.03 and 1.04. In the present study, test beams used were composed of secondary protons produced by coalescence and having momenta of 5, 7, 9, 11 and 13 GeV/c.

For the 2003 test, a selection of helium events from runs with $A/Z = 2$ and $p = 158$ GeV/c/nucleon was used. The selection of helium events was performed using scintillator charge measurements obtained from the reconstruction method described in Chapter 6. Three aerogel samples were tested, one of which (CINy02.103) had already been used in the 2002 test. The other two samples had a refractive index 1.03 from Matsushita and a refractive index 1.05 from the Boreskov Institute. Table 7.1 summarizes the samples and beam conditions used in 2002 and 2003.

The design of the radiator plane includes a foil in front of the radiator tiles. One of the aerogel samples was tested including a plastic foil which was worst in optical properties than the one to be used in the final detector.

The analysed samples from the 2002 test had a number of events ranging from $\sim 1 \times 10^4$ to $\sim 5 \times 10^4$, while the samples from 2003 had $\sim 10^5$ events each.

2002									
Sample	Refractive index	Thickness (mm)	Foil	p (GeV/c/nuc)					particle type
				5	7	9	11	13	
MECy02.103	1.03	2×11	no	✓	✓	✓	✓	✓	p
MECy02.105	1.05	2×11	no	-	✓	✓	-	✓	p
CINy02.103	1.03	30	no	✓	-	✓	-	✓	p
MECy01.103	1.03	3×11	yes	✓	✓	✓	-	✓	p
CINy02.104	1.04	30	no	✓	✓	✓	-	✓	p
2003									
Sample	Refractive index	Thickness (mm)	Foil	p (GeV/c/nuc)					particle type
				158					
CINy02.103	1.03	30	no	✓					He
MECy03.103	1.03	3×11	no	✓					He
CINy03.105	1.05	25	no	✓					He

Table 7.1: *Aerogel samples used in the 2002 and 2003 beam tests. Names starting with "MEC" correspond to samples from Matsushita, while names with "CIN" denote samples from the Boreskov Institute of Catalysis.*

7.2 Data selection

Among the data collected in 2002 and 2003 test beams, most events corresponded to particles crossing the prototype detector in a perpendicular way. Such events generated a circular Čerenkov ring in the detector matrix.

In the 2002 analysis, two kinds of background events were identified and had to be rejected from the data samples. Firstly, a significant muon contamination was present in particular at low momenta. These events, having a different velocity from protons, would have a larger Čerenkov ring signal. In addition, a significant fraction of events presented a large number of noisy hits when compared to the expected number arising from the aerogel scattering. Such noisy hits can contribute to a systematic shift in the evaluated Čerenkov ring signal. Figure 7.1 displays proton (clean and noisy) and muon events collected in the 2002 test.

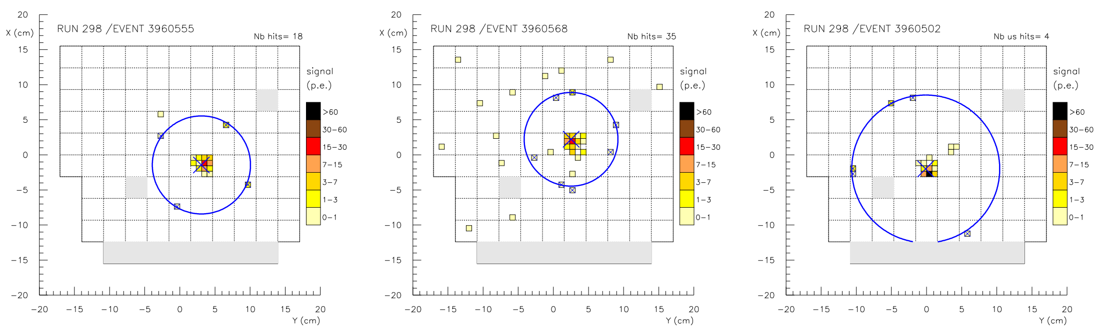

Figure 7.1: *Event displays of reconstructed rings for protons (left, centre) and muons (right) with $p = 5$ GeV/c; the second proton event contains a large number of noisy hits.*

The fact that protons and muons have different masses allows to use the velocity measurement as a discriminant observable for muon rejection. Figure 7.2 shows the reconstructed velocity distributions for radiator MECy02.103 at beam momenta of 5, 7, 9, 11 and 13 GeV/c. For lower momenta the muon peak is clearly seen at $\beta \simeq 1$, while protons peak near but not exactly at the expected velocity. The observed proton peak in the velocity distribution was used to obtain a corrected value for the beam momentum. To exclude muon events, and moreover bad reconstructions of proton events, only reconstructed velocities within 3σ (that is, in the range $\beta_{peak} \pm 0.003$) were considered. The larger the beam energy was the smaller the muon component became, vanishing at higher energies.

The accurate measurement of average proton velocity for each run, obtained from the RICH prototype, showed small differences with respect to the expected value. The RICH measurements were used to obtain a better estimate of particle momentum.

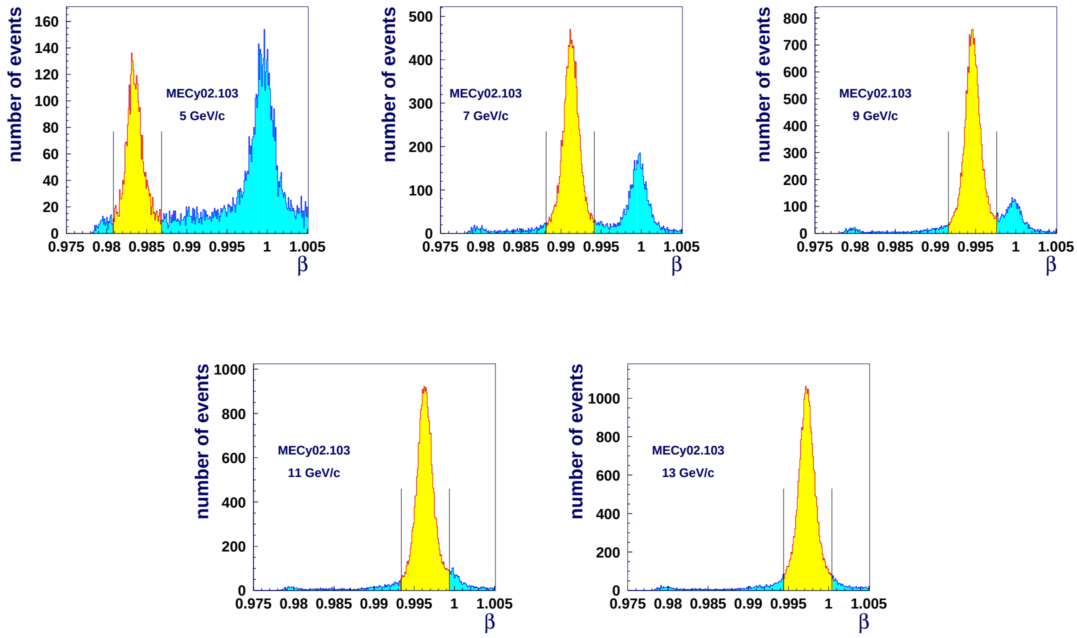

Figure 7.2: *Distributions of reconstructed velocity using the same radiator at different momenta. Vertical lines show the acceptable velocity range. Muon contamination, which is stronger at low momenta, appears as an additional peak at $\beta \simeq 1$.*

The events with noisy hits were addressed by studying the correlation between the number of hits inside and outside the Čerenkov ring. In normal conditions, the number of hits associated to the ring signal and the number of noisy hits should be uncorrelated. Figure 7.3(a) shows, for a data sample from a 5 GeV/c proton beam impinging on aerogel MECy02.103, a strong correlation above a number of noisy hits around 5. Although the fraction of noisy events is significantly smaller at higher energies, similar correlations were found for all the other test energies and aerogel samples. Therefore, a clear bias in the measured ring signal was observed. To reduce this effect in the data samples, a cut on the number of noisy hits in the event was applied. Only events with a number of noisy hits lower than 5 were selected. Figure 7.3(b) shows the distribution of all the hits in the detection matrix in terms of its active inner area, for a 5 GeV/c proton sample. After applying the noisy hits cut, the signal in the Čerenkov ring to background ratio is strongly improved. Figure 7.3(c) shows the effect on the data sample applying both the velocity and noisy hits cuts.

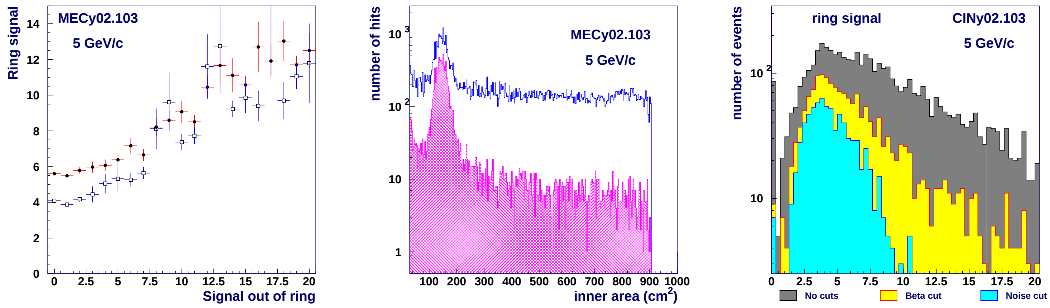

(a) (b) (c)

Figure 7.3: *Data sample of 5 GeV/c protons. (a): Average Čerenkov ring signal as function of non-ring signal before (full dots, red bars) and after (open squares, blue bars) applying the velocity cut. (b): signal distribution as function of its active inner area before (blue) and after (pink) applying the noisy hits cut. The rise to the left of the peak corresponds to the tail of the charged particle signal. (c): Čerenkov ring signal distribution after applying the different cuts.*

7.3 Light yield determination

An evaluation of the signal associated to the Čerenkov rings needs to be performed in order to determine the aerogel light yield. The reconstruction of the Čerenkov rings was performed using the LIP algorithm developed for the full-scale RICH detector [131] and adapted to the prototype setup. This approach uses a maximum likelihood method based on the calculation of distances between individual hits and the hypothetical Čerenkov rings. The estimated Čerenkov angle corresponds to the maximum probability of having the detected hits belonging to the ring. The ring signal is obtained by adding the signal of the hits within a ring distance of 1.3 cm.

In general, during both 2002 and 2003 tests, the Čerenkov rings produced by beam particles were not fully contained in the PMT matrix. Additionally, small regions of dead pixels were observed in the readout matrix as shown in Fig. 7.4(a). Therefore, the evaluation of the aerogel photon yield implies the knowledge of the visible fraction of the Čerenkov ring (ring acceptance). The procedure for the ring acceptance estimation is described in Ref. [142], for null-width rings. In this reconstruction the effect of the ring width was taken into account. Sampling the ring acceptances at five different Čerenkov angles around the fitted value, $\theta_c = \theta_c^0 + i\,\sigma_{\theta_c}$, with $i = 0, \pm1, \pm2$, the mean ring acceptance can be calculated according to $\varepsilon = \sum_i \varepsilon_i\; w_i / \sum_i w_i$. Assuming a Gaussian distribution, the weight factor is given by $w_i = e^{-i^2/2}$. Figures 7.4(b) and 7.4(c) present the evaluated ring acceptances for two data samples with $p = 13$ GeV/c/nucleon and aerogel refractive index $n = 1.03$ and 1.05. Acceptances lower than 1 observed in the case of the $n = 1.03$ aerogel data sample are essentially due to dead areas in the PMT matrix. while in addition the acceptance for the $n = 1.05$ aerogel reflects the larger Čerenkov rings which in many cases are not fully contained within the detection matrix.

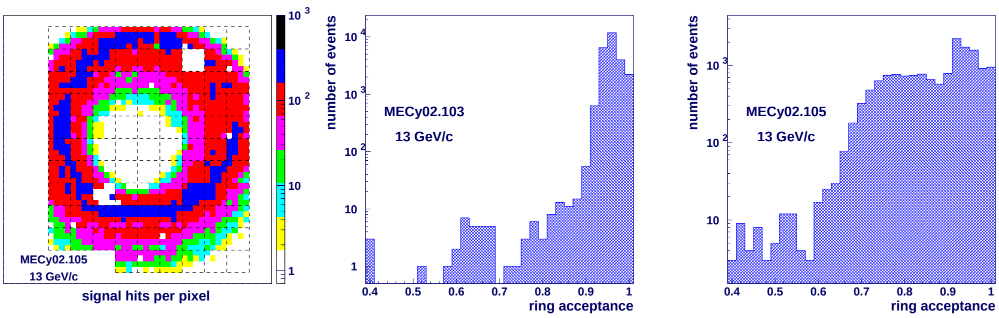

(a) (b) (c)

Figure 7.4: *(a): Distribution of the number of ring hits detected in each pixel for a single data sample at 13 GeV/c. (b,c): Ring acceptance distributions at 13 GeV/c for two radiators in the 2002 beam test.*

The signal distribution associated to a given aerogel data sample will depend on:

- **ring acceptance**

  For events having a ring acceptance ε, the mean number of photoelectrons expected (N) will be given according to $N = \varepsilon N_0$, where N_0 is the expected number of photoelectrons in a fully contained ring.

- **statistical fluctuation**

  Moreover, the observed number of hits (i) for a sample with a given acceptance

ε and a mean number of photolectrons N will fluctuate according to a Poisson law $p(i) = \frac{e^{-N} N^i}{i!}$.

- **photomultiplier gain**
  Finally, the detected signal in the photomultiplier anode is related to the number of photoelectrons generated in the photocathode, by a gain factor of the order of 10^6. This results from the photoelectron amplification along the dynode chain. The statistical nature of the amplification process induces an uncertainty in the gain of the order of 0.5-0.6 photoelectrons. The signal distributions for $i = 1$ and $i = 3, 4, 5, 6$ photoelectrons, reflecting the uncertainty in the chain amplification, are shown, respectively, in Figs. 7.5(a) and 7.5(b).

In the 2002 analysis, the radiator tiles were studied using proton beams with a relatively large spread ($\sim$ 2 cm). This implies a large variation in the ring acceptance. In addition, a low number of photoelectrons was expected. Therefore, the distribution of detected ring signals, x, may be parameterized as a function of the expected number of photoelectrons in a fully contained ring (N_0) and a normalization factor A corresponding to the total number of events being analysed,

$$f(x; N_0, A) \propto \sum_{\varepsilon_j} \sum_{i=3}^{\infty} P(\varepsilon_j) \frac{e^{-x} (\varepsilon_j N_0)^i}{i!} f_i(x)$$

where $P(\varepsilon_j)$ is the fraction of events with geometrical acceptance ε_j and $f_i(x)$ corresponds to the signal distribution for i hits. The ring signal distributions and corresponding fits for three different samples corresponding to different aerogel radiators and energies, are shown in Fig. 7.6.

In the case of the 2003 test, the aerogel tiles were studied with a selection of helium ($Z = 2$) events of 158 GeV/c/nucleon. Compared to 2002, the particle beam was narrower ($\sim$ 1 mm) and therefore the Čerenkov rings had a constant geometrical ring acceptance. Moreover, the usage of helium events implied an expected number of ring photoelectrons which was larger by a factor 4 and following a Gaussian law. In this context, the calculation of the light yield corresponding to a fully contained ring was simplified. A Gaussian fit was applied to the signal distribution (Fig. 7.7) and the result obtained was divided by the ring acceptance.

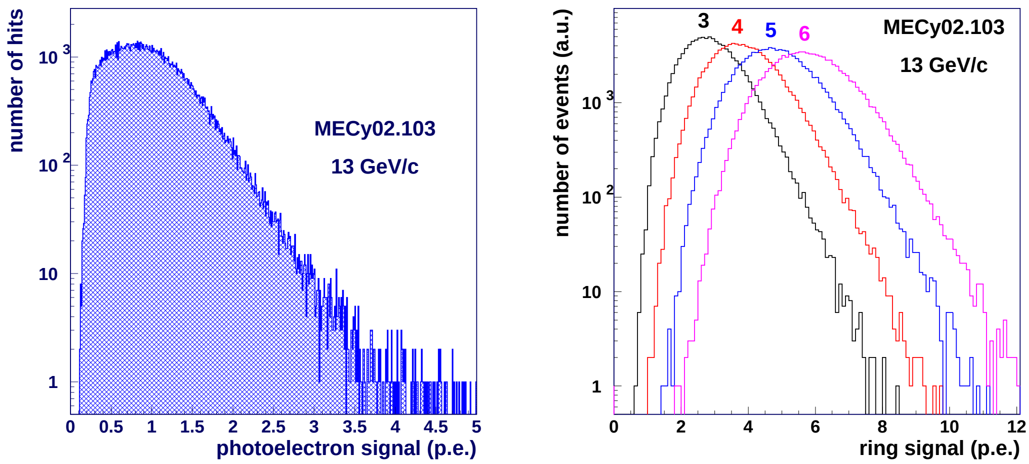

(a) (b)

Figure 7.5: *(a): Hit signal distribution for a high momentum sample. (b): Expected signal distribution for sets of 3, 4, 5, and 6 photoelectrons in this sample.*

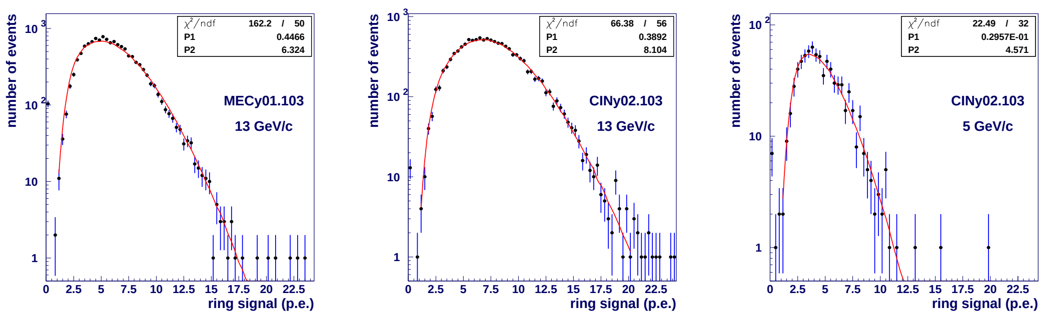

Figure 7.6: *Fit to reconstructed signal distribution for three data samples.*

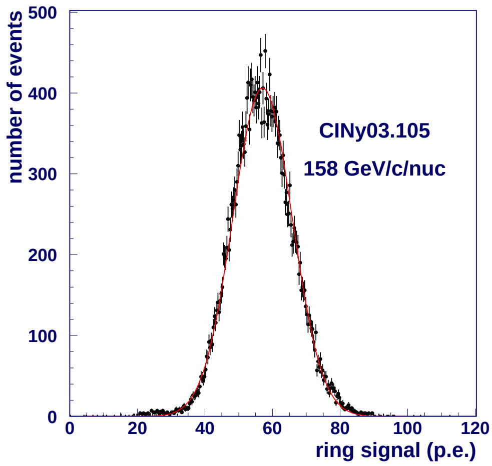

Figure 7.7: *Reconstructed signal distribution of helium events in 2003 test (CINy03.105, 158 GeV/c).*

In 2002, the presence of beams with different energies allowed to check the consistency of the different measurements. In addition, it could be used to derive the expected light yield at $\beta = 1$, for each aerogel sample. This could be attained by fitting the set of results obtained for a given radiator at different energies to the expression giving the evolution of the light yield (N_{pe}) with particle momentum:

$$N_{pe} = N_0^{(\beta=1)} \left[1 - \frac{(m/p)^2}{n^2 - 1} \right] \tag{7.1}$$

where $N_0^{(\beta=1)}$ is proportional to $\frac{n^2-1}{n^2}$ and depends linearly on the sample's thickness and radiator absorption.

7.4 Systematic corrections and uncertainties

Several factors related to signal threshold and calibration, and background from noisy hits can affect the light yield estimates. In addition, the presence of a radiator plastic foil in some of the runs lead to a reduced light yield. A full description of these effects, and their implication on the 2002 and 2003 data analysis, is reported in the following subsections.

7.4.1 Pixel noise

Despite the applied selection criteria, a significant fraction of noisy hits remained on the 2002 data samples. The signal associated to the collected hits, regardless of the proton beam energy, should reproduce the photoelectron distribution. The existence of a possible contamination on the different samples was checked. A background component, identified as an excess of low-signal hits, was observed in the lower momenta beam samples. Figure 7.8 shows the hits signal distributions for different 5 GeV/c samples. The excess of low-signal hits is clearly visible in distributions (b) and (c).

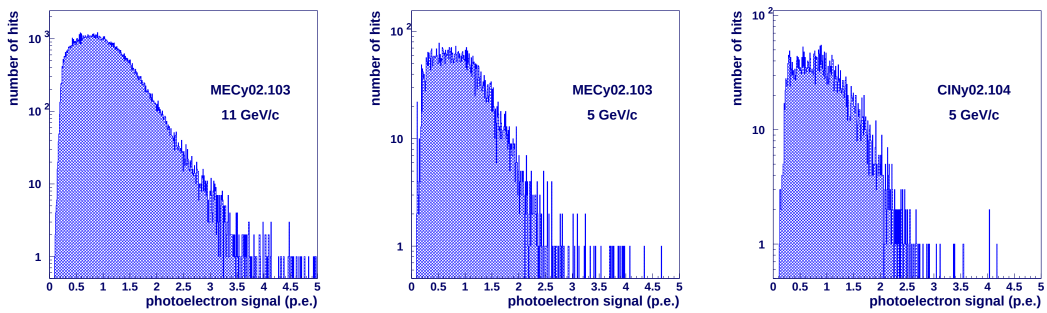

(a) (b) (c)

Figure 7.8: *Distribution of hit signals for three data samples.*

The effect of the noisy hits in the light yield evaluation may be estimated assuming that in each sample the observed ring signal S' is the sum of a true signal S and a background contribution S_B. The magnitude of the signal correction is given by the following expression:

$$\frac{< S' >}{< S >} = \frac{N_B}{N'} \frac{< S_B >}{< S >} + \frac{N}{N'}$$

where $N' = N + N_B$ is the observed number of ring hits, N is the number of signal hits and N_B is the number of background hits. For each sample a comparison of the photoelectron profile, obtained at higher momentum (13 GeV/c), with the observed hit signal profile is performed. Assuming that contamination is only present in hit signals below 0.6 p.e., the fraction of background hits N_B/N' and the average signal of background hits $\frac{<S_B>}{N_B}$ can be derived. The estimated fraction of background hits was lower than $\sim 3\%$ for beam momenta of 7 GeV/c or higher while for the 5 GeV/c samples a more significant noise correction, at the level of $\sim$ 5-10%, was derived.

7.4.2 Signal threshold

To reduce the size of RICH events in data acquisition a minimal hit signal (threshold) is applied to the gathered pixel signals. Only ADC counts clearly above the pedestal ($4\,\sigma_{ped} \sim 15$) are collected. The presence of this threshold may introduce a bias in the ring signal estimate since very low signal hits may remain undetected. On the other hand, PMT noise, if above threshold, can contribute with additional hits to the ring signal.

This signal threshold effect was evaluated by performing simulations switching on and off thresholds, for each individual data sample. Simulation results showed that such effect was negligible in the 2003 test but significant in the 2002 test where a fraction up to 8% of hits was not detected. The corresponding reduction in the total ring signal was not as significant since these non-detected hits have very low signals.

7.4.3 Sample calibration

In the 2002 analysis, the photoelectron calibration is automatically taken into account on the light yield method by the inclusion of the photoelectron signal profile in the fitting procedure.

In the case of the 2003 analysis such calibration is not feasible since the Čerenkov patterns studied corresponded to events with $Z = 2$ where a significant fraction of ring hits correspond to the detection of more than one photon. It was observed that the average signal of scattered hits, where the effect of double photons should be negligible, showed significant deviations from 1, fluctuating between runs. Such fluctuations, which cannot be estimated for ring hits, have a direct effect on the light yield evaluation and were considered as a systematic error with a magnitude of 3%.

In addition to the sample calibration, the dispersion of individual PMT gains was checked. A large statistics of hits per PMT was collected in order to ensure a good accuracy of the gain evaluations. Some non-uniformities were observed, with a spread $\sigma_{PMT} \sim 5\%$ in distribution of the average PMT signals. Figure 7.9 shows the variation of the average signal between PMTs. Since in each sample the Čerenkov rings cover an area of ~ 20 PMTs, the estimated systematic error on the photoelectron calibration is $\sigma_{cal} \sim \frac{5\%}{\sqrt{20}} \simeq 1\%$.

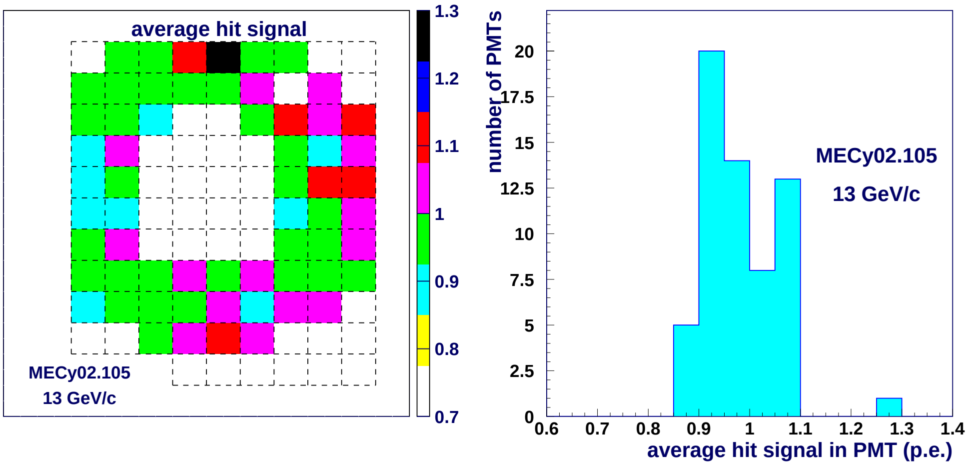

(a) (b)

Figure 7.9: *Average photoelectron signal in different PMTs as fraction of global average for a data sample: results by PMT (a), overall distribution (b). PMTs shown in white did not have significant statistics and were not included in the overall distribution.*

7.4.4 Foil attenuation

In the case of radiator MECy01.103 an additional correction had to be estimated since this was the only radiator for which a polyester foil was used. This polyester foil absorbed a significant fraction of the light produced in the aerogel. Simulations were used to estimate photon absorption, giving a light yield reduction of 17%.

7.5 Light yield results

The procedures and corrections described in the previous sections were applied to obtain light yield estimates for the aerogel samples tested in 2002 and 2003. Table 7.2 shows the mean light yield results obtained for full-acceptance rings and for the different aerogel samples tested in 2002 and 2003.

The evolution of the light yield for the aerogel samples tested in 2002 as function of the beam proton momentum is shown in Fig. 7.10. The fit to the experimental values performed using the expression 7.1 shows a good agreement with light yield measurements for the different aerogel samples. The light yields for full acceptance rings and normalized to $\beta = 1$, $N_0^{(\beta=1)}$, are derived from the fits.

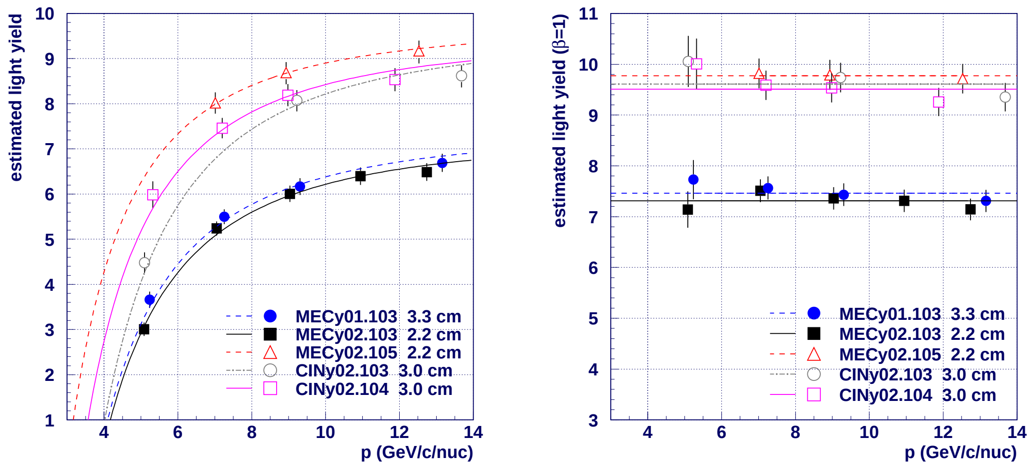

(a) (b)

Figure 7.10: *Evolution of light yield with particle momentum for the different aerogel samples tested in 2002. Points correspond to results obtained for each sample, while lines are the result of a fit to the available points for each aerogel sample. Plot (a) shows the average number of photoelectrons for a fully contained ring at each momentum, while plot (b) has all values rescaled to the $\beta = 1$ case.*

Table 7.3 summarizes the light yield results obtained for full acceptance rings and normalized to $\beta = 1$, for all aerogel samples tested in 2002 and 2003. Results for radiator MECy01.103 have been corrected to take the presence of a foil into account. One of the samples used in 2003, CINy03.105, had the highest light yield

2002				
Radiator	Foil	p (GeV/c)		Light yield
		nominal	observed	estimate
MECy02.103	no	5	5.085 ± 0.002	3.01 ± 0.15
MECy02.103	no	7	7.050 ± 0.006	5.24 ± 0.16
MECy02.103	no	9	9.036 ± 0.013	6.01 ± 0.18
MECy02.103	no	11	10.945 ± 0.023	6.40 ± 0.19
MECy02.103	no	13	12.741 ± 0.036	6.49 ± 0.20
MECy02.105	no	7	7.012 ± 0.006	8.02 ± 0.24
MECy02.105	no	9	8.933 ± 0.012	8.69 ± 0.26
MECy02.105	no	13	12.526 ± 0.034	9.17 ± 0.28
CINy02.103	no	5	5.099 ± 0.002	4.48 ± 0.22
CINy02.103	no	9	9.224 ± 0.014	8.07 ± 0.24
CINy02.103	no	13	13.681 ± 0.044	8.62 ± 0.26
MECy01.103	yes	5	5.237 ± 0.003	3.66 ± 0.18
MECy01.103	yes	7	7.258 ± 0.007	5.50 ± 0.16
MECy01.103	yes	9	9.307 ± 0.014	6.17 ± 0.18
MECy01.103	yes	13	13.161 ± 0.039	6.69 ± 0.20
CINy02.104	no	5	5.323 ± 0.003	5.99 ± 0.30
CINy02.104	no	7	7.204 ± 0.007	7.46 ± 0.22
CINy02.104	no	9	8.980 ± 0.013	8.19 ± 0.25
CINy02.104	no	13	11.881 ± 0.029	8.54 ± 0.26
2003				
Radiator	Foil	p (GeV/c/nuc)		Light yield
		nominal		estimate
CINy02.103	no	158		10.53 ± 0.37
MECy03.103	no	158		11.04 ± 0.39
CINy03.105	no	158		14.59 ± 0.51

Table 7.2: *Event data samples and corresponding light yield estimates.*

by a large margin despite having a relatively low thickness (25 mm).

2002	
Sample	$N_0^{(\beta=1)}$
MECy01.103	9.00 ± 0.15
MECy02.105	9.78 ± 0.17
CINy02.103	9.61 ± 0.19
MECy02.103	7.31 ± 0.10
CINy02.104	9.51 ± 0.16

2003	
Sample	$N_0^{(\beta=1)}$
CINy02.103	10.53 ± 0.37
MECy03.103	11.04 ± 0.39
CINy03.105	14.59 ± 0.51

Table 7.3: *Light yield estimates ($\beta = 1$) for aerogel samples. Results for radiator MECy01.103 have been corrected to account for foil absorption.*

The decision regarding the radiator to be used in the final detector required a comparison of the light yield of different aerogel samples normalized to a common thickness. The reference value for thickness was chosen to be 25 mm. Simulations were performed for each sample (except those that had a thickness of exactly 25 mm) using the real and reference thicknesses. A correction factor was derived and used to rescale the light yield values, to the reference thickness.

Figure 7.11 shows the rescaled light yield results for all aerogel samples. One sample, CINy03.105, had the highest light yield by a wide margin. The material of this sample was chosen to integrate the final radiator of the AMS-02 RICH detector.

Results obtained for the light yield at different energies with the same aerogel sample may be used to obtain an independent estimate of its refractive index. This is done by performing a fit to expression 7.1 with two free parameters, n and $N_0^{(\beta=1)}$. Table 7.4 summarizes the results obtained applying this fit to the results of the 2002 test (Fig. 7.12). The reference values of n, obtained from previous estimation [143], are shown for comparison. A good agreement is observed.

7.6 Conclusions

Different batches of aerogel samples were tested and their light yields were evaluated in the context of the AMS-02 RICH prototype tests. The analysis of the aerogel samples was performed and a method was developed for the light yield determina-

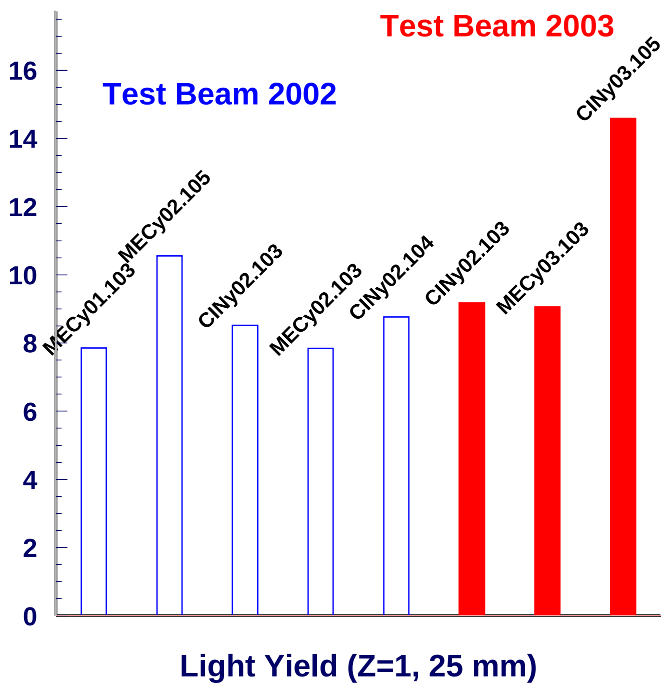

Figure 7.11: *Comparison of aerogel light yields rescaled for a thickness of 25 mm.*

Sample	Fit results		reference value
	N_0	n	
MECy01.103	8.83 ± 0.22	1.0319 ± 0.0027	1.0298
MECy02.105	9.71 ± 0.38	1.0505 ± 0.0156	1.0477
CINy02.103	9.44 ± 0.24	1.0319 ± 0.0025	1.0300
MECy02.103	7.32 ± 0.14	1.0289 ± 0.0017	1.0289
CINy02.104	9.25 ± 0.26	1.0432 ± 0.0062	1.0379

Table 7.4: *Light yield results leaving n as a free parameter.*

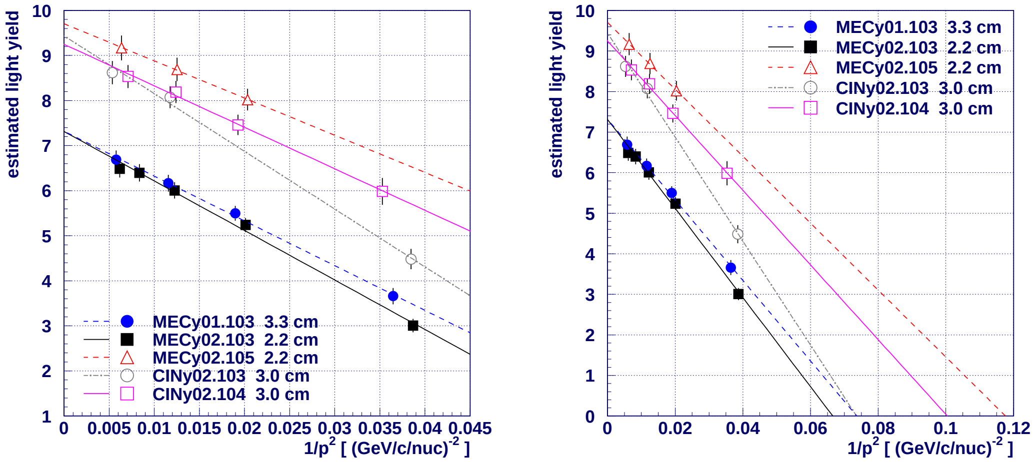

(a) (b)

Figure 7.12: *(a): Evolution of light yield with particle momentum for different aerogel samples, with a fit leaving n as a free parameter. Using $1/p^2$ instead of p makes the fit linear, with the y-axis crossing point corresponding to the light yield estimate. (b): The same plot with a different scale. The refractive index of each sample is directly determined from the value of $1/p^2$ for which the light yield reaches zero.*

tion.

The procedures detailed in this chapter allowed to make the choice of an aerogel from the Boreskov Institute of Catalysis with $n = 1.05$ which presented both good optical transparency ($C = 0.0055\ \mu\text{m}^4\ \text{cm}^{-1}$) and high light yield, with an estimate of 14.59 ± 0.51 photoelectrons obtained for full acceptance rings in the prototype setup with an aerogel thickness of 25 mm.

Chapter 8

Performance studies with the AMS-02 RICH detector

In early 2008 only one major part of the AMS-02 detector, the superconducting magnet, was still to arrive at CERN. Since the magnet was not expected to arrive until several months later, it was decided to integrate all AMS-02 components excluding the magnet, perform a set of tests to evaluate the detector's functionality and then, since it would not be possible to add the magnet directly to the integrated detector, to disassemble AMS-02 and assemble it a second time with the superconducting magnet in place.

Tests performed with AMS-02 after both assemblies included the acquisition of cosmic-ray events.

8.1 The 2008 and 2009 cosmic-ray tests

In 2008, during and after the integration of all detector components excluding the magnet, the AMS-02 detector was tested by acquiring data from the natural cosmic-ray flux. Data acquisition took place at CERN between January and June 2008. Part of the acquired data was used for the studies presented in the remainder of this chapter.

The AMS-02 superconducting magnet arrived at CERN in December 2008. The setup used in 2008 was when disassembled to allow for a full detector assembly, including the magnet.

The fully assembled detector underwent a new period of cosmic data acquisition in late 2009. Part of this acquisition was performed with the superconducting magnet turned on and working at the design current of 400 A. Data acquired in December 2009 at the design current were used in the long-term light yield stability study presented in Subsection 8.3.3.

8.2 RICH light yield evaluation in AMS-02

One of the most important indicators for the performance of the AMS RICH detector is its light yield, that is, the number of Čerenkov photons that may be expected to be detected in each event.

Light yield evaluation for aerogel samples had already been performed for the RICH prototype using data from the 2002 and 2003 in-beam tests, as described in Chapter 7. The 2008 tests provided the first opportunity to perform the same kind of evaluation for the final detector and to compare it with estimates obtained from detector simulations.

In addition, light yield estimates with a full detector and events with different topologies provided the perfect setting for a detailed evaluation of the quality of reconstruction algorithms. Displays of cosmic event patterns and the corresponding reconstructed Čerenkov rings are shown in Fig. 8.1.

8.2.1 Normalization of light yield estimates

Part of the Čerenkov photons generated in the AMS-02 radiator will not reach the detection matrix but instead fall on the central hole (where the Electromagnetic Calorimeter is inserted) or in one of the smaller gaps between the matrix grids. Finally, the matrix grids themselves have a dead area corresponding to the gaps between light guides, which correspond to 15.6% of the grid area.

The presence of a conical mirror prevents a large fraction of photons from falling out of the RICH matrix perimeter, but a fraction of those photons is in turn lost due to the non-perfect mirror reflectivity. The expected reflectivity for the AMS-02 mirror is 85%.

The definition of an aerogel light yield for AMS-02 implies a specific context.

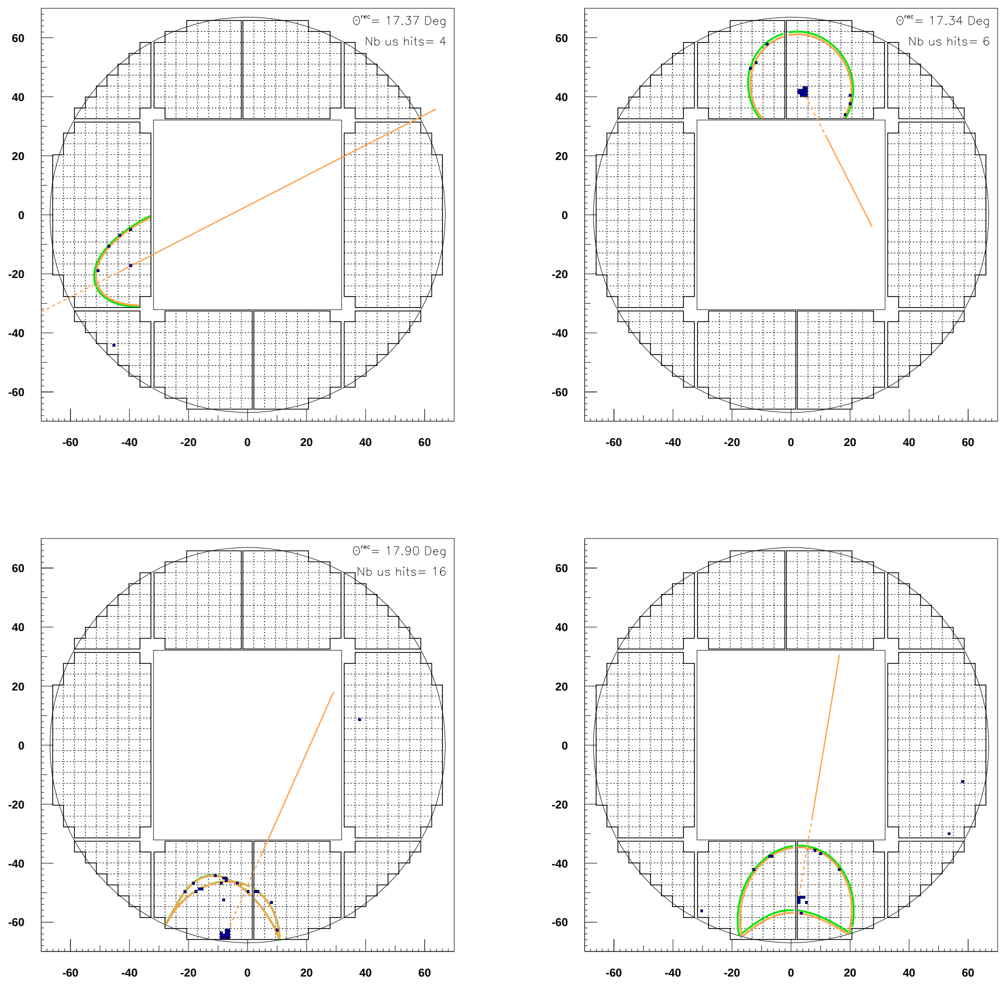

Figure 8.1: *RICH displays of four cosmic events collected in the 2008 acquisition at CERN.*

The light yield value should provide a simple measurement of the detector's typical response in terms of Čerenkov emission. It is also desirable that the light yield definition may be consistently applied for all events regardless of their specific details.

In the following discussions, two different light yield estimators will be used. The first estimator, N_0, has a simpler definition but is not independent of event geometry, while the the second, L_0, incorporates all known event characteristics and is therefore expected to be completely independent of event properties.

The estimator N_0 may be described as:

N_0 is the expected number of detected photons for a fully contained ring generated by a single-charged particle travelling at $\beta = 1$.

For a specific event, the value of N_0 may be estimated by rescaling the event's observed light yield to the standard conditions in the above definition (that is, 100% acceptance, $Z = 1$, $\beta = 1$).

The emission of Čerenkov photons is related to the particle's velocity and charge (as already mentioned in Section 4.1) according to the expression

$$\frac{d^2N}{dx\ dE} = \frac{2\pi\alpha}{hc}\ Z^2\ sin^2\theta_c = \frac{2\pi\alpha}{hc}\ Z^2\ \left(1 - \frac{1}{\beta^2 n^2}\right)$$

Rescaling light yield results obtained for a certain velocity β to the reference value $\beta = 1$ therefore implies multiplying the result by $\frac{1-1/n^2}{1-1/(\beta^2 n^2)} = \frac{n^2-1}{n^2-1/\beta^2}$. Considering the proportionality to Z^2 and the effect of the visible acceptance fraction ε_{acc} (which already incorporates the effect of non-perfect reflectivity: $\varepsilon_{acc} = \varepsilon_{dir} + 0.85\varepsilon_{mir}$), the value N_0 may be estimated from the ring signal N_{pe} as

$$N_0 = \frac{N_{pe}}{\varepsilon_{acc}\, Z^2} \frac{n^2 - 1}{n^2 - 1/\beta^2}$$

The main advantage of this estimator is providing a simple, intuitive result for the expected number of hits. It is an adequate estimator in cases where all events have a similar geometry, such as in the prototype studies of Chapter 7 where this kind of normalization was used.

However, in the full AMS-02 detector is it desirable to introduce a more comprehensive estimator. Some important event characteristics are not addressed by N_0: events with different inclinations will cross significantly different lengths of aerogel, meaning that different numbers of Čerenkov photons will be emitted and different fractions of those photons will interact in aerogel; photons produced by particles with different trajectories will also have different inclinations, which will lead to different detection efficiencies at the PMT matrix; some parts of the Čerenkov cone may not be detected due to shadows from detector components above the detection matrix.

In particular, the efficiency of photon collection at the detection matrix is known to be a function of particle trajectories. Studies performed at LIP using standalone simulations of the AMS-02 and prototype light guides in GEANT 3 [131] showed that the best values of efficiency are obtained for perpendicular photons, with very significant decreases expected for photon incidence angles above 30° as shown in Fig. 8.2.

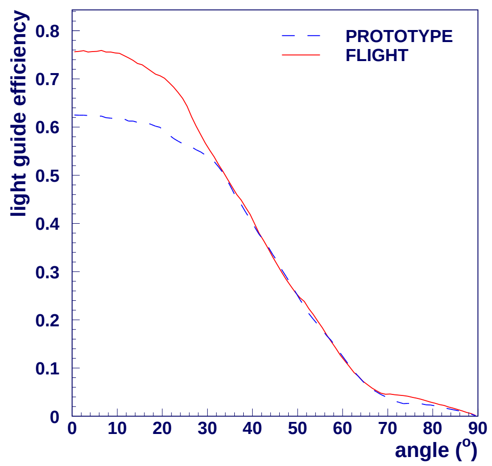

Figure 8.2: *Estimated light collection efficiency as function of photon incidence angles for the AMS prototype and flight light guides.*

Incorporating all the previously mentioned corrections, a new estimator L_0 may be described as:

L_0 is the expected number of photons reaching the active areas of the detection matrix for a fully contained ring generated by a single-charged particle travelling at $\beta = 1$ and crossing a fully transparent radiator in a perpendicular trajectory.

There are three main changes in the definition of L_0 with respect to N_0. First, the “number of detected photons” is replaced by the “number of photons reaching the active areas of the detection matrix", meaning that a factor corresponding to the detection efficiency must be included. Second, the result must now be rescaled to a fully transparent radiator, compensating for the estimated light losses in aerogel. Third, the result should now apply to a perpendicular trajectory.

In the present work, the first two changes were incorporated by replacing the geometrical acceptance ε_{acc} with a global efficiency ε_{glob} that incorporates an estimate of photon losses both at the radiator (ε_{rad}) and at the detection matrix (ε_{mat}), that is,

$$\varepsilon_{glob} = \varepsilon_{acc}\,\varepsilon_{rad}\,\varepsilon_{mat}$$

The third change is easily introduced by multiplying the result by $\cos\theta$, where θ is the particle's inclination, to account for the length of the particle's trajectory in the radiator, which is given by $\ell = \frac{h}{\cos\theta}$, where h is the aerogel thickness, if the aerogel radiator is considered as a single piece (that is, ignoring the small gaps between tiles) and excluding the rare cases where a particle enters the radiator from its side[1].

The value of L_0 may therefore be estimated from the ring signal N_{pe} according to an expression that is similar to that obtained for N_0, with ε_{glob} in place of ε_{acc} and an additional factor $\cos\theta$:

$$L_0 = \cos\theta \frac{N_{pe}}{\varepsilon_{glob} Z^2} \frac{n^2 - 1}{n^2 - 1/\beta^2}$$

This is a universal estimator that is expected to give a similar result for different event configurations.

8.2.2 Individual tile properties

Studies performed on individual aerogel tiles before assembly showed that slight variations existed in tile properties (refractive index, clarity and thickness). Detailed values of these properties were available for the 60 square tiles only. Their distributions are shown in Fig. 8.3. Results from cosmic data analysis eventually showed

[1] In this work, the estimated effects due to such gaps at the matrix (non-radiating parts of the particle trajectory and shadows from tile borders) have also been included in the calculations in the form of a correction to the global efficiency parameter ε_{glob}.

that refractive index measurements were biased, and new values were obtained, as described in Subsection 8.3.1.

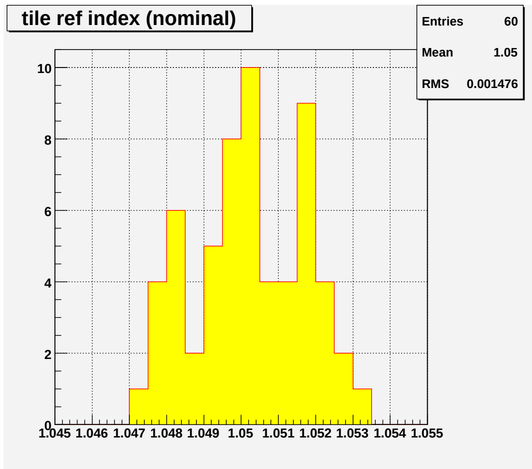

(a)

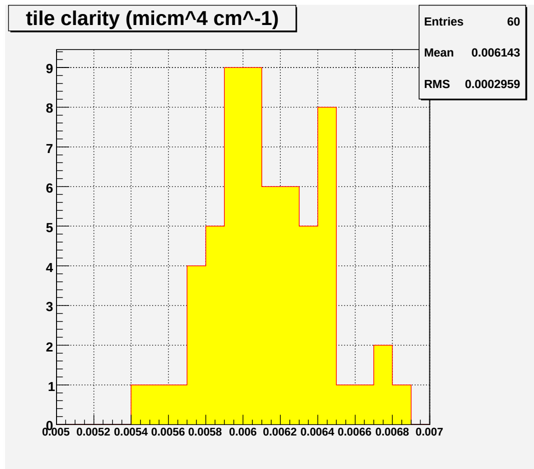

(b)

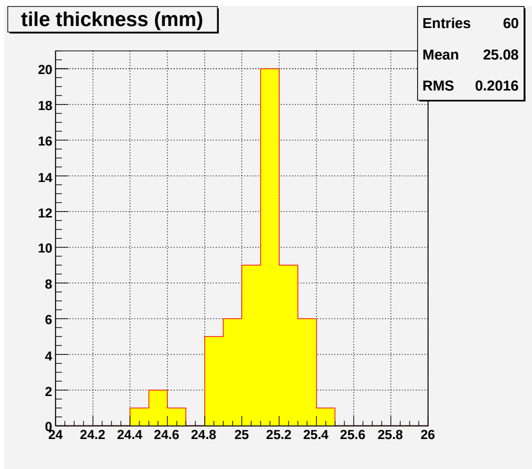

(c)

Figure 8.3: *Distribution of three properties for the square aerogel tiles: (a) refractive index (uncorrected); (b) clarity (in μm^4 cm^{-1}); (c) thickness (in mm). The distribution for the corrected refractive index in shown in Fig. 8.6.*

To account for variations in tile properties, results obtained for N_0 and L_0 in real data may be rescaled on an event-by-event basis:

- **refractive index**: rescaled to $n = 1.050$ according to $N_{pe} \propto \left(1 - \frac{1}{n^2}\right)$, which corresponds to $\frac{\Delta N_{pe}}{N_{pe}} \simeq 19.5\left(\frac{\Delta n}{n}\right)$;

- **clarity**: rescaled to $C = 0.0060\ \mu\text{m}^4\ \text{cm}^{-1}$ according to $\frac{\Delta N_{pe}}{N_{pe}} = -35\%\left(\frac{\Delta C}{C}\right)$;
- **thickness**: rescaled to $h = 25$ mm according to $\frac{\Delta N_{pe}}{N_{pe}} = 62.5\%\left(\frac{\Delta h}{h}\right)$;

The variation expected on the light yield from small changes in clarity and thickness follows estimates given in Ref. [131].

Light yield results coming from events crossing the 32 tiles at the edges, for which no such data were available, were not rescaled, and therefore were effectively assumed to have exactly the standard properties.

8.3 Experimental results

The evaluation of the AMS-02 RICH light yield and other properties was performed using cosmic-ray data (i.e. muons) from runs where the RICH and other detectors were fully functional. Track information was provided by the AMS-02 Tracker and TOF systems in the same way that is expected to occur in space. A total of 98 data runs, acquired between May 7 and June 5, 2008, were used in all studies presented in this section with the exception of the long-term light yield stability study. These runs are listed in Appendix B. For the specific study of long-term light yield stability, an additional sample of 52 data runs acquired between December 20 and 23, 2009 (also listed in Appendix B) was also used.

Results obtained were compared with those coming from two kinds of simulations: the full-scale AMS-02 simulation in the AMS software chain (see Section 3.5) and the standalone RICH simulation (see Section 4.7).

The full-scale simulation corresponded to a realistic cosmic-ray muon spectrum at the ground, therefore matching the data sample closely. The sample used in the standalone RICH simulation was slightly different, corresponding to a flight simulation of 10^6 protons with $\beta = 0.999$ generated within the RICH detector's expected flight acceptance. In the RICH simulation no tile variation was introduced, all tiles being simulated as having the reference properties ($n = 1.050$, $C = 0.0060\ \mu\text{m}^4\ \text{cm}^{-1}$, $h = 25$ mm).

All data and simulation events were reconstructed with the standard LIP algorithms (see Section 4.8) and using the same quality cuts.

The three samples were very similar in terms of event topology, as seen from the distributions of ring acceptances and track inclinations after event selection (Fig. 8.4). Ring acceptances (deliberately truncated at 40% to exclude potentially bad reconstructions based on small ring segments) were nearly identical, with events passing the truncation at 40% having an average acceptance of 72.46% for the RICH simulation, 71.75% for the full simulation and 71.63% for cosmic data. Track inclinations did not display any major differences, showing only a slightly longer tail than expected for high angles in cosmic data.

8.3.1 Velocity reconstruction and refractive index correction

When particle velocity was reconstructed for the 2008 cosmic events, it became apparent that a systematic shift was present for each individual tile. Velocity distributions, which should be superimposable for all tiles, instead showed significant displacements (Fig. 8.5).

Velocity distributions obtained for each tile were used to cross-calibrate results. It was assumed that the systematics seen originated from errors in each tile's nominal refractive index, since (unlike for clarity and thickness) a change in the assumed refractive index immediately translates into a change in reconstructed velocity. The global average of refractive indices was assumed to be the same of the nominal values.

A corrected refractive index value was obtained for each tile: $n_{corr} = (\beta/\overline{\beta})n_{nom}$. Refractive index distributions before and after applying this correction are shown in Fig. 8.6. The final refractive index distribution was roughly similar to the original one, but values of n for individual tiles were changed according to the corresponding systematics seen in β, which in some cases reached 0.001 (Fig. 8.7).

The new refractive index values replaced the nominal ones in the reconstruction algorithm, leading to an improvement in the result for velocity resolution from $\sigma_\beta/\beta = 1.52 \times 10^{-3}$ to $\sigma_\beta/\beta = 1.41 \times 10^{-3}$, as evaluated from the right-hand side of the velocity distribution (Fig. 8.8). The right-hand side is used since the distribution

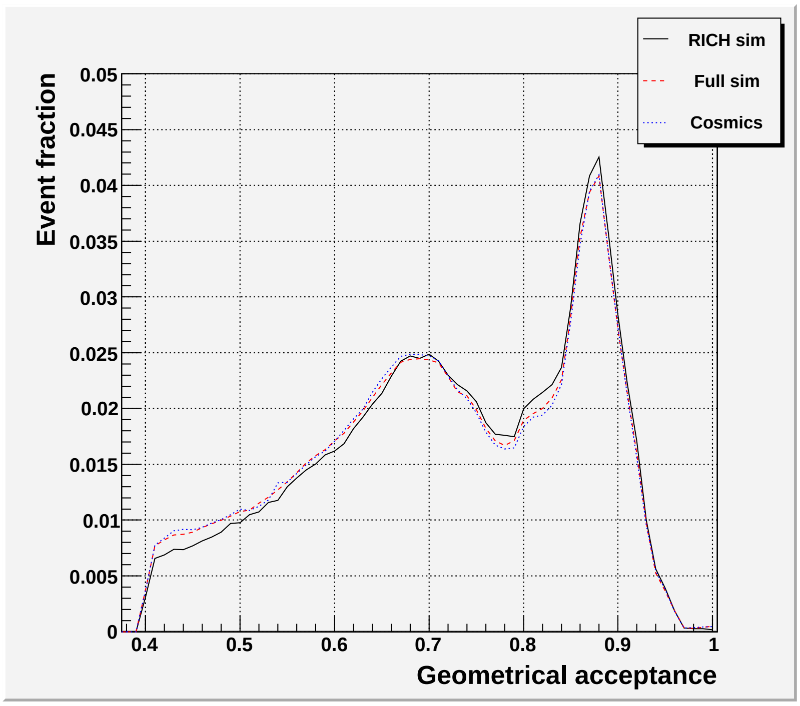

(a)

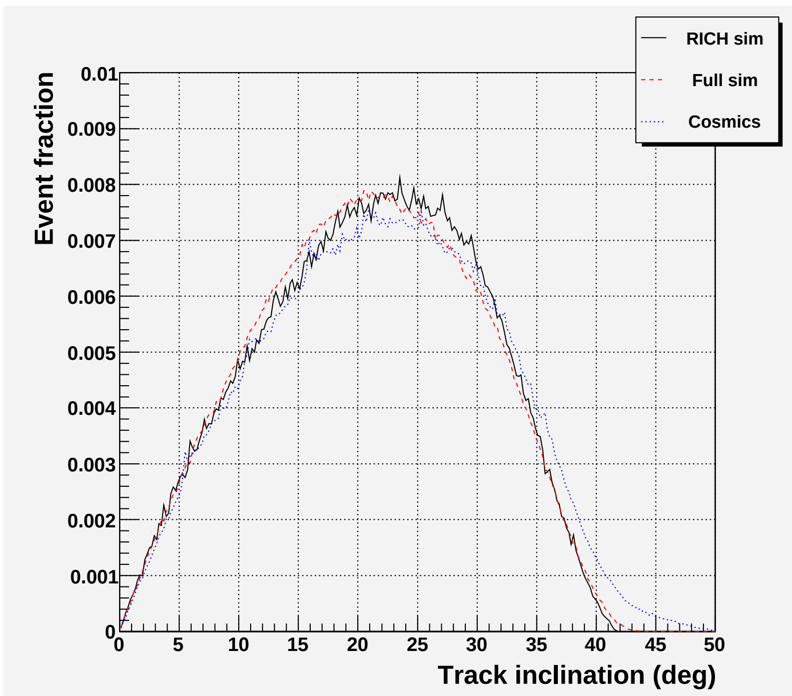

(b)

Figure 8.4: *Distributions of ring acceptances (a) and particle inclinations (b) for the three samples (cosmics, AMS simulation, RICH simulation) after event selection.*

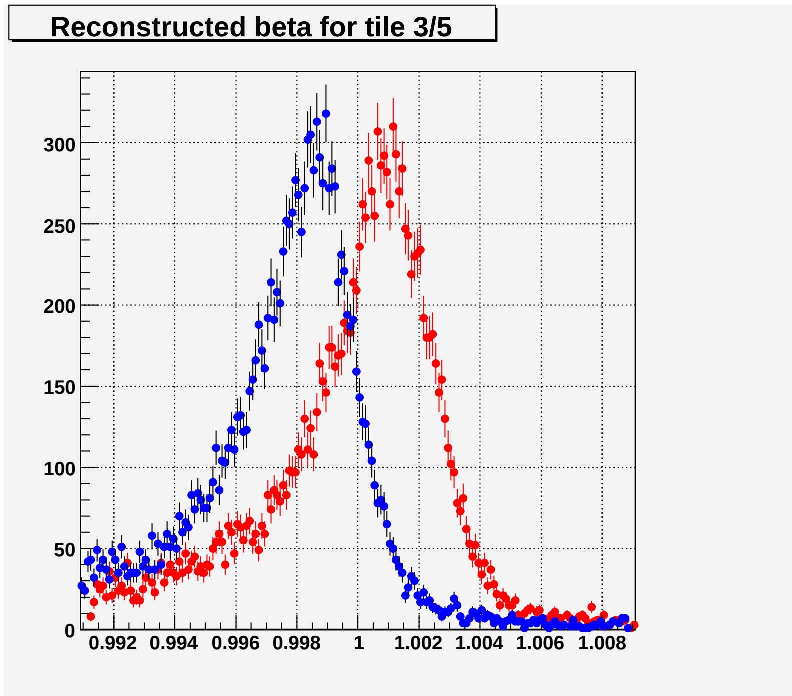

Figure 8.5: *Distribution of reconstructed velocites for particles crossing two different tiles, showing a visible systematic effect.*

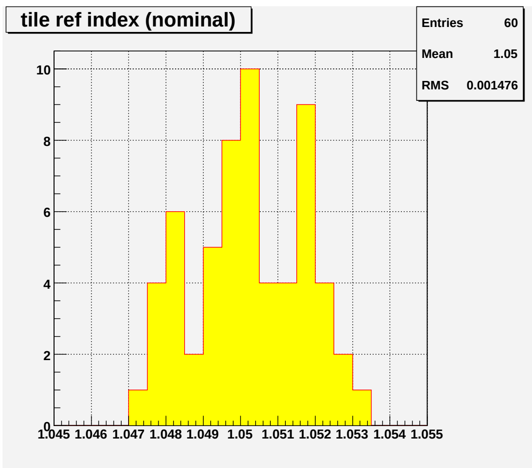

(a)

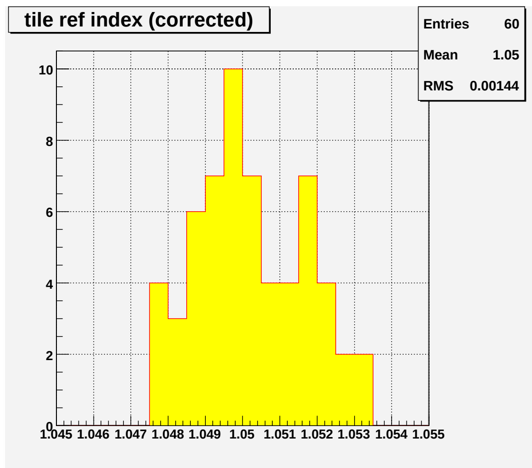

(b)

Figure 8.6: *Distribution of refractive indices for the square aerogel tiles: (a) nominal values, (b) corrected values obtained from cross calibration of velocity distributions.*

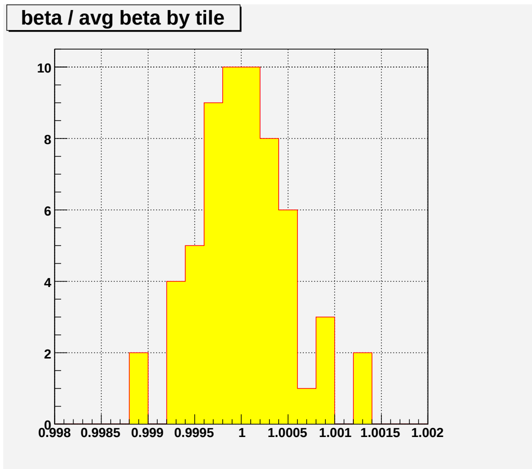

Figure 8.7: *Deviations in average reconstructed velocity seen for each square aerogel tile. The refractive index of each tile was corrected according to* $n_{corr} = (\beta/\overline{\beta})n_{nom}$.

of true velocities is limited to $\beta = 1$ on the right with a tail on the left.

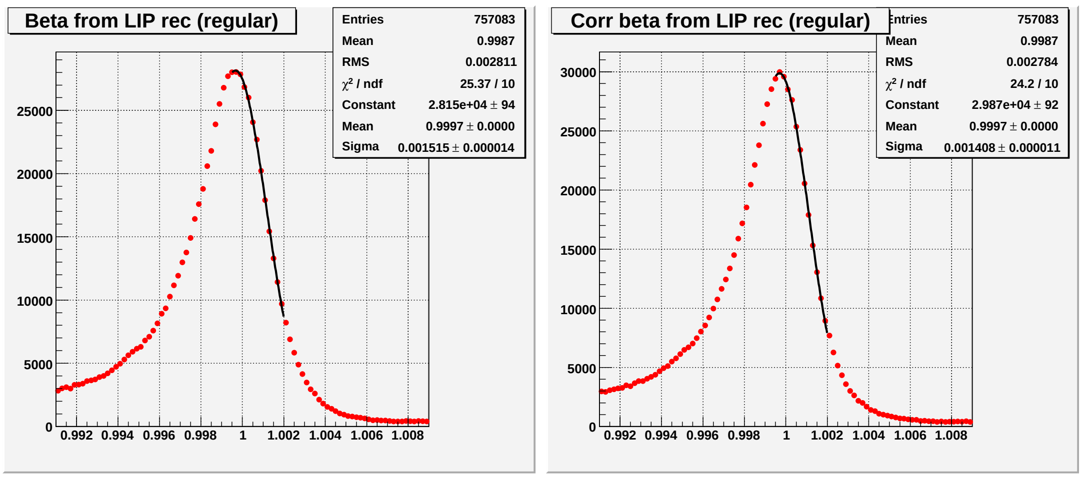

(a) (b)

Figure 8.8: *Distribution of reconstructed velocities for a set of 38 data runs before (a) and after (b) refractive index correction.*

The resolution obtained is close to the design goal of $\sigma_\beta/\beta = 1.3 \times 10^{-3}$.

8.3.2 Light yield results

To obtain the final value for light yield estimates N_0 and L_0 corresponding to a given sample or subsample, results of N_0^{est} and L_0^{est} obtained for each event were weighted according to their ring acceptance. This was done to ensure that each event's contribution to the global average corresponded to the amount of information it provided. An additional correction was applied to account for the effect of the reconstruction threshold of 3 ring hits on the light yield results. This correction was based on the assumption of the number of ring hits for a given event configuration following a Poisson distribution with an expected value related to the ring's global efficiency.

Since all events in this study corresponded to single charges, light yield calculations were based on a simple count of the number of hits instead of the number of photoelectrons. This choice removed an eventual bias from photoelectron calibrations, introducing only a small (2% or less) underestimation of the light yield due to situations of two photons being detected on the same pixel.

8.3.2.1 Results for N_0

Results obtained for N_0, the expected number of photoelectrons seen in a fully contained ring generated by a single-charged particle with $\beta = 1$, as function of particle inclination are shown in Fig. 8.9(a). Quotients between the same results are shown in Fig. 8.9(b). There is some discrepancy ($\sim 6\%$) between the results from the two simulations, and a large discrepancy between simulations and the 2008 cosmic data, with results being consistently about 15% lower than AMS simulation results and 20% lower than RICH simulation results in the 0°-30° range. The light yield observed for perpendicular incidence ($\theta \to 0°$) in the 2008 cosmic test was 9.0 p.e., while simulations showed results of 10.5 p.e. (AMS simulation) and 11.2 p.e. (RICH simulation).

The global behaviour of N_0 with inclination agrees with what was seen in simulations: the light yield tends to decrease with inclination up to about 30°, then starts to increase rapidly above 35°. Two main effects are relevant up to 30°: first, an increase in particle inclination means a longer path in aerogel and therefore a higher number of photons coming from the radiator; second, photons emitted by

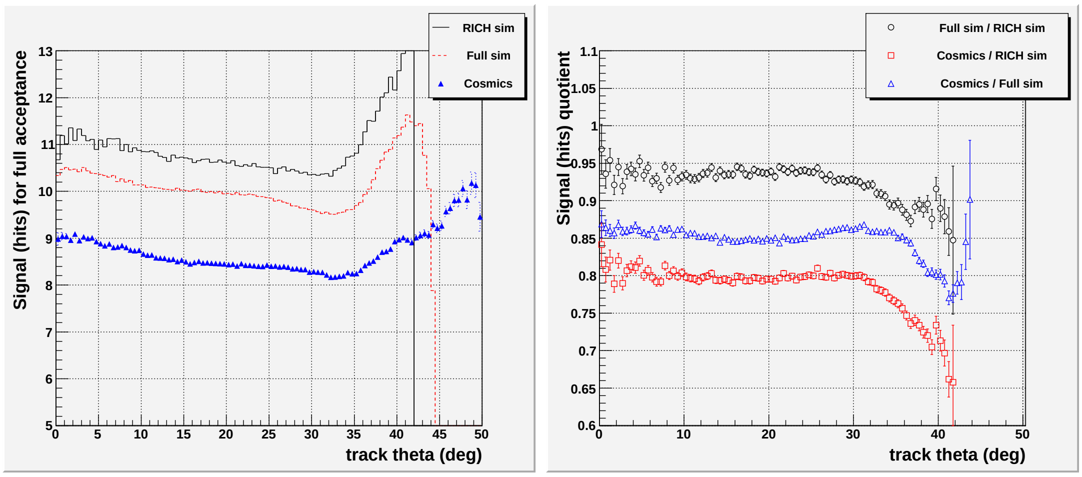

(a) (b)

Figure 8.9: *(a) Estimate of N_0 as function of track inclination for the three samples. (b) Quotients obtained from comparison of sample results.*

more inclined particles have less favourable angles for their collection in the light guides as previously mentioned. The second of these competing effects is slightly stronger, and N_0 drops by $\sim 10\%$ between $0°$ and $35°$.

For inclinations above $30°$ events have predominantly reflected rings. This fact is important for light guide collection, since the mirror's conical shape implies that photon trajectories after reflection are more favourable to light collection in the detection matrix. That is, at high particle inclinations both light emission and light collection improve, leading to an increase in N_0. The increase seen in data is not as strong as the one seen in simulations, but this could be an artifact from different samples: real data have more high-inclination events crossing the detector, meaning that the proportion of reflected photons for a given particle inclination is smaller than in simulations.

8.3.2.2 Results for L_0

If results for N_0 are expected to be function of event parameters, the value L_0 should be a robust estimator across different kinds of events. Results obtained with this estimator may also be used to directly compare light yield calculations from data and simulations. Fluctuations in L_0 should be considered systematic effects.

For the data and simulation samples, the value of L_0 was calculated as function of several event parameters. Results obtained are presented below.

A correlation was seen in data between L_0 and the radius of the radiator crossing point, as shown in Fig. 8.10(a). Central events had a higher light yield estimate, with a $\sim$ 10% decrease towards the outer border. No such effect was seen in the AMS simulation, while the RICH simulation instead showed a slight increase of L_0 with radius.

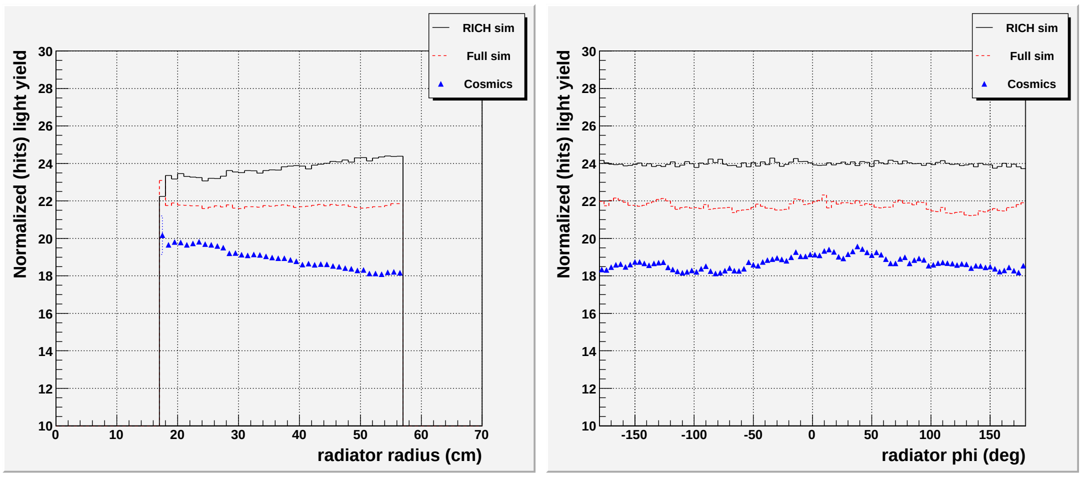

(a) (b)

Figure 8.10: *Fluctuation of normalized light yield estimate as function of position at radiator: (a) distance from centre; (b) azimuthal position.*

Figure 8.10(b) shows the results obtained as function of the azimuthal position of the radiator crossing point. Some correlation is seen for data, with the highest values in the region between 0° and 50° and the lowest around −100°. These variations are not reproduced in the AMS simulation, although some correlation is also seen there. The RICH simulation, with no variations in tile properties, shows a perfectly constant estimate as expected.

Results obtained for L_0 as function of the radius of the matrix impact point are shown in Fig. 8.11(a). A general reduction in L_0 from the inside to the outside is again seen, although a flat region is seen for small radii and again for large radii, with L_0 starting to increase above 90 cm. The AMS simulation has essentially the same behaviour of data above 60 cm, but for lower radii has a long plateau including the $40 - 60$ cm region where a reduction is seen in data. Results from the RICH simulation are globally more stable but show some features that indicate that they are essentially a tilted version of what is seen in the other samples.

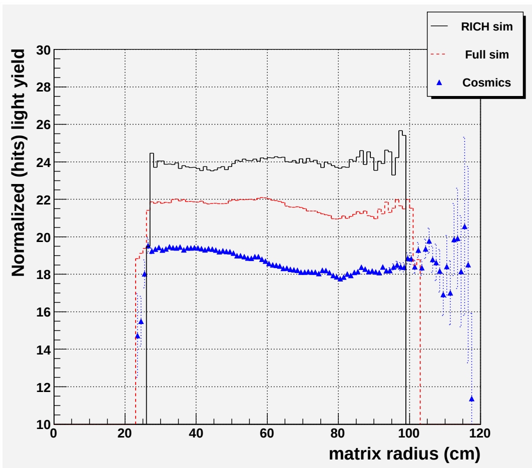

(a)

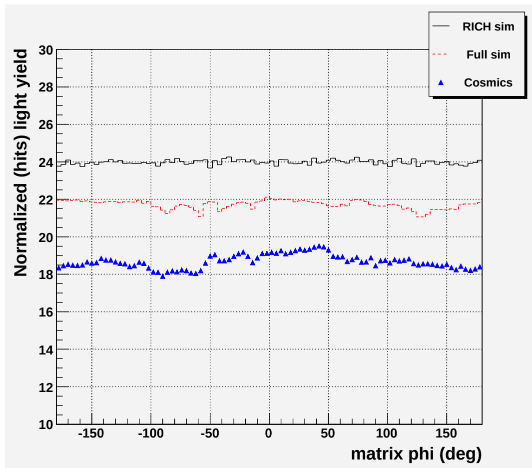

(b)

Figure 8.11: *Fluctuation of normalized light yield estimate as function of position at detection matrix: (a) distance from centre; (b) azimuthal position.*

Figure 8.11(b) shows the results obtained as function of the azimuthal position of the matrix crossing point. Results from data are quite similar to those obtained at the radiator but with clearer features, suggesting that variations in L_0 are predominantly caused by unaccounted-for features of the detection matrix. The same occurs for the AMS simulation, although the major features are at different angles. The RICH simulation again shows a featureless, flat plot.

When the light estimate is plotted against particle inclination (Fig. 8.12(a)), the behaviour observed is similar for data and for the two simulations: a plateau at low inclinations, followed by a decrease and finally an increase at high inclinations. In the case of data the decrease starts at $\sim 10°$ and is reverted at $\sim 35°$. The AMS simulation shows a longer plateau but a stronger decrease between $\sim 20°$ and $\sim 35°$. In the RICH simulation there is a slow decrease similar to what is observed in data but the increase starts slightly earlier, at $\sim 32°$.

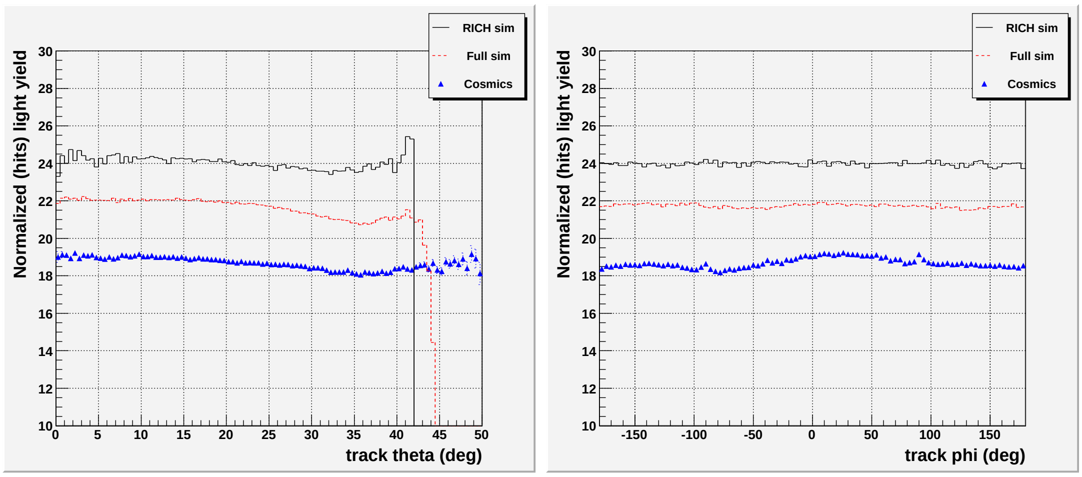

(a) (b)

Figure 8.12: *Fluctuation of normalized light yield estimate as function of particle trajectory: (a) particle inclination; (b) azimuthal angle.*

Results for L_0 as function of the particle's azimuthal orientation (Fig. 8.12(b)) show a surprising feature in cosmic data: two visible spikes at $\pm 90°$, undoubtedly due to a privileged direction in the experimental setup or in the track reconstruction. This is not a feature inherent to the RICH reconstruction algorithm or to the expected detector, since the results for the two simulations do not show this feature.

The variation of the L_0 estimate as function of the x and y coordinates of the tile crossing point is shown in Fig. 8.13. The exact coordinates used correspond to the track point at the bottom, when the particle leaves the radiator plane.

Some systematics were expected for particles crossing the radiator near or at the borders of the tiles, since Čerenkov patterns in those events are highly sensitive to the exact track parameters at sub-mm level. Such systematics were mostly absent in the case of the RICH simulation, but some effects were already seen in the AMS simulation, with a small decrease in L_0 around 1 cm from the edge followed by a rapid increase in the last few mm, especially in the x axis. Cosmic data showed an unanticipated feature, however: in addition to the expected stable region for most of the tile, asymmetric variations were clearly seen in both x and y. This suggested

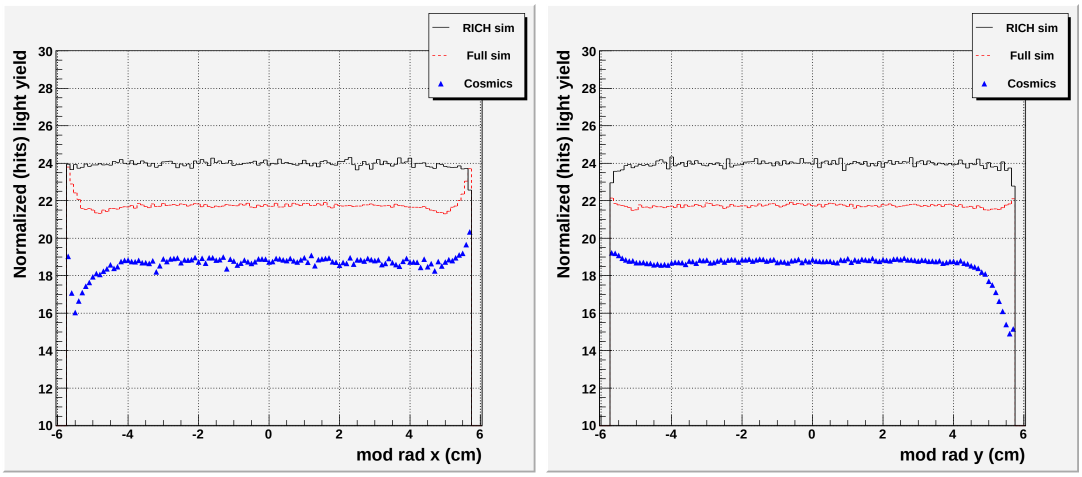

(a) (b)

Figure 8.13: *Fluctuation of normalized light yield estimate as function of tile crossing point (at bottom of tile): (a) x coordinate; (b) y coordinate.*

the possibility of an offset in the position of the radiator and/or tracker with respect to the nominal placement used as reference for event reconstruction, leading to a separate analysis that is presented in Subsection 8.3.4.

The reduction in the light yield estimate as from inner to outer events seen for cosmic data with no correspondence in simulations led to a search of a possible explanation in terms of a mirror reflectivity below the expected value of 85%. For this, the estimate of L_0 was computed as function of the event's expected component of reflected photons, that is, $f_{refl} = \frac{\varepsilon_{glob}^{(refl)}}{\varepsilon_{glob}^{(dir)} + \varepsilon_{glob}^{(refl)}}$.

The result of the computation of L_0 versus f_{refl} is shown in Fig. 8.14. There is a reduction in the light yield as the reflected component of the event increases, but a similar variation is seen in the AMS simulation (where the reflectivity is known to be 85%) and in addition cosmic data show a slight increase in L_0 towards fully reflected events. Systematics from the reconstruction itself make it difficult to reach a final conclusion on this subject, but a reduction in reflectivity does not seem likely as the main cause of this effect.

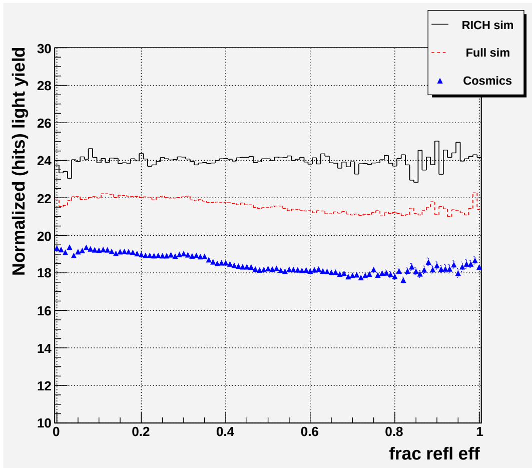

Figure 8.14: *Fluctuation of normalized light yield estimate as function of fraction of visible ring that is reflected*

8.3.3 Light yield stability

In the context of the present work, it was important to compare the results of light yield measurements obtained in different runs and different moments.

Short-term fluctuations in light yield, that is, those seen within a set of runs from the same data acquisition period, can be considered as systematic errors, expected to be essentially due to small differences in the experimental setup and acquisition that are unaccounted for. On the other hand, long-term changes such as those seen after several months or years may be evaluated to test the stability of the detector setup and of its components over long periods.

Two studies of light yield stability were performed in this work: a run-by-run study of fluctuations within the 98 runs of cosmic data collected in May/June 2008 which were used in all other studies presented in this chapter, and a long-term comparison between the 2008 data and a set of 52 runs of cosmic data collected in December 2009 after the assembly of AMS-02 with the superconducting magnet.

8.3.3.1 Run-by-run stability

The stability of light yield measurements between runs was investigated. Since all runs had similar event samples, both light yield estimators N_0 and L_0 were expected to be comparable from run to run. To evaluate the stability of the average photoelectron calibrations, estimates of N_0 and L_0 based on photoelectron signals were also calculated for each run.

Since the time interval between consecutive data runs can range from minutes to several days, values of N_0 and L_0 were plotted not only against the order of the corresponding runs but also against the time when they were collected, in order to make any correlations between consecutive runs more visible. AMS run numbers were used, since they correspond to the moment of their beginning expressed in Unix time (number of seconds elapsed since January 1st, 1970 at midnight, UTC).

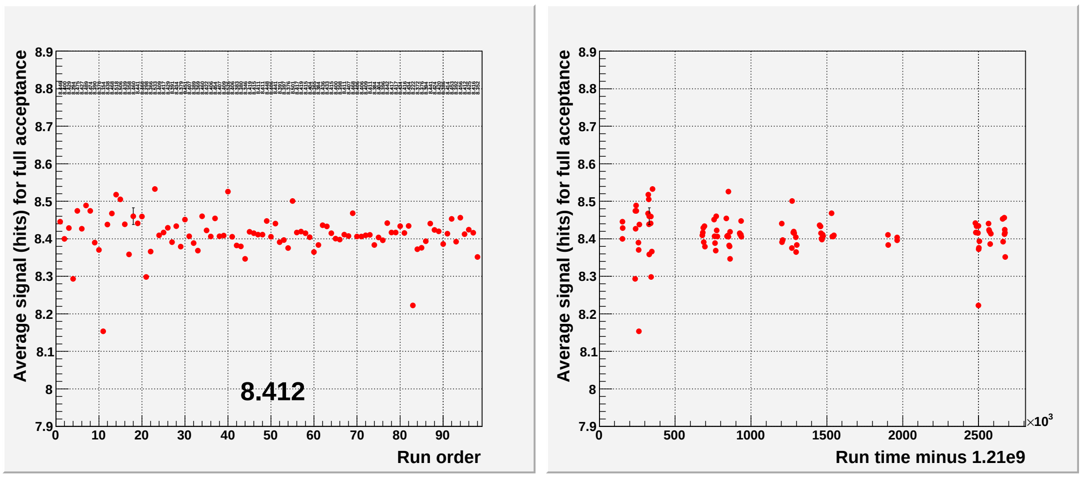

(a) (b)

Figure 8.15: *Estimate of N_0 for each run, obtained from hit counting: (a) as function of run order; (b) as function of AMS run number (Unix time).*

Figures 8.15 and 8.16 show the results obtained in each run for N_0 and L_0, respectively, using hit countings.

Values of N_0 show a global weighted average $N_0 = 8.412$ and a systematic fluctuation between runs with $\sigma_{N_0} = 0.052$, corresponding to $\frac{\sigma_{N_0}}{N_0} = 0.62\%$. Taking such systematics into account, the result obtained for the (non-weighted) average of the 98 runs is $N_0 = 8.412 \pm 0.005$.

The light yield behaviour is identical if measured from the point of view of L_0, with a global weighted average $L_0 = 18.774$ and a systematic fluctuation $\sigma_{L_0} = 0.119$, corresponding to $\frac{\sigma_{L_0}}{L_0} = 0.63\%$, leading to a non-weighted average $L_0 = 18.773 \pm 0.012$.

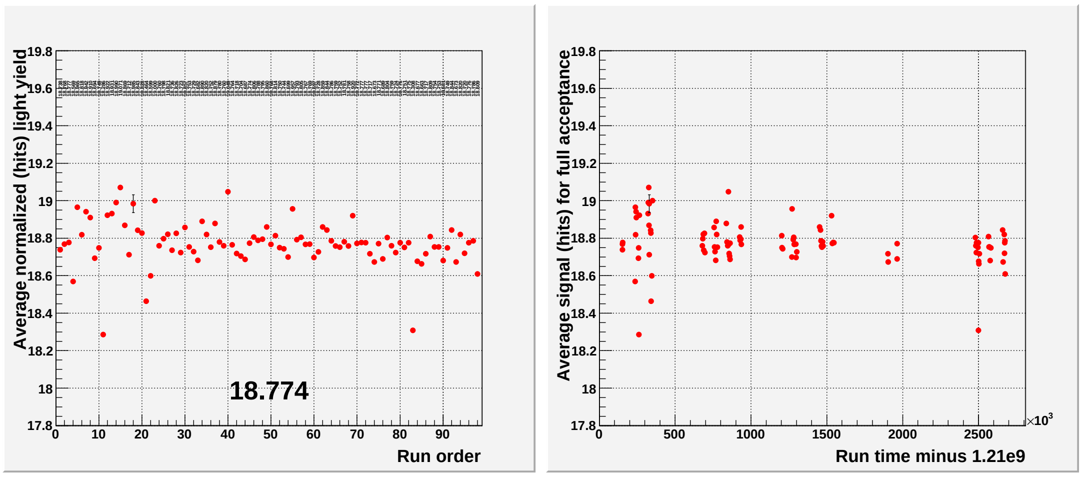

(a) (b)

Figure 8.16: *Estimate of L_0 for each run, obtained from hit counting: (a) as function of run order; (b) as function of AMS run number (Unix time).*

In both cases, fluctuations between consecutive runs are similar to those that occur after long intervals. The first 23 runs, acquired between May 7 and May 9, have a slightly higher fluctuation than later runs.

Results obtained for N_0 and L_0 estimates from photoelectron data are shown in Figs. 8.17 and 8.18. The global values obtained from this method are $N_0 = 8.603$ and $L_0 = 19.171$, giving estimates for the average hit signal of 1.0211 p.e. and 1.0227 p.e., respectively. Fluctuations from run to run are clearly stronger than the ones seen for hit-based estimates. Values of N_0 fall mostly between 8.5 and 8.8, while L_0 usually fluctuates between 18.8 and 19.6. The higher fluctuation seen in the early runs for hit-based estimates is not apparent in this case.

8.3.3.2 Long-term stability

The results presented in all other parts of this chapter are based on cosmic data acquired in a period of approximately one month in May and June, 2008. To evaluate the long-term stability of the RICH light yield, the same light yield study was performed on a second data set corresponding to 52 runs of cosmic data (listed in Appendix B) acquired between December 20 and December 23, 2009. These data

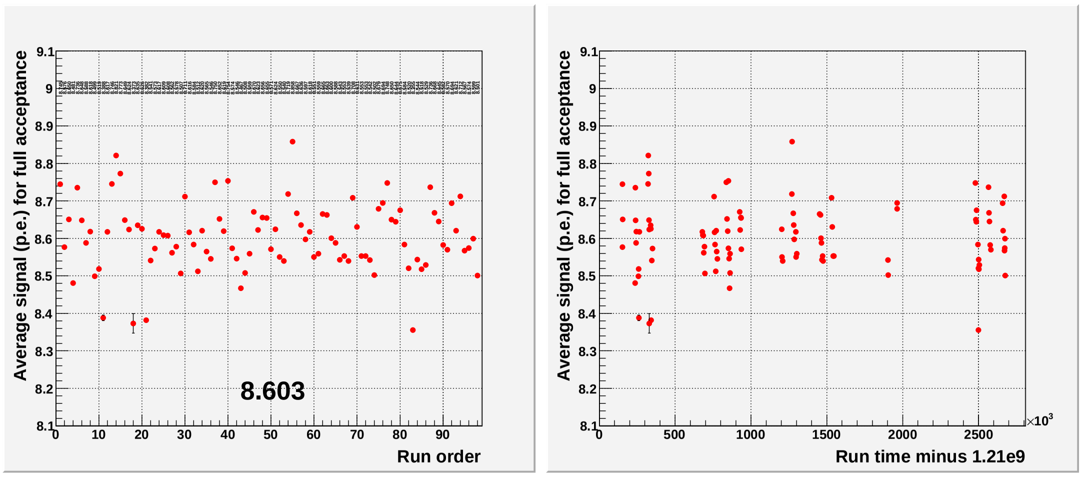

(a) (b)

Figure 8.17: *Estimate of N_0 for each run, obtained from p.e. signals: (a) as function of run order; (b) as function of AMS run number (Unix time).*

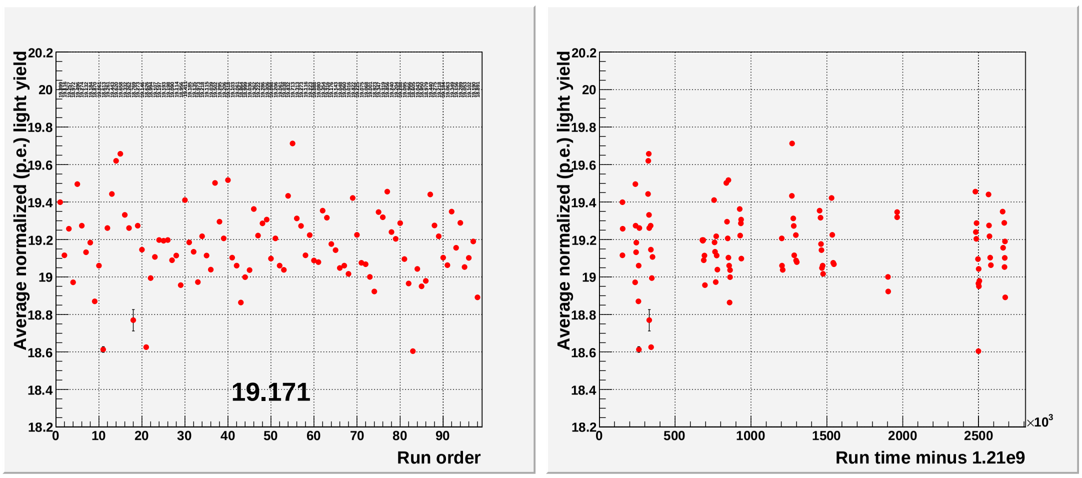

(a) (b)

Figure 8.18: *Estimate of L_0 for each run, obtained from p.e. signals: (a) as function of run order; (b) as function of AMS run number (Unix time).*

were therefore collected approximately 19 months later than the previous sample.

Following the results of the analysis of 2008 data, this study was based on light yield estimates from hit countings, which are expected to be more robust and less dependent on calibrations.

In addition to the different acquisition periods, two main differences existed between the 2008 and 2009 data samples: first, the 2008 sample was collected with the pre-assembled detector, while the 2009 sample was collected after the detector had been disassembled and assembled for a second time; and second, while in 2008 no magnetic field was present (and no magnet was present at all), the 2009 sample was collected with the superconducting magnet operating at the nominal current of 400 A corresponding to a magnetic field of 0.86 T.

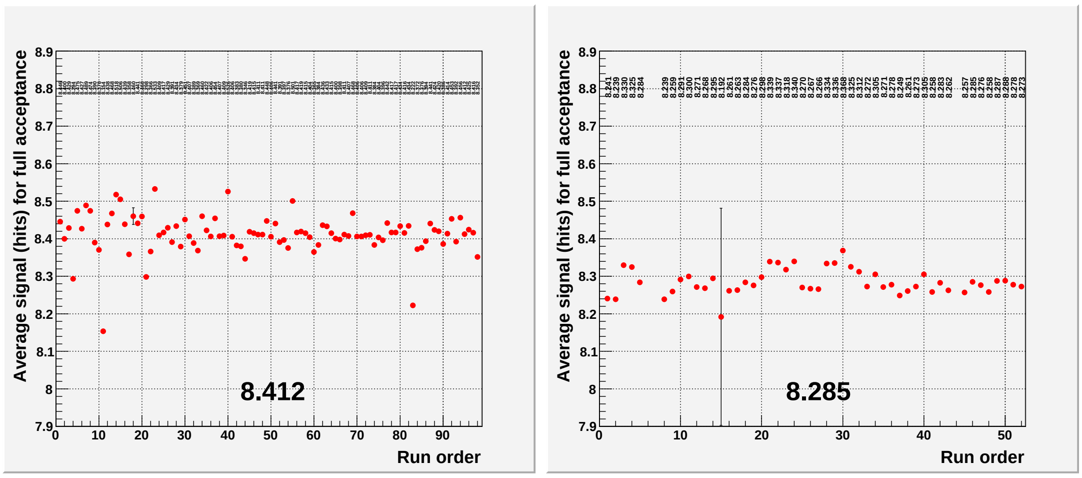

(a) (b)

Figure 8.19: *Estimate of N_0 for each run, obtained from hit counting: (a) 2008 data; (b) 2009 data.*

A comparison of the results obtained for the 2008 and 2009 data sets is presented in Figs. 8.19 and 8.20. In each case, the results for 2008 are the same that were presented earlier in this chapter (Figs. 8.15 and 8.16). From the 52 runs included in the 2009 sample, four had a very low number of events and therefore no meaningful light yield estimate was obtained for them. Such runs were also excluded from the study on systematics.

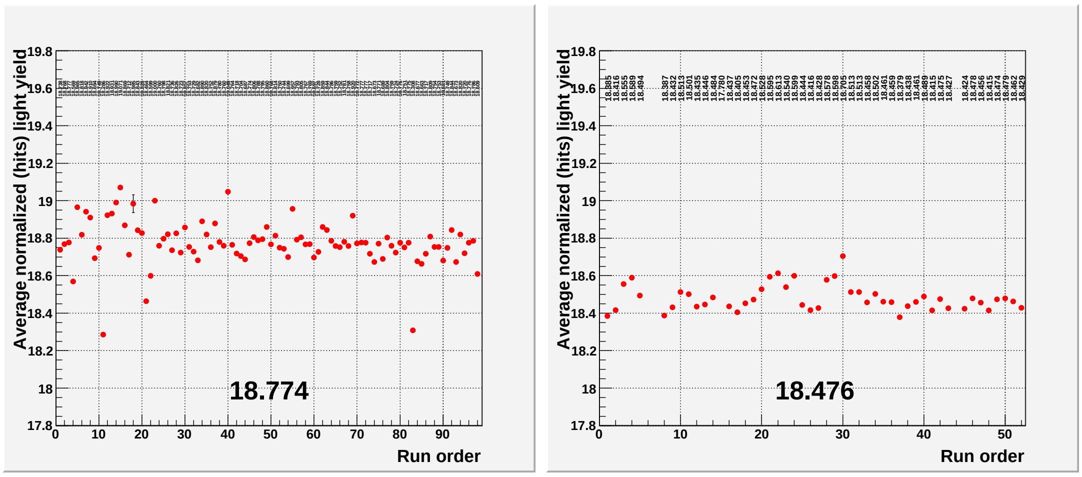

(a) (b)

Figure 8.20: *Estimate of L_0 for each run, obtained from hit counting: (a) 2008 data; (b) 2009 data.*

In the data sample collected in December 2009, values of N_0 show a global weighted average $N_0 = 8.285$ and a systematic fluctuation between runs $\sigma_{N_0} = 0.030$, corresponding to $\frac{\sigma_{N_0}}{N_0} = 0.37\%$. Considering these systematics, the result obtained for the non-weighted average of the 48 runs is $N_0 = 8.287 \pm 0.004$.

Calculating the light yield from the point of view of L_0, a global weighted average $L_0 = 18.476$ was obtained. The systematic fluctuation is $\sigma_{L_0} = 0.069$, corresponding to $\frac{\sigma_{L_0}}{L_0} = 0.37\%$, leading to a non-weighted average $L_0 = 18.480 \pm 0.010$.

The magnitude of the systematic fluctuations in 2009 is lower than the one observed in 2008. This may be due to the shortest time interval during which data from the 2009 sample were collected: approximately three days, while data from 2008 span an entire month.

Table 8.3.3.2 summarizes the results obtained for the light yield (N_0 and L_0) from the analysis of 2008 and 2009 cosmic data.

The average light yield values obtained for the 2009 data are slightly lower (approximately 1.5%) than those from 2008. This difference, although small, is large enough to rule out the systematic fluctuations observed from run to run as its main cause. Possible explanations for this change include a degradation of detector com-

Estimator		N_0	L_0
May/June 2008		8.412 ± 0.005	18.773 ± 0.012
December 2009		8.287 ± 0.004	18.480 ± 0.010
Change (%)	Total	-1.50 ± 0.08	-1.56 ± 0.08
	Yearly	-0.94 ± 0.05	-0.98 ± 0.05

Table 8.1: *Comparison of light yield results obtained from 2008 and 2009 cosmic data.*

ponents with time, or a slightly lower detector response in the presence of the stray magnetic field (up to 300 G).

If the light yield reduction observed is due to the ageing of detector components (e.g., aerogel tiles), then this study may quantify the rate of light yield degradation. Since the time period elapsed between the two acquisitions was approximately 19 months, the reduction observed corresponds to a rate of 1% per year.

8.3.4 Tile offset

The asymmetric systematics observed in the light yield estimates as function of tile position (Fig. 8.13) led to a more detailed study to quantify a possible displacement of the radiator tiles and/or the tracking system with respect to their nominal positions.

Since event reconstruction is performed from the combination of track data given by the AMS Tracker and information from the RICH detector, only a relative displacement between the two subsystems may be extracted from the asymmetric systematics. The following discussion will be made in terms of a displacement in tile position.

To confirm if the systematics seen were consistent with a displacement in tiles positions, the value of the light yield estimate N_0 as function of tile position was calculated for a two-dimensional grid with a resolution of 1 mm. Results obtained for the AMS simulation and for data are presented in Fig. 8.21. Although some fluctuations are visible throughout the tile in both cases due to the relatively low statistics in each of the more than 10^5 bins, the major feature in both cases is a drop in N_0 at the edges which is perfectly symmetrical in simulated events but appears to be shifted in real data.

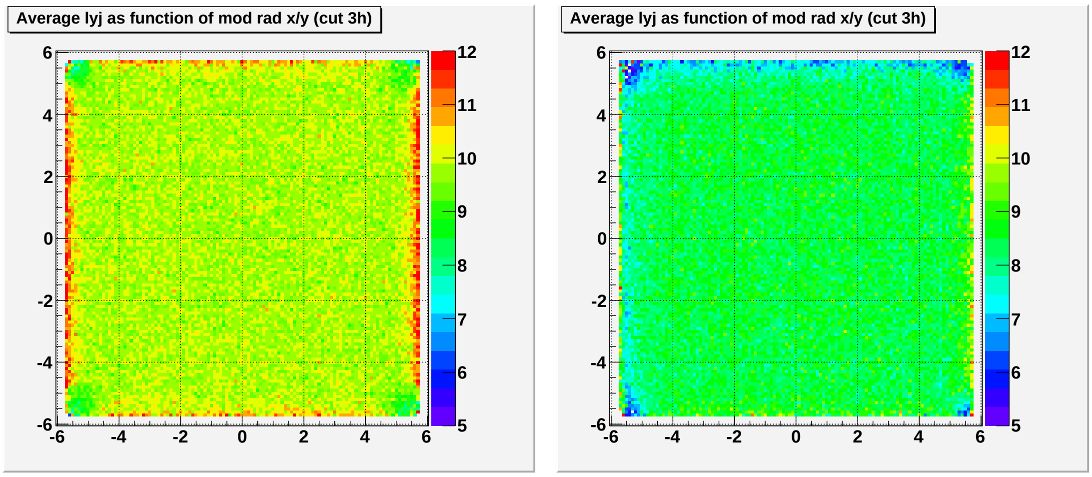

(a) (b)

Figure 8.21: *Estimate of N_0 by tile position: (a) AMS simulation; (b) Cosmic data. Dimensions are in cm.*

8.3.4.1 The N_{raw} estimator

Since the value of N_0 depends on the calculated reconstructed event efficiency, which in turn is affected by the position of gaps between tiles, it was decided to use a different variable, as independent as possible from geometry assumptions, to evaluate the exact tile displacement. The chosen estimator, denoted N_{raw}, is a simple mean of the number of ring hits observed per event without any corrections. Values of N_{raw} as function of the x and y tile coordinates were calculated for bins with a width of 0.1 mm.

The results obtained for N_{raw} as function of each coordinate in the AMS simulation are shown in Fig. 8.22. A magnification of the result in border regions is shown in Fig. 8.23. No significant asymmetry exists in any axis, although the drop in visible light is stronger in the y axis.

The same variable N_{raw} was calculated for cosmic data. Results obtained are shown in Fig. 8.24. Asymmetries in both x and y distributions are clear when the border zone is magnified, as shown in Fig. 8.25. The calculation of N_{raw} is disturbed

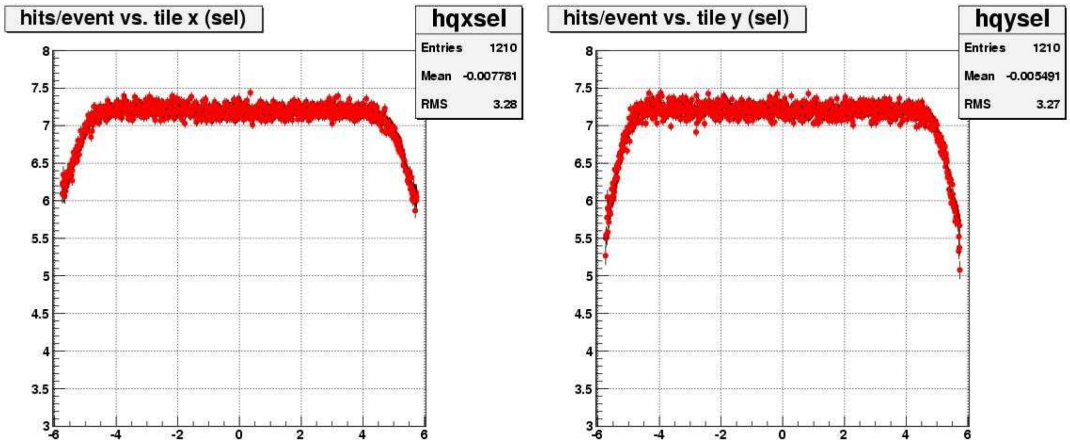

(a) (b)

Figure 8.22: *Estimate of N_{raw} by tile position for AMS simulation: (a) x axis; (b) y axis. Dimensions are in cm.*

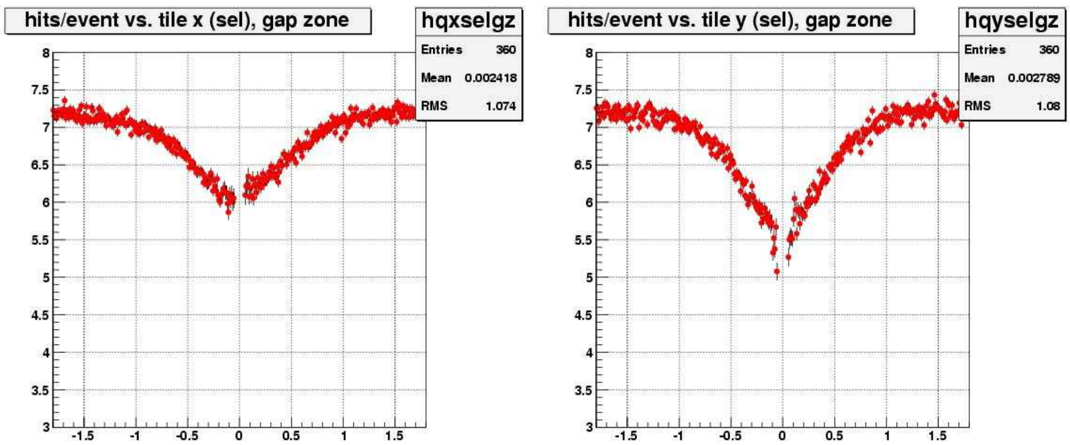

(a) (b)

Figure 8.23: *Magnification of results at border regions in Fig 8.23, with the tile gap repositioned at the centre. Dimensions are in cm.*

at the nominal gap region due to the exclusion of many events by the reconstruction procedure as not having a high enough ring acceptance.

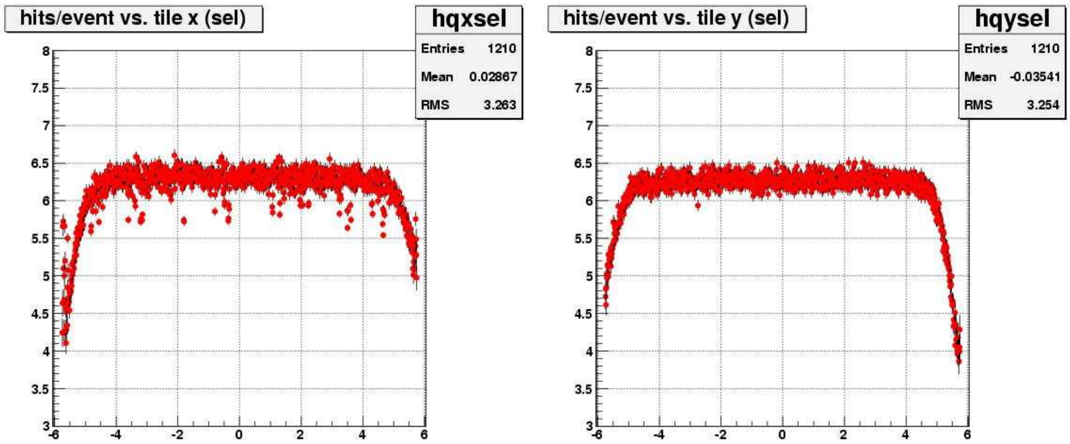

(a) (b)

Figure 8.24: *Estimate of N_{raw} by tile position for cosmic data: (a) x axis; (b) y axis. Dimensions are in cm.*

8.3.4.2 Calculation of tile displacement

The shape of the distributions obtained for N_{raw} was used to evaluate the tile displacement seen in cosmic data. As a control procedure, the algorithm was also applied to simulated events.

An asymmetry estimator was built to test results obtained for N_{raw} with respect to a variable axis by checking how well one side mirrored the other, using results obtained for individual bins:

$$E_k = \sqrt{\sum_i \left[\frac{N_{raw}^{(k-i)} - N_{raw}^{(k+i)}}{\delta\left(N_{raw}^{(k-i)} - N_{raw}^{(k+i)}\right)} \right]^2}$$

with the axis placed at bin k.

The tentative offset range tested in each axis was from -0.3 cm to 0.3 cm, corresponding to a total of 61 values of E_k. Comparisons were performed for 100 bins on each side, corresponding to distances to axis ranging from 0.5 to 1.5 cm

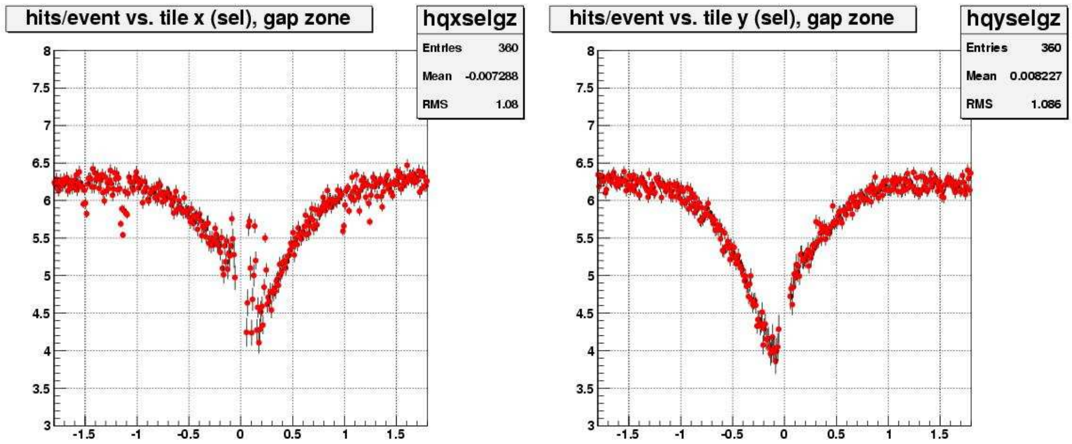

(a) (b)

Figure 8.25: *Magnification of results at border regions in Fig 8.25, with the tile gap repositioned at the centre. Dimensions are in cm.*

(smaller distances were deliberately excluded to avoid the disturbances in the gap region).

Results obtained for E_k as function of the tentative offset are shown in Figs. 8.26 (simulation) and 8.27 (cosmic data). In the case of simulation the lowest values of E_k are near zero for both axes, although in y there is a relatively wide plateau. For data it is clear that the best match between the two sides is not at zero, but at about $+0.12$ cm in the x axis and at about -0.10 cm for the y axis. The accuracy of the minima is about 0.02 cm.

This test was therefore conclusive: there was, on average, a displacement in the AMS RICH radiator of approximately 1 mm in each axis with respect to the tracking system during the 2008 cosmic test. These results are not enough to determine if the displacement is the same in all radiator plane or if there is some variation. Symmetry tests such as the one presented here cannot be performed in their present form on individual tiles due to the intrinsic asymmetry of any tile's position in the detector.

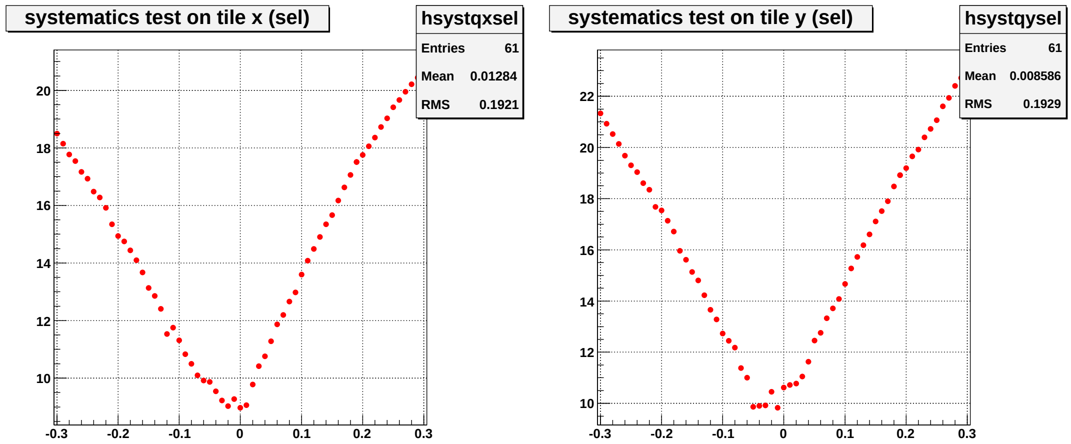

(a) (b)

Figure 8.26: *Results for asymmetry estimator E_k as function of tentative tile offset in cm (AMS simulation): (a) x axis; (b) y axis.*

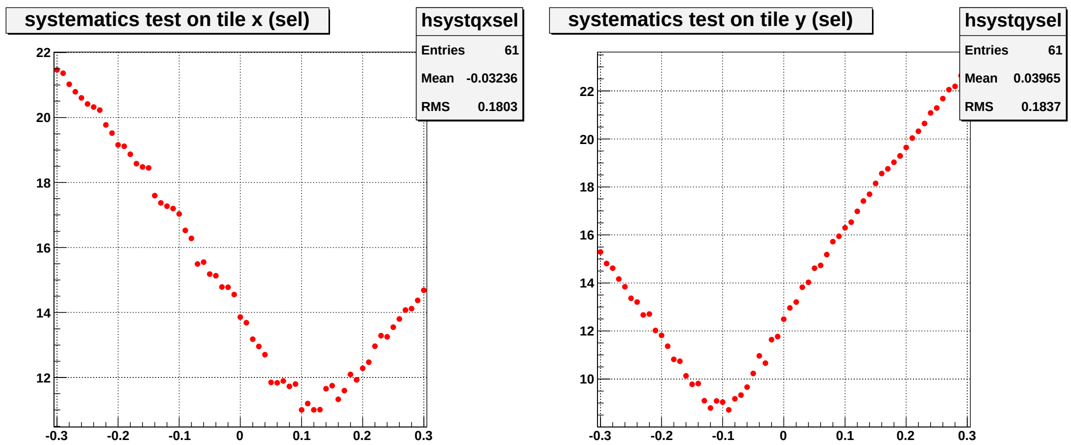

(a) (b)

Figure 8.27: *Results for asymmetry estimator E_k as function of tentative tile offset in cm (cosmic data): (a) x axis; (b) y axis.*

8.4 Extrapolation of prototype light yield results to AMS-02

Results presented in Chapter 7, obtained using the AMS RICH prototype for the light yield of aerogel samples, may be used in the case of the sample selected for the final detector (CINy03.105) to calculate an estimate for the average number of photons to be detected in AMS-02 events, this estimate being directly comparable to the values of N_0 obtained in Subsection 8.3.2.

However, such extrapolation must take into account many differences that exist between the prototype and flight configurations. Differences in event topology, such as the lower visible fraction of AMS-02 rings, compared to the almost fully-contained prototype rings, and the existence of photon reflection, are incorporated in the reconstruction algorithm but other features must be addressed.

In addition to the differences in detector layout listed in Table 5.1, it is necessary to consider that prototype events studied in Chapter 7 always had tracks that were perpendicular to the detection matrix, while events in AMS-02 have a wide variety of inclinations. Figure 8.28 shows the expected distribution of inclinations and acceptances for events in AMS-02.

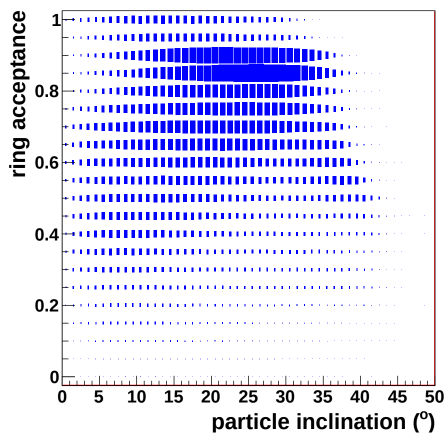

Figure 8.28: *Expected distribution of particle inclination and visible acceptance for AMS-02 events with $\beta \simeq 1$ radiating in aerogel.*

The main effect of particle inclination on Čerenkov photon detection is related to the variation of light guide efficiency with photon angle, as discussed in Subsection 8.2.1: in the prototype test for CINy03.105 all photons had an incidence angle of approximately 18.7°, while photons in AMS-02 will have angles in the 0°-50° range, as shown in Fig. 8.29.

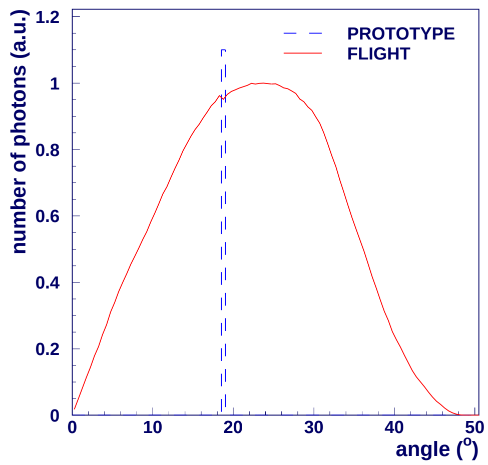

Figure 8.29: *Distribution of incidence angles with respect to vertical for photons reaching the RICH light guides. The prototype case corresponds to the aerogel sample selected for the flight configuration.*

The effects of the differences between the prototype and flight tests that have to be considered in the extrapolation may be summarized as follows:

- **Active matrix area:** the prototype matrix is fully covered with light guides, while the AMS-02 matrix has light guides with a top side length of 34 mm placed every 37 mm. The dead area between light guides therefore corresponds to $1 - (34/37)^2 = 15.6\%$ of total.

- **Light guide efficiency:** the light guides used in AMS-02 were larger than the ones used in the prototype, and were made of a different, more transparent material as previously mentioned. In addition, different photon inclinations resulted in different efficiencies. Combining the light guide efficiency curves of Fig. 8.2 with the distributions of Fig. 8.29, the average light yield efficiency was estimated to be 60% in the prototype and 71% in AMS-02.

- **Radiator foil absorption:** in the prototype test no foil was used with the CINy03.105 aerogel sample. The flight configuration included a Hesa-Glas foil which is highly transparent for wavelengths above 350 nm but becomes increasingly absorbing at lower wavelengths. The loss of photons in this foil, dominated by the reflection component, has been estimated to be 8.3% by performing simulations of the RICH detector with and without foil in the framework of the standalone RICH simulation. The simulations used photons simulated according to a Čerenkov-like spectrum and included the radiator interactions (absorption and scattering), light guide absoprtion and the photomultiplier quantum efficiency.

- **Aerogel refractive index:** aerogel tiles used in AMS-02 have an average refractive index $n = 1.050$ (Fig. 8.6(b)), while the sample tested in 2003 had $n = 1.0529$. Since the light yield (at $\beta = 1$) is proportional to $1 - 1/n^2$, a 5% reduction in light yield is expected from prototype to flight due to the change in refractive index.

- **Aerogel clarity:** the aerogel sample used in the 2003 test had a clarity $C = 0.0055\ \mu\text{m}^4\ \text{cm}^{-1}$, while the average value for the tiles used in the final detector is $C = 0.0061\ \mu\text{m}^4\ \text{cm}^{-1}$ (Fig. 8.3(b)). This increase in Rayleigh scattering due to a higher clarity is estimated to reduce the light collection by a further 4%.

When all differences between the prototype and flight setups are considered, the light yield of events with perpendicular incidence for the flight configuration can be calculated from the prototype estimate given in Table 7.3 using the factors shown in Table 8.2, obtained from the list above.

The average light yield for a fully contained, non-reflected Čerenkov ring produced by a singly charged particle travelling at $\beta \simeq 1$ and crossing the RICH detector in a trajectory orthogonal to the radiator and detection planes is therefore expected from prototype data to be around $N_0 = 12.2$ photoelectrons.

This value is higher than all results obtained in Subsection 8.3.2. It is considerably higher than simulation estimates (11.2 for RICH simulation, 10.5 for AMS simulation) and it is especially much higher than results obtained in the AMS-02 cosmic data test ($N_0 = 9.0$).

Prototype light yield		**14.59**
Changes	Active matrix area	0.84
	Light guide efficiency	1.18
	Radiator foil absorption	0.92
	Aerogel refractive index	0.95
	Aerogel clarity	0.96
Flight estimate		**12.2**

Table 8.2: *Estimation of flight light yield (perpendicular incidence) at $\beta = 1$ based on prototype result.*

8.5 Conclusions

The 2008 cosmic-ray test provided the first opportunity to evaluate the performance of the AMS-02 RICH detector and of reconstruction methods.

The light yield of the RICH detector was evaluated and results compared with simulation results and with values extrapolated from prototype results. Results obtained from data do not agree with estimates coming from simulations and from prototype extrapolation: data give $N_0 = 9.0$ photoelectrons for perpendicular inclination, while the estimates from simulations are $N_0 = 11.2$ for RICH simulation and $N_0 = 10.5$ for AMS simulation, and the extrapolation of RICH prototype results gives $N_0 = 12.2$. Discrepancies between light yield estimates may indicate that some properties of the AMS-02 RICH detector were poorly understood.

One case where existing data were incorrect was that of the refractive indices of individual tiles. Velocity measurements allowed to correct these values, improving velocity resolution from $\sigma_\beta/\beta = 1.52 \times 10^{-3}$ to $\sigma_\beta/\beta = 1.41 \times 10^{-3}$. The results are close to the design goal of $\sigma_\beta/\beta = 1.3 \times 10^{-3}$.

Detailed studies using a nominally unbiased light yield estimator detected some correlations with track parameters, with bias effects at the level of a few percent at most. These studies also led to the identification of a displacement of the RICH detector with respect to the expected track position by approximately 1 mm in both x and y.

The stability of the light signal from run to run was investigated. A total of 98 runs spanning approximately a month of data collection were processed. Fluctuations observed from run to run in the number of hits were usually lower than 1%, with fluctuations in the total signal being slightly higher. No systematic tendency was observed.

In addition, as a test for long-term stability, a similar light yield evaluation was performed for cosmic data collected in December 2009. The results obtained were approximately 1.5% lower than those collected 19 months earlier, corresponding to a light yield decrease of approximately 1% per year.

Chapter 9

RICH event reconstruction without Tracker data

The reconstruction of an event in the AMS RICH detector, as presented in this work's previous chapters, is based on an accurate knowledge of the charged particle's trajectory provided by the AMS Tracker.

The possibility of performing a reconstruction of RICH events that does not depend on Tracker data has been explored. This kind of reconstruction may be required in situations where other subdetectors of AMS are not present (e.g., ground testing) or are not working correctly. It is also a convenient way of validating results obtained from the overall AMS reconstruction procedure.

Two main approaches will be presented in this chapter: a method for standalone reconstruction based exclusively on RICH data and a family of reconstruction algorithms that use information from the AMS-02 TOF, and in some cases also from the RICH matrix, to obtain a rough estimate of the particle track.

9.1 RICH standalone reconstruction

9.1.1 The RICH signal

In each event, the signal collected in the RICH may be divided in two components: the Čerenkov ring, which is used in the standard LIP reconstruction [131]; and the particle spot, produced in the detection matrix at the charged particle's crossing point.

The existence of a particle spot is important for a RICH standalone reconstruction method since different particle trajectories may produce rings that are very similar. However, the presence of a particle spot requires that the particle trajectory crosses the detection matrix. Only $\sim 50\%$ of the events fulfill this condition.

9.1.1.1 Effective signal depth

Using the signal generated by the charged particle when it crosses the RICH matrix as a hint for the particle track requires assuming a coordinate along the z axis, since the detection matrix only provides an (x, y) point.

Considering the signal is generated along the particle trajectory in the detection matrix, it is to be expected that its position shall somehow reflect the full particle path inside the matrix and not only its entry point at the top.

In the framework of the RICH standalone reconstruction efforts, a study was performed to determine the z coordinate that better described the particle signal seen in the detection matrix. Samples of simulated proton events, produced with the full AMS simulation, were used.

In each event, the particle track as given by the AMS Tracker was used as reference. Hits detected at a distance smaller than 5 cm from the point where the track crossed the top-matrix plane were tagged as particle hit candidates.

In the simulation files used in this study, the top of the detection matrix corresponded to $z = -122.9$ cm. Values of z between -121 cm and -128 cm were tested in steps of 0.1 cm, corresponding to a broad range of matrix depths between -1.9 cm and 5.1 cm (with negative depths corresponding to distances above the top of the matrix).

The quality of each tentative vertical position z was evaluated in each of the x and y axes separately by extrapolating track coordinates (as reconstructed by the AMS Tracker), x_{track} and y_{track}, to the positions at that z and then calculating for all tagged hits in the event sample the values $\delta x = x_{hit} - x_{track}$ and $\delta y = y_{hit} - y_{track}$. Gaussian fits were then performed on the Δx and Δy distributions (weighted by each hit's signal) corresponding to each z.

Finally, the evolution of the standard deviation obtained from the fits was plotted

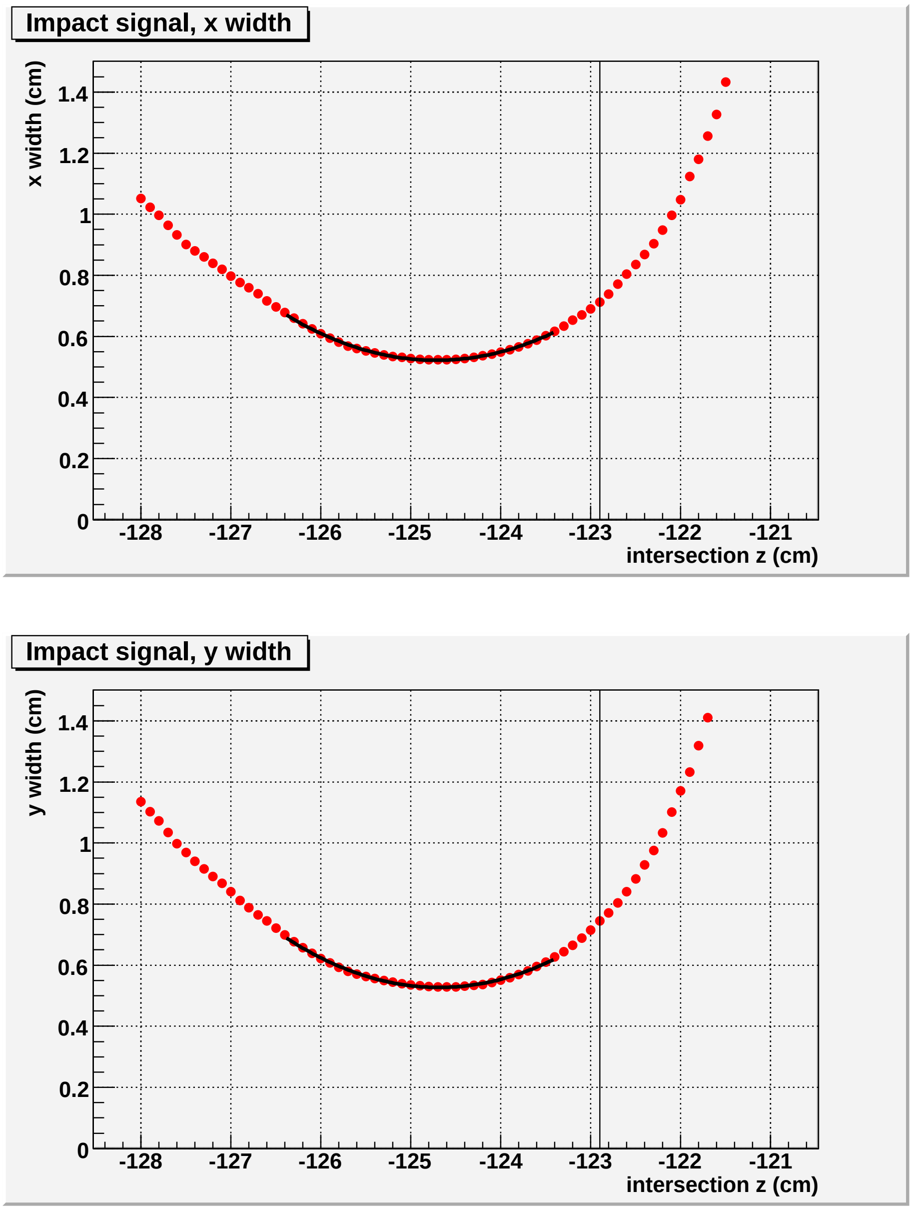

Figure 9.1: *Evolution of standard deviation obtained from Gaussian fits to distributions of* Δx *(top) and* Δy *(bottom) for particle hits as function of the tentative* z *coordinate for the particle signal. The solid curve corresponds to a quadratic fit performed on the minimum region. The vertical line at* $z = -122.9$ *cm marks the top of the light guides.*

against z and a quadratic fit was performed in the minimum region (Fig. 9.1). The following results were obtained:

- In the x axis: $z_{imp}(x) = -124.72$ cm (depth: 1.82 cm), with $\sigma_x = 0.524$ cm
- In the y axis: $z_{imp}(y) = -124.69$ cm (depth: 1.79 cm), with $\sigma_y = 0.531$ cm

These results led to the adoption of a standard depth of 1.8 cm for the particle signal.

9.1.2 Standalone reconstruction algorithm

The algorithm adopted for the RICH standalone reconstruction was based on a maximum likelihood algorithm developed at LIP and described in Ref. [131].

9.1.2.1 Modified likelihood function

The likelihood function used in the RICH standalone reconstruction was similar to the one used in the standard reconstruction. The standard likelihood, which is only function of the Čerenkov angle θ_c, is given by the expression [131]:

$$\mathcal{L}(\theta_c) = \prod_{i=1}^{N} \mathcal{P}^{n_i}[r_i(\theta_c)].$$

where N is the number of hits in the event (excluding those found less than 5 cm from the particle track's matrix crossing point, which were assumed to be due to the charged particle's crossing), n_i is the hit's signal strength (equal to the hit's number of photoelectrons if it is greater than 1, $n_i = 1$ otherwise) and r_i is the hit's distance to the reconstructed Čerenkov pattern. The probability $\mathcal{P}$ is in turn given by an expression that assumes a signal configuration with a double Gaussian distribution and an additional background component:

$$\mathcal{P}(r) = (1-b)\left(\frac{\alpha_1}{\sqrt{2\pi}\sigma_1}\exp\left[-\frac{1}{2}\left(\frac{r}{\sigma_1}\right)^2\right] + \frac{\alpha_2}{\sqrt{2\pi}\sigma_2}\exp\left[-\frac{1}{2}\left(\frac{r}{\sigma_2}\right)^2\right]\right) + \frac{b}{D}$$

The values of constants α_1 and α_2 (relative weights of the two Gaussian distributions), σ_1 and σ_2 (Gaussian widths), b (background fraction) and D (active matrix dimension) were adjusted separately in simulation studies of aerogel and NaF events to obtain an optimized event reconstruction [131]. The constant values used in the present study are shown in Table 9.1.

Table 9.1: *Constant values used for the likelihood functions (standard and 5-parameter) in each radiator.*

Constant	**aerogel**	**NaF**
α_1	0.76	0.4723
α_2	0.24	0.5277
σ_1 (cm)	0.374	0.5424
σ_2 (cm)	1.348	1.35
b	0.776	0.2059
D (cm)	134	

The generalized likelihood function applied in this chapter's 5-parameter reconstruction had the same expression (including the same constant values listed in Table 9.1), but each hit's distance r_i to the reconstructed ring was now function of five variables (θ_c, x_{rad}, y_{rad}, x_{mat}, y_{mat}) instead of the single variable θ_c. A small change had to be introduced, however, in order to make the method consistent with a variable track: hits detected near the particle track (at a distance smaller than 5 cm), which were discarded in the case of standard reconstruction, were instead included in this new version of the likelihood function as distant hits, i.e. with the same contribution to the likelihood they would have if they were at an infinite distance from the Čerenkov ring. In this way it was possible to maintain a consistent likelihood formula while changing the particle track.

If applied to the standard reconstruction, this modified likelihood function does not change the final result since $-\log \mathcal{L}$ is shifted by a value that is constant for any reconstruction of a given event. The LIP reconstruction code was therefore changed to use the new function in both standard and standalone reconstructions.

The 5-parameter likelihood will therefore incorporate four new variables describing the particle track as arguments. In the present work, the choice was to use the x-y track coordinates at two reference heights: "top of radiator" (x_{rad}, y_{rad}), corresponding to the z position of the top of the aerogel tiles, and "detection matrix" (x_{mat}, y_{mat}), corresponding to the z position of the effective depth determined in the previous section (1.8 cm below the top of the light guides).

The generalized likelihood function is therefore defined as

$$\mathcal{L}(\theta_c, x_{rad}, y_{rad}, x_{mat}, y_{mat}) = \prod_{i=1}^{N} \mathcal{P}^{n_i}[r_i(\theta_c, x_{rad}, y_{rad}, x_{mat}, y_{mat})].$$

where

$$\mathcal{P}(r) = \begin{cases} (1-b)\left(\frac{\alpha_1}{\sqrt{2\pi}\sigma_1}\exp\left[-\frac{1}{2}\left(\frac{r}{\sigma_1}\right)^2\right]+\right. & \\ \quad\left. +\frac{\alpha_2}{\sqrt{2\pi}\sigma_2}\exp\left[-\frac{1}{2}\left(\frac{r}{\sigma_2}\right)^2\right]\right)+b/D & \text{if } d_{track} > 5\text{ cm} \\ b/D & \text{if } d_{track} \leq 5\text{ cm} \end{cases}$$

9.1.2.2 The particle spot

A hint for the position of the particle track was obtained by finding the PMT with the highest signal in the detection matrix, S_{max}, and assuming this signal to correspond to the particle spot. To ensure that such an assumption was reliable, two conditions were imposed for S_{max} and its relation with the average signal among all illuminated PMTs, S_{avg}:

- $S_{max} > 6$ p.e.
- $3 < S_{max}/S_{avg} < 10$

The upper limit on the S_{max}/S_{avg} quotient is needed to exclude events where a very high noisy hit simulates a particle spot.

An additional cut was imposed on the quality of the ring: a minimum of 6 hits (instead of the usual 3 hits) was required for events to be classified as good.

The introduction of these three cuts — maximum signal, signal quotient and number of hits — excluded most events where the strongest signal was unrelated to the particle crossing point, as shown in Fig. 9.2. Distributions are similar for simulated and real events. The peak seen at a distance of 15-20 cm, which disappears when quality cuts are applied, corresponds to the misidentification of Čerenkov ring hits as being part of the particle spot. The peak distance corresponds to the typical distance of aerogel hits to the Čerenkov cone axis at the detection matrix.

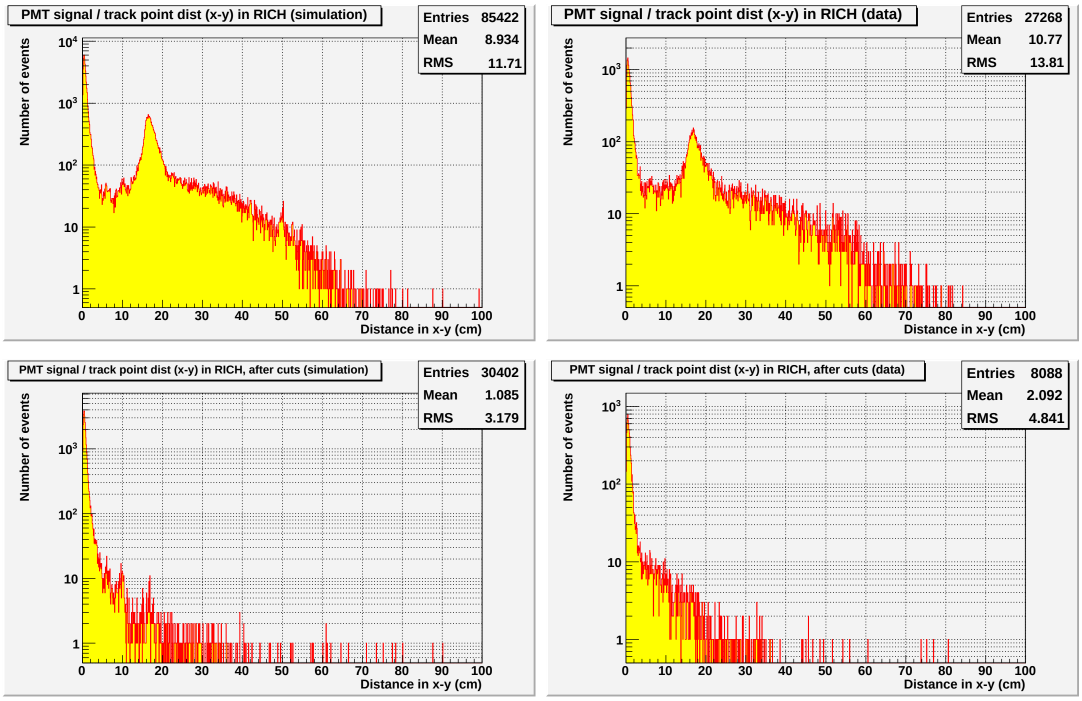

Figure 9.2: *Distance in the x-y plane between PMT matrix signal and Tracker track at the detection matrix (1.8 cm depth), before (top) and after (bottom) quality cuts: (left) AMS simulation; (right) Cosmic data.*

Since the peak on the distance distribution ended at $\simeq 5$ cm, a classification of events as function of the total (x-y) distance was introduced for this study: events were classified as "good" if they had a RICH hint less than 6 cm from the crossing point, and "bad" otherwise.

Figures 9.3 and 9.4 show distributions of S_{max} and S_{max}/S_{avg} for good and bad events, and the regions excluded by applying the corresponding quality cuts.

9.1.2.3 Hint grid and selection

In the standard event reconstruction, where the particle track is assumed to be precisely known, there is only one free parameter, the Čerenkov angle θ_c, and therefore it is easy to find the absolute maximum of the likehood function $\mathcal{L}$ (or the absolute minimum of $-\log \mathcal{L}$, which is the equivalent formulation used in LIP software). However, when track parameters are included as unknowns the problem becomes a

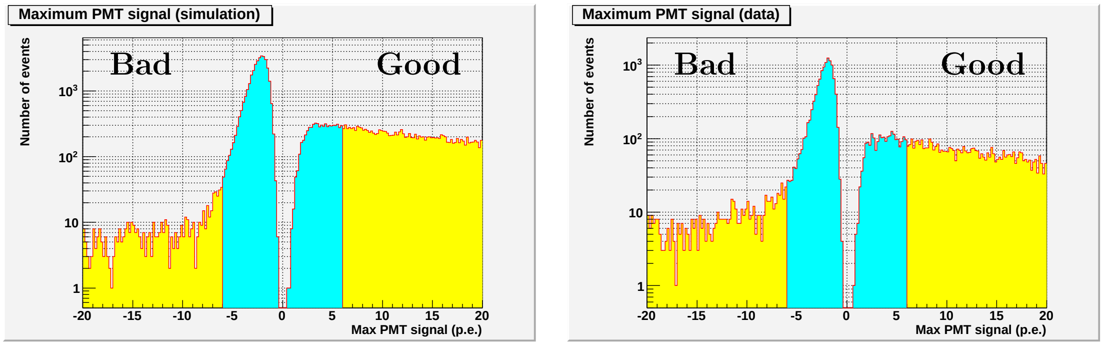

Figure 9.3: *Strongest signal in a PMT, S_{max}, for good and bad events: (left) AMS simulation; (right) Cosmic data. See main text for the definition of good events. The blue (darker) regions are excluded by the quality cut $S_{max} > 6$ p.e..*

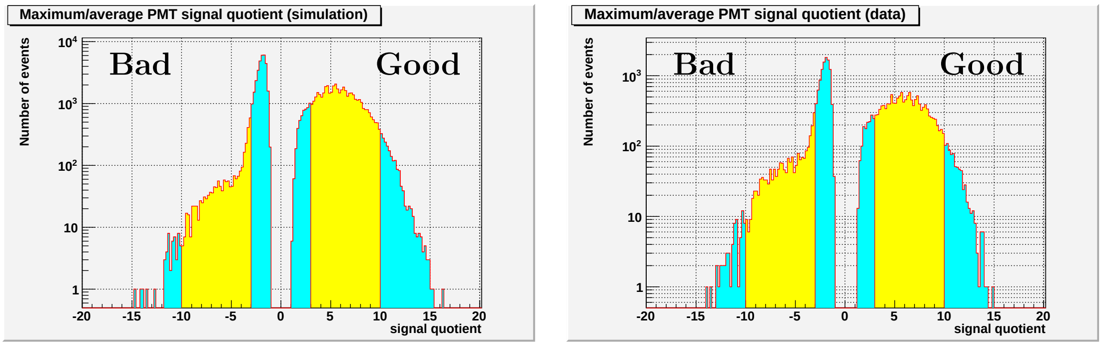

Figure 9.4: *Quotient S_{max}/S_{avg} between strongest and average PMT signals: (left) AMS simulation; (right) Cosmic data. See main text for the definition of good events. The blue (darker) regions are excluded by the quality cut $3 < S_{max}/S_{avg} < 10$.*

5-parameter minimization and finding the absolute minimum is a much more difficult task from a computational point of view.

In the reconstruction algorithm, the parameters used to represent a track are:

- x_{rad} and y_{rad}, the coordinates of the particle track at the top of the radiator plane;
- x_{mat} and y_{mat}, the coordinates of the particle track inside the light guide at the effective signal depth (1.8 cm);
- θ_c, the Čerenkov angle.

Two points were therefore used instead of a point-direction pair to define the particle track. This solution was adopted since it naturally fitted the physical limits of the detector and avoided the computational difficulties that would arise for tracks close to vertical in a minimization with angles (θ, ϕ) as parameters.

A full scan of the likelihood function in the 5-parameter space with a fine mesh is not feasible due to the number of points for which the function would have to be calculated. Therefore, the method presented here is a compromise between minimization quality and computing time.

To ensure a good coverage of the parameter space, the sets of parameters (x_{rad}, y_{rad}, x_{mat}, y_{mat}, θ_c) resulting from the combination of the following possibilities are considered:

- 6 points in x_{rad}: -50, -30, -10, 10, 30, 50 (cm)
- 6 points in y_{rad}: -50, -30, -10, 10, 30, 50 (cm)
- 3 points in x_{mat}: $x_S - 1$, x_S, $x_S + 1$ (cm)
- 3 points in y_{mat}: $y_S - 1$, y_S, $y_S + 1$ (cm)
- 5 points in θ_c: 0.68, 0.76, 0.84, 0.92, 1.00 $\times\, \theta_c^{max}$

where (x_S, y_S) is the track hint given by the barycentre of the strongest PMT signal and θ_c^{max} is the Čerenkov angle for $\beta = 1$ in the radiator corresponding to the coordinates (x_{rad}, y_{rad}), that is, approximately 17.8° for aerogel and 41.4° for NaF.

From the 36 possible combinations of x_{rad} and y_{rad} only 32 are valid since points with both coordinates at ±50 cm are outside the radiator. In the 32 valid pairs there are 4 points corresponding to the NaF radiator, those with both coordinates at ±10 cm (Fig. 9.5).

At this stage, the number of 5-parameter sets is therefore $32 \times 3 \times 3 \times 5 = 1440$. The following step is to exclude those parameter sets where the horizontal distance between radiator and matrix points is greater than 20 cm, that is, only sets with $(x_{rad} - x_{mat})^2 + (y_{rad} - y_{mat})^2 < 20^2$ are retained. This distance value was a compromise between covering a parameter space as large as possible and having an essentially unbiased estimator for the inclination θ.

For all valid parameter sets, the value of the likelihood function $\mathcal{L}$ is calculated.

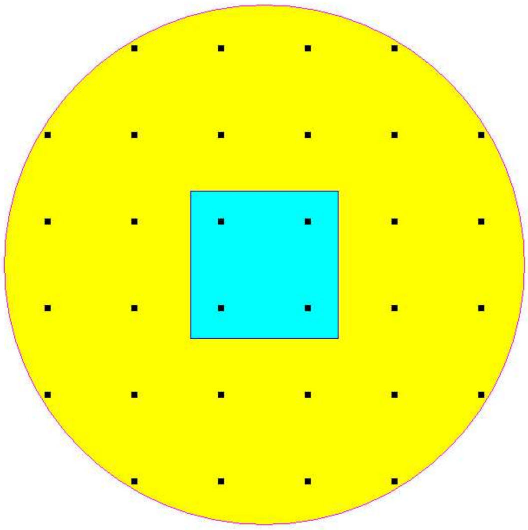

Figure 9.5: *Radiator points used in hint grid.*

9.1.2.4 Final minimizations

The 50 sets with the highest likelihood values, as determined from the procedure described above, were then used as starting points for 5-parameter minimizations using the Nelder-Mead method (also called "downhill simplex method" and "amoeba method") [144]. The result that is to be taken as the final output of the present standalone reconstruction method is the best of all minimization results. The first selection criterion is now the number of hits in the reconstructed ring, while the likelihood value is only used as a tie-breaker if more than one reconstruction shares the highest number of ring hits.

The decision to use different criteria in the selection of parameter sets before and after minimization is due to the different levels of expected agreement between the Čerenkov ring corresponding to the parameters and the hit pattern. The initial hints correspond to essentially random patterns which are generated without any information from Čerenkov hits, and therefore any close match between pattern and hits has a high probability of being accidental. On the contrary, patterns obtained after minimization are expected to match hit signals as closely as possible.

9.2 Standalone reconstruction results

The reconstruction method described above was applied to subsets of the simulated and real event samples used in Chapter 8. A lower number of events was processed due to the computational time required by the standalone reconstruction method.

The limited statistics available for this study was not sufficient to obtain meaningful results for the NaF radiator. Therefore, only the aerogel case will be treated in this section.

Results for track reconstruction quality will be presented here in terms of standard angles θ (particle inclination) and ϕ (azimuthal angle), although these are not the fundamental parameters used in the reconstruction as previously noted.

Particle inclination

Figure 9.6 shows the results obtained for the particle inclination θ. The results are poor, even after quality cuts are applied: the reconstructed angle is on average approximately 2° higher than the value given by the Tracker, with a spread of $\sigma_{\Delta\theta} = 7.6°$ in simulated events and $\sigma_{\Delta\theta} = 8.7°$ in cosmic data. The tails of the distribution extend up to $\pm 30°$.

The evolution of the results obtained for θ as function of the number of ring hits, after appying the cuts on S_{max} and S_{max}/S_{avg}, is shown in Fig. 9.7 (top). Only a slight improvement is seen as the number of hits increases. The average bias is stable at $\sim 2°$ except in the case of 3-4 hits where the bias is closer to zero.

After applying all cuts, the variation of θ reconstruction quality as function of particle inclination (given by the Tracker) is presented in Fig. 9.7 (bottom). There is a visible bias towards central inclinations, reaching $\pm 10°$ at each end.

Azimuthal angle

Figure 9.8 shows the results obtained for the azimuthal angle ϕ. After all quality cuts are applied, a rough estimate of the particle's orientation is obtained in most events, although there are significant tails right up to $\pm 180°$. These tails have a significant impact on the width of the $\Delta\phi$ distribution, which is $\sigma_{\Delta\phi} = 45.5°$ in simulation and $\sigma_{\Delta\phi} = 48.3°$ for real data.

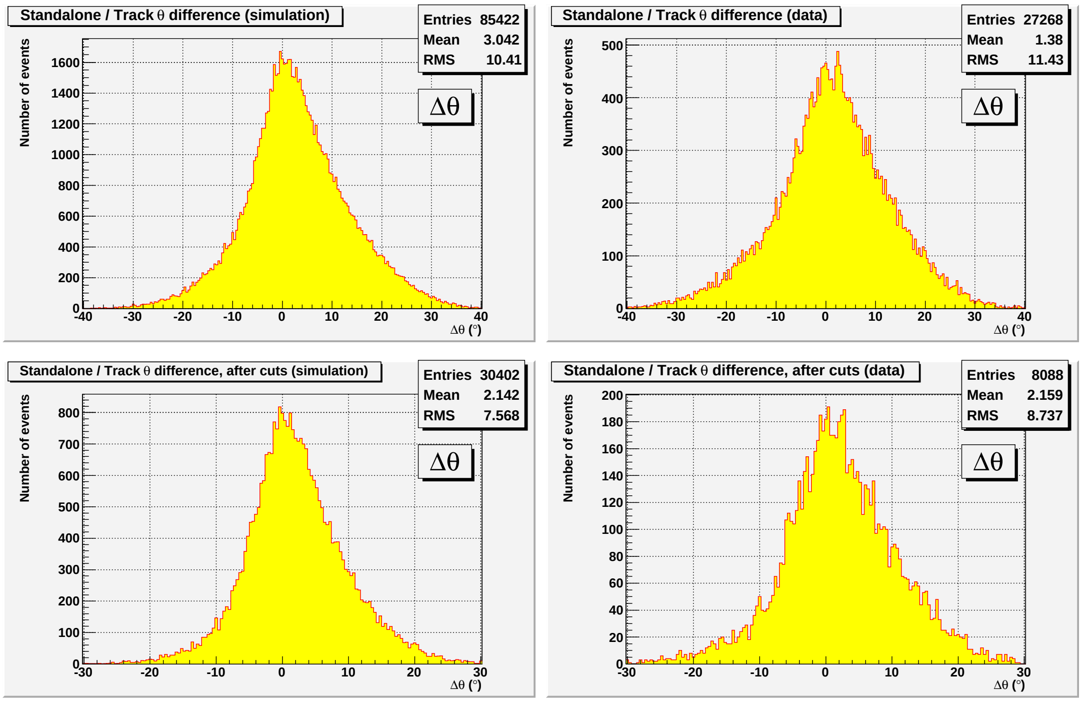

Figure 9.6: *Difference in inclination θ between standalone and Tracker track, before (top) and after (bottom) quality cuts: (left) AMS simulation; (right) Cosmic data.*

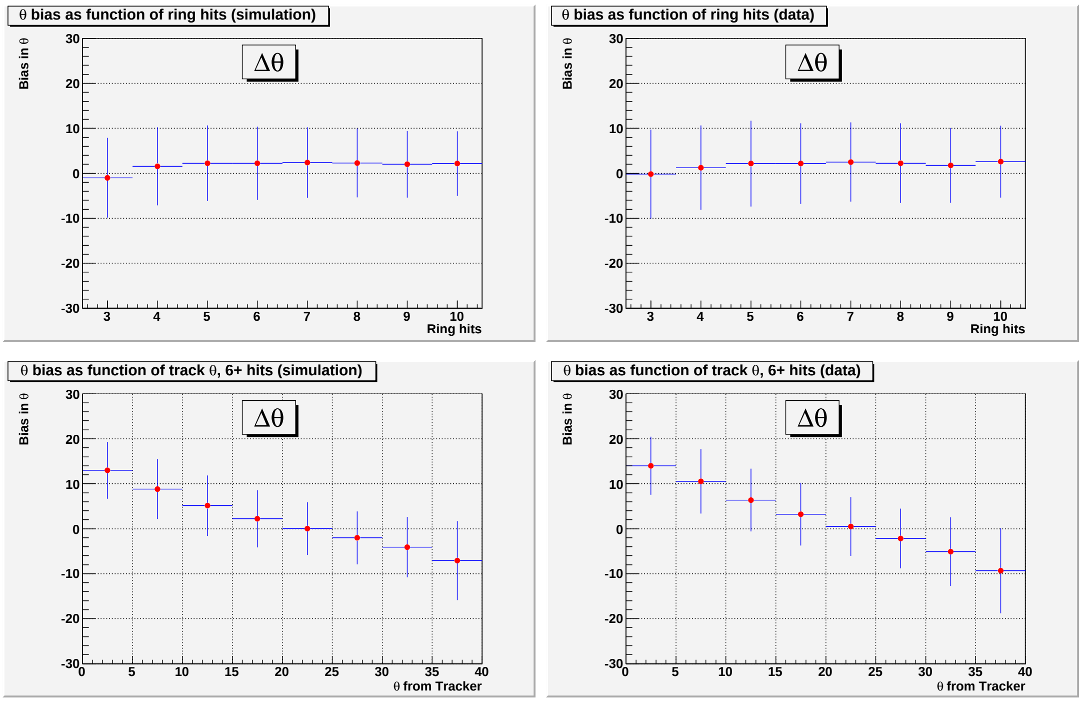

Figure 9.7: *Standalone-Tracker track θ difference as function of (top) ring hits and (bottom) track inclination: (left) AMS simulation; (right) Cosmic data. Vertical bars indicate the distribution's standard deviation.*

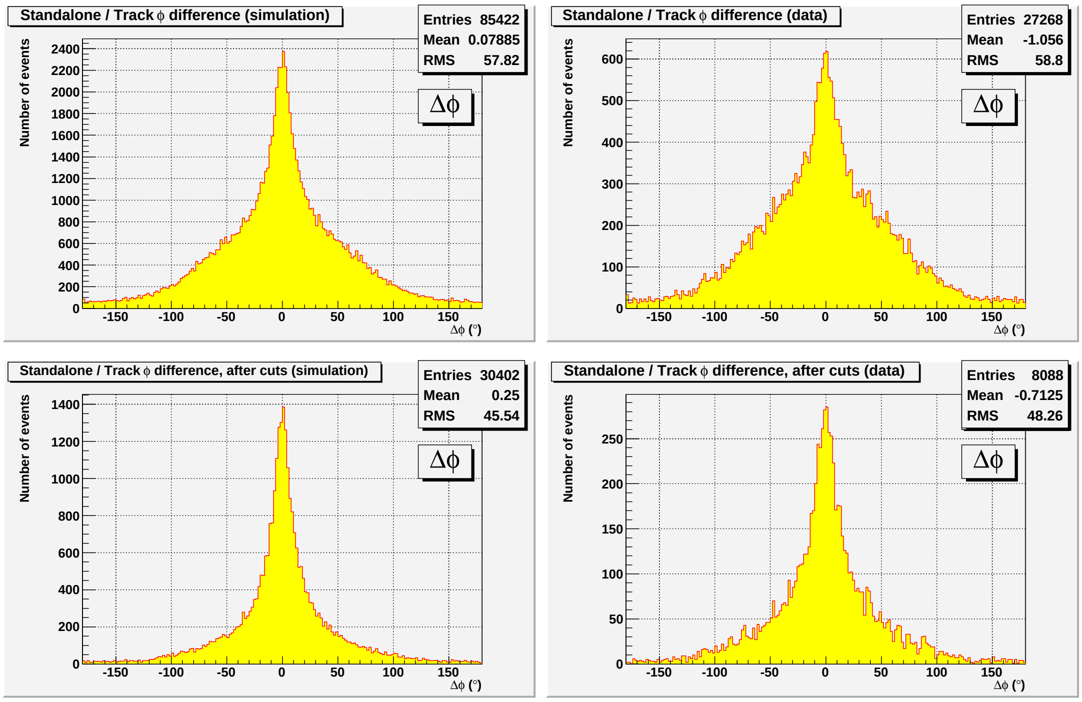

Figure 9.8: *Difference in azimuthal angle ϕ between standalone and Tracker track, before (top) and after (bottom) quality cuts: (left) AMS simulation; (right) Cosmic data.*

The evolution of the results obtained for ϕ as function of the number of ring hits, after appying the cuts on S_{max} and S_{max}/S_{avg}, is shown in Fig. 9.9 (top). A significant improvement is seen as the number of hits increases, with values $\sigma_{\Delta\phi} \simeq 65°$ for 3 hits and $\sigma_{\Delta\phi} \simeq 45°$ for 8-10 hits. There is no significant difference between the simulation and data results, meaning that the change seen in the global distribution is essentially due to the number of ring hits in data being lower than expected from simulation (see Chapter 8 for details on the observed difference in light yield results between simulation and data).

After applying all cuts, the variation of ϕ reconstruction quality as function of particle inclination (given by the Tracker) is presented in Fig. 9.9 (bottom). Events with low inclination have, as expected, very high uncertainties in ϕ, approaching the limit of total uncertainty (at which $\sigma_{\Delta\phi} \to \frac{360°}{\sqrt{12}} = 103.9°$). Reconstruction quality improves as particle inclination increases, reaching a plateau for inclinations between 20° and 35° where $\sigma_{\Delta\phi} \simeq 30°$ for simulation and $\sigma_{\Delta\phi} \simeq 35°$ for data. For very high inclinations some degradation is seen.

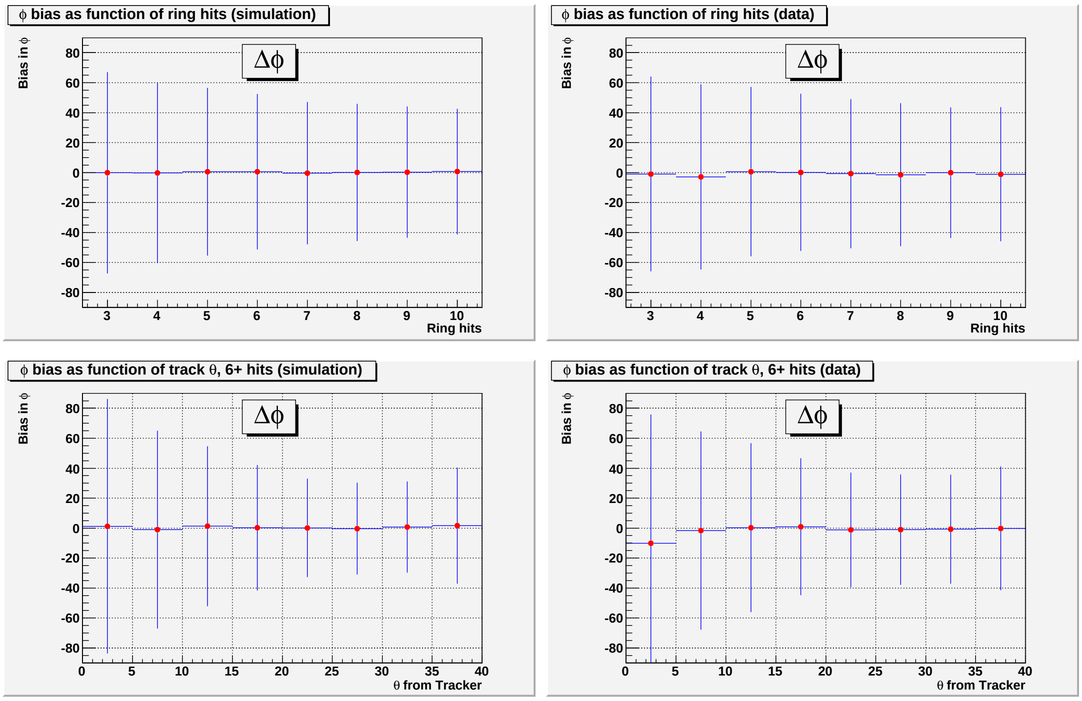

Figure 9.9: *Standalone-Tracker track ϕ difference as function of (top) ring hits and (bottom) track inclination: (left) AMS simulation; (right) Cosmic data. Vertical bars indicate the distribution's standard deviation.*

Čerenkov angle

Figure 9.10 shows the results obtained for the Čerenkov angle θ_c. In the case of simulated events, a reasonable agreement is seen between this method's result and the reference value for θ_c obtained the standard LIP algorithm (used in the analysis performed in the previous chapters) and based on Tracker data. The distribution obtained after applying the quality cuts shows a peak that is slightly asymmetric, with a mean value of $-0.25°$ and $\sigma_{\Delta\theta_c} = 1.91°$, and no significant tails are observed beyond $\pm 5°$. In the case of cosmic data the result is clearly poorer: the distribution peak is slightly wider, as expected from the small reduction in the number of hits, but a new tail extending up to $15°$ appears on the right-hand side of the distribution. Quality cuts have no significant effect on this tail. As a result, the data distribution has a mean value of $0.07°$ and the spread increases to $\sigma_{\Delta\theta_c} = 2.76°$.

The evolution of the results obtained for θ_c as function of the number of ring hits, after appying the cuts on S_{max} and S_{max}/S_{avg}, is shown in Fig. 9.11 (top). In simulated events there is a gradual improvement as the number of hits increases,

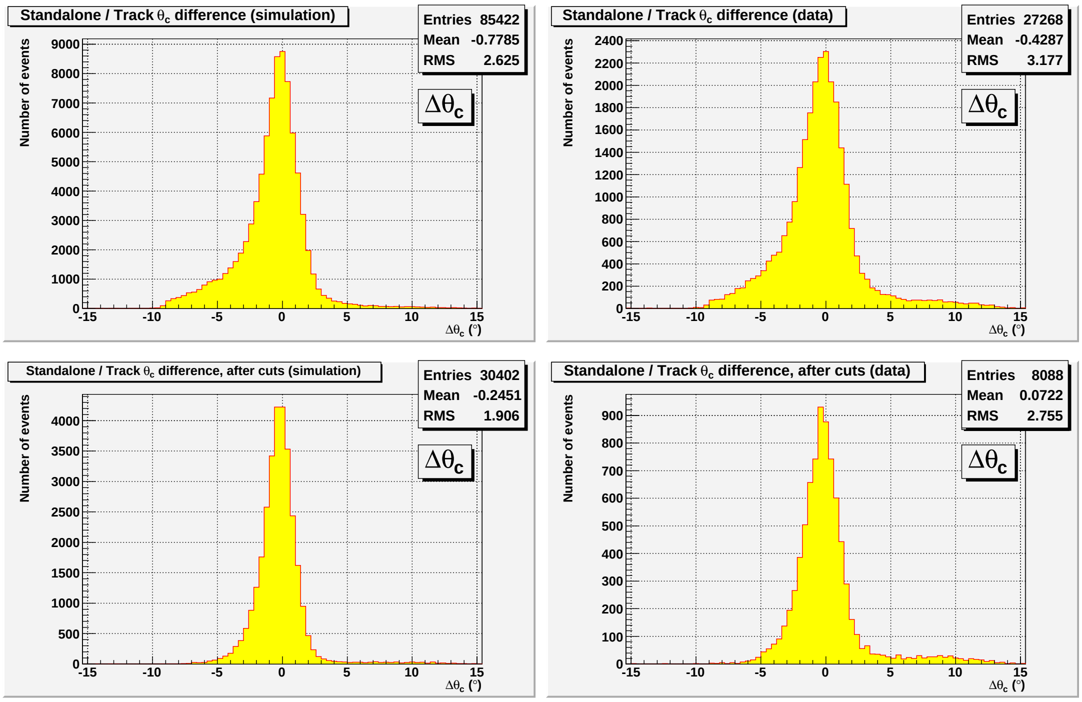

Figure 9.10: *Difference in Čerenkov angle θ_c between standalone and Tracker track, before (top) and after (bottom) quality cuts: (left) AMS simulation; (right) Cosmic data.*

although the biggest difference occurs between the cases of 3 and 4 hits. For cosmic data results are poorer, as expected from the global plot: there is again a major improvement between 3 and 4 hits, but no significant change is seen beyond 5 hits, the result appearing to be dominated by the tail at high values.

After applying all cuts, the variation of θ_c reconstruction quality as function of particle inclination (given by the Tracker) is presented in Fig. 9.11 (bottom). In the simulation case it can be seen that the bias in θ_c is correlated with inclination: the distribution of $\Delta\theta_c$ has an average value of $\simeq -1°$ for $\theta \simeq 0°$, while for high inclinations ($\theta \gtrsim 25°$) the average value becomes positive. The distribution becomes wider as the inclination increases: $\sigma_{\Delta\theta_c} \simeq 1.6°$ for $\theta \simeq 0°$, and $\sigma_{\Delta\theta_c} \simeq 2.7°$ for $\theta \simeq 35°$-$40°$. In the case of cosmic data there is a similar behaviour in the bias as function of inclination but the width of the distribution is almost constant, always falling in the 2.5°-2.8° range.

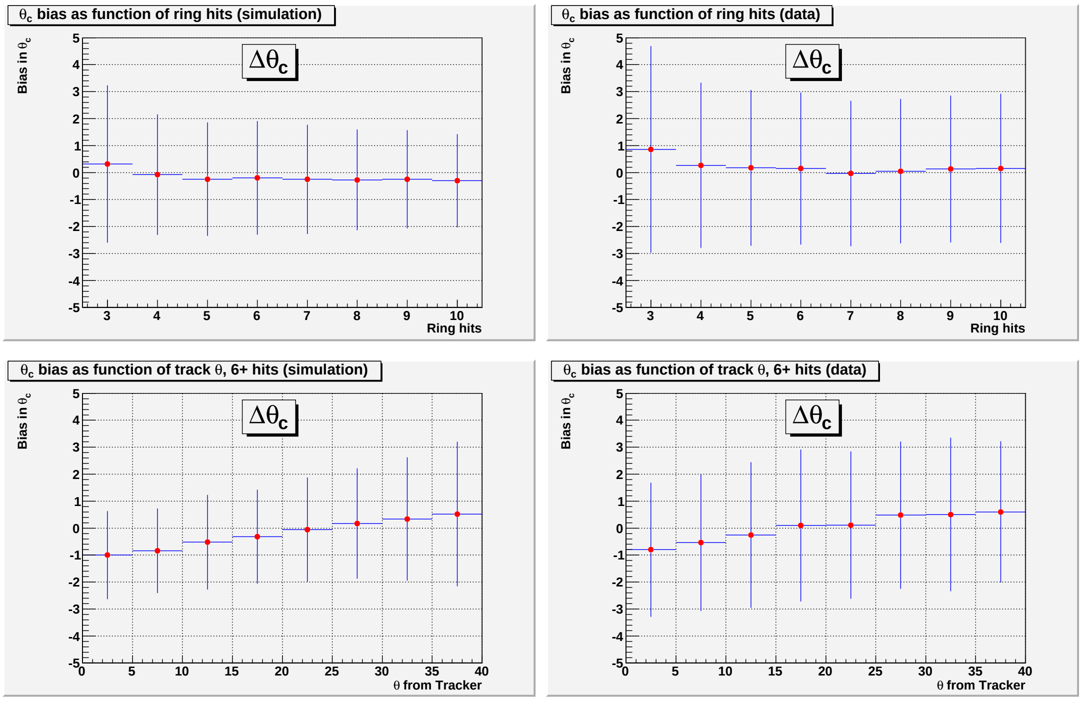

Figure 9.11: *Standalone-Tracker track θ_c difference as function of (top) ring hits and (bottom) track inclination: (left) AMS simulation; (right) Cosmic data. Vertical bars indicate the distribution's standard deviation.*

Position at radiator

Figure 9.12 shows the results obtained for the error in the particle crossing point at the top of the radiator, Δr_{rad}. The error in the radiator position is quite large, even after quality cuts are introduced: average errors are $\overline{\Delta r_{rad}} = 11.3$ cm in the simulation and $\overline{\Delta r_{rad}} = 13.2$ cm in cosmic data, with a significant fraction of events having errors as high as 30 cm.

The evolution of the results obtained for Δr_{rad} as function of the number of ring hits, after appying the cuts on S_{max} and S_{max}/S_{avg}, is shown in Fig. 9.13 (top). Some improvement is seen as the number of hits increases: in the simulation case $\overline{\Delta r_{rad}}$ improves from $\simeq 15$ cm to $\simeq 10$ cm as the number of hits increases from 3 to 10. Results for real data are slightly worse, with $\overline{\Delta r_{rad}}$ improving from $\simeq 16$ cm to $\simeq 12$ cm in the same range, showing that the reduction in the number of hits is not the only cause of the degradation seen from simulation to cosmic data.

After applying all cuts, the variation of Δr_{rad} as function of particle inclination (given by the Tracker) is presented in Fig. 9.13 (bottom). It can be seen that the

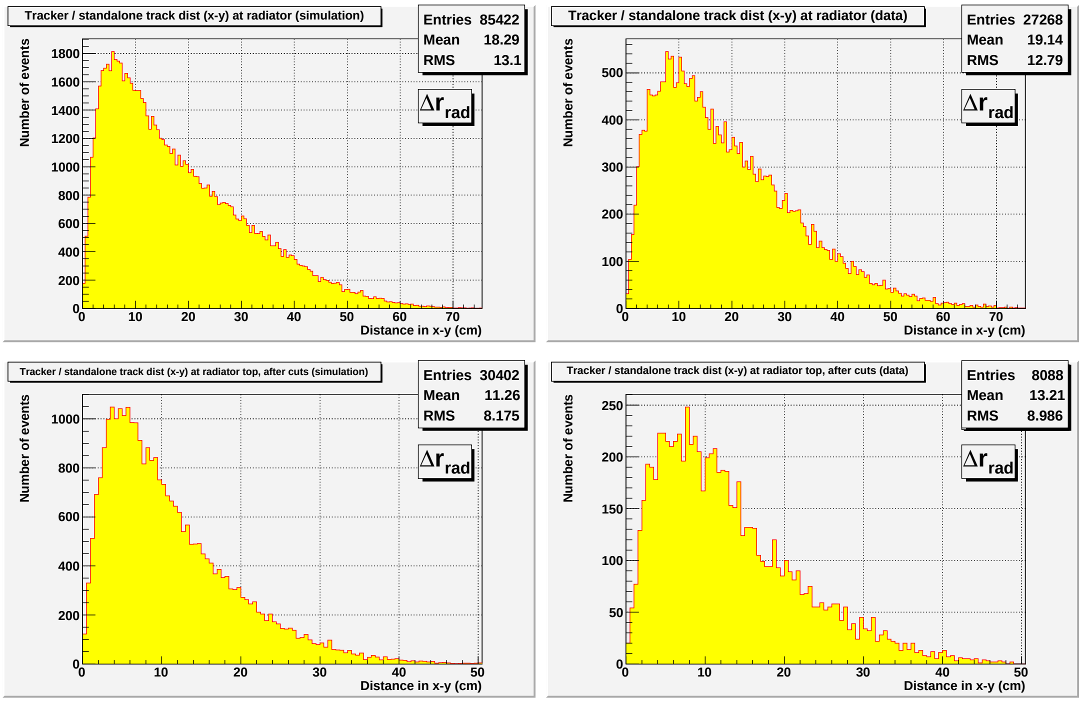

Figure 9.12: *Distance in the x-y plane between standalone and Tracker track at the top of the radiator, before (top) and after (bottom) after quality cuts: (left) AMS simulation; (right) Cosmic data.*

lowest errors are obtained for inclinations between 20° and 30°: for these cases $\overline{\Delta r_{rad}} \simeq 10$ cm in simulation and $\overline{\Delta r_{rad}} \simeq 12$ cm in data. This result is closely related to the fact of these inclinations being those for which an unbiased estimator of θ is obtained.

Position at detection matrix

Figure 9.14 shows the results obtained for the error in the particle crossing point at the detection matrix, Δr_{LG}. Results are much better than those obtained at the top of the radiator, due to the hint given by the charged particle's signal at the matrix. The bump seen between 10 and 25 cm, corresponding to the misidentification of ring hits as being produced by the charged particle, disappears after quality cuts are applied. The final distributions have average values $\overline{\Delta r_{LG}} = 1.86$ cm in simulation and $\overline{\Delta r_{LG}} = 2.95$ cm in cosmic data, with most events having errors up to 3 cm. The number of events with errors greater than 6 cm is almost zero in the simulation case, while in data a small tail is seen in that region. This tail, combined with

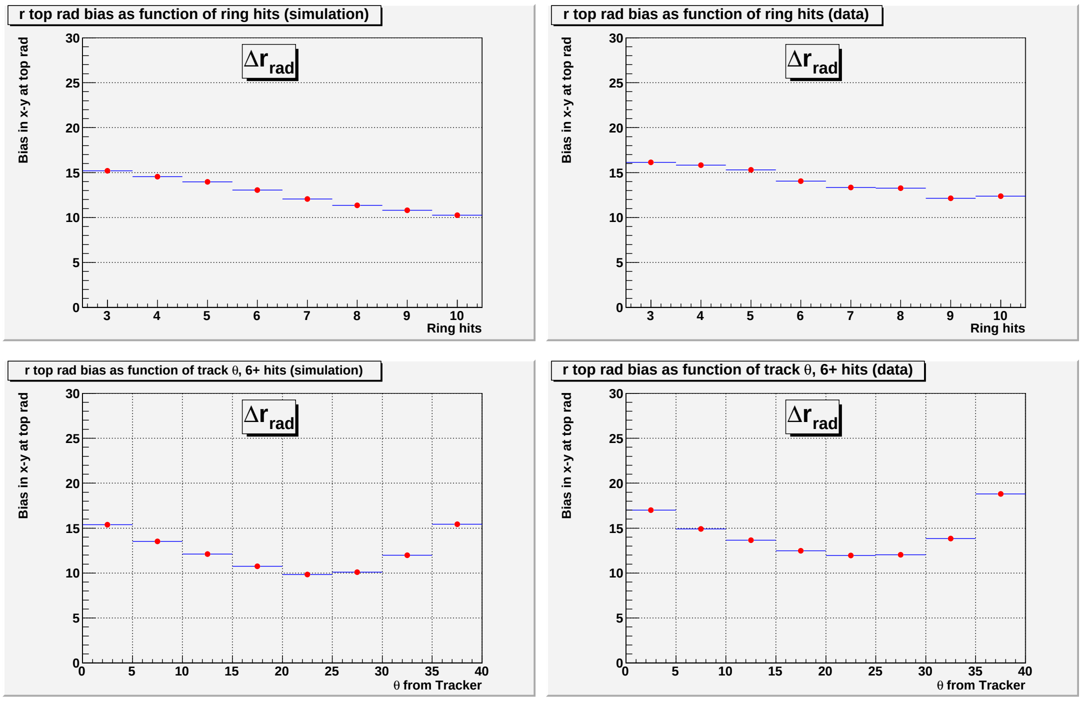

Figure 9.13: *Average standalone-Tracker track x-y distance at the top of the radiator as function of (top) ring hits and (bottom) track inclination: (left) AMS simulation; (right) Cosmic data.*

a slight increase in the width of the main peak, leads to the large difference seen between the simulation and data averages.

The evolution of the results obtained for Δr_{LG} as function of the number of ring hits, after appying the cuts on S_{max} and S_{max}/S_{avg}, is shown in Fig. 9.15 (top). In the case of simulated events there is a steady improvement as the number of hits increases, with $\overline{\Delta r_{LG}} \simeq 2.6$ cm for 3 hits and $\overline{\Delta r_{LG}} < 2$ cm for 7 or more hits. In the case of real data the average error improves from $\overline{\Delta r_{LG}} \simeq 4.6$ cm for 3 hits to $\overline{\Delta r_{LG}} \simeq 3.0$ cm for 5 hits but no further improvent is observed, the average error remaining around 3 cm up to 10 hits.

After applying all cuts, the variation of Δr_{LG} as function of particle inclination (given by the Tracker) is presented in Fig. 9.15 (bottom). In the case of simulated events, the average error is stable for inclinations up to 30°, with a value $\overline{\Delta r_{LG}} \simeq 1.8$ cm, then rises rapidly for higher angles. In the case of real data, the average error is $\simeq 3.4$ cm for $\theta < 5°$, then fluctuates in the 2.6-3.0 cm range up to $\theta = 30°$, rising for higher inclinations.

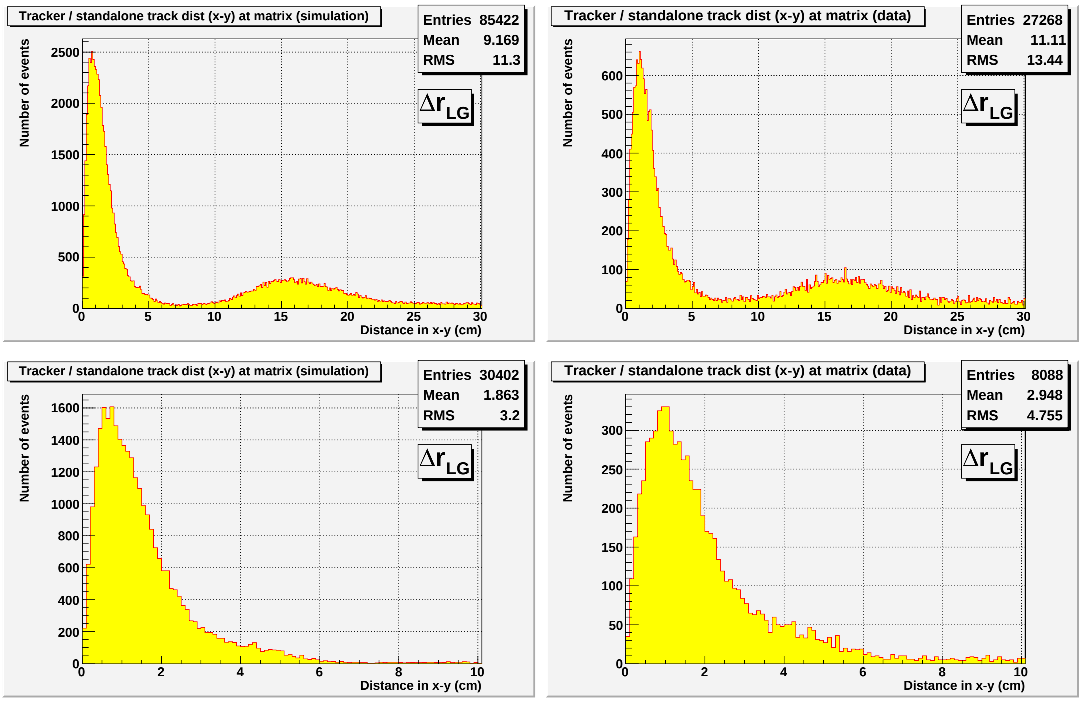

Figure 9.14: *Distance in the x-y plane between standalone and Tracker track at the detection matrix (1.8 cm depth), before (top) and after (bottom) quality cuts: (left) AMS simulation; (right) Cosmic data.*

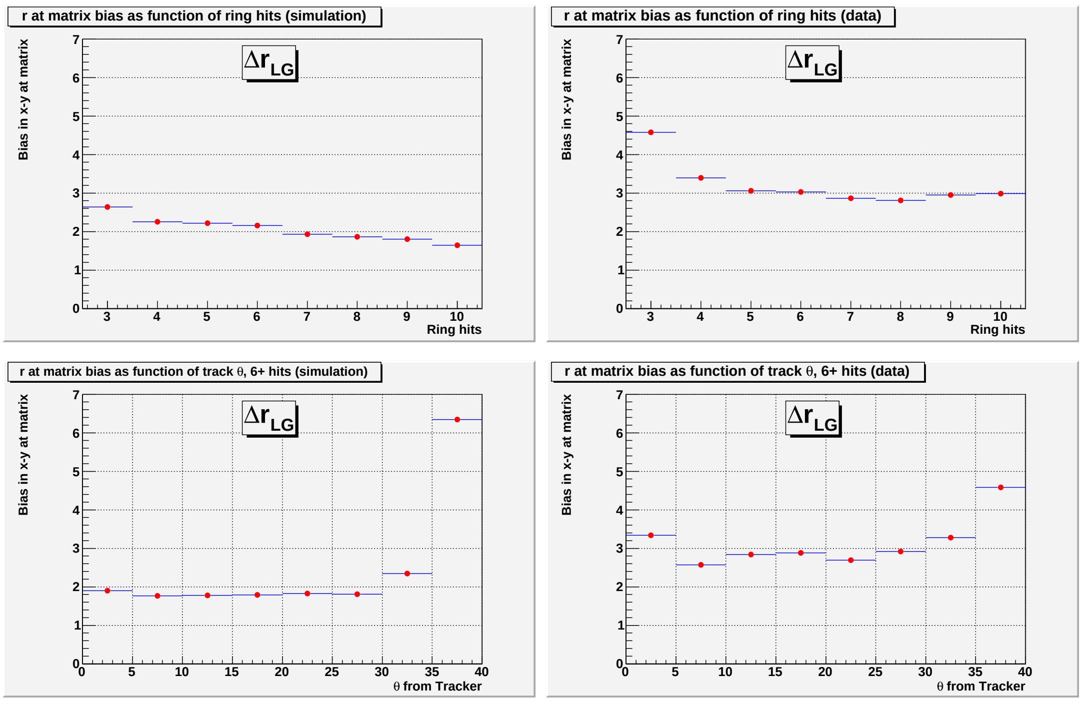

Figure 9.15: *Average standalone-Tracker track x-y distance at the detection matrix as function of (top) ring hits and (bottom) track inclination: (left) AMS simulation; (right) Cosmic data.*

Degeneracy in θ reconstruction

The bias seen in reconstructions of particle inclination θ, together with the large spread observed even for specific inclinations, led to an evaluation of the evolution not only of the bias but of the reconstructed angle itself as function of the reference value given by the Tracker. The corresponding results, obtained after applying all cuts, are shown in Fig. 9.16. It is clear that there is a degeneracy in the reconstructed inclination. In particular, any track inclination from 0° to 40° is likely to generate reconstructed values of θ in the 20°-25° region.

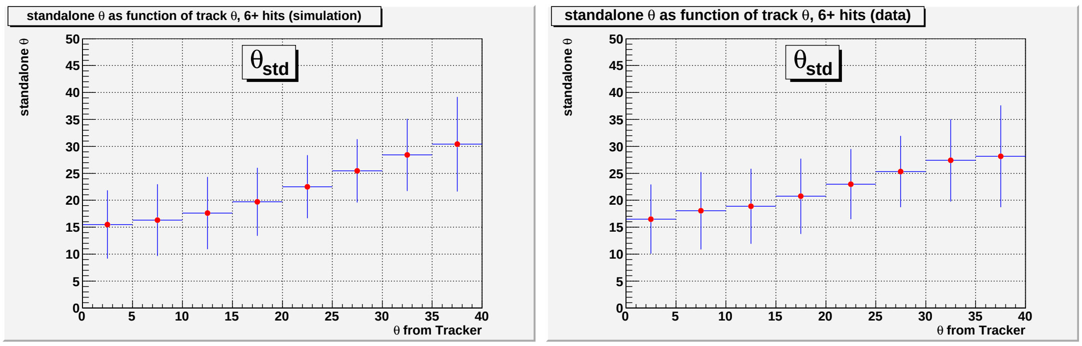

Figure 9.16: *Reconstructed track inclination θ as function of track inclination given from Tracker: (left) AMS simulation; (right) Cosmic data. Vertical bars indicate the distribution's standard deviation.*

9.3 Track reconstruction using TOF data

The difficulties posed by the reconstruction of the Čerenkov cone based solely on RICH data led to a search for other methods of reconstructing the particle's trajectory without information from the AMS Tracker.

In this context, the possibility of using data provided by the AMS Time-of-Flight detector was explored. The AMS TOF consists of a total of four planes in two pairs separated by a distance of approximately 1 m. Charged particles entering the AMS-02 detector will typically be detected by signals in those planes.

9.3.1 Quality of TOF data

The data collected by the TOF provide the x and y coordinates of particle crossings with an associated accuracy which is typically of a few cm. In some cases only one of the coordinates x and y has a meaningful measurement while the other coordinate is given as zero with a maximum uncertainty corresponding to the dimensions of the TOF plane along the corresponding coordinate divided by $\sqrt{12}$. Such cases are automatically accounted for at the moment of track fitting since the position accuracies given by the TOF are used in the fit.

9.3.2 The RICH matrix as an additional detection plane

The signal left in the RICH matrix by the charged particle, described earlier in this chapter (see 9.1.2.2) may also be used in the context of a TOF-based reconstruction. In this context, the RICH matrix plays a role similar to that of a fifth TOF plane. The z coordinate used for the RICH signal corresponds to the effective depth at which an optimal agreement with Tracker data is obtained in x and y (see 9.1.1.1).

The importance of the RICH signal for track fitting may be appreciated considering that the four TOF planes correspond in terms of z to two redundant pairs. Adding an additional point at a significant distance from the TOF planes (the RICH matrix is more than 50 cm below the lower TOF) is a major step towards a more reliable track determination.

A value had to be chosen for the uncertainty in each coordinate of the RICH signal position to be used in track fitting. The value chosen, 1.2 cm in each coordinate, was obtained from previous studies on the agreement between the Tracker track and the RICH signal.

The RICH signal was only used if it was considered to be significant. The threshold for taking this signal into consideration was set at 6 photoelectrons, in agreement with the minimum signal required in the case of standalone reconstruction.

9.3.3 Types of TOF and TOF/RICH reconstructions tested

In the present study, the concept of a TOF-based track reconstruction was implemented in four closely related algorithms using data from:

(I) upper TOF + lower TOF

(II) upper TOF + lower TOF + RICH matrix

(III) upper TOF + RICH matrix

(IV) lower TOF + RICH matrix

9.3.3.1 Reconstruction requirements

The requirements for a track to be deemed valid were the following:

- **Type I: upper TOF + lower TOF**
  4-point condition: exactly one set of aligned points from the 4 TOF planes
  or
  3-point condition: none of the above sets found, and exactly one set of aligned points from 3 TOF planes

- **Type II: upper TOF + lower TOF + RICH matrix**
  5-point condition: exactly one set of aligned points from the 4 TOF planes and the RICH matrix
  or
  4-point condition: none of the above sets found, and exactly one set of aligned points from 3 TOF planes and the RICH matrix

- **Type III: upper TOF + RICH matrix**
  3-point condition: exactly one set of aligned points from the 2 upper TOF planes and the RICH matrix
  or
  2-point condition: none of the above sets found, and exactly one point from one upper TOF plane found and a RICH matrix point available

- **Type IV: lower TOF + RICH matrix**
  3-point condition: exactly one set of aligned points from the 2 lower TOF planes and the RICH matrix
  or

2-point condition: none of the above sets found, and exactly one point from one lower TOF plane found and a RICH matrix point available

In all cases, except for the 2-point conditions, the alignment of the TOF points was determined by measuring the distance of points in the middle planes to a straight reference line connecting the two points at the highest and lowest planes (the lowest plane being the RICH matrix for reconstruction types II, III and IV). This distance was measured along the x-y plane. A point was considered to be aligned with the reference line if the distance was lower than a maximum tolerance. A broad distance limit (10 cm) was used.

In the case of the 2-point conditions, any pair of points was deemed valid provided that it was unique and the 3-point condition was not fulfilled, as described above.

The planes used for the reference line in alignment tests with more than two points were chosen according to the case being tested, and corresponded to the uppermost and lowermost planes among those being considered, as presented in Table 9.2.

In the cases where a valid set of points was found, a track hint was generated from minimum-square fits to the projections of the point coordinates in the x-z and y-z planes. The track hint was then used as an input parameter of a constrained minimization.

9.4 Results for TOF-based reconstructions

The TOF-based reconstruction algorithms described above were applied to cosmic muon events (simulated and real) in the framework of the AMS-02 software chain (Section 3.5). These event sets corresponded to the same full-scale simulation data and cosmic data used in the light yield studies presented in Chapter 8. The real events corresponded to a total of 98 data runs, acquired between May 7 and June 5, 2008, listed in Appendix B. The RICH standalone simulation was not used in this study since a full description of the TOF detector was essential in this context.

The results obtained for each type of TOF-based reconstruction are described in detail in the following subsections. Several variables were used to compare the tracks obtained from these algorithms with the reference track given by the Tracker: the

Table 9.2: *Planes used as reference in TOF-based track reconstruction algorithms using more than two planes. Planes 1 and 2 correspond to the upper TOF, planes 3 and 4 to the lower TOF, and plane 5 to the RICH matrix.*

Reconstruction type	**Condition**	**Point planes**	**Reference planes**
I	4-point	1-2-3-4	1, 4
	3-point	1-2-3	1, 3
		1-2-4	1, 4
		1-3-4	1, 4
		2-3-4	2, 4
II	5-point	1-2-3-4-5	1, 5
	4-point	1-2-3-5	1, 5
		1-2-4-5	1, 5
		1-3-4-5	1, 5
		2-3-4-5	2, 5
III	3-point	1-2-5	1, 5
IV	3-point	3-4-5	3, 5

angle α between the two tracks, the differences $\Delta\theta$, $\Delta\phi$ and $\Delta\theta_c$ in the reconstructed parameters of the Čerenkov cone (inclination θ, azimuthal angle ϕ and Čerenkov angle θ_c) and the distances Δr_{top} and Δr_{LG} between the estimated particle crossing points at the planes defined by the top of the aerogel radiator[1] and by the RICH detection matrix (at the standard depth of 1.8 cm).

For each of the six variables mentioned above, the results obtained are presented in terms of the 68.3% and 95.4% confidence regions. The decision of using these variables instead of the mean and standard deviation arose from the presence of some non-negative variables (α, Δr_{top}, Δr_{LG}) and of the highly non-Gaussian shape of many distributions for the remaining variables, especially in terms of their tails.

[1]For consistency, the plane corresponding to the top of aerogel tiles is used even in the analysis of NaF events. The top of aerogel tiles is 2 cm above the top of NaF tiles due to the greater thickness of aerogel.

The values 68.3% and 95.4% were chosen to match to the expected number of events within one and two standard deviations of the mean in a normal distribution[2]. In the case of non-negative variables the confidence regions were defined as extending from zero to the corresponding percentile. In the case of the variable $\Delta\phi$, where no asymmetry was expected to appear in the distributions[3], the confidence regions were calculated for its module $|\Delta\phi|$. For the other two variables, $\Delta\theta$ and $\Delta\theta_c$, the 68.3% and 95.4% confidence regions were determined by removing an identical fraction of events (that is, approximately 15.9% and 2.3%, respectively) on each side of the distribution. The median of each distribution is also presented as a measurement of an eventual bias.

In the case of aerogel events, the reconstruction quality for each variable is also presented as function of three important parameters: the number of hits in the Čerenkov ring, the particle's inclination (as given by the Tracker) and the radius of the point at which the particle crossed the top of the aerogel radiator. This study is not presented for NaF events due to insufficient statistics.

9.4.1 Type I: upper TOF + lower TOF

9.4.1.1 Aerogel events

Track precision

Figure 9.17 shows the results obtained for the angle α between the reconstructed track and the reference track given by the AMS Tracker. There is a reasonable agreement between the TOF-based track and the reference track given by the Tracker. The 68.3% percentile is at 3.36° in the simulation and at 3.66° in cosmic data. The tail of the distribution is more significant in data, with the 95.4% percentile at 8.26° compared with 5.97° in the case of simulation.

The evolution of the results obtained for α as function of the number of ring hits is shown in Fig. 9.18 (top). In the case of simulated events no strong dependence

[2]The exact values used in the analysis had five significant digits: 68.268% and 95.450%, corresponding to the 1-σ and 2-σ percentiles of a normal distribution, respectively.

[3]In fact, one instance of an asymmetric distribution of $\Delta\phi$ appeared in the course of this study, for the case of reconstruction type IV (lower TOF+RICH matrix) applied to aerogel events from the 2008 cosmic data.

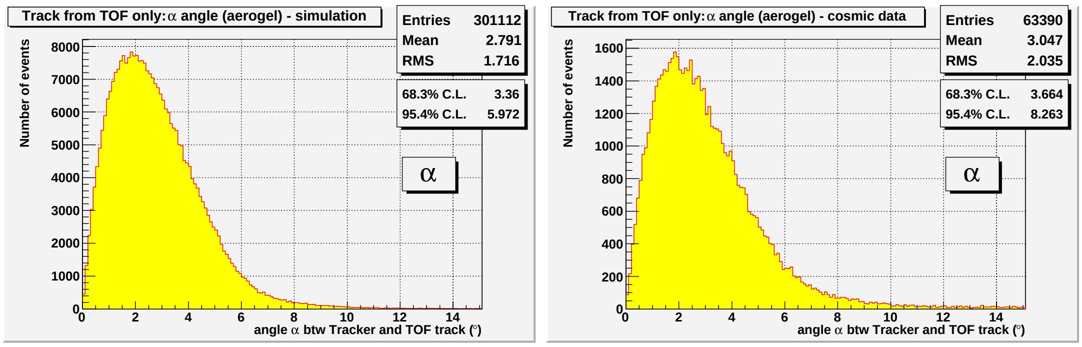

Figure 9.17: *Angle α between TOF-based track (type I) and Tracker track (aerogel events): (left) AMS simulation; (right) Cosmic data.*

is seen, although the 95.4% percentile improves clearly when the number of hits increases from 3 to 5 or more. For ≥ 5 hits there are no significant variations. In real data the dependence on the number of hits is more important, and it can be seen that the reconstruction quality is higher for 5-7 hits and then degrades for higher hit counts. This degradation may indicate that, at least in the case of data, the increase in the number of hits from 5-7 to ~ 10 implies a significant addition of noisy hits in the total count.

The variation of α as function of particle inclination (given by the Tracker) is presented in Fig. 9.18 (centre). The quality of track reconstruction increases with inclination both in simulation and in data. In the case of real data the tail is very long for small inclinations, with the 95.4% percentile reaching $\sim 15°$.

Results of α as function of the radius of the particle's crossing point at the radiator are presented in Fig. 9.18 (bottom). Some variation is observed: in the case of simulation the best results are obtained for inner and outer events, while in data the best results are for outer events, with inner events having long tails.

Particle inclination

Figure 9.19 shows the results obtained for the particle inclination θ. A good reconstruction is obtained for most events. Global distributions have a nearly Gaussian peak, with a slight bias towards positive differences: the distribution's median is $+0.12°$ in simulation and $+0.16°$ in cosmic data. The peak is is slighlty wider in data: the half-width of the 68.3% confidence region is $2.08°$ for simulation and $2.30°$

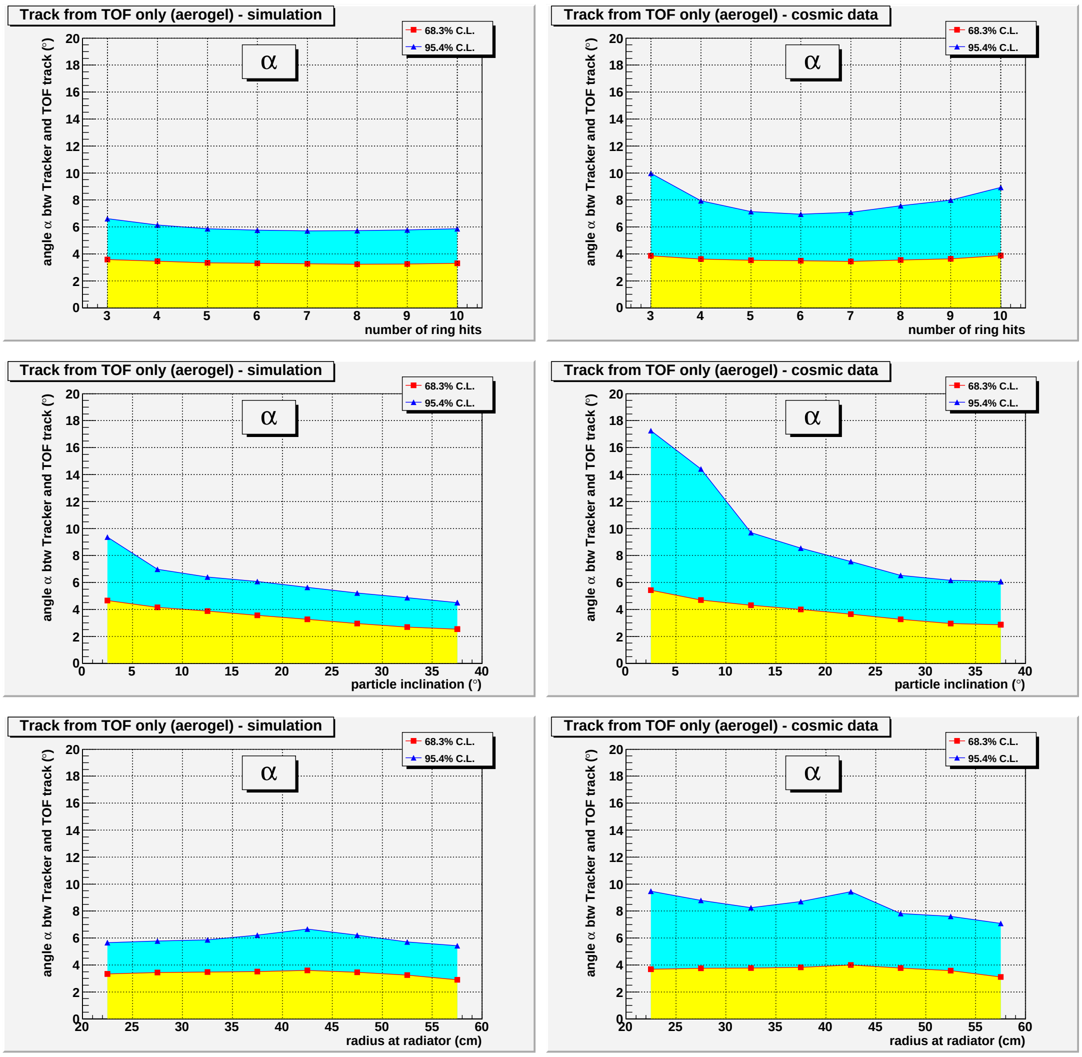

Figure 9.18: *Contours for angle α between TOF (type I) and Tracker tracks as function of (top) ring hits, (centre) track inclination and (bottom) radius of radiator impact point (aerogel events): (left) AMS simulation; (right) Cosmic data.*

for data. The difference between simulation and data is larger in the case of tails, with the 95.4% confidence region having a half-width of 4.53° in simulation and 5.77° in data.

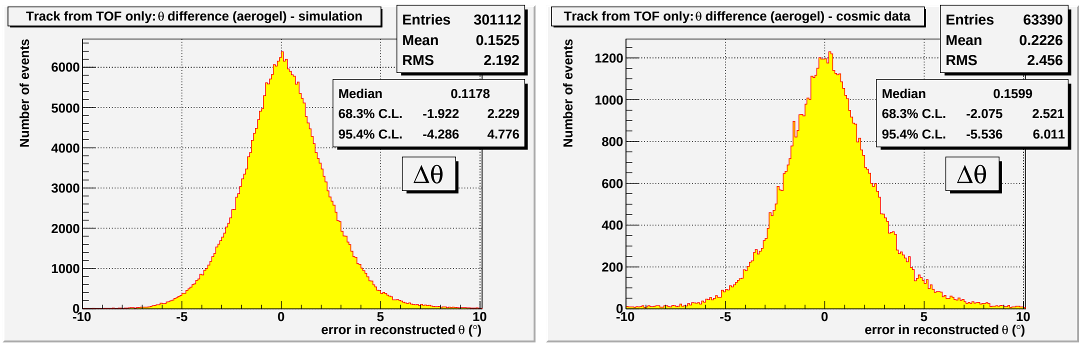

Figure 9.19: *Difference in inclination θ between TOF-based track (type I) and Tracker track (aerogel events): (left) AMS simulation; (right) Cosmic data.*

The evolution of the results obtained for θ as function of the number of ring hits is shown in Fig. 9.20 (top). In the case of simulation there is some improvement (essentially in tails) as the number of hits increases from 3 to 5, and no significant changes are seen beyond 5 hits. In data there is a significant improvement in tails from 3 to 5 hits but some degradation is then seen between 5 and 10 hits, essentially in the tail at positive values.

The variation of θ reconstruction quality as function of particle inclination (given by the Tracker) is presented in Fig. 9.20 (centre). In simulated events the reconstruction quality for θ improves as the inclination increases. Some bias is seen for very small inclinations, but this is a natural consequence of the available reconstruction space. In data, the peak region is only slightly wider but there are longer tails, especially for $\theta < 10°$ and $\theta > 35°$.

Results of θ reconstruction quality as function of the radius of the particle's crossing point at the radiator are presented in Fig. 9.20 (bottom). In simulation results are stable across all the radiator, the only significant change being an increase in the right-hand tail for intermediate radii (35-50 cm). In data a similar behaviour is observed, but tails are longer: for lower radii (up to 45 cm) it is the right-hand tail that is extended, while for high radii (above 50 cm) the left-hand tail is the widest.

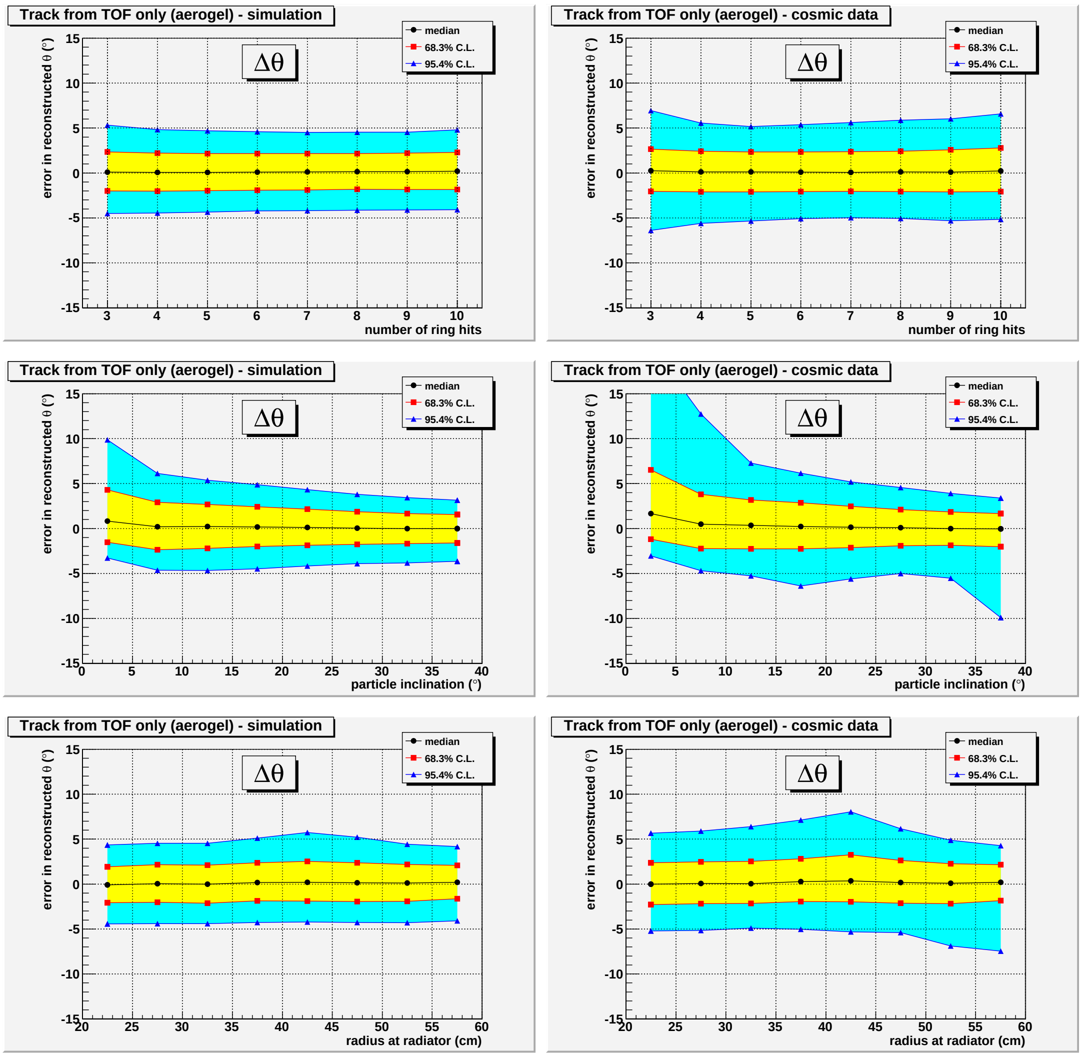

Figure 9.20: *Contours for θ difference between TOF (type I) and Tracker tracks as function of (top) ring hits, (centre) track inclination and (bottom) radius of radiator impact point (aerogel events): (left) AMS simulation; (right) Cosmic data.*

Azimuthal angle

Figure 9.21 shows the results obtained for the azimuthal angle ϕ. Good results are obtained. There is almost no difference in peak width between simulation and data, with the 68.3% percentile corresponding to an error of 7.22° in simulation and 7.32° in data. Some difference is seen in tails, however: the 95.4% percentile is reached at 26.8° in simulation but only at 32.0° in data.

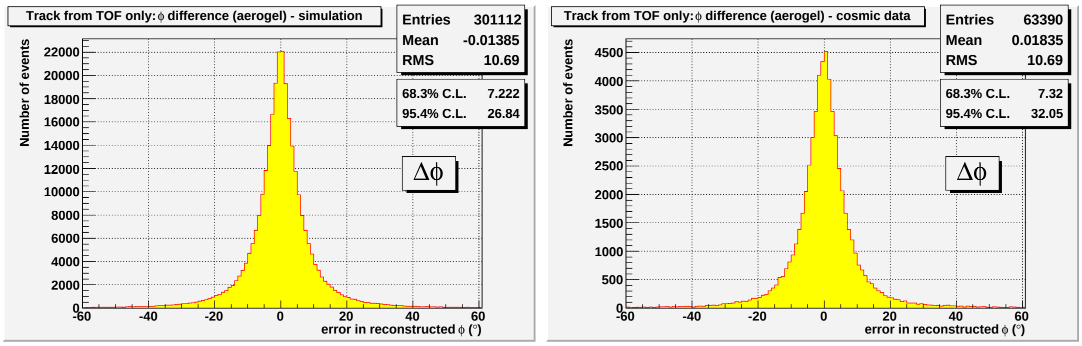

Figure 9.21: *Difference in azimuthal angle ϕ between TOF-based track (type I) and Tracker track (aerogel events): (left) AMS simulation; (right) Cosmic data.*

The evolution of the results obtained for ϕ as function of the number of ring hits is shown in Fig. 9.22 (top). In simulation an improvement in reconstruction quality is seen as the number of hits increases. Results for cosmic data show some degradation which is more significant for events with a higher number of hits, leading to a degradation of reconstruction quality beyond 7 hits.

The variation of ϕ reconstruction quality as function of particle inclination (given by the Tracker) is presented in Fig. 9.22 (centre). Results are slightly better in simulation and improve as particle inclination increases, as expected. In both simulation and data, the 68.3% percentile falls below 10° for $\theta > 15°$ and below 5° for $\theta > 30°$.

Results of ϕ reconstruction quality as function of the radius of the particle's crossing point at the radiator are presented in Fig. 9.22 (bottom). Reconstruction quality is better for events crossing the outer part of the radiator. Tails are much smaller for high radii. The main difference between simulation and data is in inner events ($r \lesssim 35$ cm) for which there are significantly longer tails in real data.

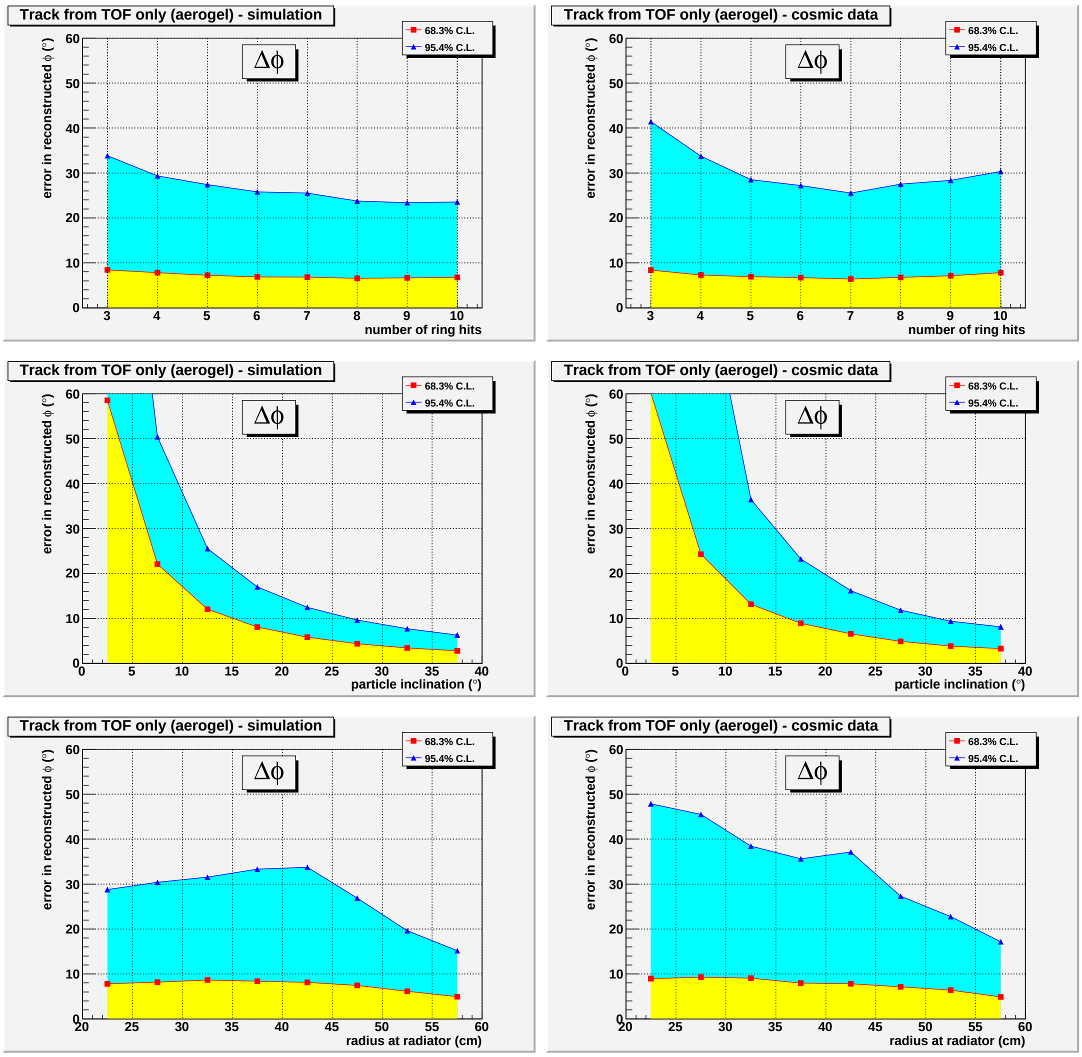

Figure 9.22: *Contours for ϕ difference between TOF (type I) and Tracker tracks as function of (top) ring hits, (centre) track inclination and (bottom) radius of radiator impact point (aerogel events): (left) AMS simulation; (right) Cosmic data.*

Čerenkov angle

Figure 9.23 shows the results obtained for the Čerenkov angle θ_c. Good results are obtained for most events. The distribution of the reconstruction error shows a main peak at zero and a secondary bump to the right at 1°-2°. This bump is more significant in real data than in simulation. As a result, the median for $\Delta\theta_c$ is positive in both cases: +0.17° in simulation and +0.38° in cosmic data. The 68.3% confidence region has a half-width of 1.15° in simulation and 1.51° in data. In addition, results have a significant tail on the right-hand side of the distribution, especially in the case of cosmic data: the 95.4% confidence region extends up to 6.4° in simulation and up to 12.7° in cosmics. This tail corresponds essentially to aerogel events being mistakenly reconstructed as NaF events, where Čerenkov angles can be much higher (up to $\simeq 41°$ compared to $\simeq 18°$ in aerogel).

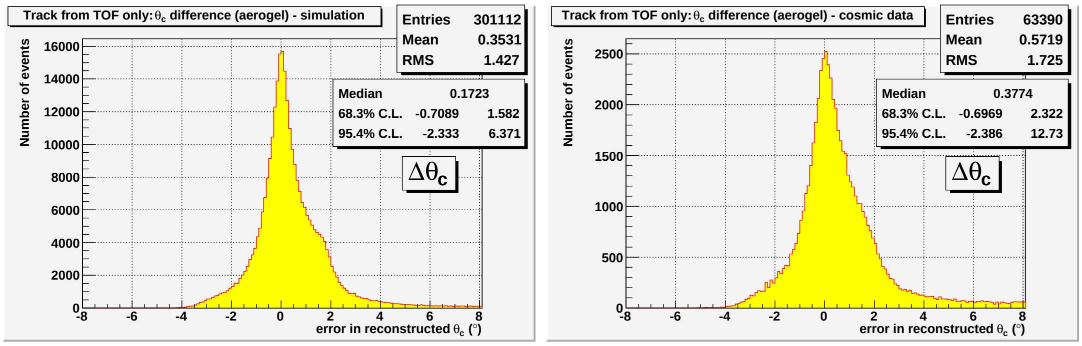

Figure 9.23: *Difference in Čerenkov angle θ_c between TOF-based track (type I) and Tracker track (aerogel events): (left) AMS simulation; (right) Cosmic data.*

The evolution of the results obtained for θ_c as function of the number of ring hits is shown in Fig. 9.24 (top). In the simulation case there is an improvement in the reconstruction quality as the number of hits increases, as expected. For 8-10 hits a slight increase is seen in the tail width, however. For cosmic data the improvement with the number of hits is not as strong and the peak region itself starts to become wider for a number of hits greater than 8. In this case the tail width remains approximately constant, showing that it is not sensitive to the number of hits.

The variation of θ_c reconstruction quality as function of particle inclination (given by the Tracker) is presented in Fig. 9.24 (centre). In the simulation case, the peak width is essentially constant except in the case of very small inclinations where it becomes slightly larger. The main change is seen in the right-hand tail, which decreases with inclination. For $\theta \simeq 0°$ the 95.4% confidence region is extended up to a difference of $\simeq 20°$, meaning that a significant number of events is mistanekly reconstructed as coming from the NaF region. In cosmic data the main change with respect to simulation is the greater importance of the right-hand tail, which leads to the 95.4% confidence region extending beyond $+20°$ for $\theta < 20°$.

Results of θ_c reconstruction quality as function of the radius of the particle's crossing point at the radiator are presented in Fig. 9.24 (bottom). Again, the main variations occur in the right-hand tail. In simulation a very long tail appears for events at inner positions, that is, with tracks closer to the NaF region and therefore more prone to being assigned to the wrong radiator. For the remaining distances the tail reaches its maximum length at intermediate radii (40-45 cm). Cosmic data have a similar behaviour, although the right-hand tail has a greater importance, the lower quality reconstruction at intermediate radii having an effect in the width of the peak region itself.

Position at radiator

Figure 9.25 shows the results obtained for the error in the particle crossing point at the top of the radiator, Δr_{rad}. A resonable agreement is obtained between the reference track given by the Tracker and the TOF-based track. Typical errors are up to 8 cm. In simulation the 68.3% percentile is at 4.43 cm, while in real data it is at 4.92 cm. The tail of the distribution is more important in the case of data: the 95.4% percentile is at 8.60 cm in simulated events and at 12.52 cm in cosmic data.

The evolution of the results obtained for Δr_{rad} as function of the number of ring hits is shown in Fig. 9.26 (top). In simulated events a slight improvement is seen as the number of hits increases, the 68.3% percentile moving from $\simeq 5$ cm for 3 hits to $\simeq 4$ cm for 9-10 hits. A visible improvement is observed in tails between 3 and 6 hits, leading to a significant reduction in the 95.4% percentile. In this case there is no visible change beyond 6 hits. In the case of real data a slight improvement is observed for the central peak only up to 6 hits, and tails only improve between 3 and 5 hits. Further increases in the number of hits show a degradation similar to what was observed in other variables, indicating that noise is being introduced.

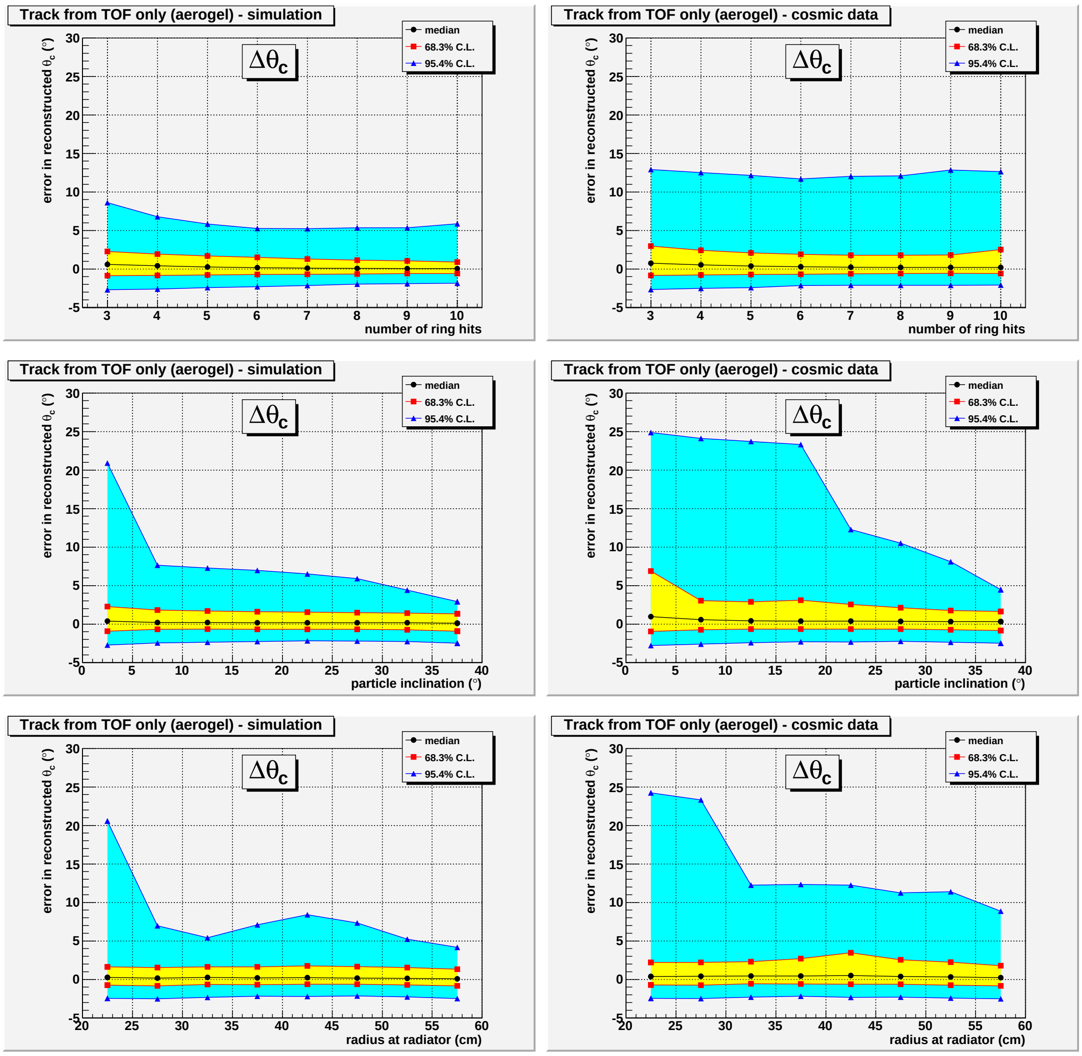

Figure 9.24: *Contours for θ_c difference between TOF (type I) and Tracker tracks as function of (top) ring hits, (centre) track inclination and (bottom) radius of radiator impact point (aerogel events): (left) AMS simulation; (right) Cosmic data.*

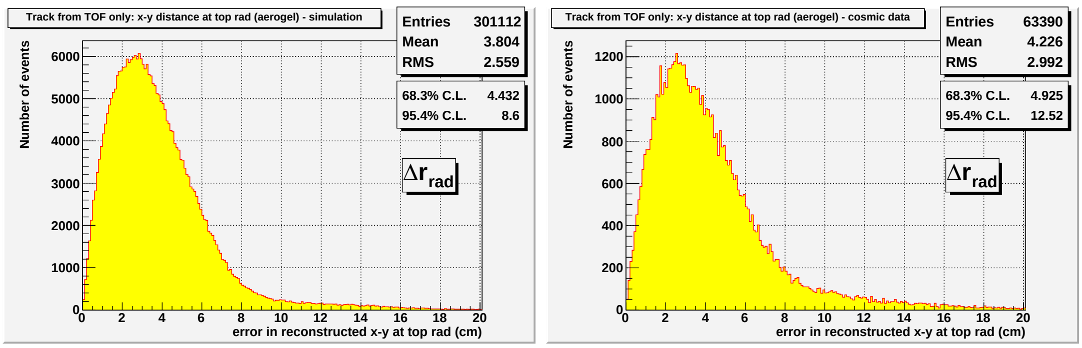

Figure 9.25: *Distance along in the x-y plane between TOF-based track (type I) and Tracker track at the top of the radiator (aerogel events): (left) AMS simulation; (right) Cosmic data.*

The variation of Δr_{rad} as function of particle inclination (given by the Tracker) is presented in Fig. 9.26 (centre). Reconstruction quality for the radiator position is clearly a function of inclination, with the best results being obtained for high inclinations. The main difference between simulation and data results is the longer spread of the distribution tail in data. For high inclinations (30°-40°) the 68.3% percentile is at $\simeq 4$ cm in simulation and $\simeq 4.5$ cm in data.

Results of Δr_{rad} as function of the radius of the particle's crossing point at the radiator are presented in Fig. 9.26 (bottom). There are no major changes in the peak width as function of radius, although results are slightly poorer for the outer part of the radiator ($r > 40$ cm). Tails are more important for intermediate radii (35-50 cm), this feature being more evident in the simulation case. Inner events are more affected by the increase in noise from simulation to data.

Position at detection matrix

Figure 9.27 shows the results obtained for the error in the particle crossing point at the detection matrix, Δr_{LG}. A reasonable agreement between the reference distribution from the Tracker and the TOF-based distribution is obtained. In both simulation and data, the distribution has a peak at small distances (< 1 cm) but extends towards much bigger distances, with tails beyond ~ 10 cm being more important in the case of data. The 68.3% percentile is at 3.07 cm in simulation and at 4.16 cm in data, while the 95.4% percentile changes from 10.8 cm in simulation to 18.6 cm in data, showing that a non-negligible fraction of events have very poor reconstructions.

The evolution of the results obtained for Δr_{LG} as function of the number of ring hits is shown in Fig. 9.28 (top). In simulation, the quality of the peak region increases steadily from 3 to 10 hits, with the 68.3% percentile reaching $\simeq 2$ cm for 10 hits. For high numbers of hits some degradation is seen in tails, however, with the position of the 95.4% percentile starting to increase beyond 7 hits. In cosmic data the best results for the 68.3% percentile are reached for 7-9 hits ($\simeq 3$ cm), while optimal results for tails are obtained for 5 hits, the behaviour of the tails being very similar to what was observed for the error at the top of the radiator.

The variation of Δr_{LG} as function of particle inclination (given by the Tracker)

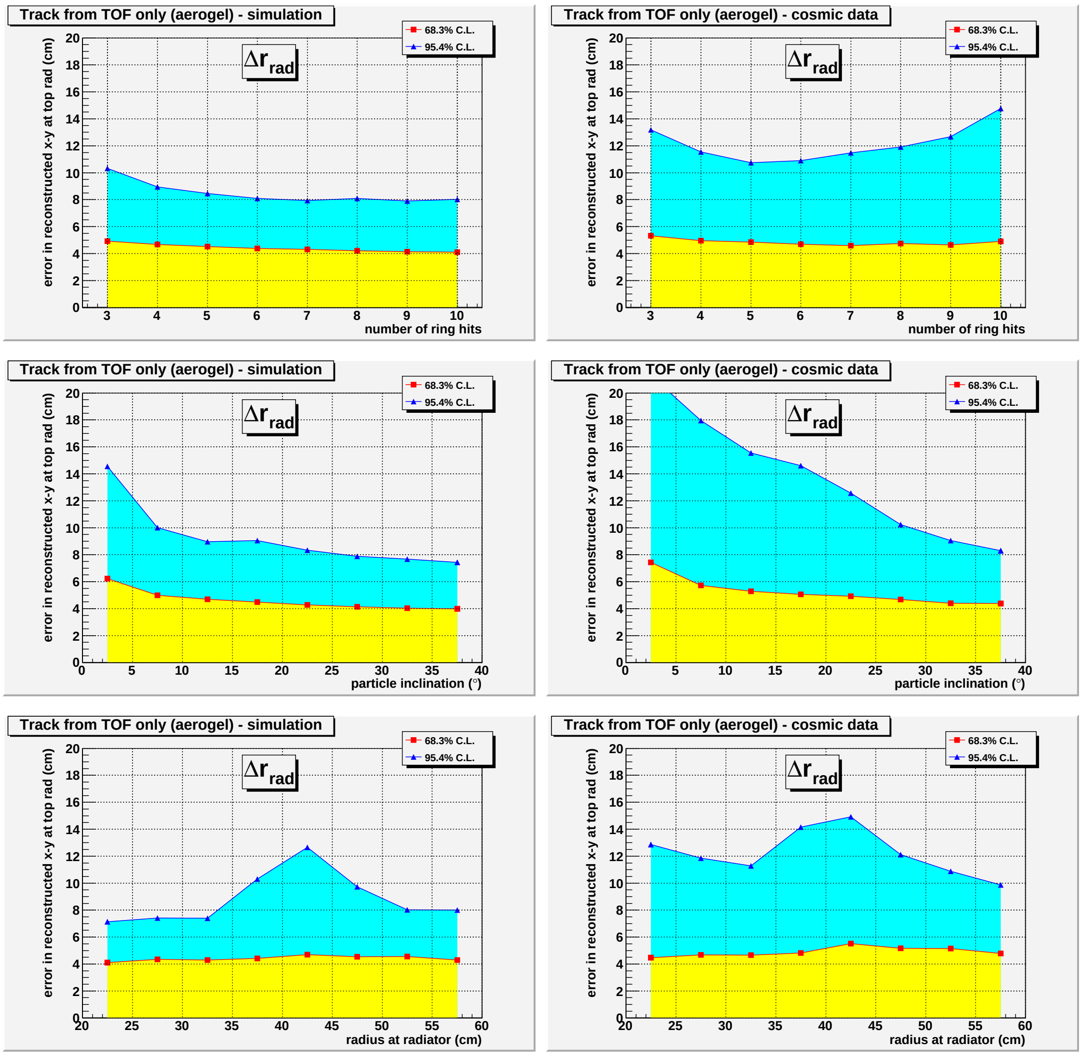

Figure 9.26: *Contours for x-y distance at the top of the radiator between TOF (type I) and Tracker tracks as function of (top) ring hits, (centre) track inclination and (bottom) radius of radiator impact point (aerogel events): (left) AMS simulation; (right) Cosmic data.*

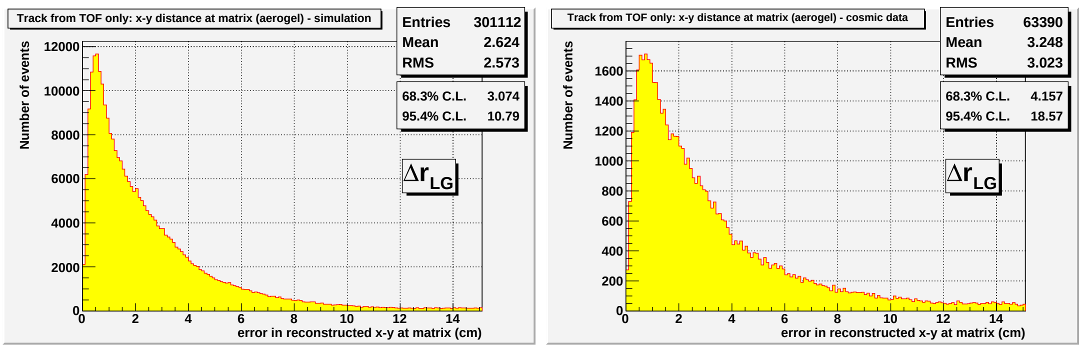

Figure 9.27: *Distance in the x-y plane between TOF-based track (type I) and Tracker track at the detection matrix (aerogel events): (left) AMS simulation; (right) Cosmic data.*

is presented in Fig. 9.28 (centre). The peak width, as evaluated from the 68.3% percentile, is very stable, with a slight increase with inclination, with the exception of very small inclinations ($\theta < 5°$) where there is a clear degradation. The distribution's tails become smaller as inclination increases. Similar results are observed in cosmic data, but with much longer tails. The difference between the simulation and data tails becomes smaller as inclination increases.

Results of Δr_{LG} as function of the radius of the particle's crossing point at the radiator are presented in Fig. 9.28 (bottom). The behaviour observed is similar to what was seen for the position at the top of the radiator: results in the peak region are better for the inner part of the radiator ($r < 40$ cm), while tails in simulation are longer at intermediate radii (35-50 cm), an effect that is partially hidden in data by the greater increase in tails at low radii.

9.4.1.2 NaF events

Track precision

Figure 9.29 shows the results obtained for the angle α between the reconstructed track and the reference track given by the AMS Tracker. In the simulation case, a good agreement is obtained between the Tracker and TOF-based tracks, with the distribution in α essentially ending at 8°. The 68.3% and 95.4% percentiles are at 2.64° and 5.54°, respectively. These results are better than those obtained for aerogel (3.36° and 5.97°). In the case of cosmic data, however, there is a significant drop in reconstruction quality, with a long tail appearing: the 68.3% and 95.4% percentiles are at 4.46° and 21.8°, respectively, a result that is slightly inferior to the aerogel result in the case of the first percentile (3.66°) and much poorer in the second case (8.26° in aerogel). This implies that a significant fraction of events have bad reconstructions.

Particle inclination

Figure 9.30 shows the results obtained for the particle inclination θ. Like in aerogel events, the distribution of $\Delta\theta$ is slightly shifted to the right, with the median at +0.15° in simulation and +0.27° in data. In simulation the reconstruction quality is

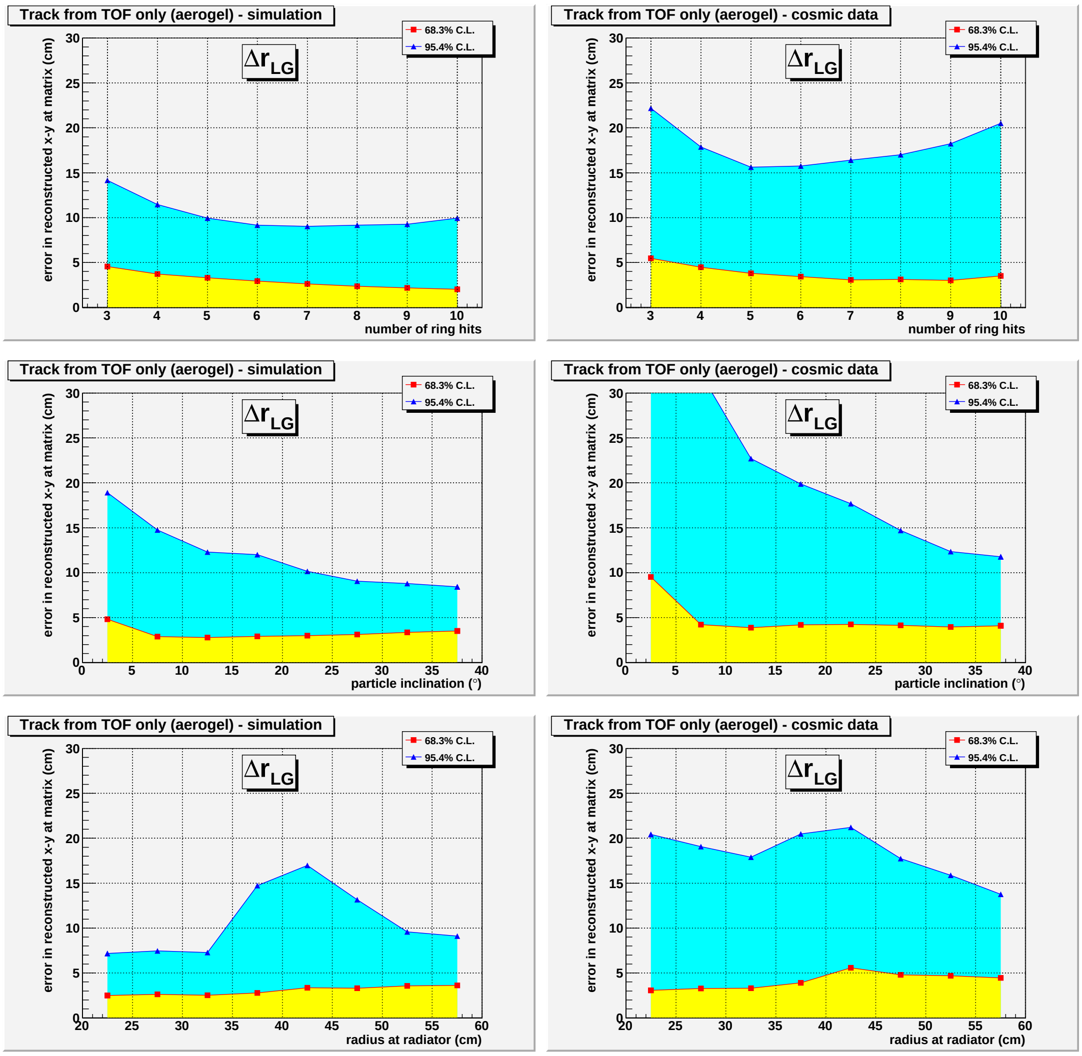

Figure 9.28: *Contours for x-y distance at the detection matrix difference between TOF (type I) and Tracker tracks as function of (top) ring hits, (centre) track inclination and (bottom) radius of radiator impact point (aerogel events): (left) AMS simulation; (right) Cosmic data.*

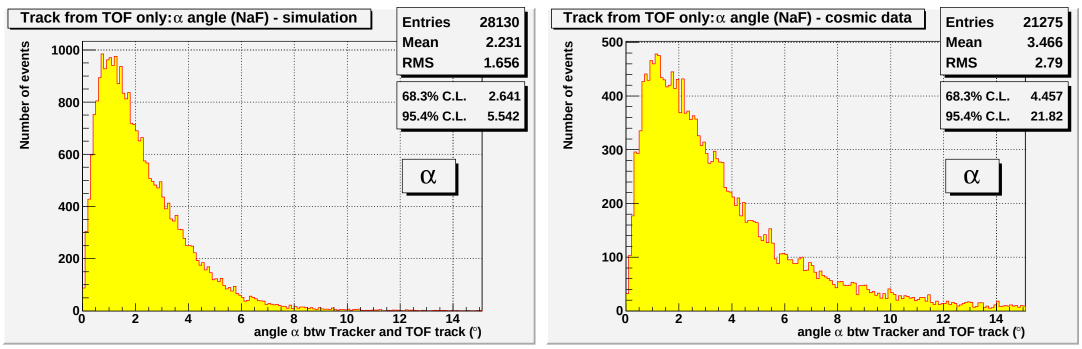

Figure 9.29: *Angle α between TOF-based track (type I) and Tracker track (NaF events): (left) AMS simulation; (right) Cosmic data.*

generally good, with a slightly better quality than in aerogel events: half-widths for the 68.3% and 95.4% confidence regions are 1.89° and 4.39° (compared to 2.08° and 4.53° in aerogel). In real data there is still a good central peak, with a half-width of 2.70° for the 68.3% confidence region (compared to 2.30° in aerogel) but the tails of bad reconstructions make the 95.4% confidence region extend from −15.7° to +6.1°.

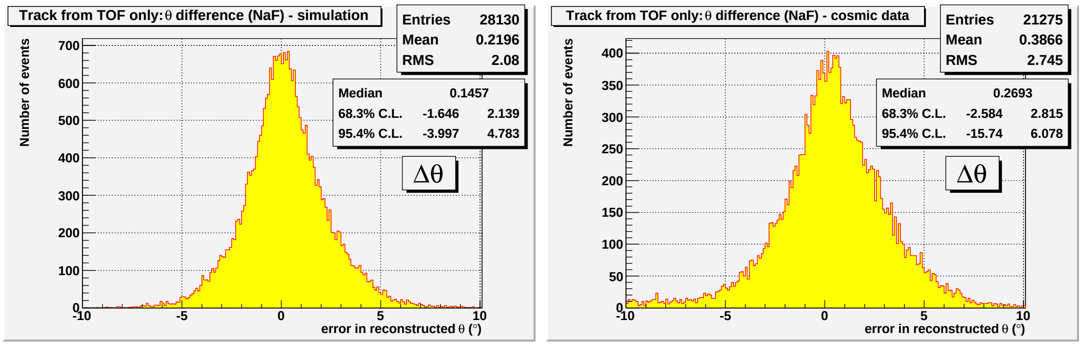

Figure 9.30: *Difference in inclination θ between TOF-based track (type I) and Tracker track (NaF events): (left) AMS simulation; (right) Cosmic data.*

Azimuthal angle

Figure 9.31 shows the results obtained for the azimuthal angle ϕ. In simulation a good reconstruction is seen, with a result that is better than the one from aerogel. Results for the 68.3% and 95.4% percentiles in $\Delta\phi$ are 5.84° and 22.8°, respectively (compared to 7.22° and 26.8° in aerogel). In cosmic data a significant fraction of events have bad results: the 68.3% percentile is at 17.4° and the 95.4% percentile is at 105°.

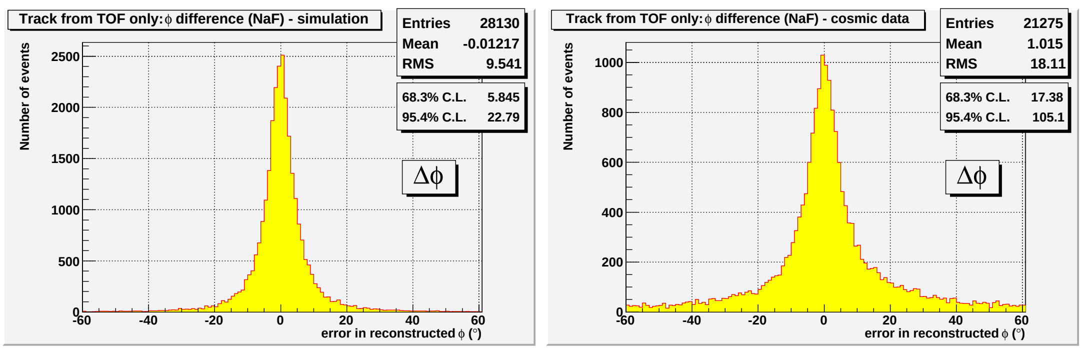

Figure 9.31: *Difference in azimuthal angle ϕ between TOF-based track (type I) and Tracker track (NaF events): (left) AMS simulation; (right) Cosmic data.*

Čerenkov angle

Figure 9.32 shows the results obtained for the Čerenkov angle θ_c. In simulation there is a good agreement between the angle obtained from the standard LIP reconstruction and the result of ring reconstruction from the TOF-based track. A slight bias is observed, with the median being at $\Delta\theta_c = +0.27°$. The overwhelming majority of events have errors smaller than 4°. The 68.3% and 95.4% confidence regions for $\Delta\theta_c$ have half-widths of 1.36° and 4.54°, respectively, the latter being affected by a small tail on the right-hand side of the distribution. In cosmic data the main change is the significant increase in the right-hand tail, which leads to a degradation in results: the median of the distribution moves to +0.55° and the half-widths of the 68.3% and 95.4% confidence regions are now 1.76° and 8.37°, respectively.

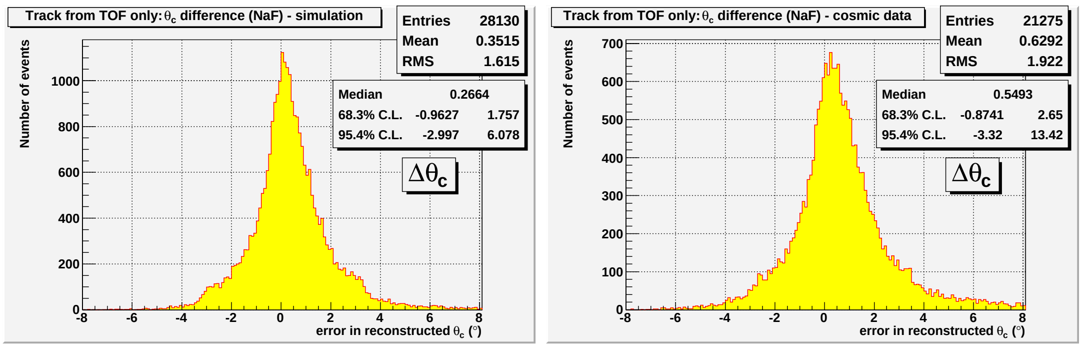

Figure 9.32: *Difference in Čerenkov angle θ_c between TOF-based track (type I) and Tracker track (NaF events): (left) AMS simulation; (right) Cosmic data.*

Position at radiator

Figure 9.33 shows the results obtained for the error in the particle crossing point at the top of the radiator, Δr_{rad}. In the case of simulation good results are generally obtained. The 68.3% and 95.4% percentiles are at 4.46 cm and 8.11 cm, respectively, a result similar to what was obtained in aerogel (4.43 cm and 8.60 cm). In real data results are clearly poorer, with the 68.3% and 95.4% percentiles being placed at 5.74 cm and 10.4 cm.

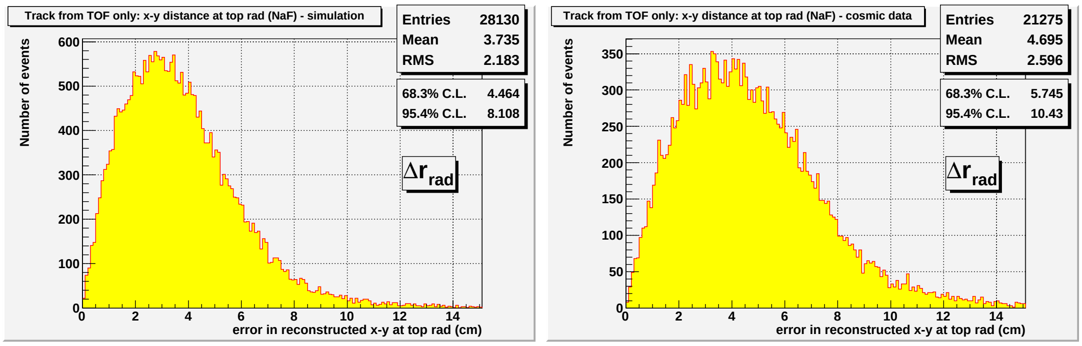

Figure 9.33: *Distance along in the x-y plane between TOF-based track (type I) and Tracker track at the top of the radiator (NaF events): (left) AMS simulation; (right) Cosmic data.*

Position at detection matrix

Figure 9.34 shows the results obtained for the error in the particle crossing point at the detection matrix, Δr_{LG}. In simulation good results are obtained for most events, with the 68.3% percentile being placed at 4.40 cm. A significant tail is present, however, and the 95.4% percentile is at 9.74 cm. When compared to the aerogel case, the peak region is wider (in aerogel the 68.3% percentile is at 3.07 cm) but the tails are smaller (the 95.4% percentile is at 10.8 cm in aerogel). In the case of real events there is a significant degradation of reconstruction quality, with the 68.3% percentile being placed at 7.77 cm and the much larger tails moving the 95.4% percentile to 25.9 cm.

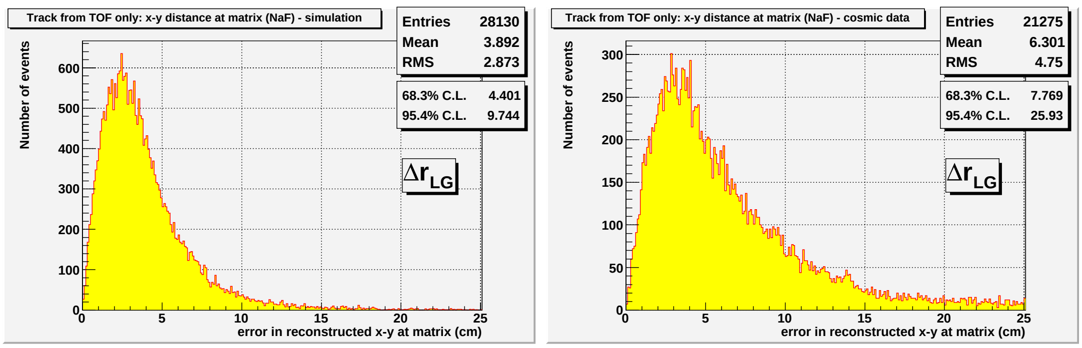

Figure 9.34: *Distance in the x-y plane between TOF-based track (type I) and Tracker track at the detection matrix (NaF events): (left) AMS simulation; (right) Cosmic data.*

9.4.2 Type II: upper TOF + lower TOF + RICH matrix

9.4.2.1 Aerogel events

Track precision

Figure 9.35 shows the results obtained for the angle α between the reconstructed track and the reference track given by the AMS Tracker. A good reconstruction is obtained. In simulated events the 68.3% percentile is placed at 1.71°. The tail of the distribution is not very long, with the 95.4% percentile placed at 3.67°. In cosmic data there is some increase in the peak width and tails, but the results obtained are still good: the 68.3% and 95.4% percentiles are reached at 2.12° and 4.88°, respectively.

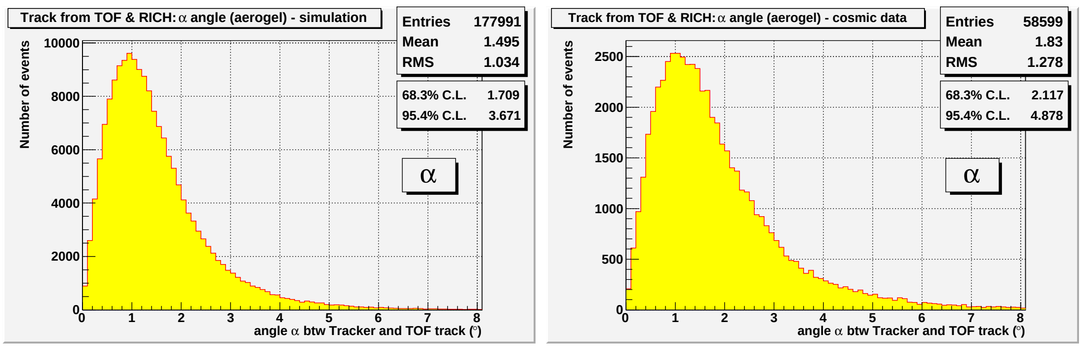

Figure 9.35: *Angle α between TOF-based track (type II) and Tracker track (aerogel events): (left) AMS simulation; (right) Cosmic data.*

The evolution of the results obtained for α as function of the number of ring hits is shown in Fig. 9.36 (top). A steady improvement in track quality is seen as the number of hits increases, both in simulation and in cosmic data. In the case of simulation the 68.3% percentile improves from $\simeq 1.9°$ for 3 hits to $\simeq 1.6°$ for 9-10 hits, while the 95.4% percentile improves from $\simeq 4.5°$ to $\simeq 3.2°$. For cosmic data the 68.3% percentile improves from $\simeq 2.4°$ to $\simeq 1.9°$, while 95.4% percentile improves from $\simeq 5.5°$ to $\simeq 4.2°$ as the number of ring hits increases from 3 to 10.

The variation of α as function of particle inclination (given by the Tracker) is presented in Fig. 9.36 (centre). There is a general tendency for an improvement in reconstruction quality as inclination increases, but for very high inclinations ($> 35°$) there is a significant increase in tails. The degradation of the reconstruction quality seen between simulation and data is more important for small inclinations (up to 10°).

Results of α as function of the radius of the particle's crossing point at the radiator are presented in Fig. 9.36 (bottom). Reconstruction results do not show large variations as function of radius, although the quality of reconstructions is slightly better for inner events. In cosmic data a sharp increase in tails is seen for events close to the outer edge of the radiator ($r > 55$ cm).

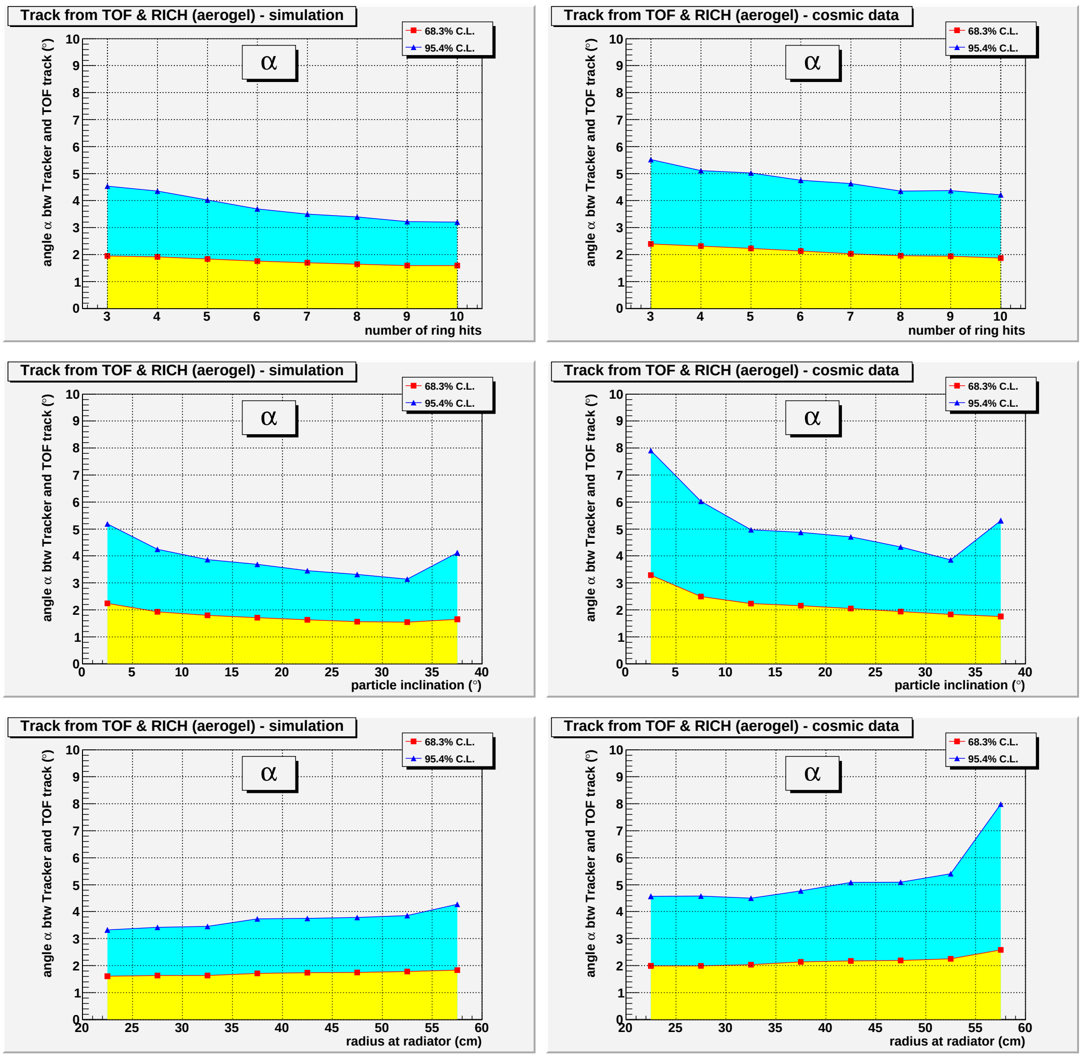

Figure 9.36: *Contours for angle α between TOF (type II) and Tracker tracks as function of (top) ring hits, (centre) track inclination and (bottom) radius of radiator impact point (aerogel events): (left) AMS simulation; (right) Cosmic data.*

Particle inclination

Figure 9.37 shows the results obtained for the particle inclination θ. This reconstruction provides a very good estimator for particle inclination in both simulation and data: the estimator is almost unbiased, with the median of the error distribution $\Delta\theta$ being placed at 0.00° in simulation and at +0.04° in the case of cosmic data. There are no long tails in the distribution. The right-hand tail is slightly longer, introducing a very small asymmetry in the shape of the peak. Reconstruction quality is slightly better in simulation than in data: in simulated events the half-widths for the 68.3% and 95.4% confidence regions are 1.07° and 2.66°, respectively, while in cosmic data the half-widths are 1.32° and 3.43°.

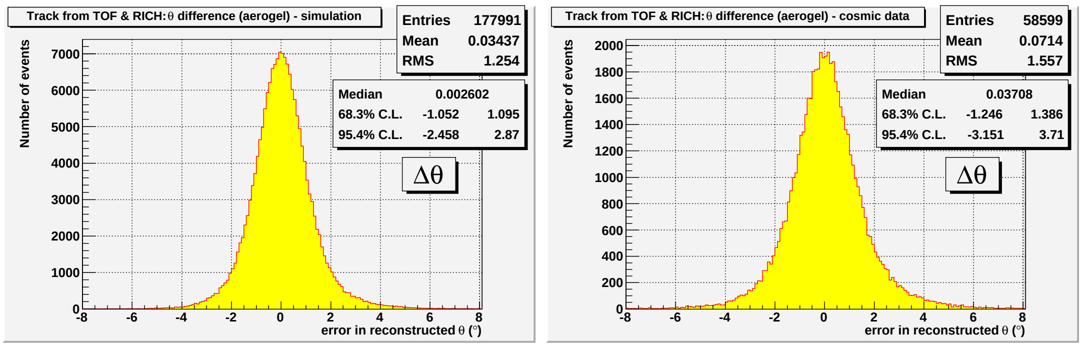

Figure 9.37: *Difference in inclination θ between TOF-based track (type II) and Tracker track (aerogel events): (left) AMS simulation; (right) Cosmic data.*

The evolution of the results obtained for θ as function of the number of ring hits is shown in Fig. 9.38 (top). In both simulation and data the quality of the reconstruction improves slightly as the number of hits increases, but it is already very good for the case of 3 hits, with half-widths for the 68.3% confidence region of $\simeq 1.2°$ in simulation and $\simeq 1.5°$ in cosmic data.

The variation of θ reconstruction quality as function of particle inclination (given by the Tracker) is presented in Fig. 9.38 (centre). The main feature present in both simulation and data is the significant tail that appears at each end of the distribution, which is essentially a result of the limits in the space of possible reconstructions. Apart from this feature, there is a slight improvement in the reconstruction quality as θ increases.

Results of θ reconstruction quality as function of the radius of the particle's crossing point at the radiator are presented in Fig. 9.38 (bottom). The quality of the reconstruction is quite stable, although inner events have slightly better results. For events at the outer edge of the radiator ($r > 55$ cm) the left-hand tail becomes more important, especially in the data case, but this is essentially an edge effect similar to those seen when the reconstruction quality is plotted against particle inclination.

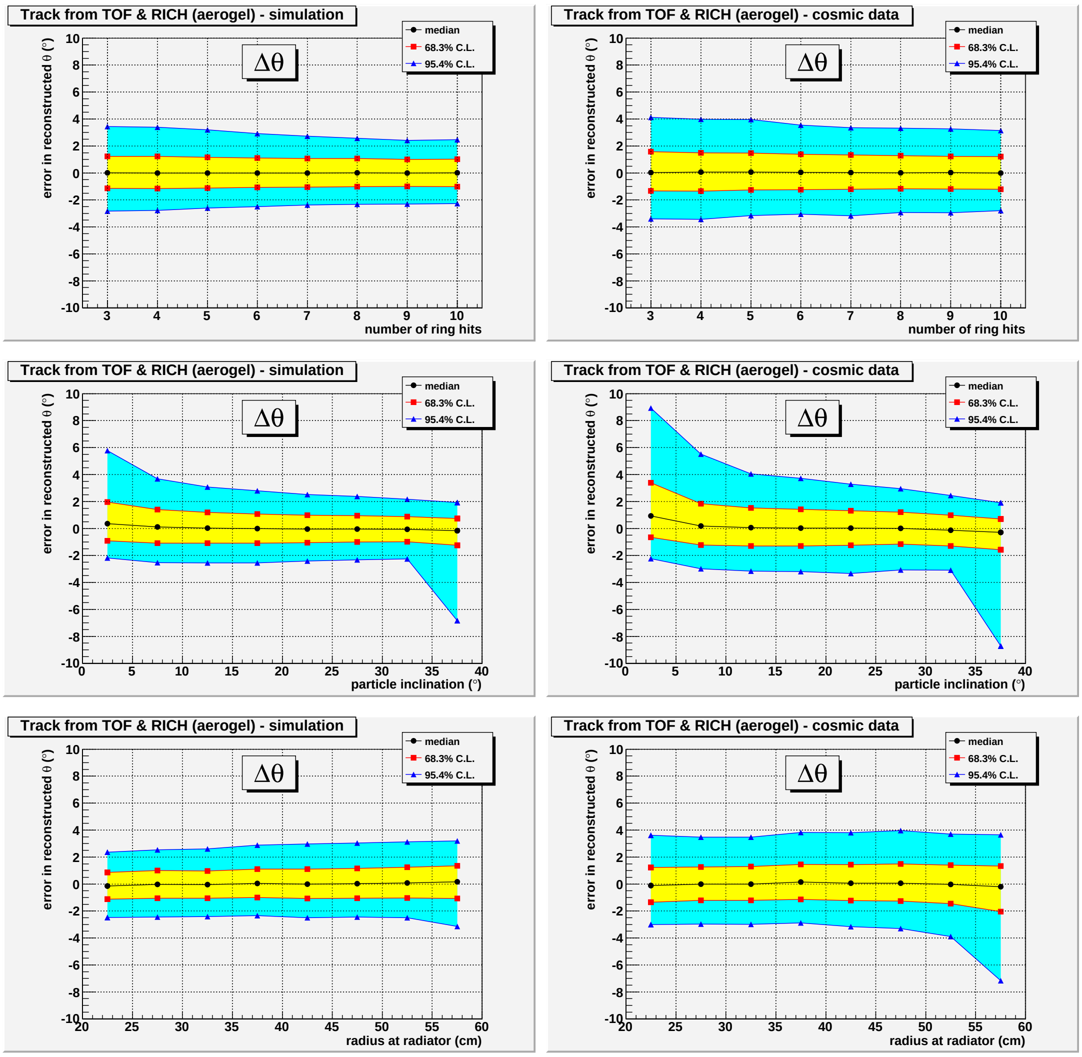

Figure 9.38: *Contours for θ difference between TOF (type II) and Tracker tracks as function of (top) ring hits, (centre) track inclination and (bottom) radius of radiator impact point (aerogel events): (left) AMS simulation; (right) Cosmic data.*

Azimuthal angle

Figure 9.39 shows the results obtained for the azimuthal angle ϕ. A good result is obtained in both simulation and data. In the case of simulation, the 68.3% and 95.4% percentiles are at 3.97° and 14.7°, while in cosmic data results are slightly poorer, with the same percentiles placed at 4.64° and 17.4°. In both cases only a negligible fraction of events has an error in ϕ greater than 20°, which means that the azimuthal angle is well reconstructed in almost all events.

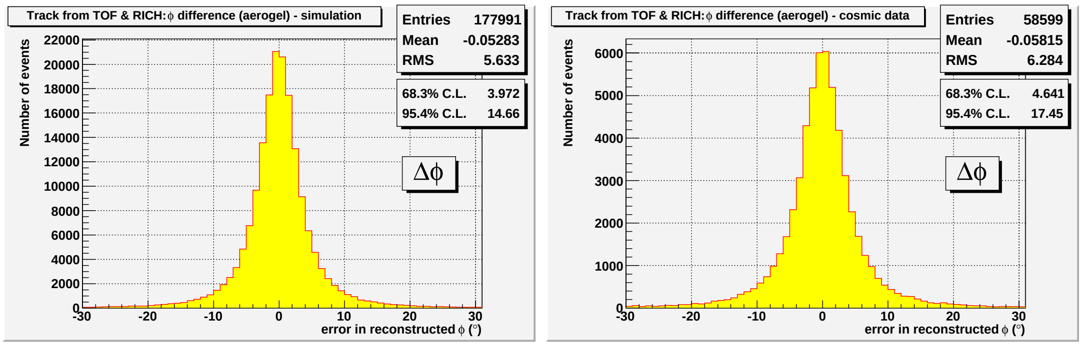

Figure 9.39: *Difference in azimuthal angle ϕ between TOF-based track (type II) and Tracker track (aerogel events): (left) AMS simulation; (right) Cosmic data.*

The evolution of the results obtained for ϕ as function of the number of ring hits is shown in Fig. 9.40 (top). In both simulation and data there is no major variation in peak width, and only a very slight reduction occurs as the number of hits increases. Some improvement is seen in tails, with the 95.4% percentile changing from $\simeq 17°$ to $\simeq 13°$ in simulation and from $\simeq 20°$ to $\simeq 14°$ in data as the number of hits increases from 3 to 10.

The variation of ϕ reconstruction quality as function of particle inclination (given by the Tracker) is presented in Fig. 9.40 (centre). There is an improvement in the quality of the reconstruction as inclination increases, as expected, in both simulation and data. For high inclinations the 68.3% percentile of the distribution is at $\simeq 2°$ in both cases.

Results of ϕ reconstruction quality as function of the radius of the particle's crossing point at the radiator are presented in Fig. 9.40 (bottom). The best results are obtained for inner events, where the 68.3% percentile of the distribution is at $\simeq 3°$ in both simulation and data. The reconstruction becomes poorer as the radius at radiator increases, reaching $\simeq 6°$ in simulation and $\simeq 8°$ in data for $r > 55$ cm. The tails of the distribution also tend to become larger as the radius increases, but the variation is not smooth: the increase in the 95.4% percentile occurs mostly around r = 30-35 cm, with two plateau regions above and below the transition zone.

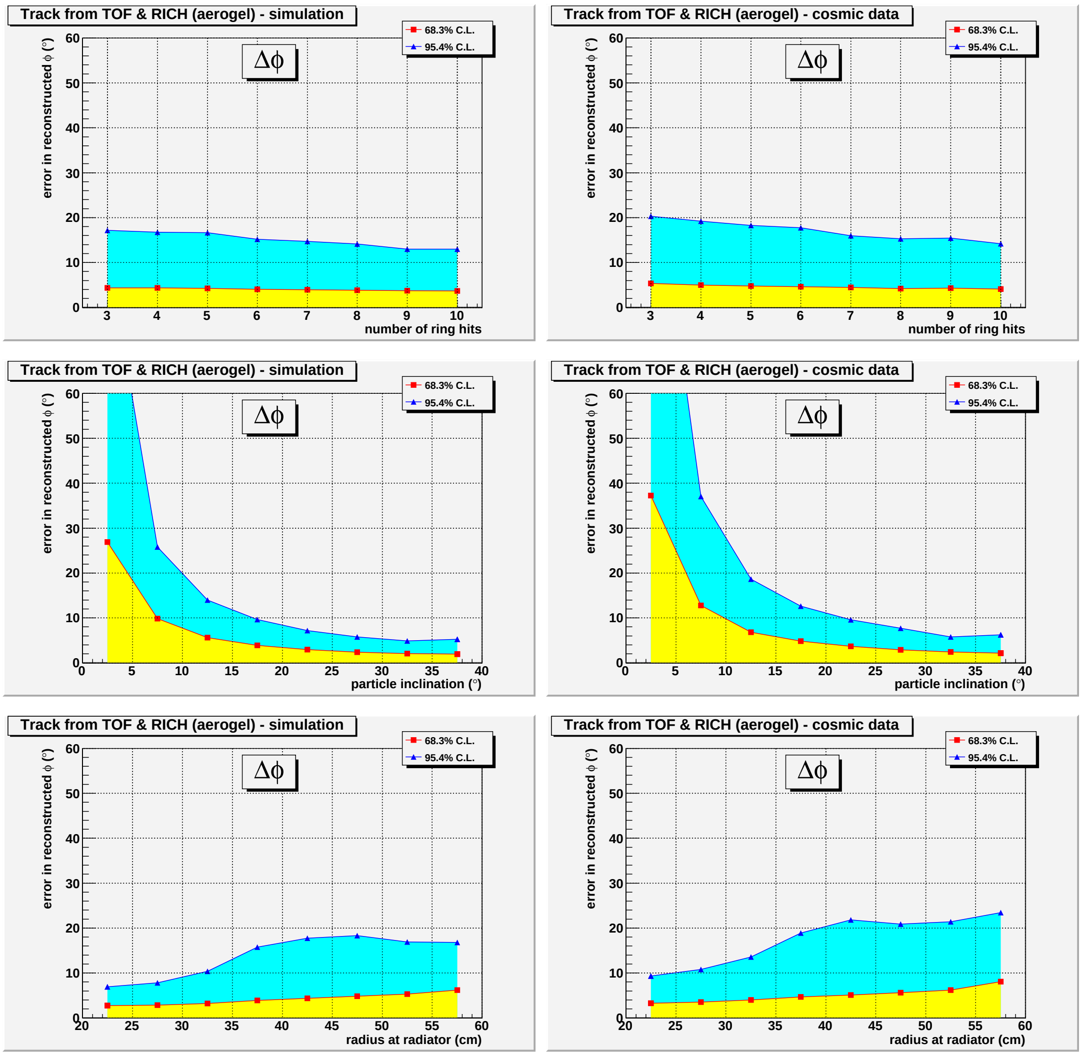

Figure 9.40: *Contours for ϕ difference between TOF (type II) and Tracker tracks as function of (top) ring hits, (centre) track inclination and (bottom) radius of radiator impact point (aerogel events): (left) AMS simulation; (right) Cosmic data.*

Čerenkov angle

Figure 9.41 shows the results obtained for the Čerenkov angle θ_c. A good reconstruction is obtained in simulation as well as in cosmic data. In simulation the peak in the reconstruction error $\Delta\theta_c$ is perfectly symmetric, but with slightly asymmetric tails: the right-hand tail is longer. In the case of cosmic data there is a more significant asymmetry, with larger tails and a small asymmetry visible in the peak itself. The median of the distribution is at $+0.03°$ in the simulation and at $+0.07°$ in data. The lower limits of confidence regions are only slightly changed from simulation to data, with the 68.3% limit moving from $-0.33°$ to $-0.39°$ and the 95.4% limit from $-1.16°$ to $-1.33°$. In the case of the upper limits, however, there are major changes: from $+0.54°$ to $+0.98°$ in the case of the 68.3% limit, and from $+3.84°$ to $+10.0°$ for the 95.4% limit, reflecting the significant increase in the right-hand tail.

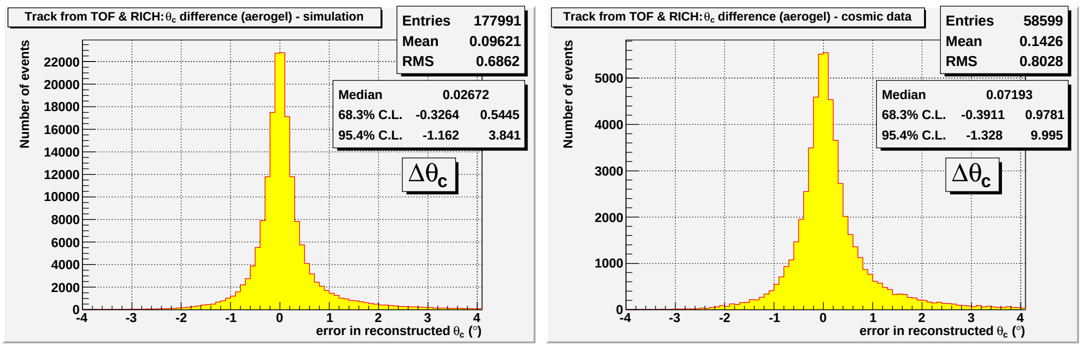

Figure 9.41: *Difference in Čerenkov angle θ_c between TOF-based track (type II) and Tracker track (aerogel events): (left) AMS simulation; (right) Cosmic data.*

The evolution of the results obtained for θ_c as function of the number of ring hits is shown in Fig. 9.42 (top). The main effect of an increase in the number of hits is the reduction of the right-hand tail of events, with the 68.3% confidence region becoming much more symmetric and, in the simulation case, the right-hand limit of the 95.4% confidence region dropping sharply. In cosmic data the 95.4% right-hand limit remains stable due to the more significant fraction of events with very high errors. The left-hand tail of the distribution is essentially unaffected by the increase in the number of hits.

The variation of θ_c reconstruction quality as function of particle inclination (given by the Tracker) is presented in Fig. 9.42 (centre). In the simulation case the reconstruction quality is quite stable, with a slight degradation at each end, except for the right-hand tail which becomes significantly larger for high inclinations ($\theta > 25°$). In the case of cosmic data the peak quality clearly improves from lower to higher inclinations, while the 95.4% right-hand limit remains at $\simeq 10°$ up to $\theta_c \simeq 35°$, after which it increases in a way similar to what is seen in the simulation case.

Results of θ_c reconstruction quality as function of the radius of the particle's crossing point at the radiator are presented in Fig. 9.42 (bottom). In the simulation case the reconstruction quality is essentially constant, with only a slight improvement seen as the radius increases. The only significant change as function of radius is on right-hand tail, with visible spikes in the 95.4% right-hand limit at r = 25-30 cm and $r > 55$ cm. In the case of real data the reconstruction quality is again stable as function of the radiator radius, with the exception of outer events ($r > 50$ cm) for which there is a clear degradation.

Position at radiator

Figure 9.43 shows the results obtained for the error in the particle crossing point at the top of the radiator, Δr_{rad}. A good reconstruction is obtained in both simulation and data, although a significant tail of poor reconstructions is present in the case of real data. In the simulation case the 68.3% and 95.4% percentiles are at 1.65 cm and 3.49 cm, respectively, while in real data the 68.3% percentile moves to 2.01 cm and the 95.4% percentile increases to 5.69 cm reflecting the presence of a long tail.

The evolution of the results obtained for Δr_{rad} as function of the number of ring hits is shown in Fig. 9.44 (top). The peak width is virtually independent of the number of hits, both in simulation and in cosmic data. The only visible change is a reduction in the tail of bad events which occurs essentially between 3 and 6 hits. This reduction is more important in the case of real data.

The variation of Δr_{rad} as function of particle inclination (given by the Tracker) is presented in Fig. 9.44 (centre). In the case of simulation the results are almost uniform, with intermediate inclinations having a slightly better result. For very high inclinations (above 35°) there is a significant increase in tail width. Real data show a similar behaviour, with an additional degradation seen for $\theta < 5°$.

Results of Δr_{rad} as function of the radius of the particle's crossing point at the radiator are presented in Fig. 9.44 (bottom). The peak width is essentially independent of the radiator radius, while for tails there is a visible increase at high radii ($r > 50$ cm in simulation and $r > 55$ cm in data).

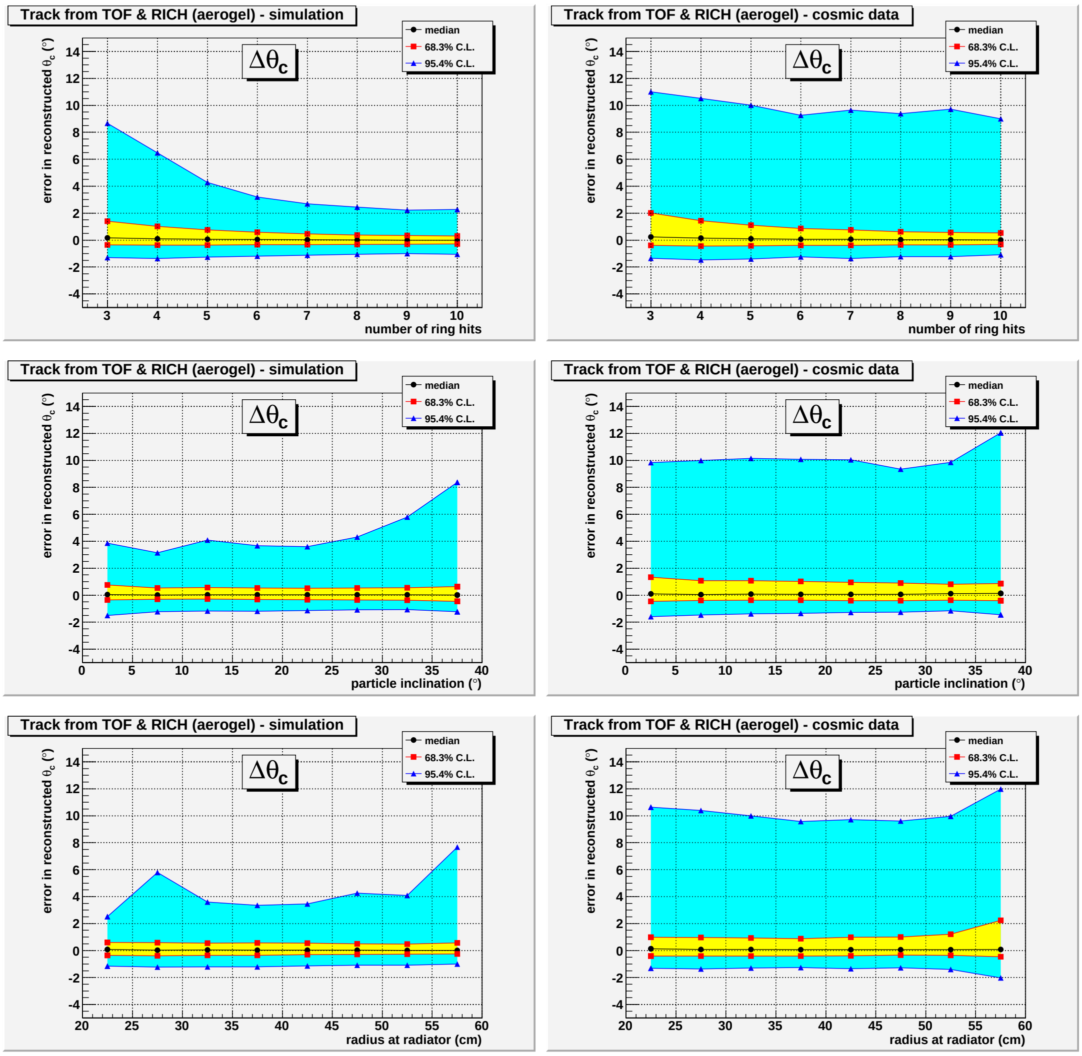

Figure 9.42: *Contours for θ_c difference between TOF (type II) and Tracker tracks as function of (top) ring hits, (centre) track inclination and (bottom) radius of radiator impact point (aerogel events): (left) AMS simulation; (right) Cosmic data.*

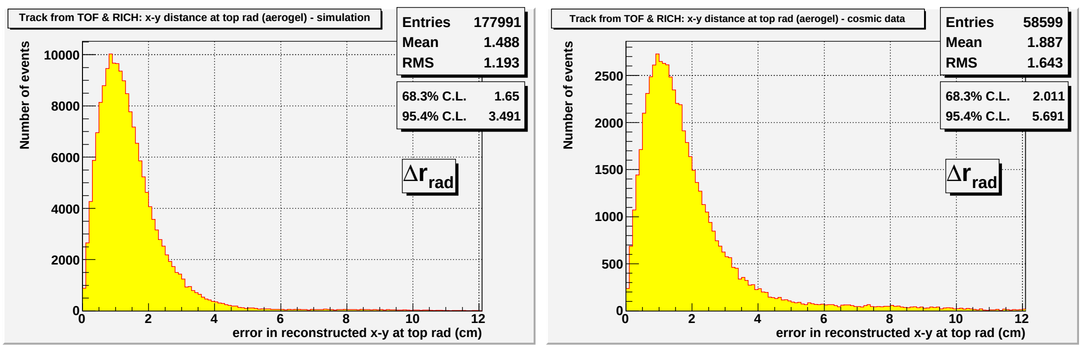

Figure 9.43: *Distance along in the x-y plane between TOF-based track (type II) and Tracker track at the top of the radiator (aerogel events): (left) AMS simulation; (right) Cosmic data.*

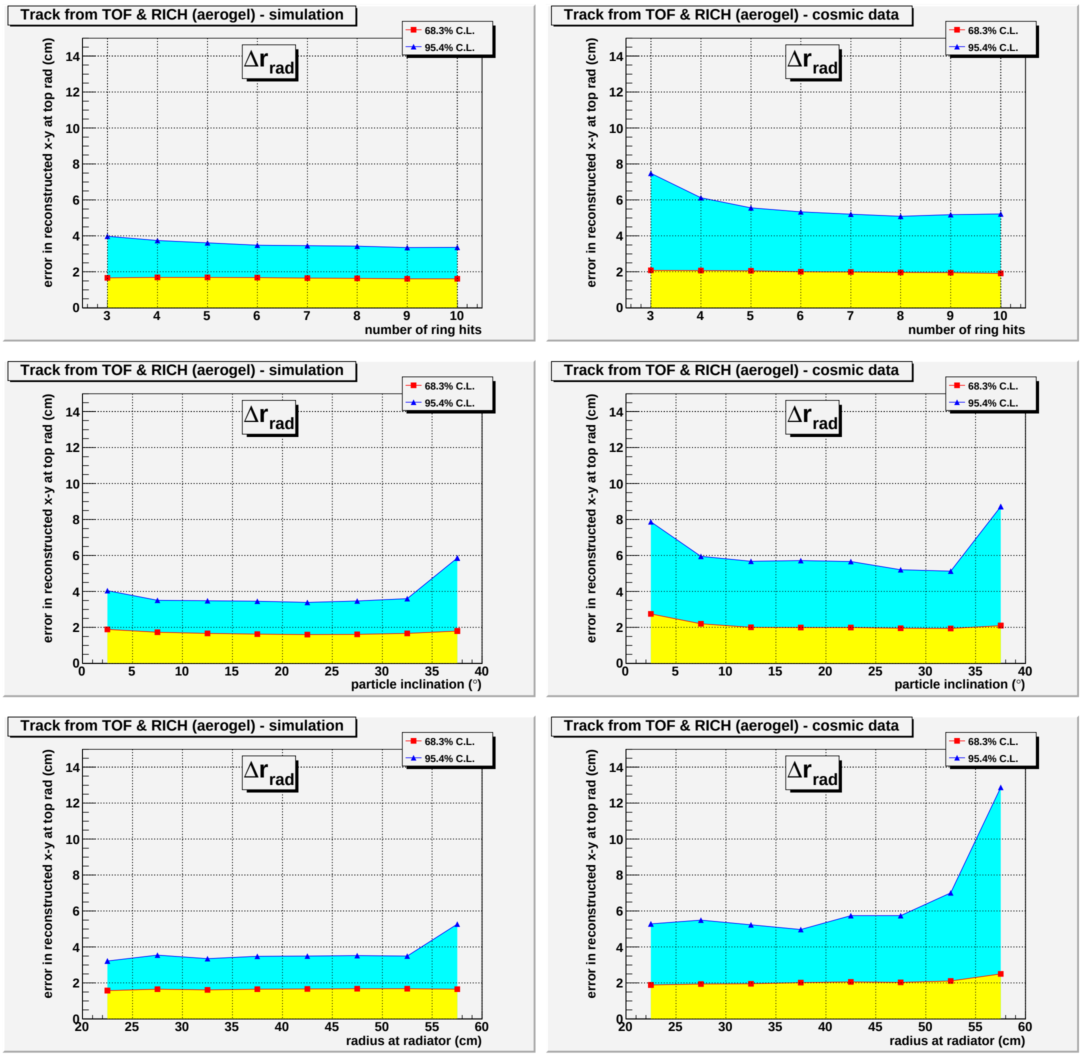

Figure 9.44: *Contours for x-y distance at the top of the radiator between TOF (type II) and Tracker tracks as function of (top) ring hits, (centre) track inclination and (bottom) radius of radiator impact point (aerogel events): (left) AMS simulation; (right) Cosmic data.*

Position at detection matrix

Figure 9.45 shows the results obtained for the error in the particle crossing point at the detection matrix, Δr_{LG}. Events are in general well reconstructed, with the overwhelming majority having errors not greater than a few cm. In the case of simulation the 68.3% and 95.4% percentiles are placed at 0.85 cm and 3.06 cm, respectively. Cosmic data have a slightly lower reconstruction quality, with the 68.3% percentile placed at 1.18 cm, and a more significant tail, moving the 95.4% percentile to 6.76 cm.

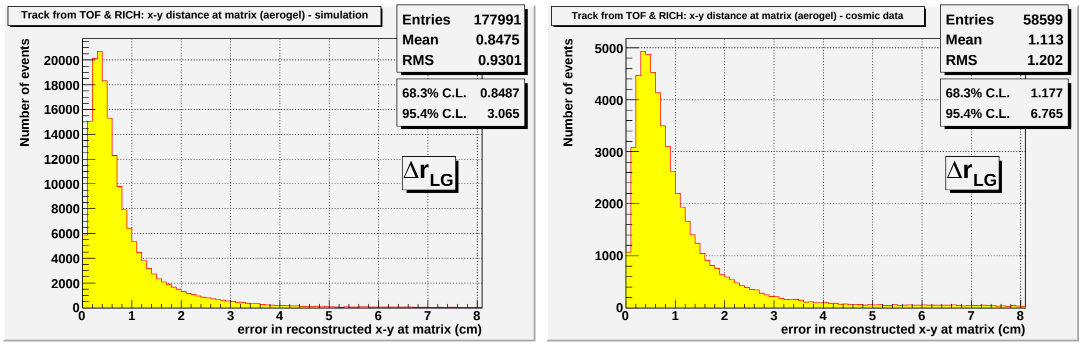

Figure 9.45: *Distance in the x-y plane between TOF-based track (type II) and Tracker track at the detection matrix (aerogel events): (left) AMS simulation; (right) Cosmic data.*

The evolution of the results obtained for Δr_{LG} as function of the number of ring hits is shown in Fig. 9.46 (top). There is a steady improvement of the reconstruction quality as the number of hits improves. In the case of simulated events the improvement is similar in the 68.3% and 95.4% percentiles, while in data the position of the 95.4% percentile becomes stable from 6 hits onwards, suggesting that a significant component of noisy events cannot be removed by simply adding more ring hits.

The variation of Δr_{LG} as function of particle inclination (given by the Tracker) is presented in Fig. 9.46 (centre). Results show that the results are essentially independent of particle inclination, with the exception of events with $\theta > 35°$ and, in the case of real data, also of events with $\theta < 5°$, where there is an increase in the importance of tails.

Results of Δr_{LG} as function of the radius of the particle's crossing point at the radiator are presented in Fig. 9.46 (bottom). The behaviour is similar to what was seen for Δr_{rad}, with an almost constant peak width and tails having only a significant increase at high radii ($r > 50$ cm in simulation and $r > 55$ cm in data).

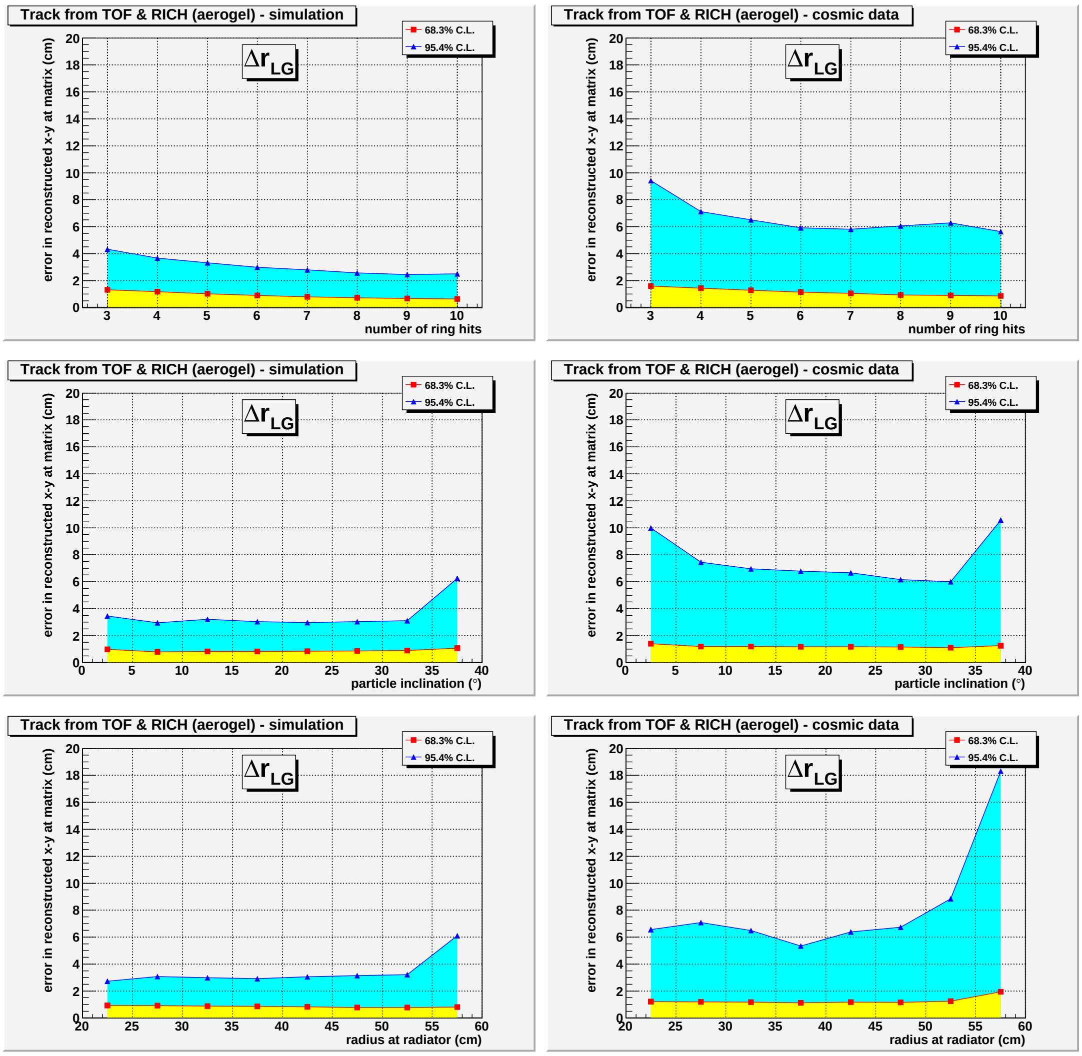

Figure 9.46: *Contours for x-y distance at the detection matrix difference between TOF (type II) and Tracker tracks as function of (top) ring hits, (centre) track inclination and (bottom) radius of radiator impact point (aerogel events): (left) AMS simulation; (right) Cosmic data.*

9.4.2.2 NaF events

Track precision

Figure 9.47 shows the results obtained for the angle α between the reconstructed track and the reference track given by the AMS Tracker. A good result is obtained for most events, but a long tail of bad reconstructions is present. In the case of simulation the 68.3% percentile is at 1.78°, while the 95.4% percentile is at 11.2°.

For cosmic data the main peak is wider, with the 68.3% percentile placed at 2.57°, but there is a slight improvement in tails, with the 95.4% percentile at 10.0°. The quality of the reconstruction is comparable to what was obtained for aerogel in terms of peak width (in aerogel the 68.3% percentile was at 1.71° and 2.12° for simulation and data, respectively) but the tails are much more important in NaF (the 95.4% percentiles for aerogel were 3.67° and 4.88°).

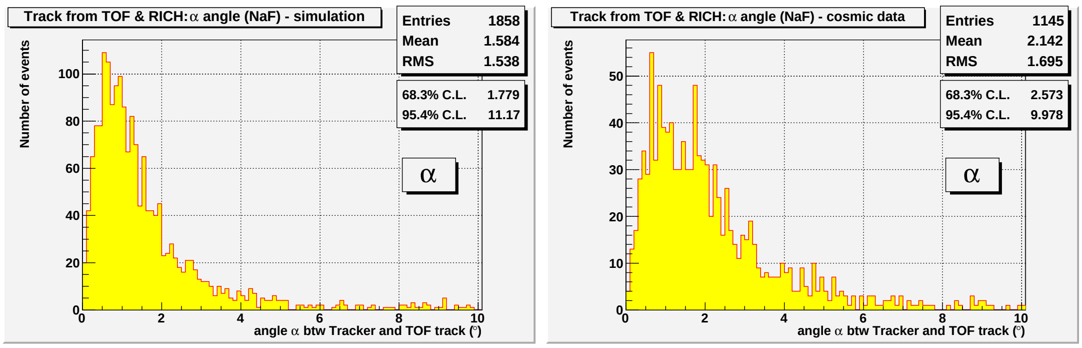

Figure 9.47: *Angle α between TOF-based track (type II) and Tracker track (NaF events): (left) AMS simulation; (right) Cosmic data.*

Particle inclination

Figure 9.48 shows the results obtained for the particle inclination θ. A good reconstruction quality is obtained in general, with a tail of poor reconstructions on the right-hand side of the peak. The peak itself is slightly biased: the median of the $\Delta\theta$ distribution is at +0.12° in simulation and at +0.36° in data. The peak is narrower in simulation, with half-widths for the 68.3% confidence region being 1.19° in simulation and 1.70° in the case of data, but the tails are similar in both cases. Half-widths for the 95.4% confidence region are 5.30° in simulation and 5.35° in data. Results are poorer than in aerogel in terms of peak width (half-widths for the 68.3% confidence region in aerogel were 1.07° in simulation and 1.32° in data) and in particular in tails, where the 95.4% confidence region is approximately twice as wide as in aerogel.

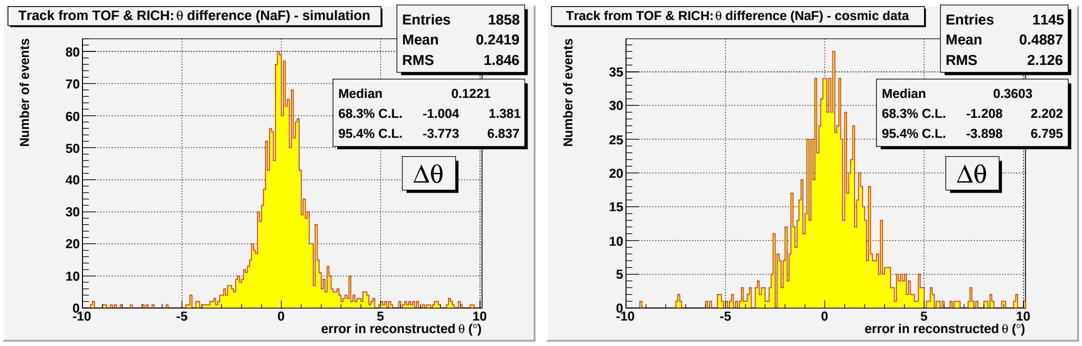

Figure 9.48: *Difference in inclination θ between TOF-based track (type II) and Tracker track (NaF events): (left) AMS simulation; (right) Cosmic data.*

Azimuthal angle

Figure 9.49 shows the results obtained for the azimuthal angle ϕ. Very good results are obtained in terms of peak width, with the 68.3% percentile placed at 2.46° in simulation and at 3.61° in cosmic data. Some tails are present, leading to a comparatively large 95.4% confidence region, with percentiles placed at 27.2° and 25.9° for simulation and data, respectively. Again, there is a clear degradation in the peak from simulation to data but similar tails in both cases. When compared to aerogel, these results are better in terms of peak width (in aerogel the 68.3% percentile is at 3.97° for simulation and 4.64° for data) but poorer in tails (the 95.4% percentiles in aerogel are 14.7° and 17.4°).

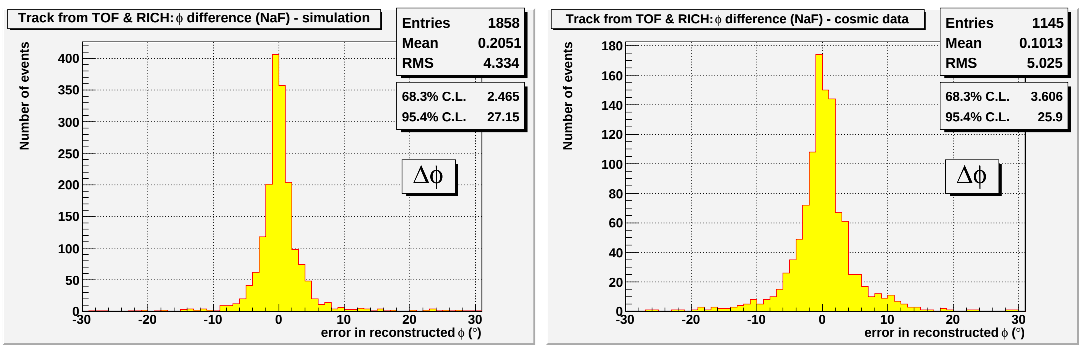

Figure 9.49: *Difference in azimuthal angle ϕ between TOF-based track (type II) and Tracker track (NaF events): (left) AMS simulation; (right) Cosmic data.*

Čerenkov angle

Figure 9.50 shows the results obtained for the Čerenkov angle θ_c. A good reconstruction is obtained for most events, with the peak in $\Delta\theta_c$ being slightly biased: the median of the distribution is $+0.14°$ for simulated events and $+0.36°$ for cosmic data. The 68.3% confidence region has a half-width of 1.57° in simulation and 2.46° in data. Long tails extend to each side of the peak, leading to half-widths for the 95.4% confidence region of almost 19° in simulation and almost 26° in data.

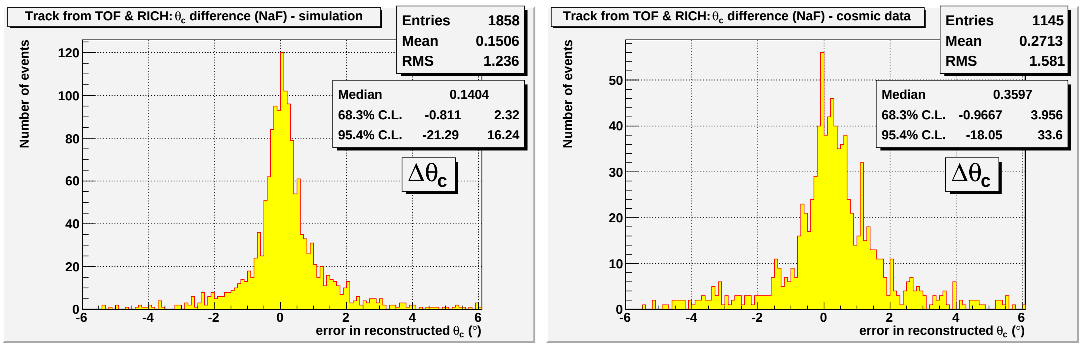

Figure 9.50: *Difference in Čerenkov angle θ_c between TOF-based track (type II) and Tracker track (NaF events): (left) AMS simulation; (right) Cosmic data.*

Position at radiator

Figure 9.51 shows the results obtained for the error in the particle crossing point at the top of the radiator, Δr_{rad}. Results are good for most events, with a better resolution in the case of simulation, but there is a long tail of bad reconstructions in both simulation and data. The 68.3% percentile is at 2.01 cm in simulation and at 3.07 cm in data, while the 95.4% percentile is at 32.0 cm in simulation and 17.6 cm in data. These results are clearly poorer than those obtained in aerogel where the corresponding 68.3% percentiles were at 1.65 cm and 2.01 cm and the 95.4% percentiles at 3.49 cm and 5.69 cm.

Position at detection matrix

Figure 9.52 shows the results obtained for the error in the particle crossing point at the detection matrix, Δr_{LG}. Again good results are obtained for most events but there is a very long tail of bad reconstructions in both simulation and data. In the

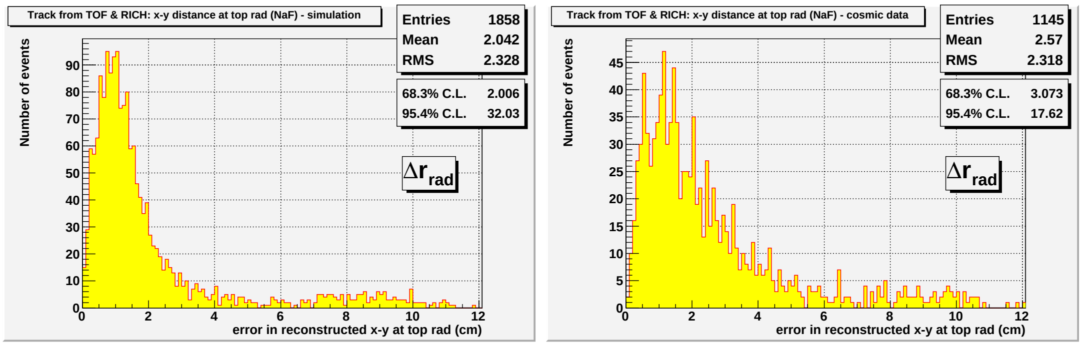

Figure 9.51: *Distance along in the x-y plane between TOF-based track (type II) and Tracker track at the top of the radiator (NaF events): (left) AMS simulation; (right) Cosmic data.*

case of simulated events the 68.3% percentile is placed at 2.12 cm, while data have a slightly broader peak with the 68.3% percentile at 2.49 cm. The 95.4% percentile is at 42.8 cm in simulation and at 25.2 cm in data.

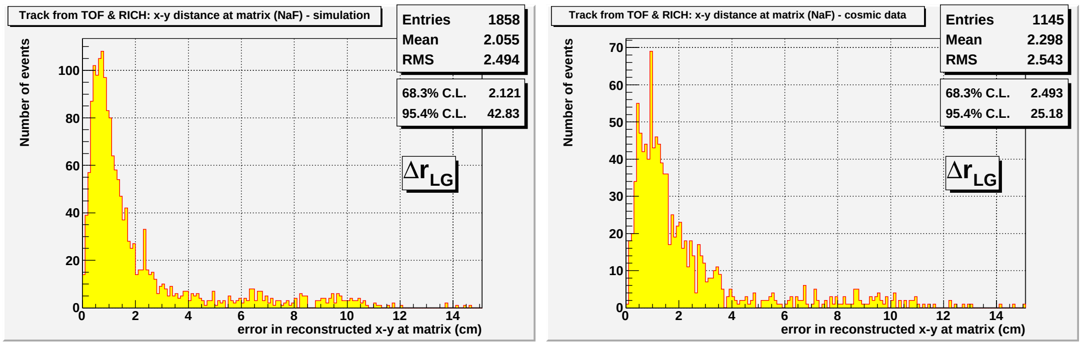

Figure 9.52: *Distance in the x-y plane between TOF-based track (type II) and Tracker track at the detection matrix (NaF events): (left) AMS simulation; (right) Cosmic data.*

9.4.3 Type III: upper TOF + RICH matrix

9.4.3.1 Aerogel events

Track precision

Figure 9.53 shows the results obtained for the angle α between the reconstructed track and the reference track given by the AMS Tracker. In simulation a good reconstruction is obtained, with a sharp peak and no significant tails. The 68.3% and 95.4% percentiles are placed at 1.63° and 3.54°, respectively. In cosmic data, however, results are clearly poorer: not only the peak is wider, leading to a result of 3.94° for the 68.3% percentile, but a completely new tail of bad reconstructions appears as a plateau with errors up to $\simeq 20°$, leading to a 95.4% percentile of 15.2°.

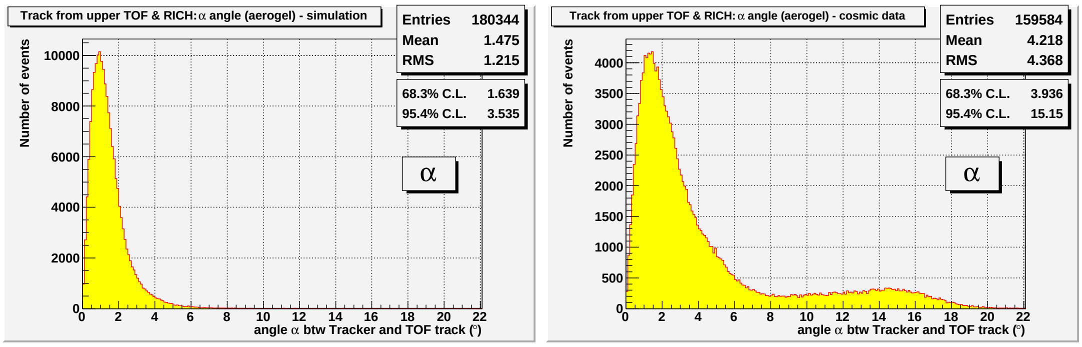

Figure 9.53: *Angle α between TOF-based track (type III) and Tracker track (aerogel events): (left) AMS simulation; (right) Cosmic data.*

The evolution of the results obtained for α as function of the number of ring hits is shown in Fig. 9.54 (top). In the case of simulation the peak width is essentially constant, while the tails become smaller, as reflected in the 95.4% percentile. In cosmic data there is some improvement in both percentiles with the number of ring hits, but in all cases the reconstruction quality is very far from what is seen in simulation.

The variation of α as function of particle inclination (given by the Tracker) is presented in Fig. 9.54 (centre). In the simulation case results are essentially independent of inclination, with the exception of the 95.4% percentile which reaches much higher values for very high inclinations ($\theta > 35°$). In data the best results are obtained for inclinations of 15°-20°, with some degradation seen for lower inclinations and a huge increase in errors for higher inclinations ($\theta > 25°$), with the 68.3% percentile reaching $\simeq 15°$ for $\theta > 30°$.

Results of α as function of the radius of the particle's crossing point at the radiator are presented in Fig. 9.54 (bottom). Simulation results are independent of radius, with the exception of an increase in tail width at the outer edge of the radiator ($r > 55$ cm). In cosmic data the peak width is relatively stable except for the inner part of the radiator ($r < 25$ cm) where a clear increase is seen in the 68.3% percentile. The best results are obtained at intermediate radii (45-50 cm). The tail width, as evaluated from the 95.4% percentile, decreases as the radius increases but a very large tail is present for all radii.

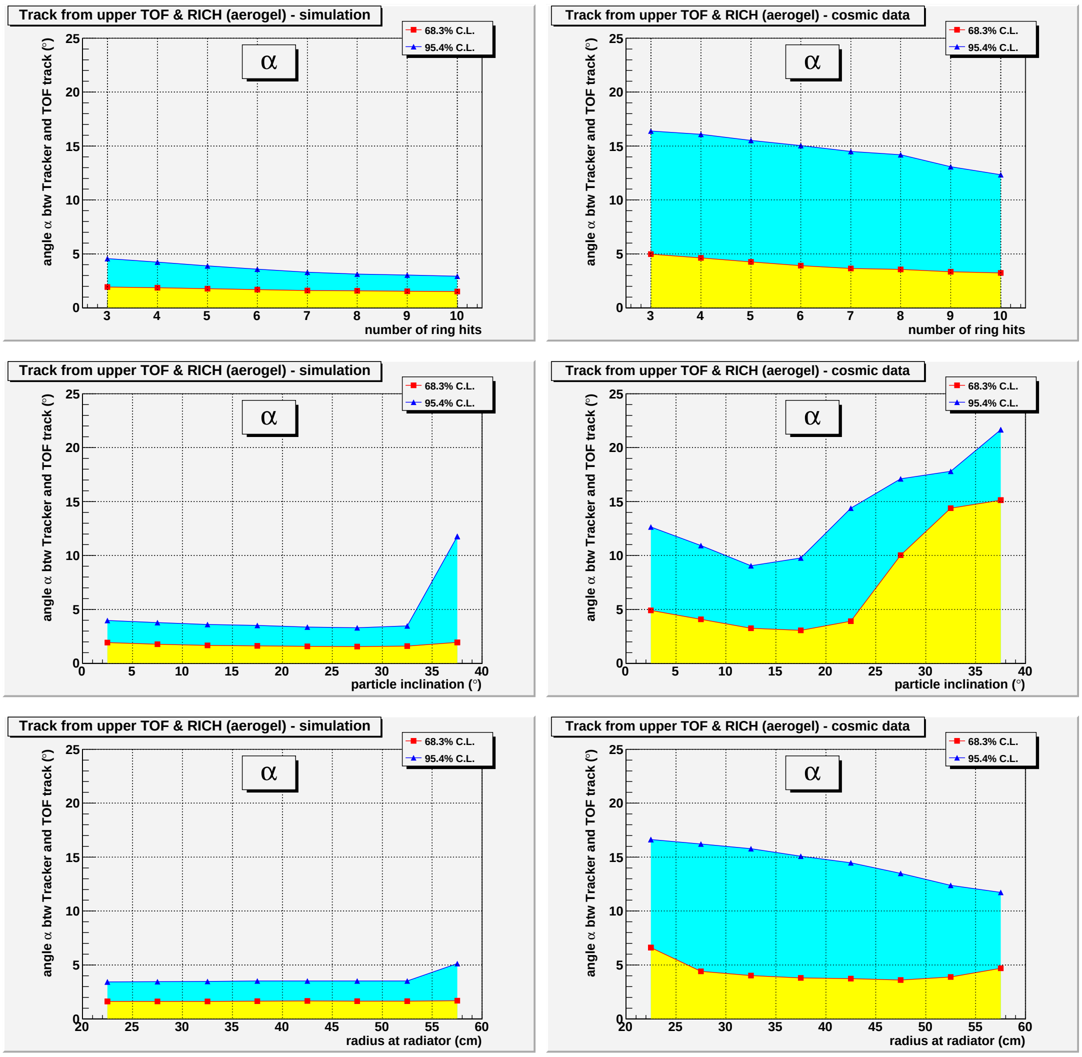

Figure 9.54: *Contours for angle α between TOF (type III) and Tracker tracks as function of (top) ring hits, (centre) track inclination and (bottom) radius of radiator impact point (aerogel events): (left) AMS simulation; (right) Cosmic data.*

Particle inclination

Figure 9.55 shows the results obtained for the particle inclination θ. Very good results are obtained in simulated data, with an almost unbiased estimator being obtained: the median of the $\Delta\theta$ distribution is at $-0.08°$. No significant tails are present. The half-widths for the 68.3% and 95.4% confidence regions are 1.04° and 2.55°, respectively. In the case of cosmic data the situation is very different: the main peak is still unbiased, although wider than in simulation, but the bad events seen previously now appear as a tail on the left-hand side of the distribution. As a consequence, the median moves to $-0.25°$ and the lower limits of confidence regions are severely affected, with the 68.3% confidence region now extending from $-3.62°$ to $+1.80°$ and the 95.4% confidence region from $-13.9°$ to $+5.23°$.

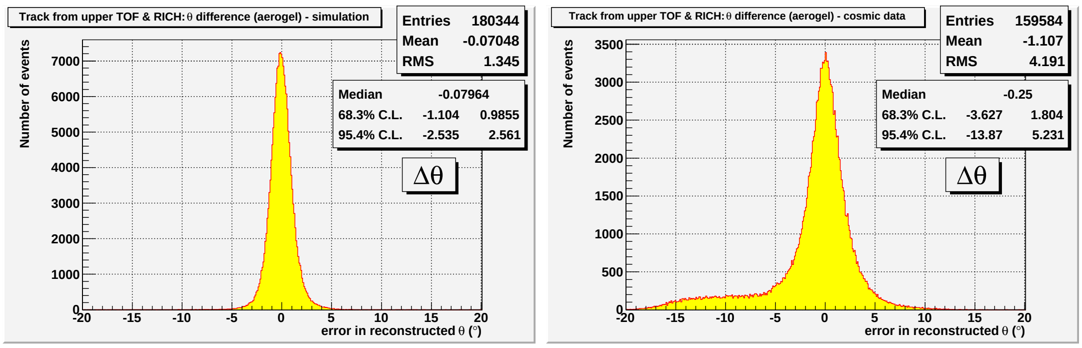

Figure 9.55: *Difference in inclination θ between TOF-based track (type III) and Tracker track (aerogel events): (left) AMS simulation; (right) Cosmic data.*

The evolution of the results obtained for θ as function of the number of ring hits is shown in Fig. 9.56 (top). In the case of simulation the reconstruction is very good in all cases, with an improvement in the peak resolution as the number of hits increases. For cosmic data the distribution is qualitatively similar for any number of hits, but there is some improvement in the left-hand tail as the number of hits increases, with the right half of the distribution being virtually unchanged.

The variation of θ reconstruction quality as function of particle inclination (given by the Tracker) is presented in Fig. 9.56 (centre). In simulation the reconstruction quality in not sensitive to inclination except for very high angles ($\theta > 35°$) where a significant left-hand tail appears. In the case of data there are two separate effects: the peak region tends to become narrower as inclination increases, but for inclinations above 20° the large left-hand tail dominates the distribution, with the lower end of the 68.3% and 95.4% confidence regions falling below −10° and −15°, respectively, for $\theta > 25°$.

Results of θ reconstruction quality as function of the radius of the particle's crossing point at the radiator are presented in Fig. 9.56 (bottom). In the simulation case the reconstruction quality is constant for all radii, with only an increase in the left-hand tail of the distribution senn for the highest radii ($r > 55$ cm). On the other hand, in cosmic data there is a visible dependency of reconstruction quality with the radius at the radiator: inner events have a strong bias towerds lower angles, while outer events have a more or less unbiased θ reconstruction. In all cases the quality of the reconstruction is far from the simulation expectations, however.

Azimuthal angle

Figure 9.57 shows the results obtained for the azimuthal angle ϕ. Good results are obtained in simulation, with the 68.3% and 95.4% percentiles in the $\Delta\phi$ distribution placed at 3.80° and 13.7°, respectively. In the case of real data the main peak is broader and a significant tail of bad reconstructions appears. The 68.3% and 95.4% percentiles move to 9.44° and 37.9°.

The evolution of the results obtained for ϕ as function of the number of ring hits is shown in Fig. 9.58 (top). In the simulation case, additional hits reduce the length of the distribution tails, leaving the main peak width unchanged. In cosmic data some improvement is seen in both percentiles, but even for 10 hits the results are dominated by the large tails.

The variation of ϕ reconstruction quality as function of particle inclination (given by the Tracker) is presented in Fig. 9.58 (centre). The simulation results follow the expected pattern, with precision in ϕ improving as inclination increases. For very high inclinations ($\theta > 35°$) there is an increase in the distribution tail, however. In data the best results are achieved for intermediate inclinations ($\theta \simeq 20°$). For higher inclinations the distribution becomes much wider, reflecting the increase of the bad event component present in cosmic data.

Results of ϕ reconstruction quality as function of the radius of the particle's crossing point at the radiator are presented in Fig. 9.58 (bottom). In simulated

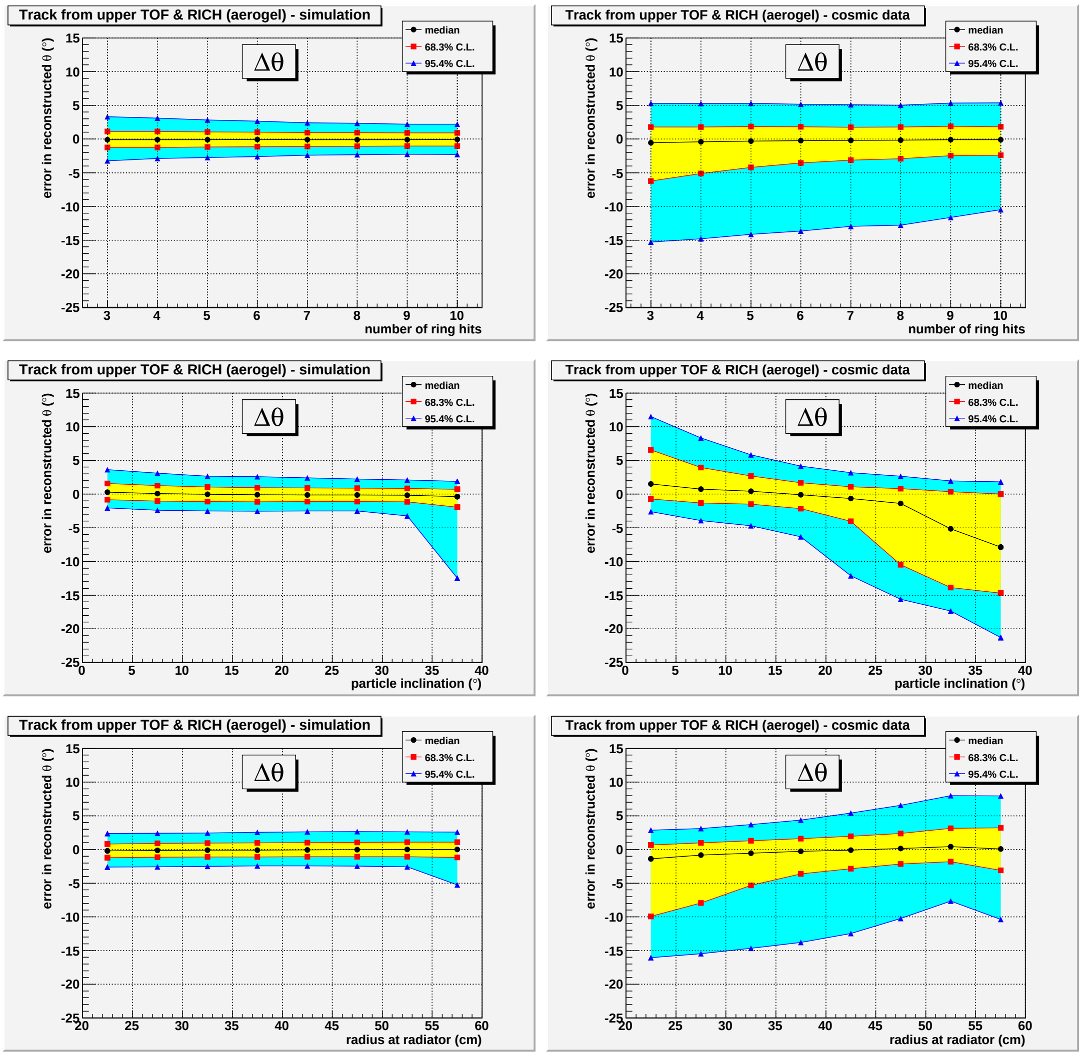

Figure 9.56: *Contours for θ difference between TOF (type III) and Tracker tracks as function of (top) ring hits, (centre) track inclination and (bottom) radius of radiator impact point (aerogel events): (left) AMS simulation; (right) Cosmic data.*

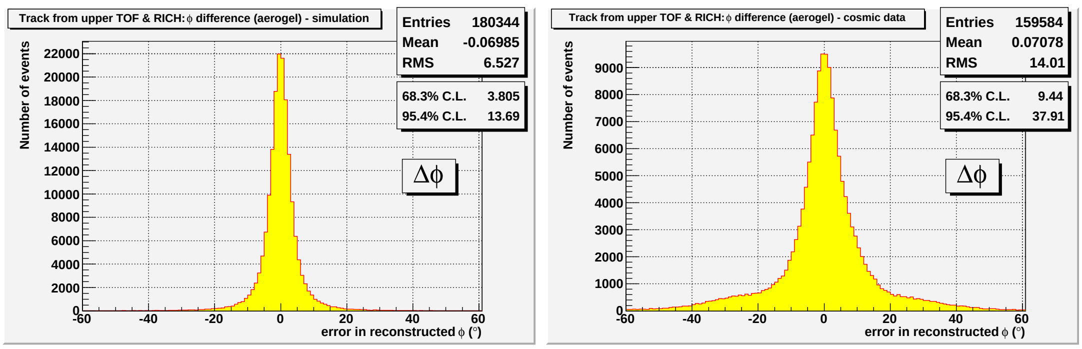

Figure 9.57: *Difference in azimuthal angle ϕ between TOF-based track (type III) and Tracker track (aerogel events): (left) AMS simulation; (right) Cosmic data.*

events the best results are achieved at low radii, with the width of the distribution gradually increasing with radius. The tails become larger with radius up to $\simeq 40$ cm, then stabilize for higher radii. For cosmic data there is no large variation in the peak width as function of radius, with the 68.3% percentile stable at $\simeq 10°$. The 95.4% percentile shows some variation, increasing from $\simeq 30°$ for $r < 30$ cm to $\simeq 45°$ for $r \simeq$ 40-45 cm and then decreasing to $\simeq 35°$ for $r > 55$ cm.

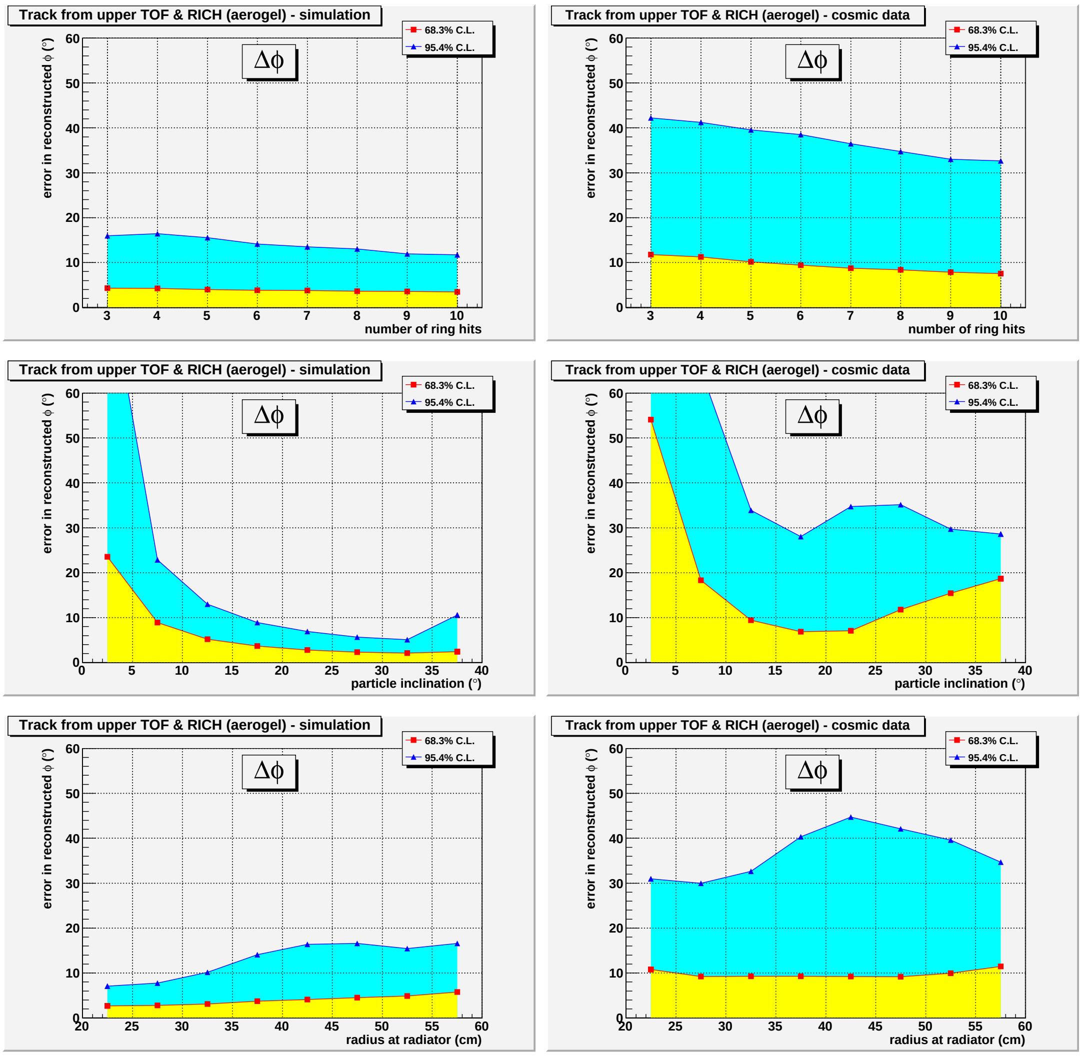

Figure 9.58: *Contours for ϕ difference between TOF (type III) and Tracker tracks as function of (top) ring hits, (centre) track inclination and (bottom) radius of radiator impact point (aerogel events): (left) AMS simulation; (right) Cosmic data.*

Čerenkov angle

Figure 9.59 shows the results obtained for the Čerenkov angle θ_c. In simulated events a good reconstruction is obtained, with an almost unbiased estimator for θ_c: the median of the $\Delta\theta_c$ distribution is at $+0.03°$. The tails of the distribution are slightly asymmetric, with more events in the right-hand tail. The 68.3% confidence region has a half-width of $0.81°$, while the 95.4% confidence region has a half-width of $2.48°$, extending from $-1.12°$ to $+3.84°$. In cosmic data the reconstruction is visibly poorer, with a broader peak and a much larger right-hand tail. The peak is still essentially unbiased, with the median of the distribution at $+0.11°$, but the 68.3% and 95.4% confidence regions are highly asymmetric, with half-widths of $0.83°$ and $5.38°$, respectively.

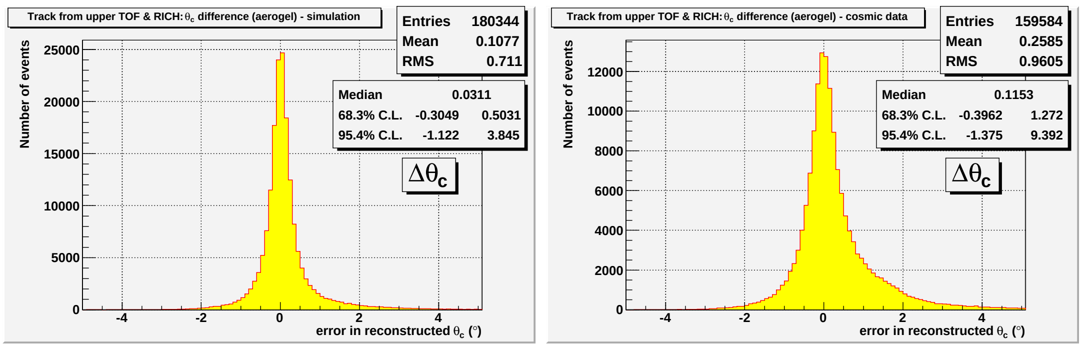

Figure 9.59: *Difference in Čerenkov angle θ_c between TOF-based track (type III) and Tracker track (aerogel events): (left) AMS simulation; (right) Cosmic data.*

The evolution of the results obtained for θ_c as function of the number of ring hits is shown in Fig. 9.60 (top). In the simulation case there is a clear improvement as the number of hits increases, which is essentially reflected on the right-hand half of the distribution, in both 68.3% and 95.4% confidence regions. Even for 8-10 hits there are still asymmetric tails, however. In the case of cosmic data there is also a significant improvement in the right-hand part of the distribution as the number of hits increases, but this is mostly reflected in the peak region, while the right-hand tail remains very long.

The variation of θ_c reconstruction quality as function of particle inclination (given by the Tracker) is presented in Fig. 9.60 (centre). In simulation the peak width remains stable except for some degradation seen at very high inclinations ($\theta > 35°$).

The main effect of inclination is on the long right-hand tail, which tends to increase with inclination, particularly for $\theta > 25°$. In cosmic data, on the other hand, the main effect of an increase in inclination is the widening of the central zone of the distribution for $\theta > 25°$, while the long right-hand tail remains essentially independent of inclination.

Results of θ_c reconstruction quality as function of the radius of the particle's crossing point at the radiator are presented in Fig. 9.60 (bottom). In the case of simulation there is an improvement in the peak region as the radius increases up to $\simeq$ 50 cm, then some degradation at the highest radii. The left-hand tail remains essentially constant across all radii, while the right-hand tail shows a tendency to become larger as the radius increases but with two spikes, the first at 25-30 cm and the second above 55 cm. In cosmic data there is again an improvement in the peak region up to $\simeq$ 50 cm, followed by a loss of quality which is very significant above 55 cm. Tail lengths are not significantly affected by the radius at the radiator.

Position at radiator

Figure 9.61 shows the results obtained for the error in the particle crossing point at the top of the radiator, Δr_{rad}. In simulation a very good reconstruction is obtained, with the distance distribution peaking below 1 cm and almost all events having errors lower than 5 cm. The 68.3% and 95.4% percentiles are at 1.59 cm and 3.44 cm, respectively. In real data the width of the distribution peak increases and a long tail of bad events appears, extending up to $\simeq$ 20 cm, leading to 68.3% and 95.4% percentiles of 3.95 cm and 15.4 cm, respectively.

The evolution of the results obtained for Δr_{rad} as function of the number of ring hits is shown in Fig. 9.62 (top). In simulation the peak width remains essentially constant, while there is some reduction in tails as the number of hits increases, especially from 3 to 4 hits. In cosmic data there is a some improvement as function of the number of hits, but the results are always much poorer than in simulation.

The variation of Δr_{rad} as function of particle inclination (given by the Tracker) is presented in Fig. 9.62 (centre). In simulation there is a slight increase in the width of the distribution, as evaluated by the 68.3% and 95.4% percentiles, when inclination increases. For the highest inclinations ($\theta > 35°$) the tail width increases

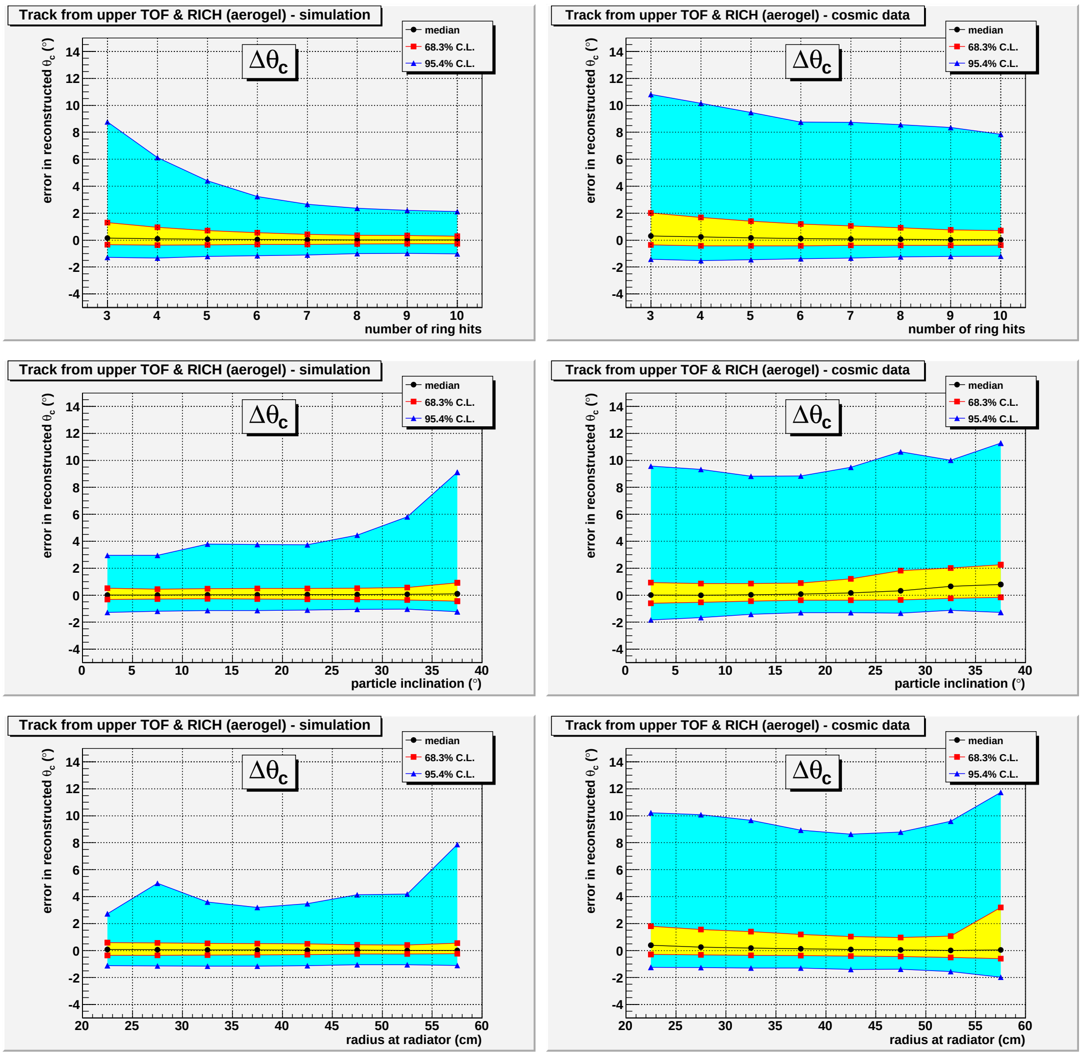

Figure 9.60: *Contours for θ_c difference between TOF (type III) and Tracker tracks as function of (top) ring hits, (centre) track inclination and (bottom) radius of radiator impact point (aerogel events): (left) AMS simulation; (right) Cosmic data.*

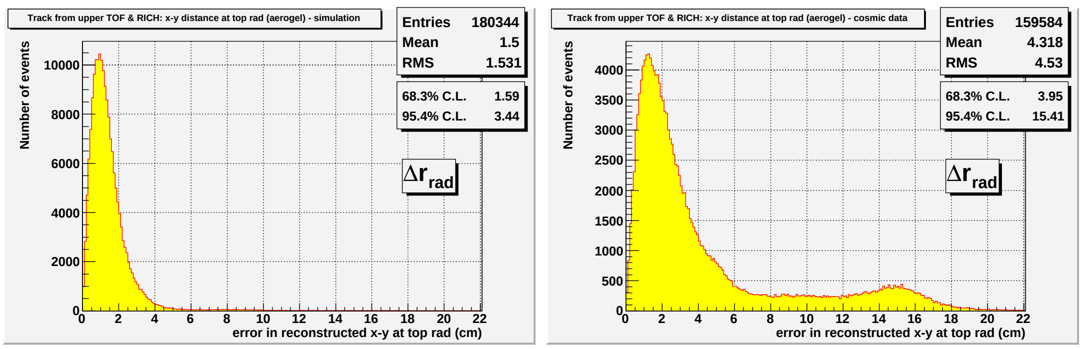

Figure 9.61: *Distance along in the x-y plane between TOF-based track (type III) and Tracker track at the top of the radiator (aerogel events): (left) AMS simulation; (right) Cosmic data.*

dramatically. Results for cosmic data are completely different, with the 68.3% percentile relatively stable for inclinations between 0° and 25° (reaching its lowest values for 10°-20°) but then climbing rapidly at higher inclinations. The 95.4% percentile follows roughly the same trend.

Results of Δr_{rad} as function of the radius of the particle's crossing point at the radiator are presented in Fig. 9.62 (bottom). In simulation there is essentially no change of reconstruction quality with radius except for the sharp increase in tails at the outer edge ($r > 55$ cm). For cosmic data, on the contrary, there is a significant variation, with the 68.3% percentile rising at each end of the distribution and the 95.4% percentile showing a slow decrease from inner to outer events with the exception of the outer edge where it rises sharply.

Position at detection matrix

Figure 9.63 shows the results obtained for the error in the particle crossing point at the detection matrix, Δr_{LG}. A good reconstruction is obtained in both simulation and data, although simulation results are better both in terms of peak width and of distribution tails. In simulation the 68.3% and 95.4% percentiles are at 0.80 cm and 3.03 cm, respectively, while in cosmic data the corresponding values are 1.27 cm and 6.98 cm.

The evolution of the results obtained for Δr_{LG} as function of the number of ring hits is shown in Fig. 9.64 (top). A similar behaviour is observed in simulation and data, with both the 68.3% and 95.4% percentiles improving steadily as the number of hits increases. The width of the distributions is reduced by a factor ~ 2 between 3 and 10 hits.

The variation of Δr_{LG} as function of particle inclination (given by the Tracker) is presented in Fig. 9.64 (centre). In simulation there is only a very slight increase in the width of the distribution as inclination increases. For events with very high inclinations ($\theta > 35°$) there is a sudden, sharp increase in tails. In cosmic data the reconstruction quality improves slightly with inclination up to $\simeq 15°$, where the best values for the percentiles are reached, and then becomes poorer for higher inclinations. The sharp incrase at very high inclinations is also seen here.

Results of Δr_{LG} as function of the radius of the particle's crossing point at

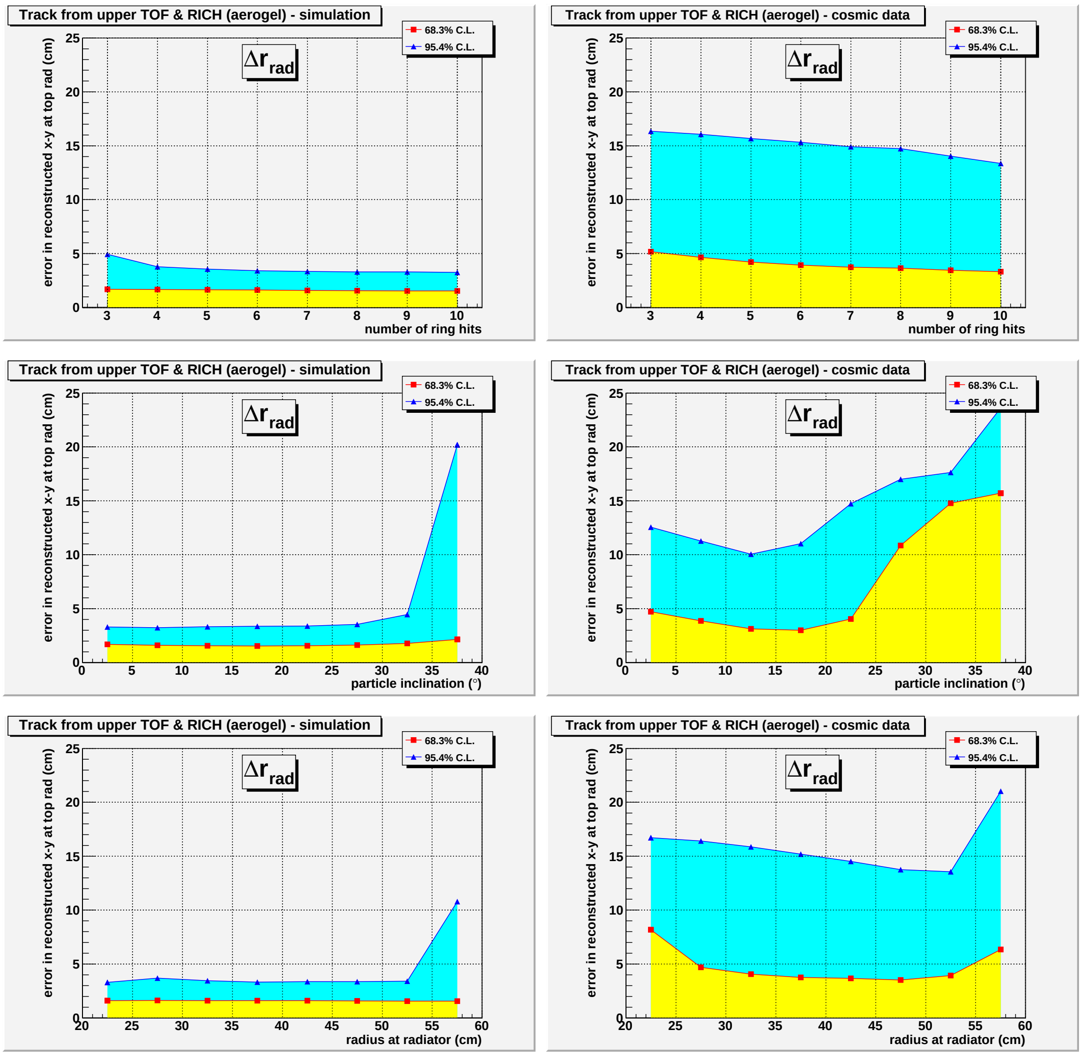

Figure 9.62: *Contours for x-y distance at the top of the radiator between TOF (type III) and Tracker tracks as function of (top) ring hits, (centre) track inclination and (bottom) radius of radiator impact point (aerogel events): (left) AMS simulation; (right) Cosmic data.*

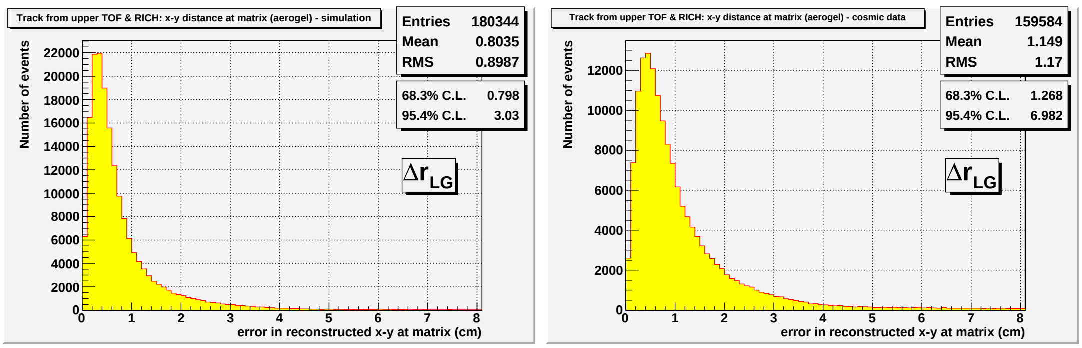

Figure 9.63: *Distance in the x-y plane between TOF-based track (type III) and Tracker track at the detection matrix (aerogel events): (left) AMS simulation; (right) Cosmic data.*

the radiator are presented in Fig. 9.64 (bottom). In simulation there is a very slight tendency for a decrease in the 68.3% percentile and an increase in the 95.4% percentile as the radius at the radiator increases. In addition, a sharp increase is observed at the outer edge of the radiator ($r > 55$ cm). In the case of real data the best reconstruction quality is obtained for intermediate radii (35-50 cm), with some degradation seen, especially in tails, for lower radii and a sharp increase in tails seen from 50 cm onwards with the peak zone also being affected near the outer edge.

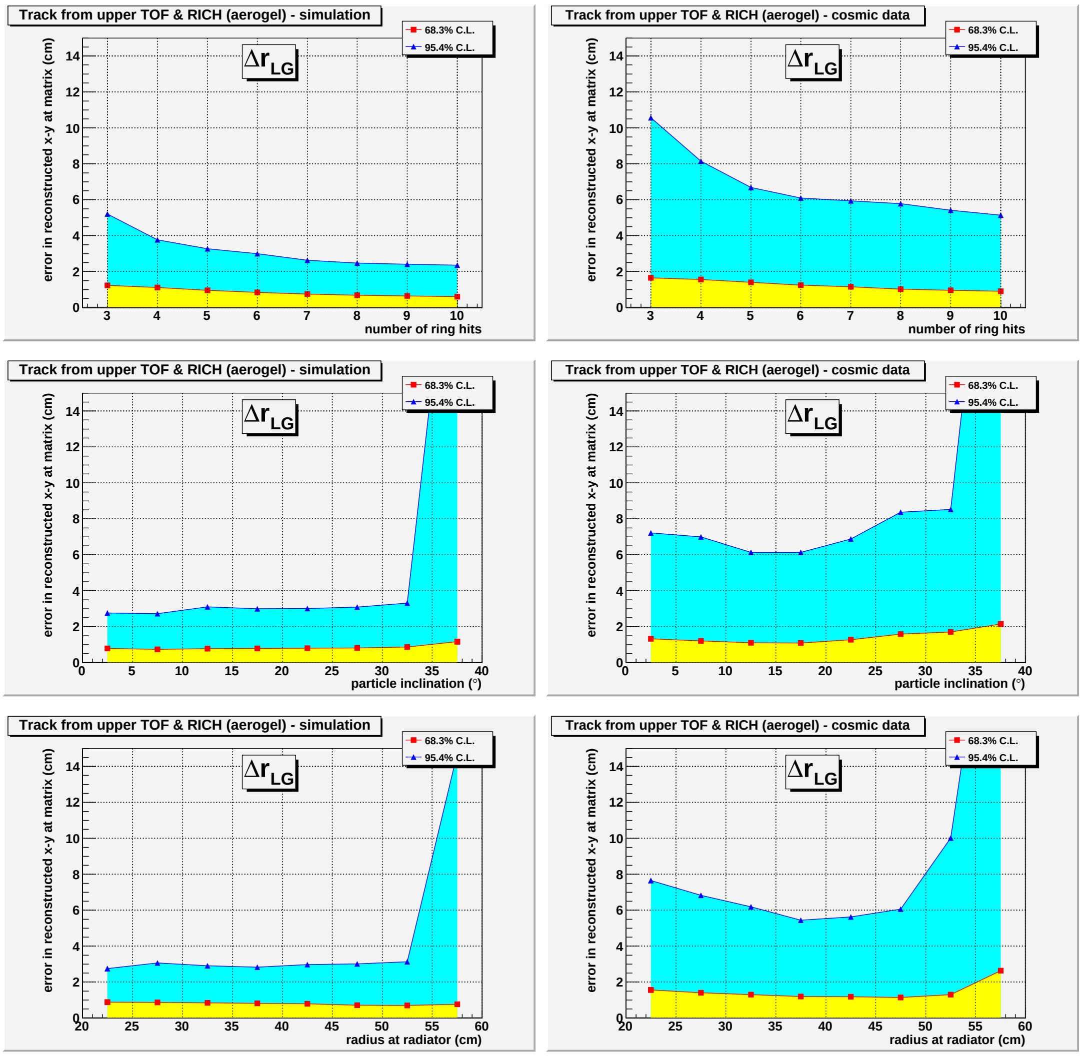

Figure 9.64: *Contours for x-y distance at the detection matrix difference between TOF (type III) and Tracker tracks as function of (top) ring hits, (centre) track inclination and (bottom) radius of radiator impact point (aerogel events): (left) AMS simulation; (right) Cosmic data.*

9.4.3.2 NaF events

Track precision

Figure 9.65 shows the results obtained for the angle α between the reconstructed track and the reference track given by the AMS Tracker. For most events a good reconstruction is obtained, but a long tail of bad reconstructions is present, especially in the case of real data. For simulated events the 68.3% percentile is at 1.88°, while the 95.4% percentile reflects the importance of the bad event tail, being placed at 13.6°. In real data a combination of a broader peak and larger fraction of events in the tail leads to a 68.3% percentile of 6.01°, while the 95.4% percentile is placed at 21.3°. These results are clearly inferior to those obtained for aerogel where the 68.3% and 95.4% percentiles were placed at 1.64° and 3.54°, respectively, in simulation, and at 3.94° and 15.1° in data.

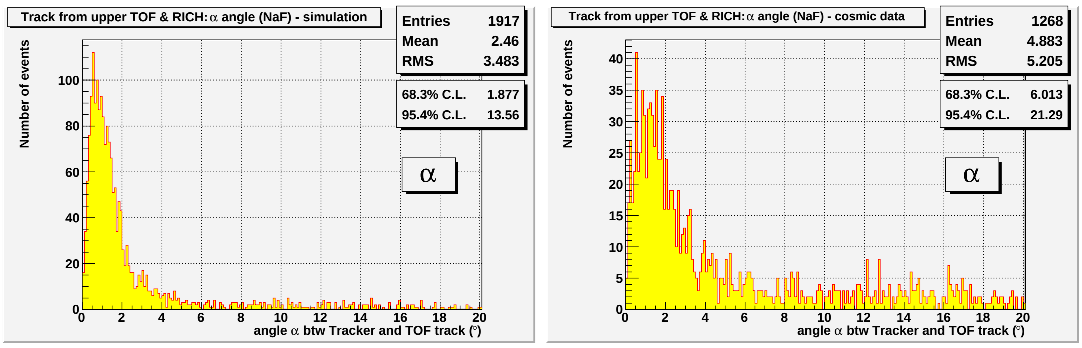

Figure 9.65: *Angle α between TOF-based track (type III) and Tracker track (NaF events): (left) AMS simulation; (right) Cosmic data.*

Particle inclination

Figure 9.66 shows the results obtained for the particle inclination θ. In simulation good results are obtained for most events, with an unbiased peak in the $\Delta\theta$ distribution but with significant tails being present, particularly on the right-hand side of the distribution. The median of the distribution is at +0.08° and the half-widths for the 68.3% and 95.4% confidence regions are 1.31° and 6.84°, respectively. These results are poorer than in aerogel, especially in the case of tails: the widths for the confidence regions in aerogel were 1.04° and 2.55°. In cosmic data the peak of the distribution beacomes broader and the importance of tails increases, the left- and right-hand tails having a similar number of events. The median of the distribution is at $+0.18°$ and the half-widths for the 68.3% and 95.4% confidence regions are $3.12°$ and $12.6°$, respectively. When these results are compared to those obtained for aerogel, the main change that is observed is the appearance of a right-hand tail that is similar to the left-hand tail which was already present in aerogel and remained essentially unchanged in NaF. In aerogel the median of the $\Delta\theta$ distribution was negative ($-0.25°$) as consequence of the highly asymmetric tails. The lower limits of the 68.3% and 95.4% confidence regions changed from $-3.63°$ and $-13.9°$ in aerogel to $-3.02°$ and $-13.7°$ in NaF, while the corresponding upper limits changed from $+1.80°$ and $+5.23°$ to $+3.22°$ and $+11.4°$.

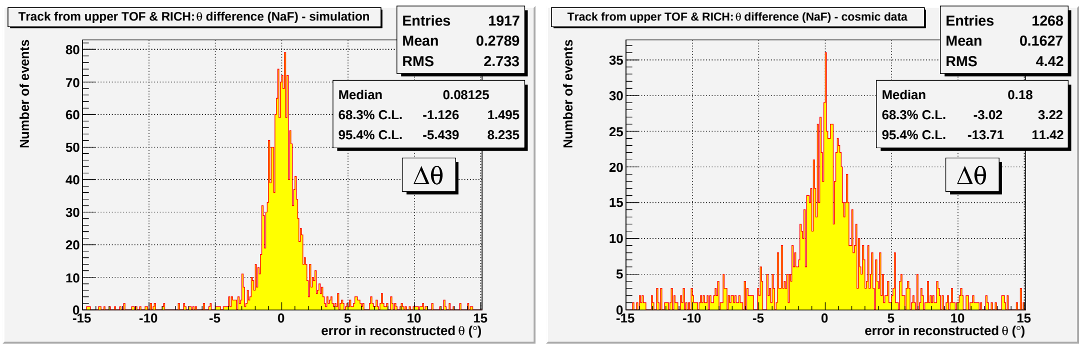

Figure 9.66: *Difference in inclination θ between TOF-based track (type III) and Tracker track (NaF events): (left) AMS simulation; (right) Cosmic data.*

Azimuthal angle

Figure 9.67 shows the results obtained for the azimuthal angle ϕ. A good reconstruction quality is obtained for most events but a tail of bad reconstructions is present and, in the case of cosmic data, a significant number of events is reconstructed with an azimuthal angle that is virtually uncorrelated with the reference angle given by the Tracker. For simulated events the 68.3% and 95.4% percentiles are placed at $2.65°$ and $37.8°$, while in cosmic data the corresponding values are $9.38°$ and $112°$, respectively. When compared to aerogel, the results for the peak region, as evaluated by the 68.3% percentile, improve in simulation ($3.80°$ in aerogel) and are identical in cosmic data ($9.44°$ in aerogel). In tails, however, results are clearly poorer in NaF:

the 95.4% percentiles for aerogel were 13.7° for simulated events and 37.9° for real data.

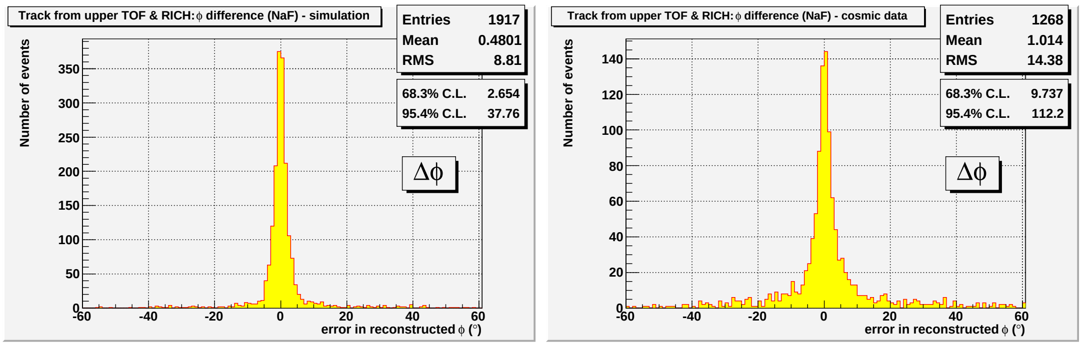

Figure 9.67: *Difference in azimuthal angle ϕ between TOF-based track (type III) and Tracker track (NaF events): (left) AMS simulation; (right) Cosmic data.*

Čerenkov angle

Figure 9.68 shows the results obtained for the Čerenkov angle θ_c. In the case of simulation a good reconstruction is obtained for most events, but a significant fraction fraction of bad reconstructions is present in the form of long tails. The median of the distribution for the reconstruction error $\Delta\theta_c$ is at +0.09° and the half-width for the 68.3% confidence region is 1.74°, while the 95.4% confidence region has a half-width of 23.4° due to the tails. In cosmic data results are poorer, with about half of all events falling outside of the main peak. The median of the distribution is at +0.22° and the half-widths for the 68.3% and 95.4%confidence regions reach the very high values of 10.7° and 28.2°, respectively.

Position at radiator

Figure 9.69 shows the results obtained for the error in the particle crossing point at the top of the radiator, Δr_{rad}. In simulation most events have a good reconstruction, leading to a 68.3% percentile of 2.37 cm. However, a very long tail of bad reconstructions is present, and the 95.4% percentile is placed at 35.3 cm. In cosmic data results are much poorer due to an even greater importance of the tail of bad events: the 68.3% and 95.4% percentiles are placed at 14.0 cm and 45.1 cm, respectively. All these results are much poorer than those obtained in aerogel, where the same

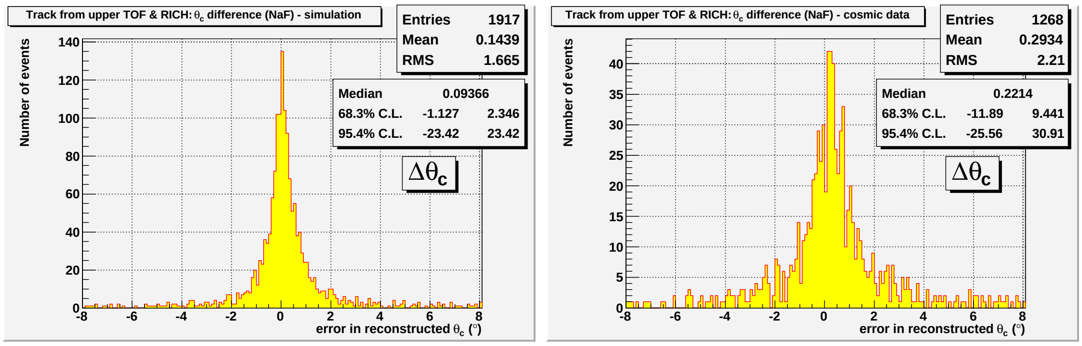

Figure 9.68: *Difference in Čerenkov angle θ_c between TOF-based track (type III) and Tracker track (NaF events): (left) AMS simulation; (right) Cosmic data.*

percentiles were placed at 1.59 cm and 3.44 cm in simulation and at 3.95 cm and 15.4 cm in data.

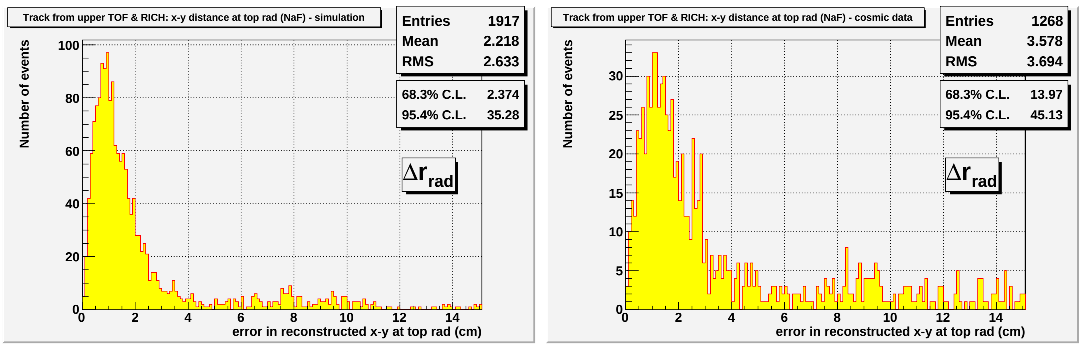

Figure 9.69: *Distance along in the x-y plane between TOF-based track (type III) and Tracker track at the top of the radiator (NaF events): (left) AMS simulation; (right) Cosmic data.*

Position at detection matrix

Figure 9.70 shows the results obtained for the error in the particle crossing point at the detection matrix, Δr_{LG}. The quality of the results is very similar to what was obtained for the position at the radiator, with very long tails of bad reconstruction, especially in cosmic data. In simulation the 68.3% and 95.4% percentiles are placed at 2.38 cm and 47.7 cm, respectively, while in data the same percentiles are at 10.8 cm and 62.0 cm. These results are in sharp contrast with the fair reconstruction obtained in aerogel, where the same percentiles were placed at 0.80 cm and 3.03 cm in simulation and at 1.27 cm and 6.98 cm in data.

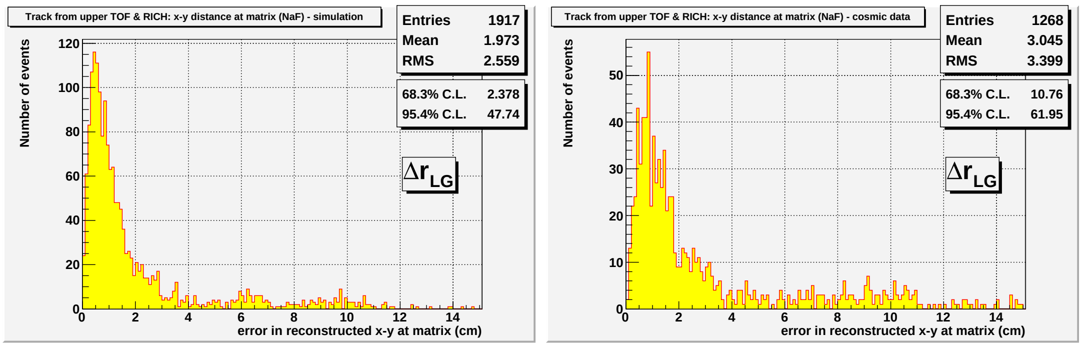

Figure 9.70: *Distance in the x-y plane between TOF-based track (type III) and Tracker track at the detection matrix (NaF events): (left) AMS simulation; (right) Cosmic data.*

9.4.4 Type IV: lower TOF + RICH matrix

9.4.4.1 Aerogel events

Track precision

Figure 9.71 shows the results obtained for the angle α between the reconstructed track and the reference track given by the AMS Tracker. In the case of simulation a resonably good reconstruction is obtained, with most events having errors up to a few degrees: the 68.3% percentile for the α distribution is at $2.94°$, while the 95.4% percentile is placed at $6.21°$. In the case of cosmic data the peak of the distribution is very similar to the one obtained in simulation, but a very long tail of bad reconstructions appears, leading to the 68.3% and 95.4% percentiles being placed at $4.31°$ and $19.6°$, respectively.

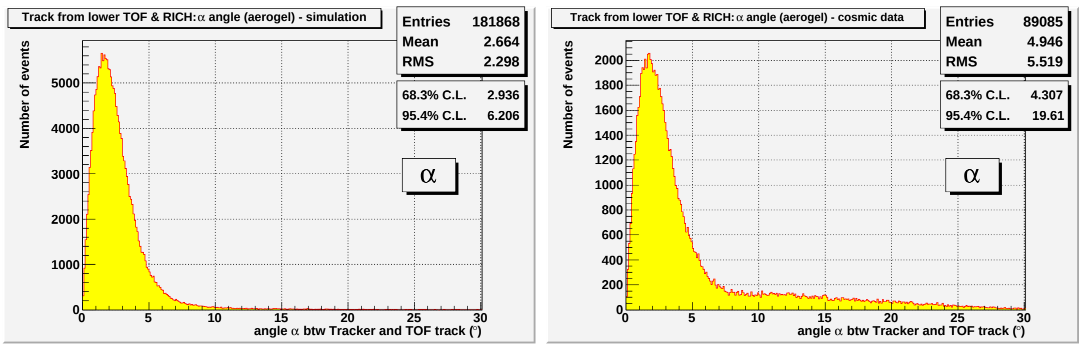

Figure 9.71: *Angle α between TOF-based track (type IV) and Tracker track (aerogel events): (left) AMS simulation; (right) Cosmic data.*

The evolution of the results obtained for α as function of the number of ring hits is shown in Fig. 9.72 (top). There is some improvement in reconstruction quality when the number of hits increases in both simulation and data, although the results obtained for the two situations are rather different.

The variation of α as function of particle inclination (given by the Tracker) is presented in Fig. 9.72 (centre). Results are clearly better for higher inclinations, although in the simulation case an increase in the tail of bad events is observed for very high inclinations ($\theta > 35°$). In cosmic data the variation in reconstruction quality is larger than in simulation, with the long tail of bad events almost disappearing for $\theta > 30°$.

Results of α as function of the radius of the particle's crossing point at the radiator are presented in Fig. 9.72 (bottom). The quality of the reconstruction improves from the outer to the inner part of the radiator. This effect is especially important in the case of cosmic data, where results for the innermost radii ($r < 25$ cm) are comparable to those obtained for simulation in terms of the 68.3% percentile, while for the outer edge of the radiator ($r < 55$ cm) the results for that same percentile differ by a factor $\simeq 4$.

Particle inclination

Figure 9.73 shows the results obtained for the particle inclination θ. In simulated events a good reconstruction is obtained although the results are somewhat biased, with the peak of the $\Delta\theta$ distribution offset by a few tenths of a degree. The median of the distribution is at 0.47°, while the 68.3% and 95.4% confidence regions haeve half-widths of 1.77° and 4.21°. In cosmic data, however, the population of bad reconstructions appears as a tail to the right of the main peak, which happens to be less biased than in simulation. The median of the distribution is placed at 0.26° and the 68.3% confidence region has a half-width of 2.87°. The 95.4% region is highly asymmetric, ranging from $-5.52°$ to $+18.4°$.

The evolution of the results obtained for θ as function of the number of ring hits is shown in Fig. 9.74 (top). In both simulation and data, a small improvement is seen in the reconstruction quality as the number of hits increases. In the case of simulations this improvement is seen essentially in tails, as reflected in the 95.4% percentile. For cosmic data there is a visible improvement in the peak region itself,

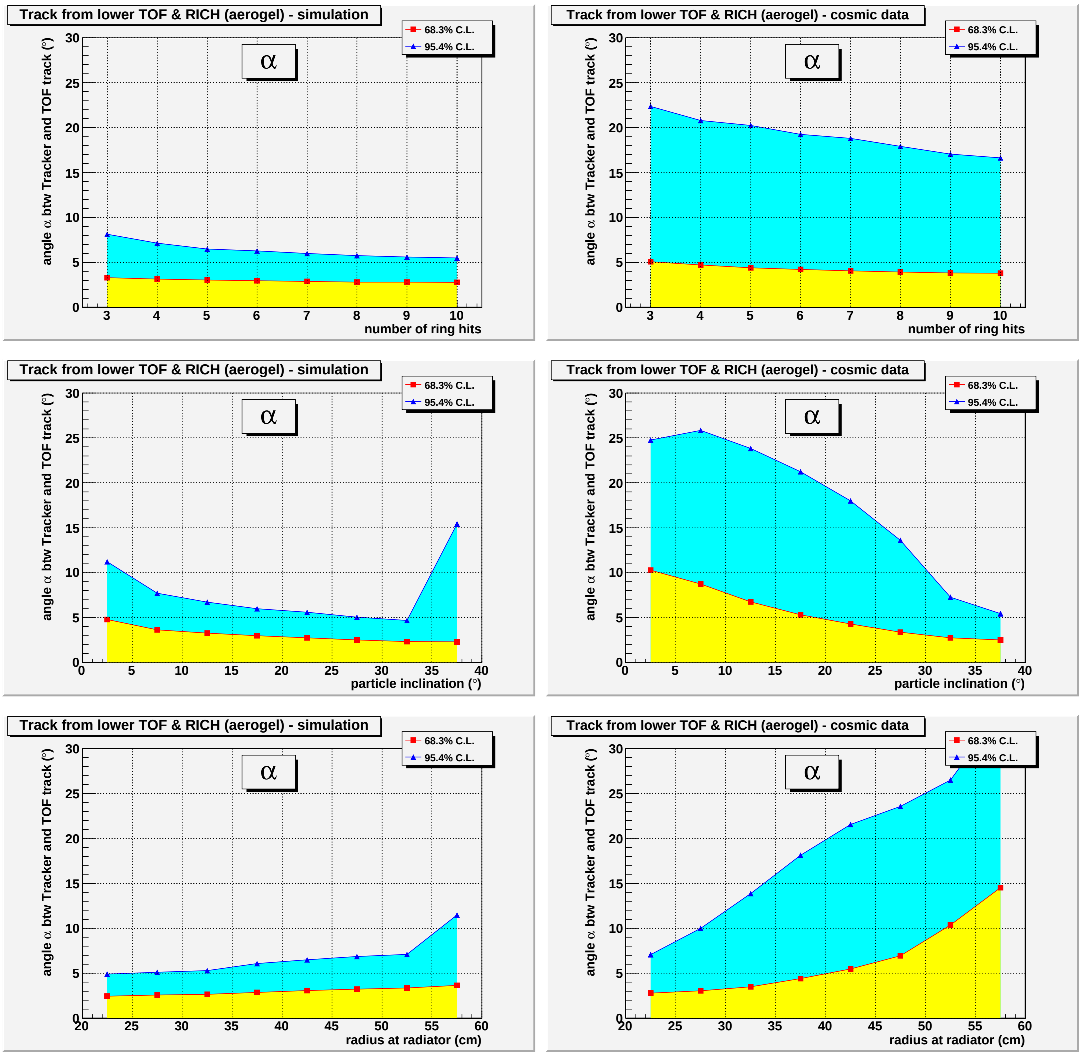

Figure 9.72: *Contours for angle α between TOF (type IV) and Tracker tracks as function of (top) ring hits, (centre) track inclination and (bottom) radius of radiator impact point (aerogel events): (left) AMS simulation; (right) Cosmic data.*

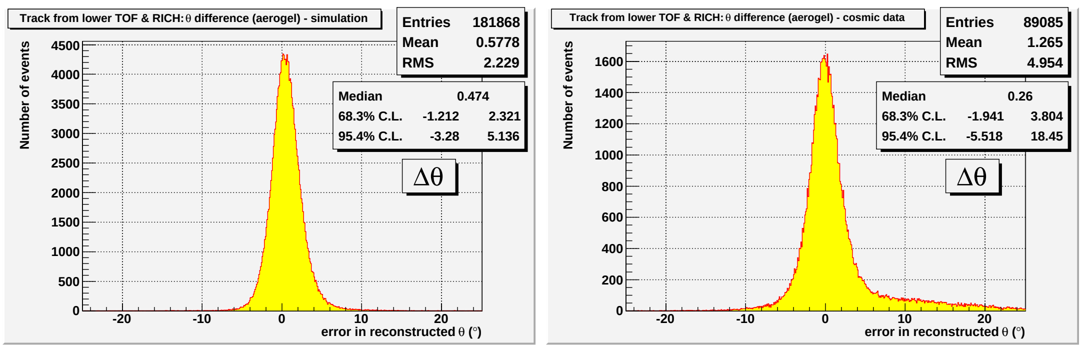

Figure 9.73: *Difference in inclination θ between TOF-based track (type IV) and Tracker track (aerogel events): (left) AMS simulation; (right) Cosmic data.*

although even for 10 hits the quality of the results remains very far from what is observed in simulation.

The variation of θ reconstruction quality as function of particle inclination (given by the Tracker) is presented in Fig. 9.74 (centre). In simulation the reconstruction quality improves slightly with inclination. For small inclinations there is a larger bias in θ as a natural consequence of the available parameter space. At very high inclinations ($\theta > 35°$) there is a significant increase in the left-hand tail. Results for cosmic data show a strong improvement as the inclination increases, with the reconstruction quality being comparable to what was obtained for simulation in the case of inclinations above 30°. In this case no increase in tails is observed at the highest inclinations.

Results of θ reconstruction quality as function of the radius of the particle's crossing point at the radiator are presented in Fig. 9.74 (bottom). In simulation there is some correlation between the radius at the radiator and reconstruction quality, with the best results being obtained on the inner part of the radiator. This is also where the θ estimator is less biased. In the case of real data there is a strong variation in reconstruction quality, similar to what was described in the previous paragraph, with events at the inner part of the radiator ($r < 25$ cm) having a reconstruction quality not very far from simulation expectations but with errors increasing rapidly towards the outer part of the radiator.

Azimuthal angle

Figure 9.75 shows the results obtained for the azimuthal angle ϕ. In simulation a generally good reconstruction is obtained, although errors up to $\simeq 40°$ are obtained for a small part of events. The 68.3% and 95.4% percentiles for $\Delta\phi$ are placed at 6.65° and 26.0°, respectively. In cosmic data the results are poorer and an asymmetric tail appears: this is a unique feature that is not present in an other reconstruction. The 68.3% and 95.4% percentiles are placed at 9.24° and 54.0°.

The evolution of the results obtained for ϕ as function of the number of ring hits is shown in Fig. 9.76 (top). In simulation some improvement is observed in the reconstruction quality, especially in tails as reflected in the 95.4% percentile. A slight improvement is also observed in the 68.3% percentile. In cosmic data, where

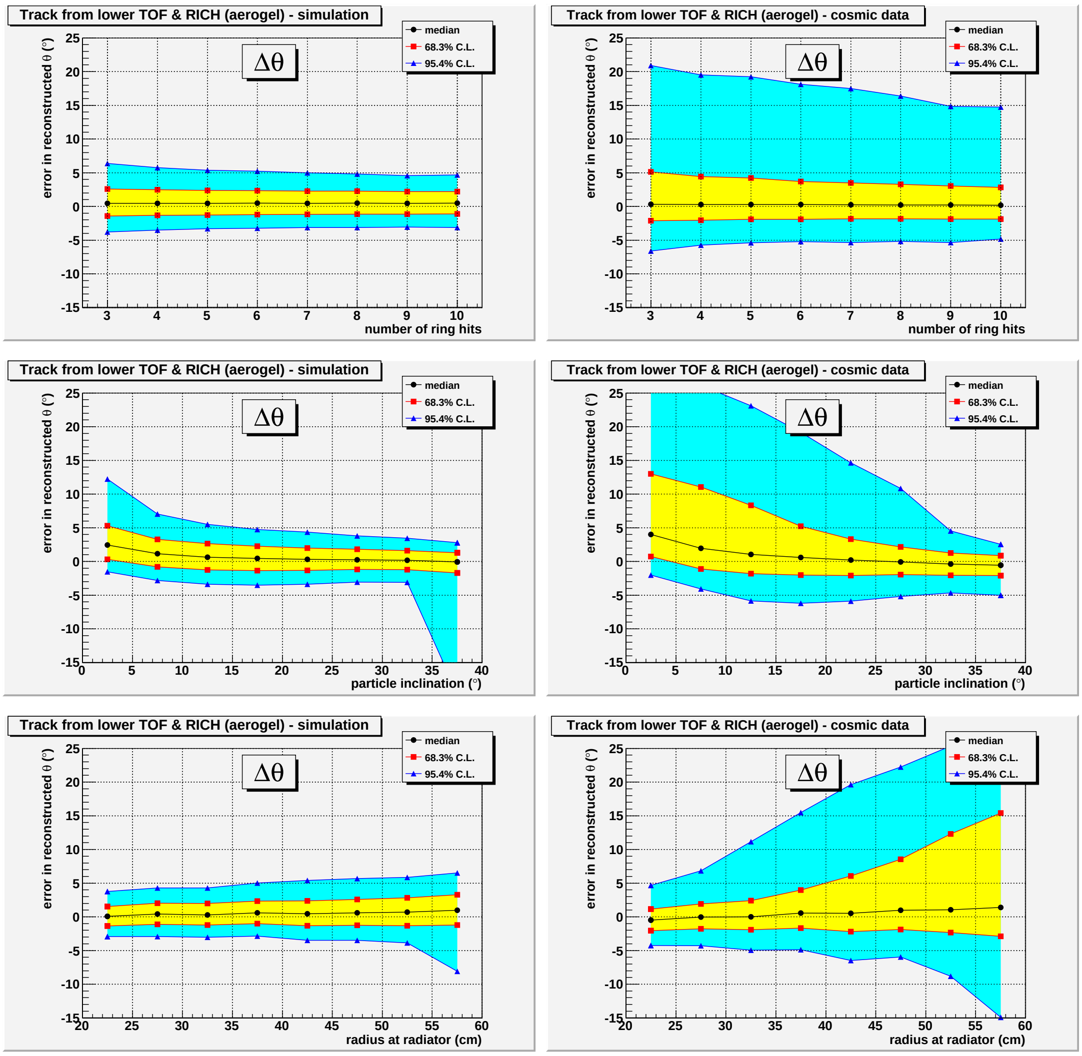

Figure 9.74: *Contours for θ difference between TOF (type IV) and Tracker tracks as function of (top) ring hits, (centre) track inclination and (bottom) radius of radiator impact point (aerogel events): (left) AMS simulation; (right) Cosmic data.*

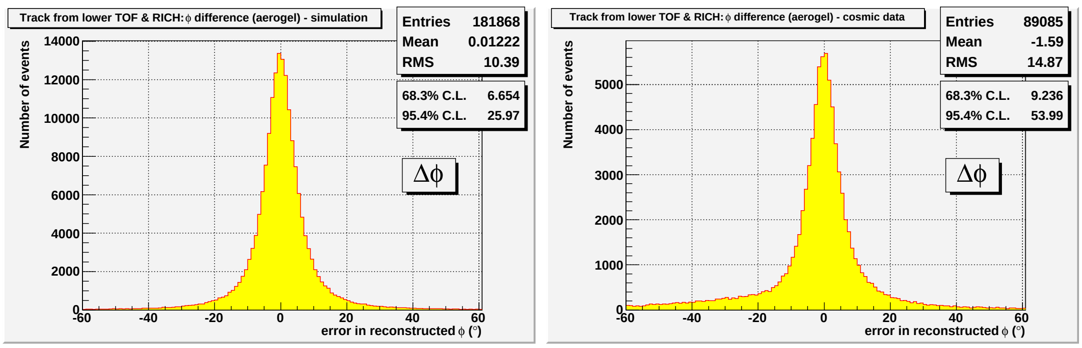

Figure 9.75: *Difference in azimuthal angle ϕ between TOF-based track (type IV) and Tracker track (aerogel events): (left) AMS simulation; (right) Cosmic data.*

results are much poorer, there is a slight improvement with the number of hits in both percentiles.

The variation of ϕ reconstruction quality as function of particle inclination (given by the Tracker) is presented in Fig. 9.76 (centre). The expected improvement with particle inclination is seen for both simulation and data. The difference between the two cases becomes smaller as inclination increases, and for high inclinations ($\theta > 30°$) the reconstruction quality in data is comparable to that of the simulation case.

Results of ϕ reconstruction quality as function of the radius of the particle's crossing point at the radiator are presented in Fig. 9.76 (bottom). The reconstruction quality is clearly higher for events at small radii, both for the main peak and for tails. The difference between the simulation and data cases is also smaller for inner events ($r < 30$ cm), where the 68.3% percentile is similar for both cases but the tails are still significantly longer in cosmic data.

Čerenkov angle

Figure 9.77 shows the results obtained for the Čerenkov angle θ_c. A good reconstruction is obtained for both simulation and data, with an essentially unbiased peak and the reconstruction tails being slightly asymmetric. In the simulation case the median of the distribution is $-0.02°$ and the half-widths for the 68.3% and 95.4% confidence regions are $0.52°$ and $2.61°$, respectively. In the case of cosmic data the peak is wider and the right-hand tail is longer. The median of the distribution is $+0.06°$ and the half-widths for the 68.3% and 95.4% confidence regions are $0.82°$ and $5.85°$.

The evolution of the results obtained for θ_c as function of the number of ring hits is shown in Fig. 9.78 (top). In the case of simulation there is a clear improvement in the quality of the reconstruction as the number of hits increases, both in peak width and on the right-hand tail of the distribution. The results for cosmic data also show an improvement in the distribution peak, but the right-hand tail remains very long for any number of hits.

The variation of θ_c reconstruction quality as function of particle inclination (given by the Tracker) is presented in Fig. 9.78 (centre). In the case of simulation the best

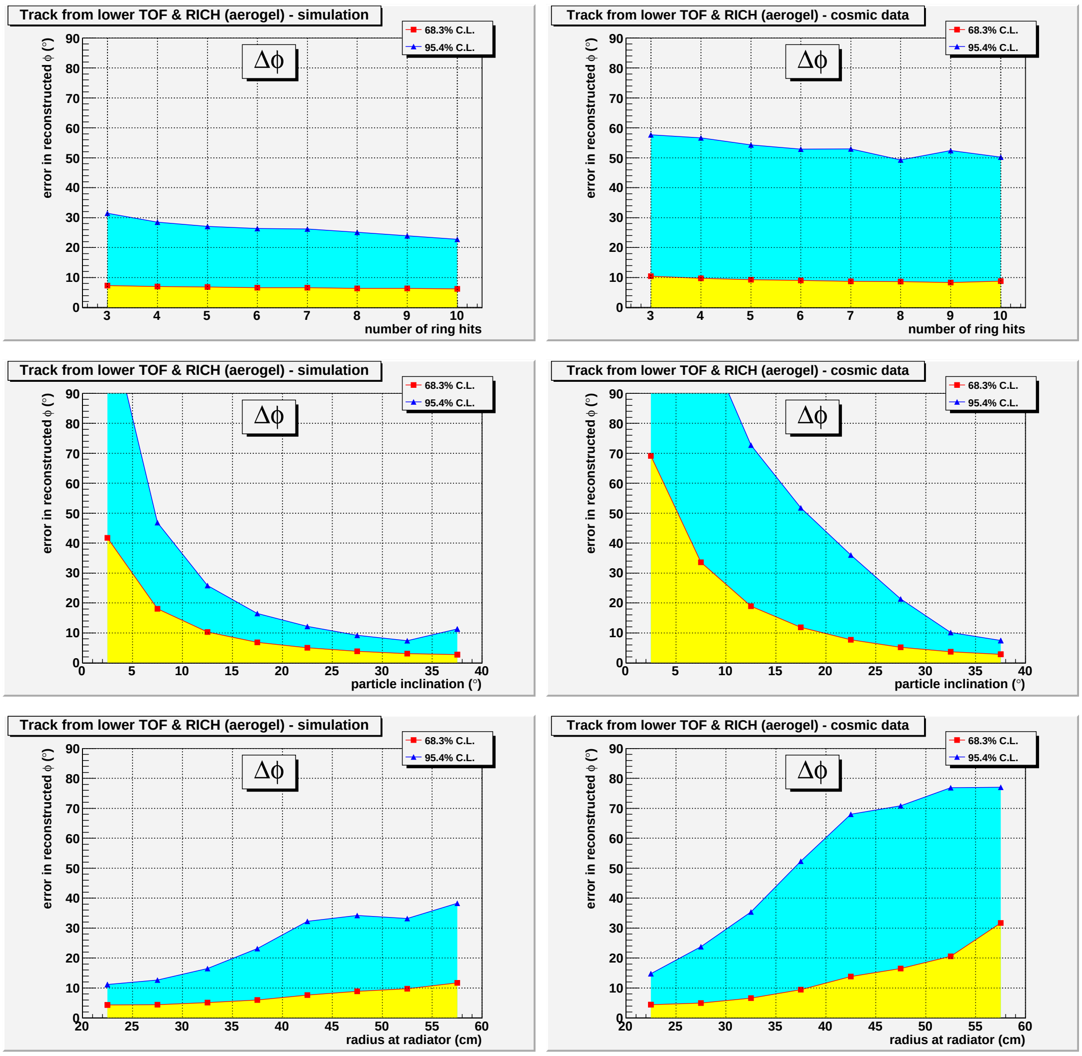

Figure 9.76: *Contours for ϕ difference between TOF (type IV) and Tracker tracks as function of (top) ring hits, (centre) track inclination and (bottom) radius of radiator impact point (aerogel events): (left) AMS simulation; (right) Cosmic data.*

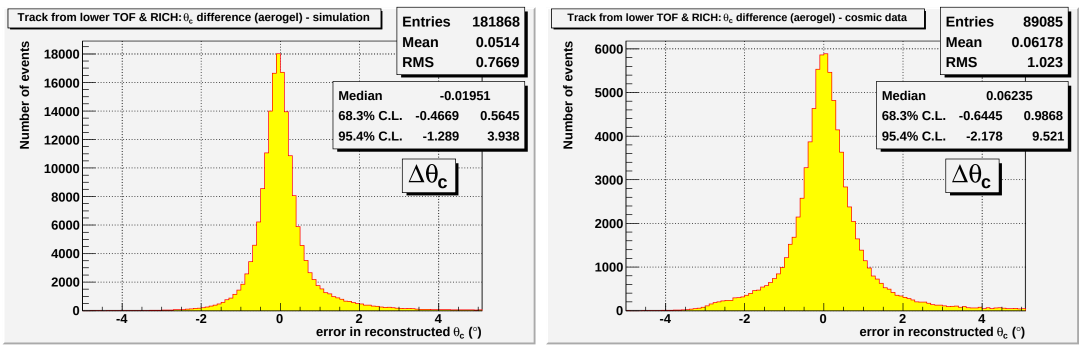

Figure 9.77: *Difference in Čerenkov angle θ_c between TOF-based track (type IV) and Tracker track (aerogel events): (left) AMS simulation; (right) Cosmic data.*

results are obtained for inclinations between 5° and 25°. For very small inclinations there is some degradation in peak quality, while for $\theta > 25°$ there is a strong increase in the right-hand tail of the distribution combined with some loss in peak quality. For real data the results are quite different: the quality of the peak improves steadily with inclination, while in the tails there is a visible improvement in the smaller left-hand tail for inclinations above 25° but no significant change in the more important right-hand tail.

Results of θ_c reconstruction quality as function of the radius of the particle's crossing point at the radiator are presented in Fig. 9.78 (bottom). In simulation the results obtained have no major variation as function of radius. A slight improvement is seen in the peak region as inclination increases. The size of the right-hand tail, as evaluated by the 95.4% confidence region, is relatively stable with the exception of two spikes at $r \simeq$ 25-30 cm and $r > 55$ cm. For real data a different behaviour is seen, with the peak region and the left-hand tail becoming wider as the radius at radiator increases, while the long right-hand tail remains relatively stable across all radii.

Position at radiator

Figure 9.79 shows the results obtained for the error in the particle crossing point at the top of the radiator, Δr_{rad}. A good result is obtained for simulated events, with errors typically of the order of a few cm and no long tails in the error distribution. The 68.3% and 95.4% percentiles are at 2.93 cm and 5.78 cm, respectively. For cosmic data the width of the main peak is similar to what is seen in simulation, but a long tail of bad reconstructions appears. This is reflected in the results for the 68.3% and 95.4% percentiles, which are now placed at 4.11 cm and 19.6 cm.

The evolution of the results obtained for Δr_{rad} as function of the number of ring hits is shown in Fig. 9.80 (top). In simulation the peak width remains unchanged and only the tail region is slightly affected by the number of hits: the 95.4% percentile becomes smaller as the number of hits increases, with most of the improvement occurring between 3 and 4 hits. For cosmic data there is a slight improvement in both 68.3% and 95.4% percentiles as the number of hits increases.

The variation of Δr_{rad} as function of particle inclination (given by the Tracker)

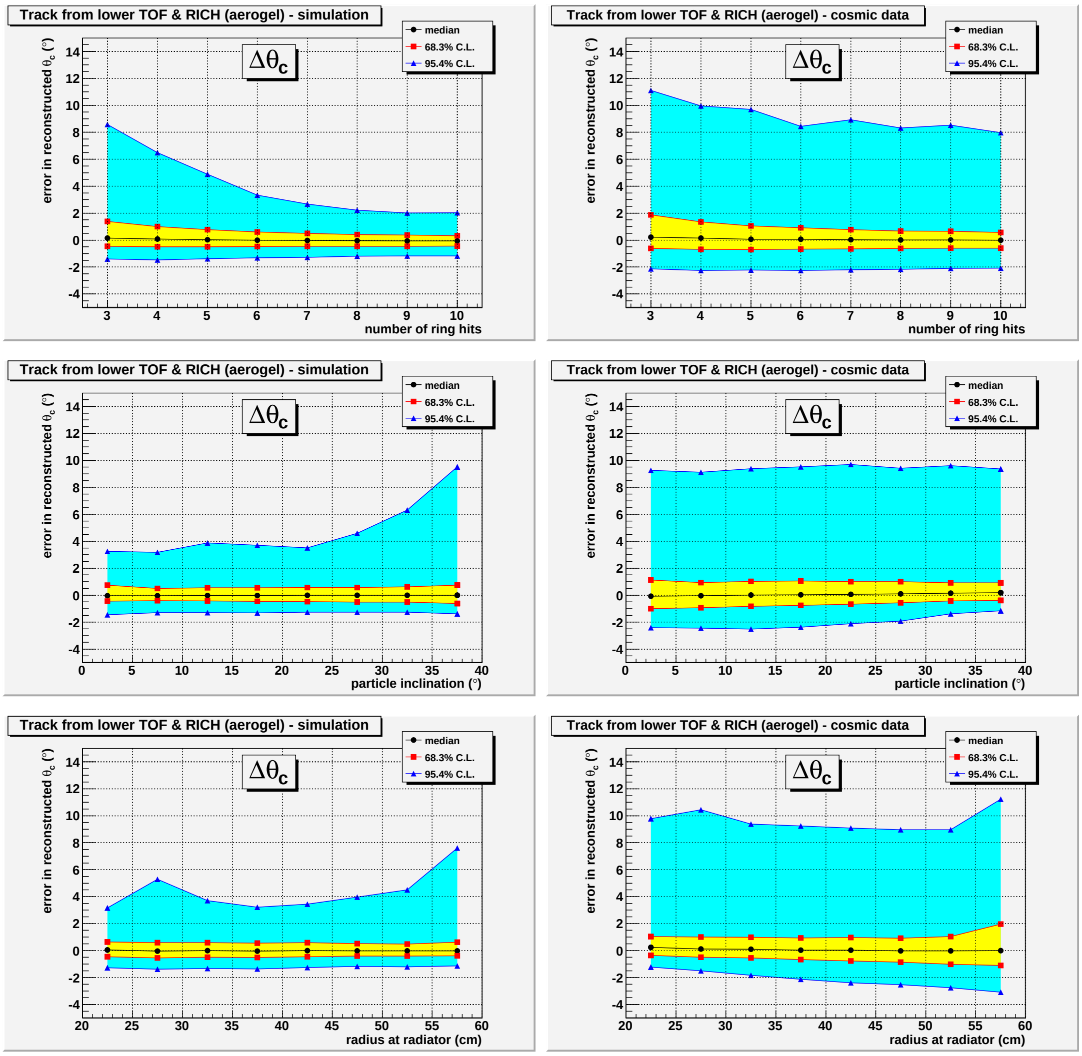

Figure 9.78: *Contours for θ_c difference between TOF (type IV) and Tracker tracks as function of (top) ring hits, (centre) track inclination and (bottom) radius of radiator impact point (aerogel events): (left) AMS simulation; (right) Cosmic data.*

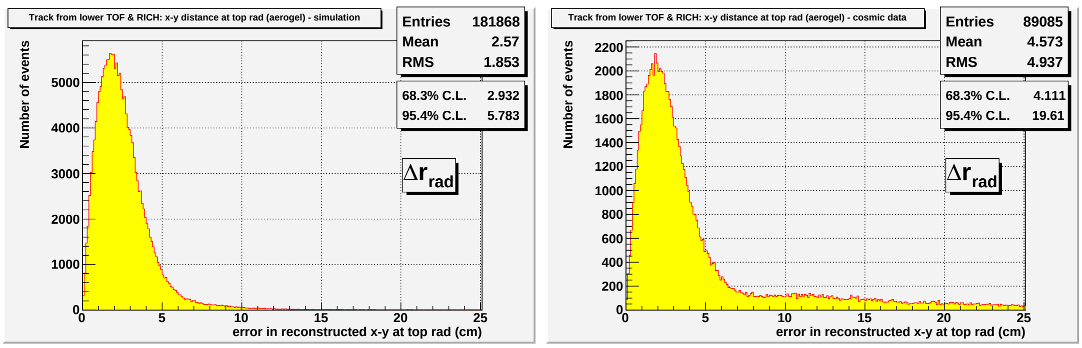

Figure 9.79: *Distance along in the x-y plane between TOF-based track (type IV) and Tracker track at the top of the radiator (aerogel events): (left) AMS simulation; (right) Cosmic data.*

is presented in Fig. 9.80 (centre). In simulated events some improvement, both in the peak region and in tails, is seen when inclination incrass. For very high inclinations ($\theta > 35°$) there is an increase in tail width. In cosmic data there is a very strong improvement of reconstruction quality with inclination: while for events with $\theta \lesssim 20°$ the reconstruction is extremely poor, with the 95.4% percentile being higher than 20 cm, for very high inclinations the reconstruction quality becomes comparable to the one obtained for simulated events of the same inclination.

Results of Δr_{rad} as function of the radius of the particle's crossing point at the radiator are presented in Fig. 9.80 (bottom). In both simulation and cosmic data there is an improvement in the quality of the reconstruction from the outer to the inner part of the radiator. The scale of the variations is very different, however: while in simulation only a marginal improvement is seen, the quality of the results for cosmic data changes completely, with results on the outer edge being very poor while at smaller radii ($r < 35$ cm) the peak width becomes comparable to the corresponding simulation value, the tail width becoming similar to typical simulation values for $r < 25$ cm.

Position at detection matrix

Figure 9.81 shows the results obtained for the error in the particle crossing point at the detection matrix, Δr_{LG}. In both cases a good reconstruction of the crossing point is obtained, with errors no higher than a few cm for almost all events, although results for real data are somewhat poorer than those from simulation. For simulated events the 68.3% and 95.4% percentiles are placed at 0.90 cm and 3.14 cm, respectively, while for cosmic data the correspnding percentile values are 1.38 cm and 7.13 cm.

The evolution of the results obtained for Δr_{LG} as function of the number of ring hits is shown in Fig. 9.82 (top). The reconstruction quality improves, for peak and tail regions, in both simulation and data as the number of hits increases.

The variation of Δr_{LG} as function of particle inclination (given by the Tracker) is presented in Fig. 9.82 (centre). In the case of simulation the results obtained are essentially independent of inclination, although the peak width is slight higher at each end. The most prominent feature is the appearance of a long tail of bad recon-

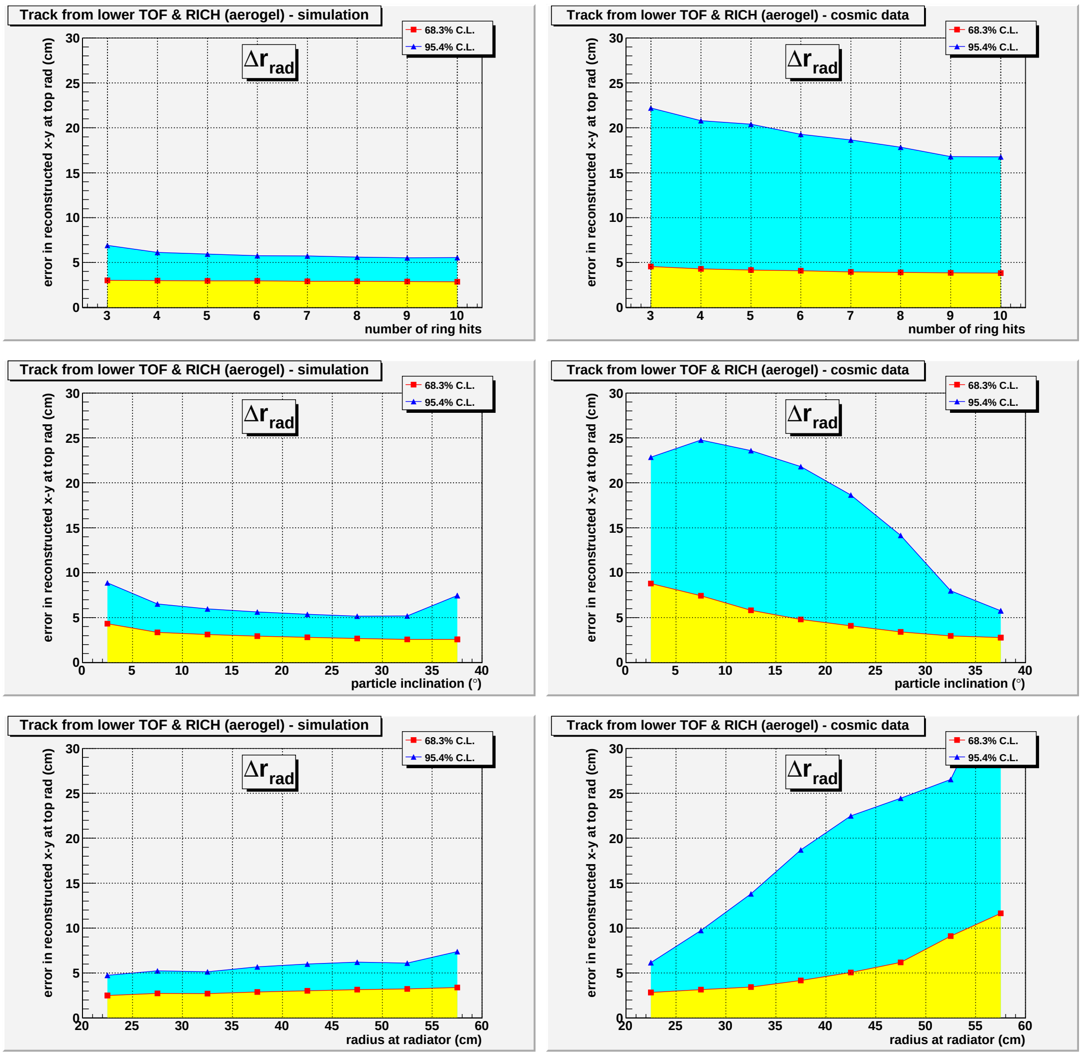

Figure 9.80: *Contours for x-y distance at the top of the radiator between TOF (type IV) and Tracker tracks as function of (top) ring hits, (centre) track inclination and (bottom) radius of radiator impact point (aerogel events): (left) AMS simulation; (right) Cosmic data.*

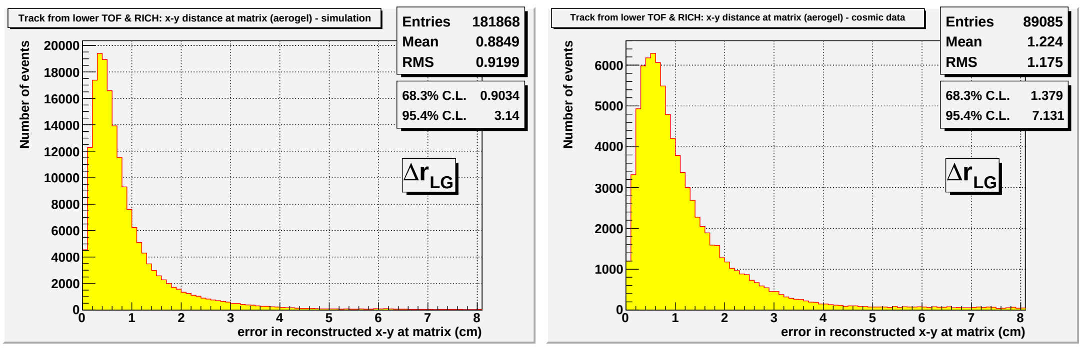

Figure 9.81: *Distance in the x-y plane between TOF-based track (type IV) and Tracker track at the detection matrix (aerogel events): (left) AMS simulation; (right) Cosmic data.*

structions for very high inclinations ($\theta > 35°$). In cosmic data a slight improvement is seen with inclinations, both in terms of peak width and of tail length.

Results of Δr_{LG} as function of the radius of the particle's crossing point at the radiator are presented in Fig. 9.82 (bottom). Simulation results show almost no variation with radius with the exception of a long tail which appears for events at the outer edge of the radiator ($r > 55$ cm). For cosmic data some variation is observed in the peak width as evaluated from the 68.3% percentile, which increases slowly with radius. The distribution's tail, given from the 95.4% percentile, is essentially constant for radii up to 50 cm but increases rapidly at higher radii.

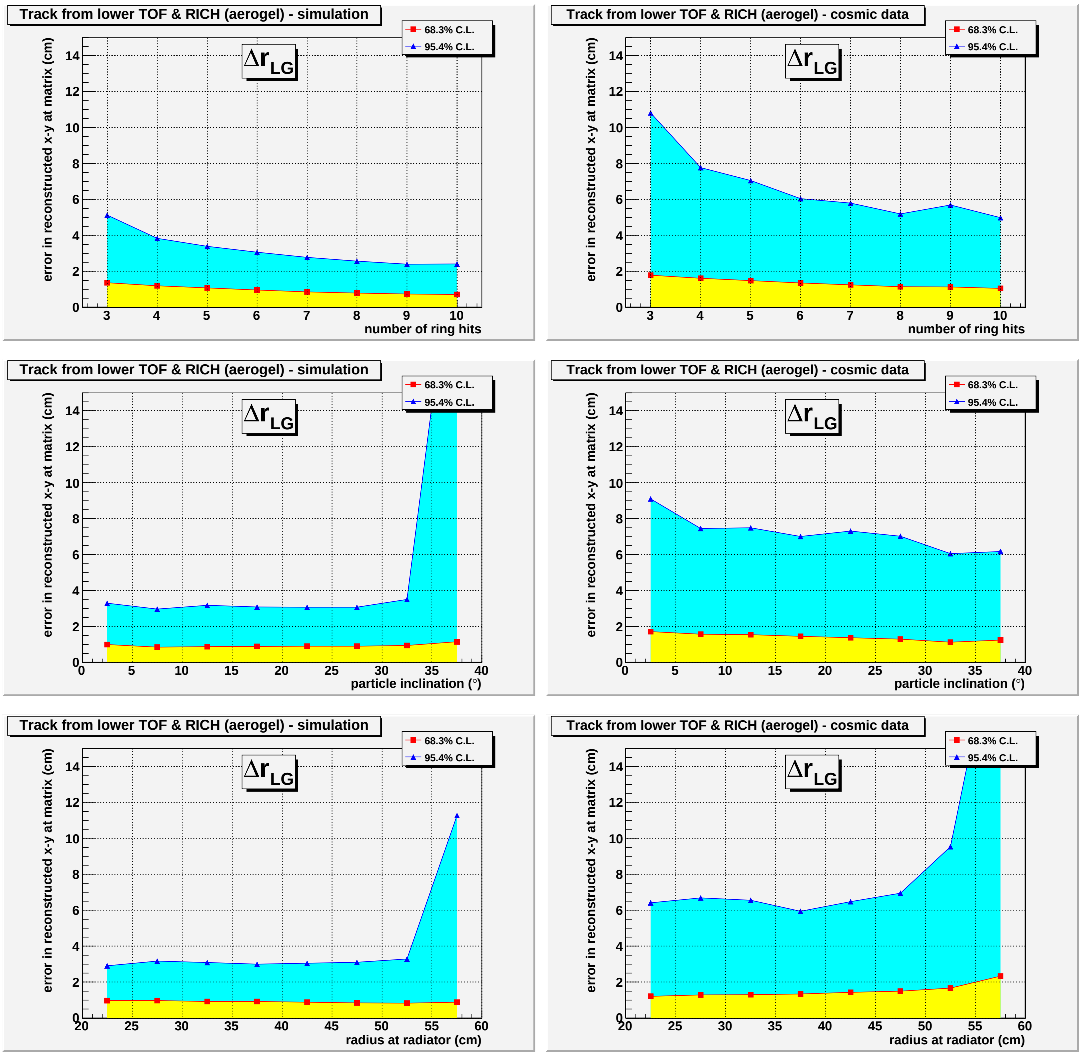

Figure 9.82: *Contours for x-y distance at the detection matrix difference between TOF (type IV) and Tracker tracks as function of (top) ring hits, (centre) track inclination and (bottom) radius of radiator impact point (aerogel events): (left) AMS simulation; (right) Cosmic data.*

9.4.4.2 NaF events

Track precision

Figure 9.83 shows the results obtained for the angle α between the reconstructed track and the reference track given by the AMS Tracker. In both simulation and data a good reconstruction is obtained for most events, but a significant long tail of bad reconstructions is also present. In simulation the 68.3% percentile is at 2.87°, while the 95.4% percentile reflects the effect of tails, being at 23.0°. These results are similar to those obtained for aerogel in terms of peak width (the 68.3% percentile in aerogel is at 2.94°) but are significantly poorer in tails, where the aerogel result was 6.21° for the 95.4% percentile. The reconstruction quality for cosmic data in NaF is similar to the one from simulation, with 68.3% and 95.4% percentiles of 3.39° and 16.5°. These results are slightly better than those from aerogel, where the 68.3% and 95.4% percentiles were 4.31° and 19.6°.

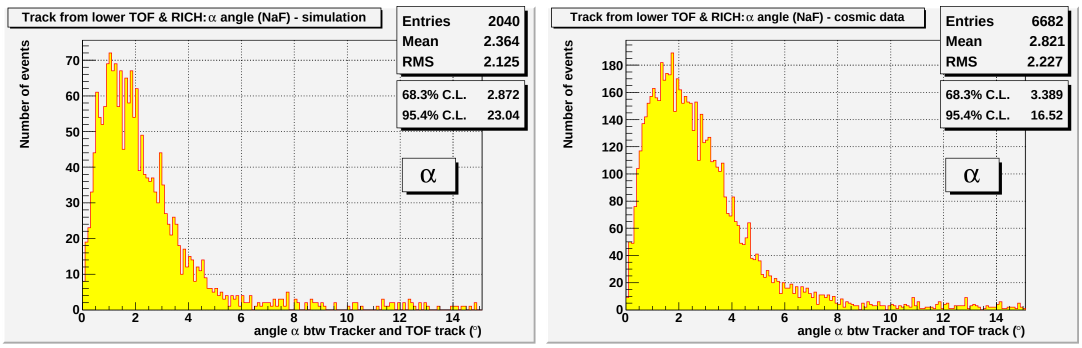

Figure 9.83: *Angle α between TOF-based track (type IV) and Tracker track (NaF events): (left) AMS simulation; (right) Cosmic data.*

Particle inclination

Figure 9.84 shows the results obtained for the particle inclination θ. A good reconstruction is obtained for most events, both in simulation and data, with errors of the order of a few degrees, but significant tails are present in the $\Delta\theta$ distribution, especially to the right of the main peak. In the case of simulation, the peak of the distribution is slightly biased, with a median of +0.86°. The 68.3% confidence region extends from −0.90° to +3.03°, with a half-width of 1.97°, while the 95.4%

confidence region ranges between $-3.25°$ to $+19.3°$, corresponding to a half-width of $11.3°$. These results are similar to those obtained for aerogel in terms of lower limits for the 68.3% and 95.4% confidence regions ($-1.21°$ and $-3.28°$, respectively in aerogel), but the upper limits are much higher than the aerogel ones ($+2.32°$ and $+5.14°$ for 68.3% and 95.4%, respectively). In cosmic data the median of the distribution is $+0.52°$, the 68.3% confidence region ranges from $-1.65°$ to $+3.24°$, corresponding to a half-width of $2.45°$, while the 95.4% confidence region extends from $-3.95°$ to $+15.6°$, with a half-width of $9.78°$. These results are slightly better than those obtained for aerogel, where the median was $+0.26°$ and the half-widths for the 68.3% and 95.4% confidence regions were $2.87°$ and $12.0°$, respectively, with a similar tail asymmetry.

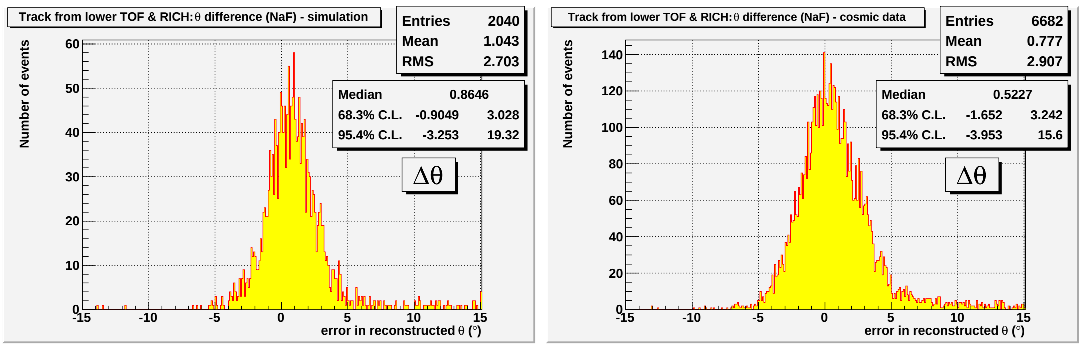

Figure 9.84: *Difference in inclination θ between TOF-based track (type IV) and Tracker track (NaF events): (left) AMS simulation; (right) Cosmic data.*

Azimuthal angle

Figure 9.85 shows the results obtained for the azimuthal angle ϕ. A good reconstruction is obtained in most cases, but tails of bad reconstructions appear in both simulated and real events. In the case of simulation, the 68.3% and 95.4% percentiles in $\Delta\phi$ are $3.38°$ and $50.2°$. The result for 68.3% is clearly better than what was obtained for aerogel ($6.65°$) but the 95.4% percentile is poorer ($26.0°$ in aerogel). In cosmic data the 68.3% and 95.4% percentiles in $\Delta\phi$ are $3.78°$ and $26.6°$, respectively. These results are much better than those obtained for aerogel ($9.24°$ and $54.0°$), and in particular the asymmetry seen in the aerogel distribution is absent in this case.

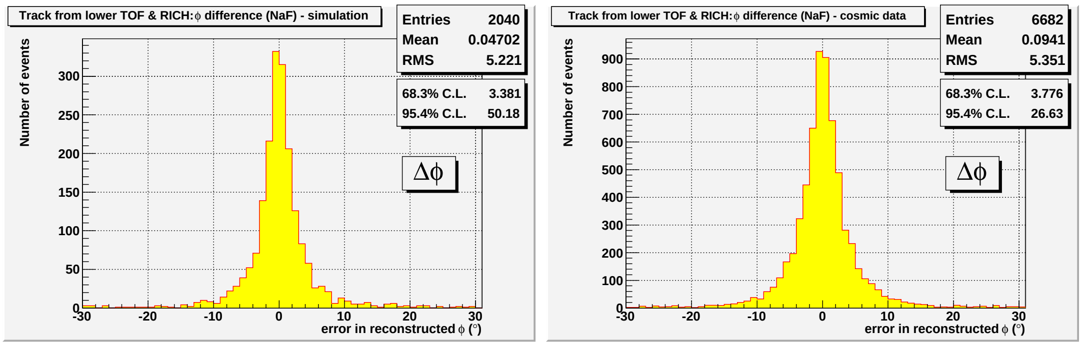

Figure 9.85: *Difference in azimuthal angle ϕ between TOF-based track (type IV) and Tracker track (NaF events): (left) AMS simulation; (right) Cosmic data.*

Čerenkov angle

Figure 9.86 shows the results obtained for the Čerenkov angle θ_c. In the case of simulation a good peak is obtained in the distribution of the reconstruction error $\Delta\theta_c$, but long tails of bad reconstructions are present. The peak itself is slightly biased, with the median of the distribution at $+0.24°$. The 68.3% and 95.4% confidence region have half-widths of $2.58°$ and $26.2°$. For real data the peak is broader but the left-hand tail is less significant. The median of the distribution is at $+0.26°$, with half-widths for the 68.3% and 95.4% confidence regions of $1.58°$ and $19.4°$, respectively.

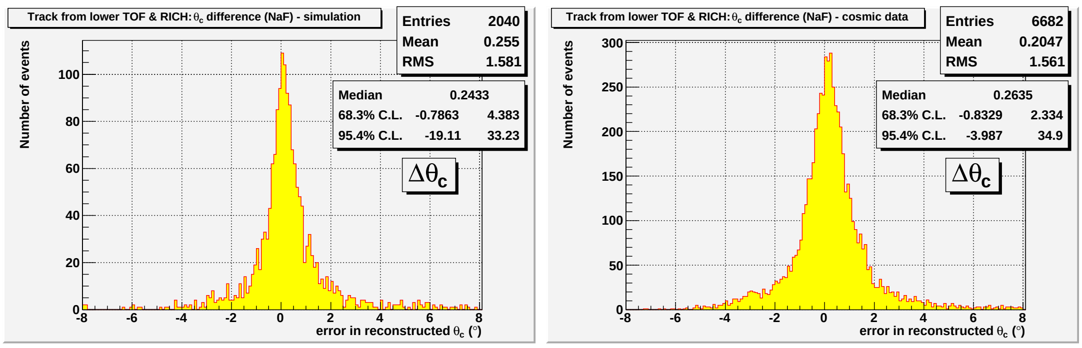

Figure 9.86: *Difference in Čerenkov angle θ_c between TOF-based track (type IV) and Tracker track (NaF events): (left) AMS simulation; (right) Cosmic data.*

Position at radiator

Figure 9.87 shows the results obtained for the error in the particle crossing point at the top of the radiator, Δr_{rad}. In simulation there is a good reconstruction for most events, with the main peak of the error distribution extending up to $\simeq 5$ cm, but a significant fraction of events fall on a long tail that extends up to $\simeq 15$ cm. The 68.3% and 95.4% percentiles are placed at 3.27 cm and 13.1 cm, respectively. These results are poorer than those obtained for aerogel, especially in terms of tails: the corresponding percentiles in aerogel were 2.93 cm and 5.78 cm. In cosmic data the results obtained for NaF are slightly poorer than those from simulation in terms of peak width, but better for tails. The 68.3% and 95.4% percentiles are at 3.74 cm and 9.72 cm, respectively. These are in turn better than the corresponding aerogel results, which had the 68.3% and 95.4% percentiles placed at 4.11 cm and 19.6 cm.

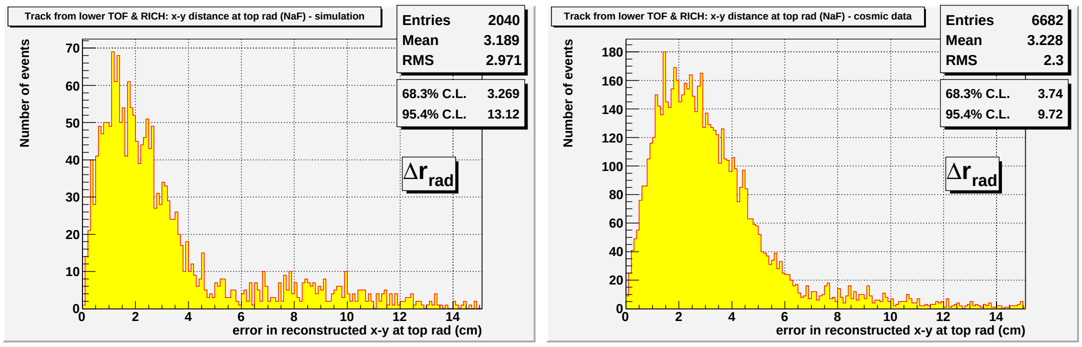

Figure 9.87: *Distance along in the x-y plane between TOF-based track (type IV) and Tracker track at the top of the radiator (NaF events): (left) AMS simulation; (right) Cosmic data.*

Position at detection matrix

Figure 9.88 shows the results obtained for the error in the particle crossing point at the detection matrix, Δr_{LG}. There is again a good reconstruction for the majority of events, with the main peak of both distributions ending at $\simeq 4$ cm, but very long tails are present in both simulation and cosmic data. In simulation the 68.3% percentile is at 2.33 cm, while the 95.4% percentile suffers the effect of bad reconstructions and is placed at 39.4 cm. Results in for cosmic data are slightly better than those from simulation, having the 68.3% and 95.4% percentiles at 2.04 cm and 24.2 cm, respectively. All these results are clearly poorer than those obtained for aerogel, where the same percentiles were placed at 0.90 cm and 3.14 cm in simulation and at 1.38 cm and 7.13 cm in cosmic data.

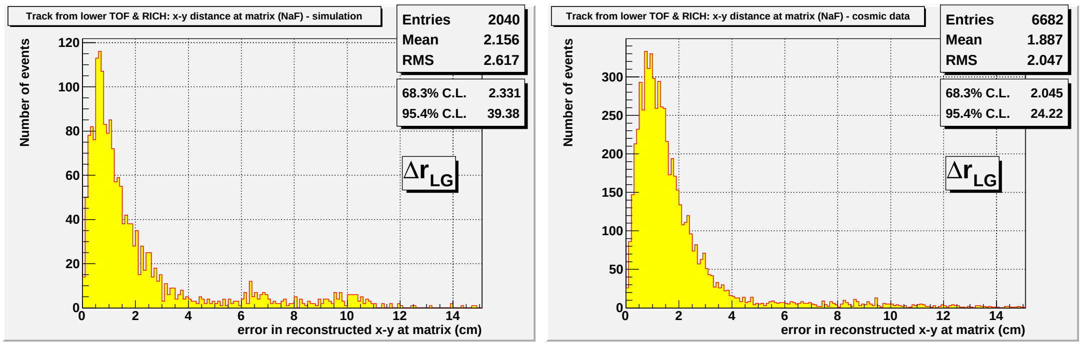

Figure 9.88: *Distance in the x-y plane between TOF-based track (type IV) and Tracker track at the detection matrix (NaF events): (left) AMS simulation; (right) Cosmic data.*

9.4.5 Reconstruction comparison

In this subsection a comparison of the results obtained for the four TOF-based reconstruction types is presented. As in the previous discussions, the reconstruction types are designated by Roman numerals for simplicity:

- **Type I**: upper TOF + lower TOF
- **Type II**: upper TOF + lower TOF + RICH matrix
- **Type III**: upper TOF + RICH matrix
- **Type IV**: lower TOF + RICH matrix

The comparison plots show, for each variable, the results of the 68.3% percentile (for α, $\Delta\phi$, Δr_{rad} and Δr_{LG}) or the half-width of the 68.3% confidence region (for $\Delta\theta$ and $\Delta\theta_c$).

9.4.5.1 Aerogel events

Track precision

Figure 9.89 shows the results obtained for the angle α between the reconstructed track and the reference track given by the AMS Tracker. In simulation the best results are obtained for reconstructions of types II and III, which have identical quality. The other two reconstruction types give clearly poorer results. Among these, Type IV is the best in most situations. In cosmic data two reconstruction types, III and IV, suffer heavily from the appearance of tails of bad events. Therefore, the best results are clearly those from type II.

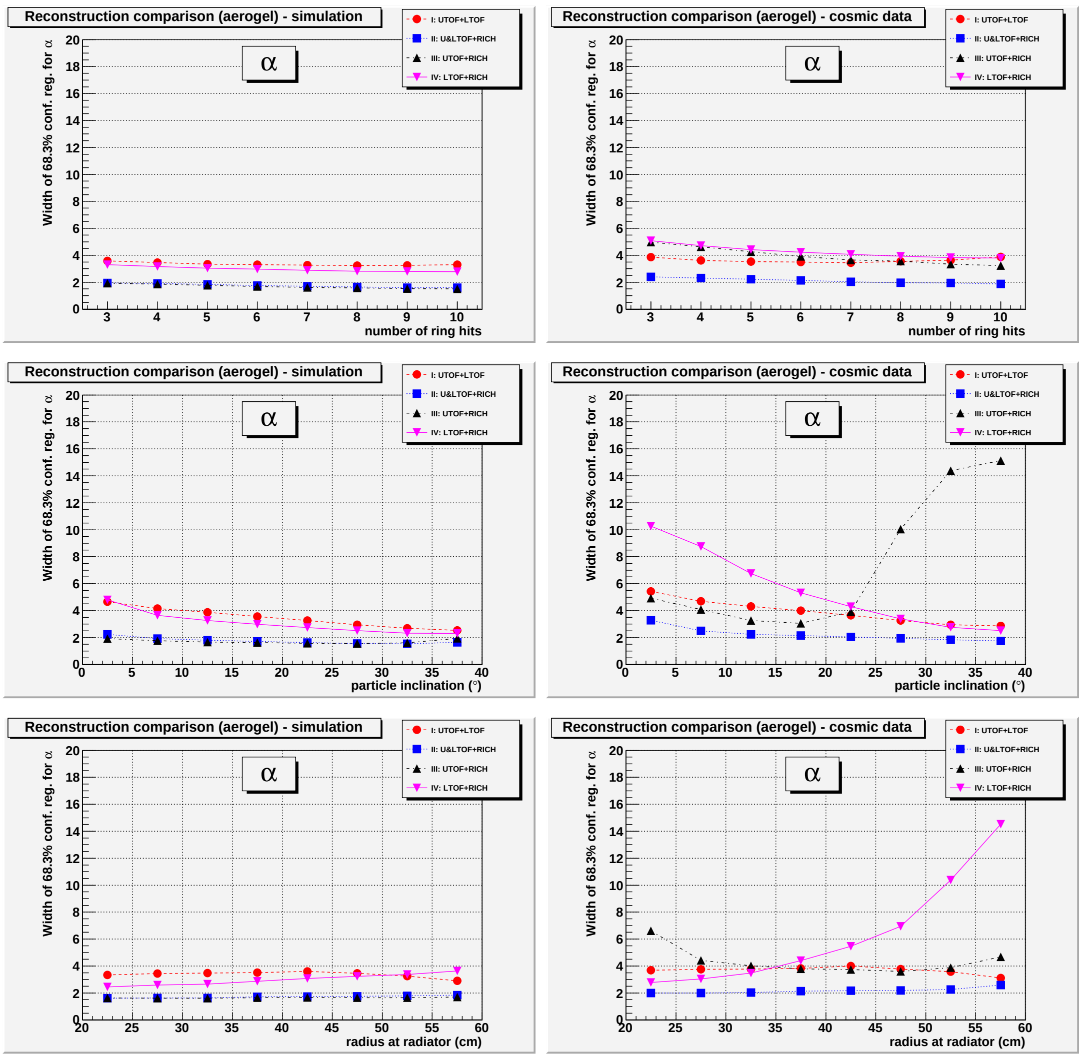

Figure 9.89: *Comparison of results (68.3% percentile) obtained for angle α between TOF-based tracks and Tracker track as function of (top) ring hits, (centre) track inclination and (bottom) radius of radiator impact point (aerogel events): (left) AMS simulation; (right) Cosmic data.*

Particle inclination

Figure 9.90 shows the results obtained for the particle inclination θ. The situation is similar to that observed for α. In simulation reconstruction types II and III have similar quality, followed by type IV and finally type I. For cosmic data the reconstruction for types III and IV has long tails and the best results therefore come from type II.

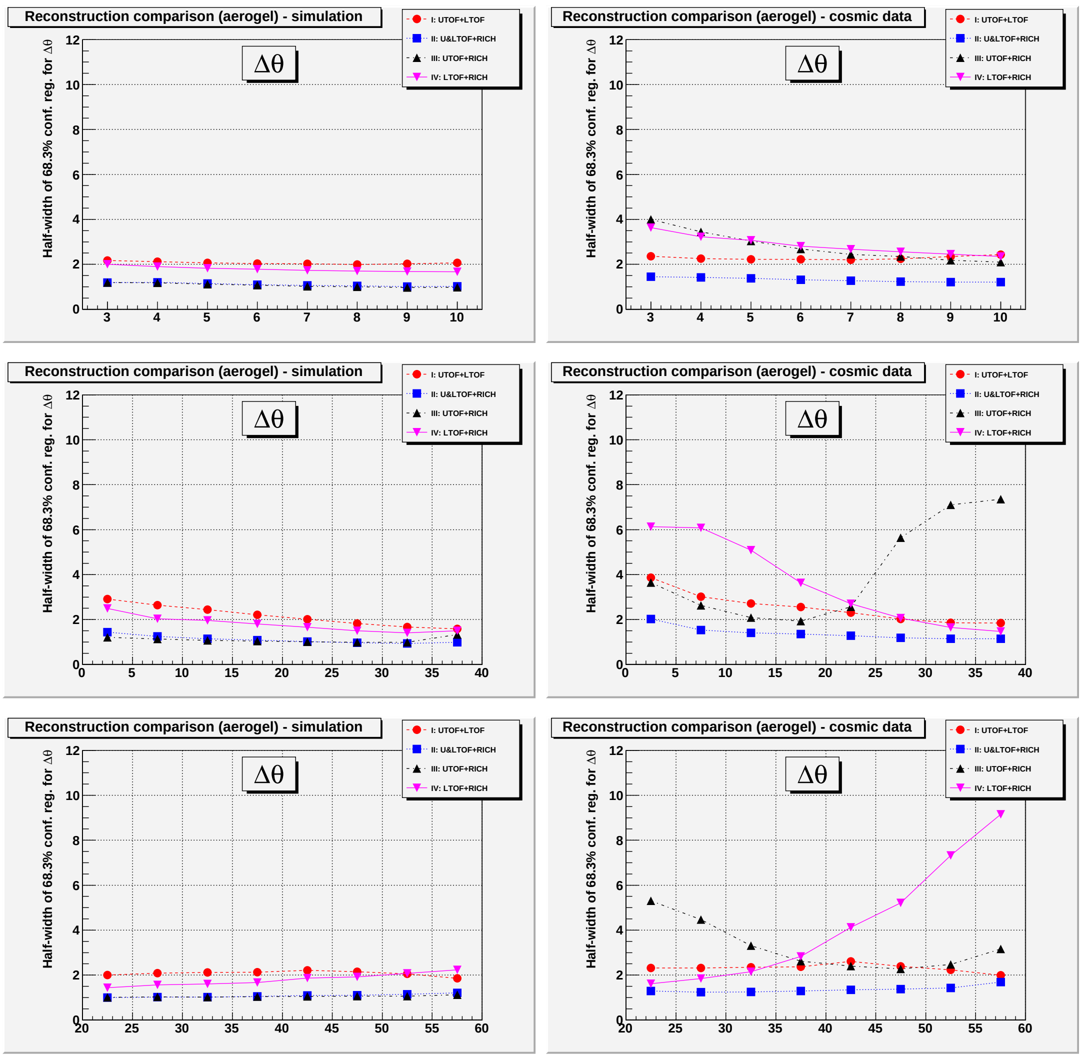

Figure 9.90: *Comparison of results (half-width of 68.3% confidence region) obtained for θ difference between TOF-based tracks and Tracker track as function of (top) ring hits, (centre) track inclination and (bottom) radius of radiator impact point (aerogel events): (left) AMS simulation; (right) Cosmic data.*

Azimuthal angle

Figure 9.91 shows the results obtained for the azimuthal angle ϕ. In the case of simulation the results obtained for types II and III are nearly identical, and better than those obtained for types I and IV. Among the latter, type IV has slightly better results. When the reconstruction quality is displayed as function of the radius at the radiator, it can be seen that, while types II and III have similar good results across all radii, type IV is better for low radii while type I has better results for higher radii, which for $r > 50$ cm are similar to those from types II and III. In the case of cosmic data there is a change in the relative quality of reconstructions due to the additional tails of bad events. Type II has the best results in almost every situation, the exception being events coming from the outer edge of the radiator for which type I is better than type II.

Čerenkov angle

Figure 9.92 shows the results obtained for the Čerenkov angle θ_c. In simulated events three reconstruction types (II, III and IV) have a similar quality, with the best result being obtained for type III, followed closely by types II and IV. Type I, the only one which does not use information from the RICH matrix, has a clearly poorer result. For cosmic data the results obtained are globally similar, althogh some event configurations have poorer results for certain reconstructions. Type II has the best global results.

Position at radiator

Figure 9.93 shows the results obtained for the error in the particle crossing point at the top of the radiator. In the case of simulation the results obtained are clear, with the best reconstruction quality being obtained for types II and III, followed by type IV. In the case of real data the best results are obtained for type II, since type III is strongly affected by tails.

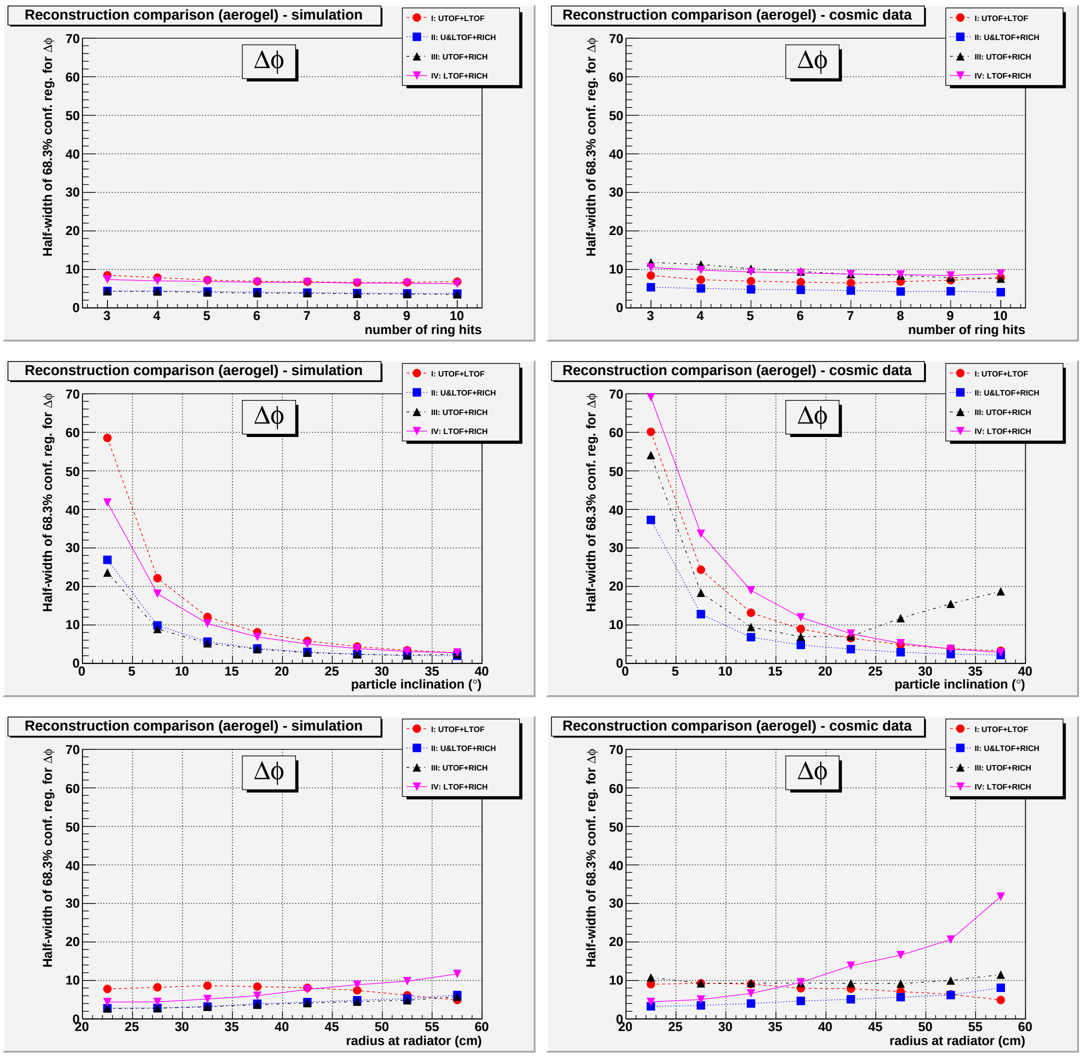

Figure 9.91: *Comparison of results (68.3% percentile) obtained for ϕ difference between TOF-based tracks and Tracker track as function of (top) ring hits, (centre) track inclination and (bottom) radius of radiator impact point (aerogel events): (left) AMS simulation; (right) Cosmic data.*

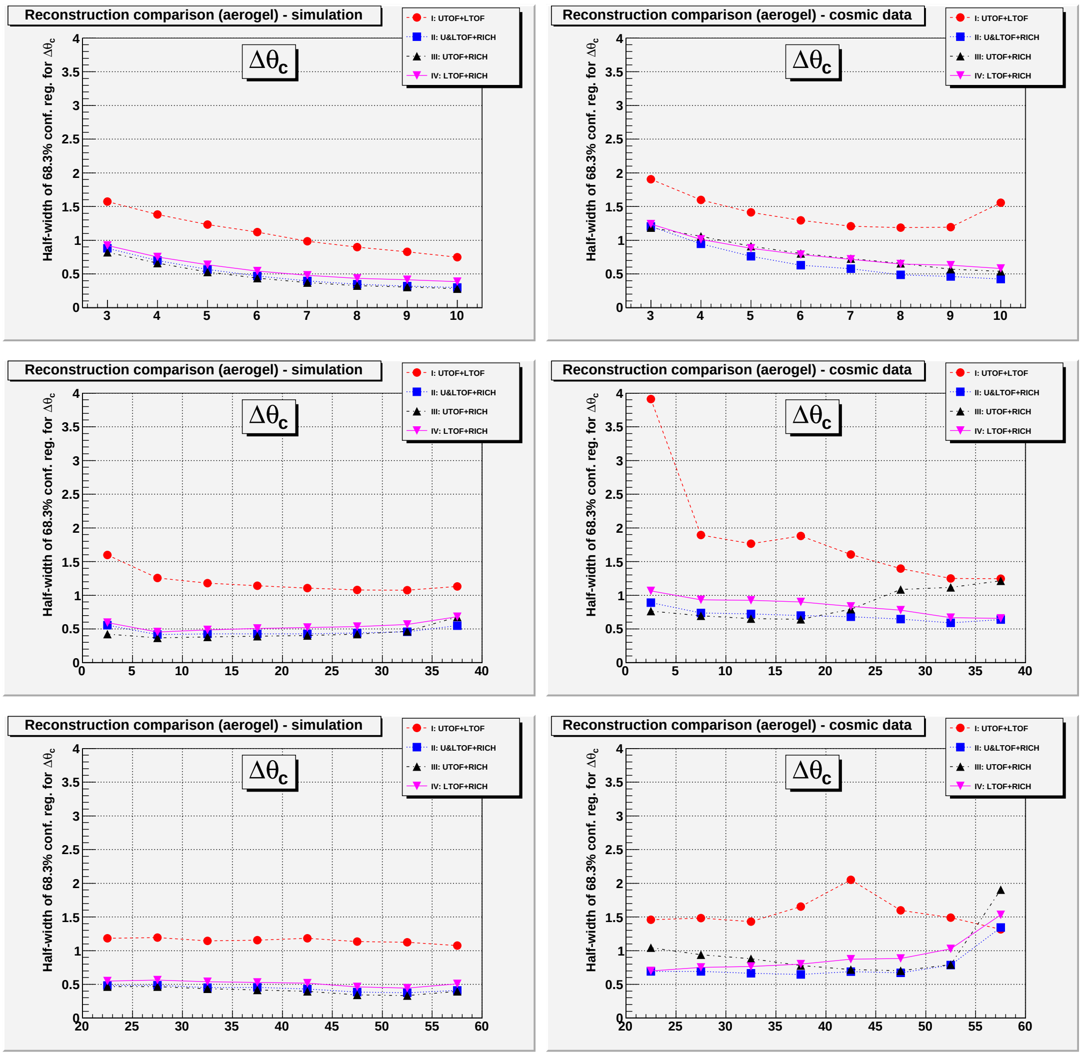

Figure 9.92: *Comparison of results (half-width of 68.3% confidence region) obtained for θ_c difference between TOF-based tracks and Tracker track as function of (top) ring hits, (centre) track inclination and (bottom) radius of radiator impact point (aerogel events): (left) AMS simulation; (right) Cosmic data.*

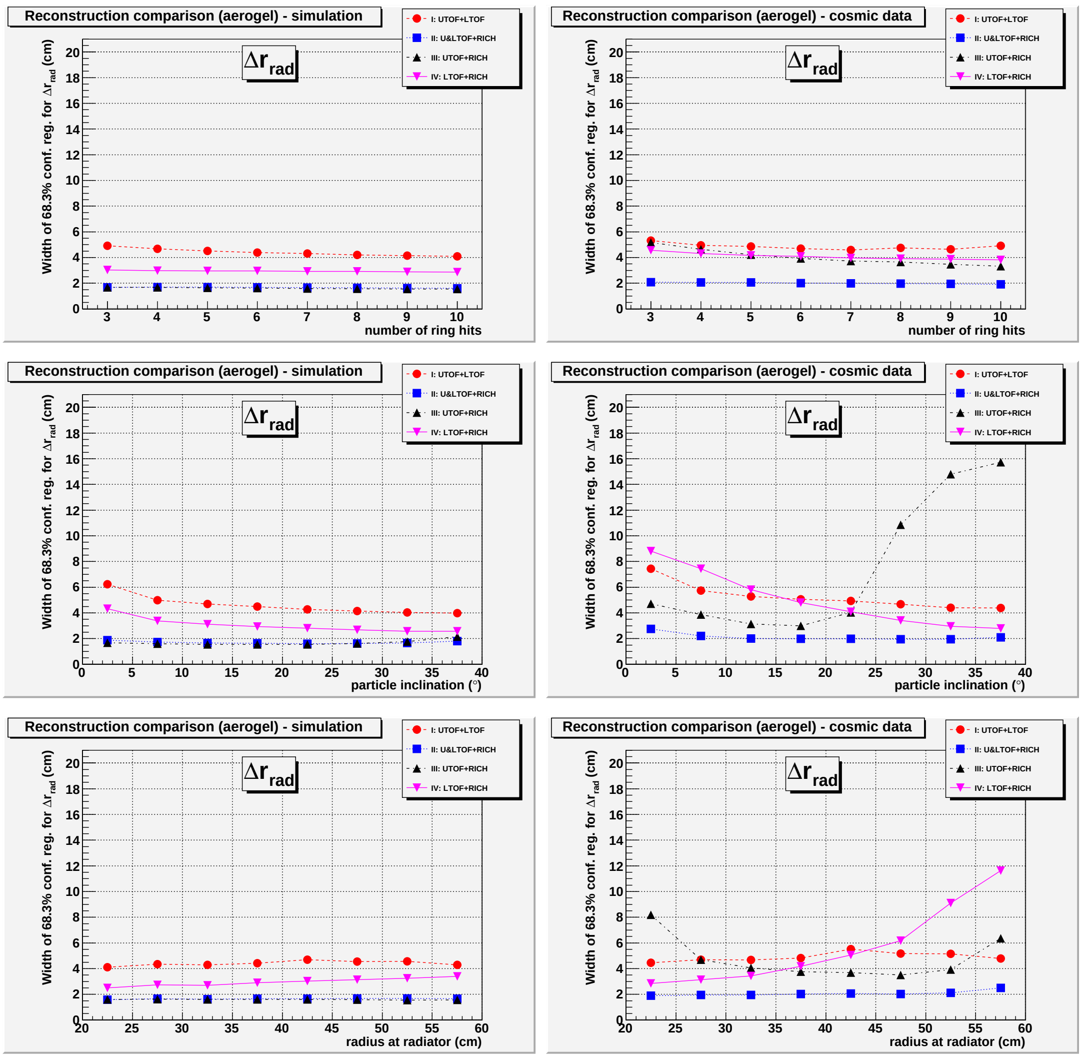

Figure 9.93: *Comparison of results (68.3% percentile) obtained for x-y distance at the top of the radiator between TOF-based tracks and Tracker track as function of (top) ring hits, (centre) track inclination and (bottom) radius of radiator impact point (aerogel events): (left) AMS simulation; (right) Cosmic data.*

Position at detection matrix

Figure 9.94 shows the results obtained for the error in the particle crossing point at the detection matrix. In simulation the reconstruction quality is nearly identical for types II, III and IV, with type III being the best of the three by a very slight margin, and clearly poorer for type I, the only one for which no information from the RICH spot is used. The results for cosmic data are affected by tails in the case of some configurations. In this case, the best global results are obtained for type II.

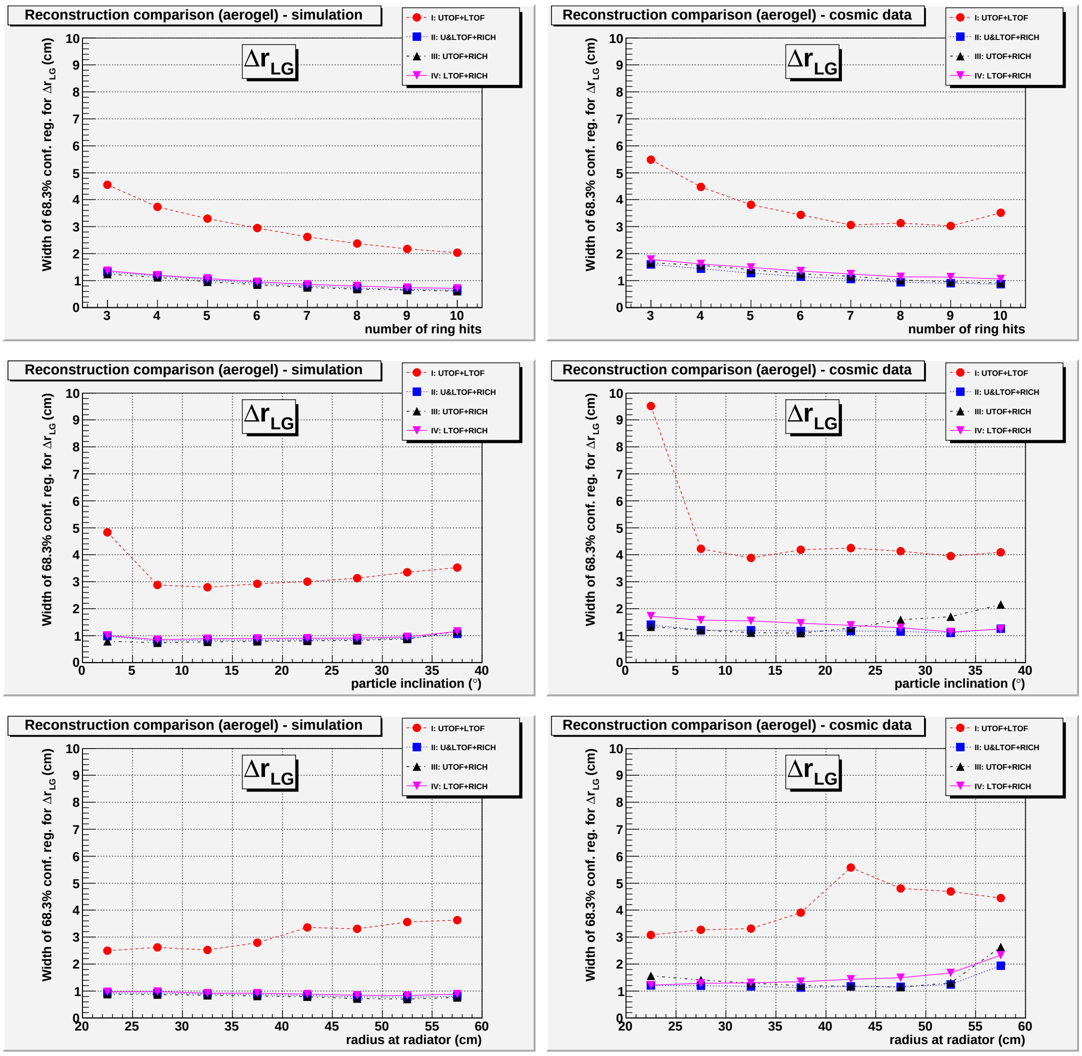

Figure 9.94: *Comparison of results (68.3% percentile) obtained for x-y distance at the detection matrix between TOF-based tracks and Tracker track as function of (top) ring hits, (centre) track inclination and (bottom) radius of radiator impact point (aerogel events): (left) AMS simulation; (right) Cosmic data.*

Result summary

A summary of all results obtained with the four reconstruction types for aerogel events is presented in Table 9.3.

AEROGEL RESULTS

Sample		Simulation				Data			
Rec. type		I	II	III	IV	I	II	III	IV
(planes)		UTOF + LTOF	UTOF +LTOF +RICH	UTOF + RICH	LTOF + RICH	UTOF + LTOF	UTOF +LTOF +RICH	UTOF + RICH	LTOF + RICH
α	68.3%	3.36	1.71	1.64	2.94	3.66	2.12	3.94	4.31
(°)	95.4%	5.97	3.67	3.54	6.21	8.26	4.88	15.2	19.6
$\Delta\theta$	95.4% low	−4.29	−2.46	−2.54	−3.28	−5.54	−3.15	−13.9	−5.52
(°)	68.3% low	−1.92	−1.05	−1.10	−1.21	−2.08	−1.25	−3.63	−1.94
	median	+0.12	0.00	−0.07	+0.47	+0.16	+0.04	−0.25	+0.26
	68.3% high	+2.23	+1.10	+0.99	+2.32	+2.52	+1.39	+1.80	+3.80
	95.4% high	+4.78	+2.87	+2.56	+5.14	+6.01	+3.71	+5.23	+18.4
$\Delta\phi$	68.3%	7.22	3.97	3.80	6.65	7.32	4.64	9.44	9.24
(°)	95.4%	26.8	14.7	13.7	26.0	32.0	17.4	37.9	54.0
$\Delta\theta_c$	95.4% low	−2.33	−1.16	−1.12	−1.29	−2.39	−1.33	−1.38	−2.18
(°)	68.3% low	−0.71	−0.33	−0.30	−0.47	−0.70	−0.39	−0.40	−0.64
	median	+0.17	+0.03	+0.03	−0.02	+0.38	+0.17	+0.12	+0.06
	68.3% high	+1.58	+0.54	+0.50	+0.56	+2.32	+0.98	+1.27	+0.99
	95.4% high	+6.37	+3.84	+3.84	+3.94	+12.7	+10.0	+9.39	+9.52
Δr_{rad}	68.3%	4.43	1.65	1.59	2.93	4.92	2.01	3.95	4.11
(cm)	95.4%	8.60	3.49	3.44	5.78	12.5	5.69	15.4	19.6
Δr_{LG}	68.3%	3.07	0.85	0.80	0.90	4.16	1.18	1.27	1.38
(cm)	95.4%	10.8	3.06	3.03	3.14	18.6	6.76	6.98	7.13

Table 9.3: *Summary of percentile results for TOF-based reconstructions of aerogel events.*

For simulated events the best results are obtained for reconstruction types II (upper TOF+lower TOF+RICH) and III (upper TOF+RICH). Results are very similar for these two reconstructions, but type III gives slightly better results for most parameters, indicating that the additional information provided by the lower TOF is not necessary when data are available for the upper TOF and RICH spot. Reconstruction types I and IV have poorer results, but each of them may be useful in specific situations. Type I is the only one that does not rely on a RICH spot and can therefore be used for the large number of events in which no such spot is present. Type IV, on the other hand, is the only one that does not rely on data from the upper TOF, and still provides a good reconstruction for the matrix impact point and Čerenkov angle, comparable to what is obtained from types II and III. For the best reconstruction types, the typical reconstruction errors are of the order of 2° in track precision, 1° in inclination, 0.5° in Čerenkov angle and 1-2 cm for the particle crossing points at the radiator and at the detection matrix.

The results obtained for cosmic data are clearly poorer than those from simulation and reflect not only a lower reconstruction quality in terms of the main peak of each distribution but also to the appearance of important tails of bad reconstructions, particularly in the case of reconstruction types III and IV. The best results are obtained for type II. Here, unlike the simulation case, the cross-check of information provided by the unique combination of data from the upper TOF, lower TOF and RICH used in this type of reconstruction becomes essential to remove tails and ensure that a good track is obtained in almost every case. There is still some degradation with respect to simulation data, however.

9.4.5.2 NaF events

A summary of all results obtained with the four reconstruction types for NaF events is presented in Table 9.4.

One major feature of NaF results is reduced number of events for which reconstructions of types II (upper TOF+lower TOF+RICH), III (upper TOF+RICH) and IV (lower TOF+RICH) can be obtained. This is due to the central position of the NaF radiator: a large fraction of charged particles generating NaF events do not cross the RICH detection matrix but instead escape through the large central ECAL hole. Only type I (upper TOF+lower TOF) avoids this problem by not using a RICH signal.

The results obtained for simulated events follow the same pattern seen in the case of aerogel, with the best reconstruction quality being obtained for reconstruction types II and III. However, in this case type II has slightly better results than type III. Typical results are $\sim 2°$ for track precision, $\sim 1°$ for particle inclination, $\sim$ 1-2° for Čerenkov angle and $\sim$ 2 cm for the particle crossing points at the radiator and

NaF RESULTS

Sample		**Simulation**				**Data**			
Rec. type		**I**	**II**	**III**	**IV**	**I**	**II**	**III**	**IV**
(planes)		UTOF + LTOF	UTOF +LTOF +RICH	UTOF + RICH	LTOF + RICH	UTOF + LTOF	UTOF +LTOF +RICH	UTOF + RICH	LTOF + RICH
α	68.3%	2.64	1.78	1.88	2.87	4.46	2.57	6.01	3.39
(°)	95.4%	5.54	11.2	13.6	23.0	21.8	9.98	21.3	16.5
$\Delta\theta$	95.4% low	−4.00	−3.77	−5.44	−3.25	−15.7	−3.90	−13.7	−3.95
(°)	68.3% low	−1.65	−1.00	−1.13	−0.90	−2.58	−1.21	−3.02	−1.65
	median	+0.15	+0.12	+0.08	+0.86	+0.27	+0.36	+0.18	+0.52
	68.3% high	+2.14	+1.38	+1.50	+3.03	+2.82	+2.20	+3.22	+3.24
	95.4% high	+4.78	+6.84	+8.24	+19.3	+6.08	+6.80	+11.4	+15.6
$\Delta\phi$	68.3%	5.84	2.46	2.65	3.38	17.4	3.61	9.74	3.78
(°)	95.4%	22.8	27.2	37.8	50.2	105	25.9	112	26.6
$\Delta\theta_c$	95.4% low	−3.00	−21.3	−23.4	−19.1	−3.32	−18.0	−25.6	−3.99
(°)	68.3% low	−0.96	−0.81	−1.13	−0.79	−0.87	−0.97	−11.9	−0.83
	median	+0.27	+0.14	+0.09	+0.24	+0.55	+0.36	+0.22	+0.26
	68.3% high	+1.76	+2.32	+2.35	+4.38	+2.65	+3.96	+9.44	+2.33
	95.4% high	+6.08	+16.2	+23.4	+33.2	+13.4	+33.6	+30.9	+34.9
Δr_{rad}	68.3%	4.46	2.01	2.37	3.27	5.74	3.07	14.0	3.74
(cm)	95.4%	8.11	32.0	35.3	13.1	10.4	17.6	45.1	9.72
Δr_{LG}	68.3%	4.40	2.12	2.38	2.33	7.77	2.49	10.8	2.04
(cm)	95.4%	9.74	42.8	47.7	39.4	25.9	25.2	62.0	24.2

Table 9.4: *Summary of percentile results for TOF-based reconstructions of NaF events.*

detection matrix. Results for type IV are poorer but comparable to those from the types II and III. Very long tails are significant in the three types II, III and IV, meaning that the results obtained are not highly reliable. Results for type I are more interesting from the point of view of reliability, since they have much smaller tails. In addition, a much larger number of events may be reconstructed using type I. The drawback is the precision obtained for the typical track reconstructions, which is not as good as in other types: typical results are $\sim 3°$ for track precision, $\sim 2°$ for particle inclination, $\sim$ 1-2° for Čerenkov angle (the only variable for which there is no significant loss in accuracy) and ~ 4 cm for the particle crossing points.

The results obtained for cosmic data show some differences from simulation. There is a general loss of quality in peak results, which is especially pronounced in the case of type III. The tails of bad reconstructions become important in all cases, including type I, which therefore loses its main advantage. In the case of types II and IV there is in fact a slight improvement in tail results with respect to simulation, but the importance of tails remains very high.

9.5 Conclusions

A method for reconstructing the particle's trajectory and the Čerenkov angle based only on RICH data was developed. The new method was based on the already existing maximum likelihood method developed at LIP. Expansion to a 5-parameter space required the development of a grid of hints and a set of minimizations from selected points. The likelihood function was adapted to be consistent with an uncertain particle track. The charged particle's impact signal on the detection matrix was used as hint. The importance of this hint led to the development of a method for determining the effective depth of the signal produced by a charged particle crossing the detector, which was estimated at 1.8 cm.

The standalone reconstruction method was applied to simulated events generated with the full AMS software and also to real cosmic events collected at CERN in 2008. Results obtained for the aerogel radiator were presented. The results obtained are more satisfactory in the case of the Čerenkov angle θ_c, which was reconstructed with an accuracy better than 2° for simulated events and better than 3° for cosmic data, and for the particle's crossing point at the detection matrix, which is determined with an accurary of a few cm. For other track parameters, however, the results were not satisfactory. The particle's crossing point at the radiator is reconstructed with a typical accuracy of $\sim$ 10-15 cm, meaning that individual events cannot be assigned to a specific location in the radiator. The azimuthal angle ϕ is only roughly determined. Estimates for track inclination θ tend to be biased towards intermediate values, a fact that in combination with spreads $\Delta\theta \gtrsim 7°$ obtained for each specific value of θ means that little information is provided by the reconstruction result.

The limited results of the standalone reconstruction method led to a second approach for track reconstruction with no information from the AMS Tracker. This approach used information from the four planes of the AMS TOF detector in addition to the RICH signal. Four reconstruction variants were developed, each one based on a different kind of track hint: (I) upper and lower TOF; (II) upper and lower TOF plus RICH; (III) upper TOF plus RICH; (IV) lower TOF plus RICH.

Results for each type of reconstruction were presented in detail for both aerogel and NaF events. This approach provided much better results than those obtained from the standalone reconstruction. In simulation the best results were obtained for reconstructions II and III, which proved to be essantially identical, while types I and IV had poorer results, showing that to achieve the best possible track reconstruction it is essential to have information from the two ends of the track (upper TOF and RICH matrix). Precisions of $\sim 2°$ for the particle track, 1-2 cm for crossing positions at the radiator and detection matrix and $\sim 0.5°$ for the Čerenkov angle were obtained in aerogel events.

For cosmic data a lower precision was obtained and unexpected tails of bad reconstructions appeared. Such difference between simulation and data results indicates that improvements will be needed for AMS detector to perform at the expected level. In particular, some bad data appear to be coming from the AMS TOF, especially in events with relatively low inclinations that cross the outermost part of the radiator. The reconstruction of type II, combining data from three distant positions (upper TOF, lower TOF and RICH matrix) proved to be more robust.when dealing with such bad data. The Čerenkov ring itself helps to improve the precision of track reconstruction but it is not free from noise, which appeared to be a problem in events with a high number of ring hits, indicating that the introduction of quality cuts on RICH data may be important in this context. Results from events crossing the outer edge of the radiator and the region near the aerogel/NaF inteface were consistently poorer, indicating that events from such regions are very problematic when dealing with an uncertain track.

The analysis of NaF events was limited by the available statistics and also by the geometry of the detector which essentially excludes any kind of reconstruction using the charged particle's signal on the detection matrix, that is, only reconstruction type I can be applied to a number of events high enough to be considered as a viable method. The precisions obtained for this type of reconstruction are $\sim 2°$ for the particle track, ~ 4 cm for crossing positions at the radiator and detection matrix and $\sim 1°$ for the Čerenkov angle.

Results for the TOF-based reconstruction methods were therefore globally positive, with the algorithms providing reliable rough estimates of the trajectory of charged particles.

Part IV
Physics analysis

Chapter 10

Physics analysis

The AMS-02 detector is expected to provide measurements of the cosmic ray flux in the Earth's vicinity with unprecedented statistics. One of the most important features of the detector will be its capability for mass separation of single-charged particles and mass isotopes, leading to important insights on the origin and propagation of cosmic rays.

To evaluate the detector's mass separation capabilities, detailed studies were performed with simulated events reproducing the expected fluxes of different particles at the International Space Station. It should be noted that all studies presented in this chapter were performed with the pre-April 2010 detector configuration, that is, with the superconducting magnet, and that the subsequent change in the detector may have some impact on mass separation results.

10.1 Motivations for mass separation

Protons are the most abundant component ($\sim 90\%$) of charged cosmic rays reaching the Earth's vicinity. The remaining fraction is essentially made of atomic nuclei (mostly ^{4}He) and single-charged particles such as e^-, e^+ and $\overline{p}$.

Precise measurements of the smaller components present in the cosmic-ray spectrum are essential in the context of the study of cosmic-ray production and acceleration. The required precision can only be attained through very effective charge and mass discrimination methods since the abundances of different components differ by several orders of magnitude.

Ratios such as D/p, ^{3}He/^{4}He and B/C give information on the interstellar medium since all compare the abundances of secondary and primary species. The beryllium isotope ratio ^{10}Be/^{9}Be is a probe for galactic confinement times since both isotopes are secondaries but one of them, ^{10}Be, is unstable, with a half-life of 1.51×10^6 years [145].

The lightest neutralino ($\tilde{\chi}^0_1$), predicted by supersymmetric models, is a strong dark matter candidate. If it exists and accounts for the unexplained dark matter density ($\Omega_c \simeq \Omega_m - \Omega_b \simeq 0.2$) or at least for a significant part of it, neutralino annihilation ($\tilde{\chi}^0_1 \tilde{\chi}^0_1 \rightarrow ...$) must take place and contribute to the observed cosmic ray composition, with the more visible effects occurring in the spectra of antiparticles like e^+, $\overline{p}$ and especially $\overline{\mathrm{D}}$ [64]. Fig. 10.1 shows a comparison between the expected $\overline{\mathrm{D}}$ fluxes from secondary production and from dark matter annihilation.

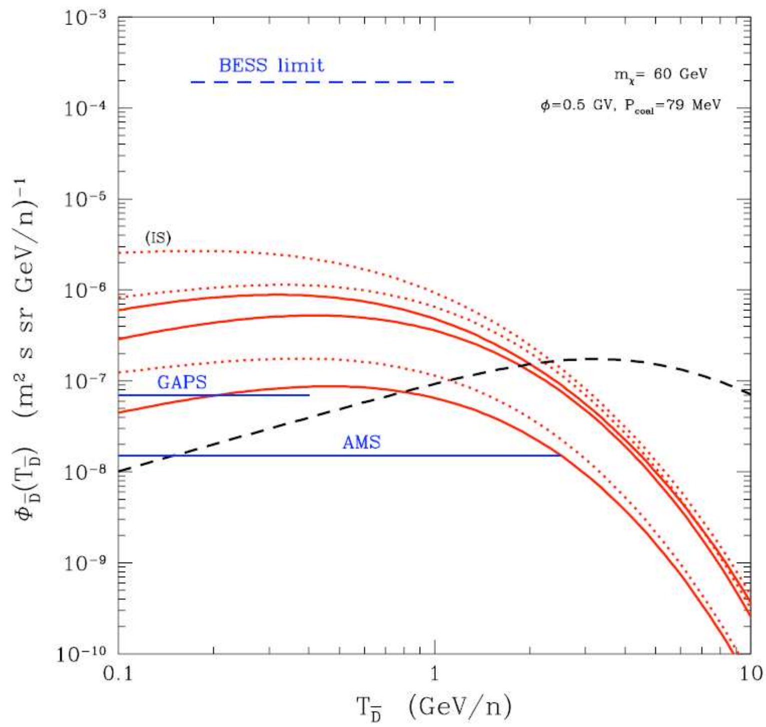

Figure 10.1: *Comparison between expected antideuteron flux from secondary processes (dashed line) and the flux from the annihilation of a 60 GeV dark matter particle (solid lines: solar minimum; dotted lines: interstellar flux). Fluxes from dark matter annihilation are shown for three sets of propagation parameters. (from Ref.* [64]*)*

10.2 D/p and $\overline{\mathrm{D}}/\overline{\mathrm{p}}$ separation

To evaluate the capabilities of AMS-02 for mass separation of deuterons and antideuterons from other particles with the same charge, studies have been performed using the case of deuteron versus proton separation. Separation efficiency for the corresponding antiparticles is expected to be similar.

The large difference between proton and deuteron abundances (D/p $\sim$ 1%) increases the importance of a very effective mass separation to isolate the deuteron signal from a large background of proton events. In the antiparticle case, with $\overline{\mathrm{D}}/\overline{\mathrm{p}} \sim 10^{-5}$, that importance is even bigger.

In the study of D/p separation the full AMS detector simulation was used. Particles were simulated as coming from the top plane of a cube with a side of 3.9 m, corresponding to an acceptance of 47.78 $\mathrm{m}^2\cdot\mathrm{sr}$. Three data samples were chosen. Table 10.1 shows the momentum ranges and number of events simulated in each sample.

Sample	**Momentum range**	**No. events**
p (low momentum)	$0.5 - 10$ GeV/c	3.1×10^8
p (high momentum)	$10 - 200$ GeV/c	1.3×10^8
D	$0.5 - 20$ GeV/c	5.6×10^7

Table 10.1: *Samples used in the D/p separation studies*

For each sample, $\frac{dN}{d(\ln p)}$ = constant. Variable weights were assigned to events in order to compensate for the statistics in each sample and to reproduce a realistic spectrum (Fig. 10.2):

- The simulated proton spectrum followed $dN/dE \propto E^{-2.7}$;
- The simulated deuteron spectrum was calculated combining the proton spectrum above with D/p ratios taken from Ref. [146].

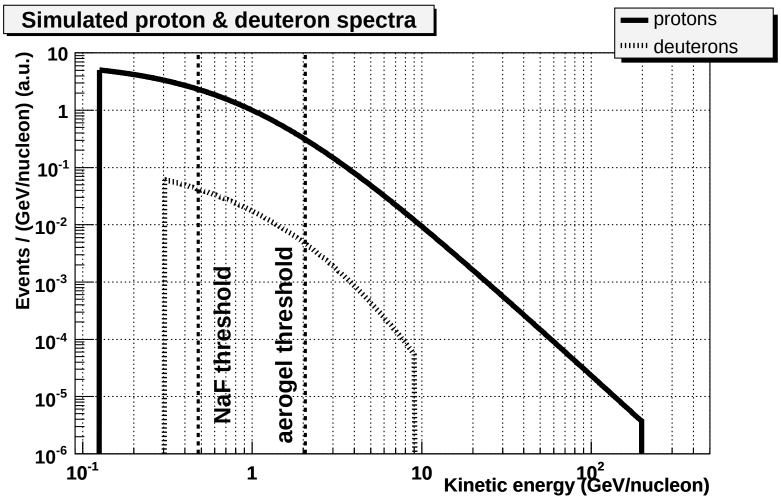

Figure 10.2: *Simulated proton and deuteron spectra used in D/p separation study.*

10.2.1 Preliminary quality cuts

The kind of event reconstruction that is performed with the RICH detector is based on the precise knowledge of the particle's trajectory. Such knowledge, given by the AMS Tracker, is critical for a good reconstruction since it provides four of the five parameters of the Čerenkov cone.

In each event a set of preliminary data selection cuts using readings from different subdetectors of AMS-02 was applied to reduce the fraction of events with a bad reconstruction. These cuts were based on information from the different AMS subdetectors that provided an indication of the reliability of the particle's reconstructed track.

Only downgoing events ($\beta > 0$) were accepted. In addition, events were accepted if the following conditions were satisfied:

- Only one particle was detected in the event;
- A particle track was reconstructed by the Silicon Tracker;
- No clusters were found in the Anti-Coincidence Counters;
- Clusters from at least 3 TOF planes (out of 4) were used for event reconstruction;
- At most one additional cluster was allowed in the TOF;

- At least 6 Tracker layers (out of 8) were used in the track reconstruction;
- Compatibility was required for the rigidity measurements obtained from two different algorithms, with $\Delta R/R < 3\%$;
- Compatibility was also required for the rigidity measurements obtained from each half of the Tracker (upper and lower), with $\Delta R/R < 50\%$;
- The particle's impact point on the RICH radiator was less than 58 cm from the centre (i.e. more than 2 cm from the mirror);
- At most one track was present in the TRD;
- The TOF and Tracker charge reconstructions were compatible.

Among the events that triggered the detector, $\sim 15\%$-20% of proton events and $\sim 10\%$-15% of deuteron events in the relevant region of kinetic energy (few GeV/nucleon) passed this set of preliminary cuts, corresponding to an acceptance of ~ 0.3 m^2·sr for protons and ~ 0.2 m^2·sr for deuterons.

10.2.2 RICH quality cuts

The reconstruction of particle masses was then performed for events having a signal in the RICH detector. The extremely accurate velocity measurement provided by the RICH ($\Delta\beta/\beta \sim 10^{-3}$ in the case of protons and deuterons) is crucial to reduce the background level. For the final distributions the inverse of the reconstructed particle mass $1/m$ was used instead of the mass due to a more symmetric peak being expected for this variable. A series of event selection cuts were introduced, based on data provided by the RICH and the results of two reconstruction algorithms, the standard LIP maximum likelihood method and a geometrical method developed at CIEMAT [147]. These cuts were developed to test the robutsness of ring reconstruction, their purpose being to exclude bad events where a poor velocity reconstruction would lead to particle misidentification.

The cuts applied to RICH events were the following:

- A Čerenkov ring was reconstructed using each method, and at least 3 hits were used in both cases;

- The total ring signal was not higher than 10 photoelectrons in NaF events, and not higher than 15 photoelectrons in aerogel events;
- A Kolmogorov test to the uniformity of the hits azimuthal distribution in the ring gave a result of at least 0.2 in the case of NaF events, and 0.03 in the case of aerogel events;
- Compatibility was required for the velocity measurements from the TOF and RICH detectors, with $\Delta\beta/\beta < 10\%$;
- Compatibility was also required for the velocity measurements obtained from the two RICH reconstruction methods, with $\Delta\beta/\beta < 0.3\%$ for NaF events, and $\Delta\beta/\beta < 0.1\%$ for aerogel events;
- The reconstructed, rounded electric charge obtained from the geometrical method was 1 or 2;
- The reconstructed, non-rounded electric charge obtained from the likelihood method was between 0.5 and 1.5 in NaF events, and between 0.6 and 1.4 in aerogel events;
- The ring acceptance (visible fraction), as estimated by the likelihood method, was at least 20% in NaF events, and at least 40% in aerogel events;
- The number of noisy hits not associated to the crossing of the charged particle (i.e., hits that were far from the reconstructed ring and far from the estimated crossing point of the charged particle in the detection matrix) was not higher than 2 in NaF events, and not higher than 3 in aerogel events.

10.2.3 Analysis results

Results obtained show that mass separation of particles with $Z = 1$ is feasible even if one species is orders of magnitude more abundant than the other. This is the case of D/p separation, which is possible up to $E_{kin} \sim 8$ GeV/nucleon. Some examples of the mass distributions obtained are shown in Figs. 10.3 and 10.4. Solid lines show the mass distributions before the RICH cuts were taken into consideration.

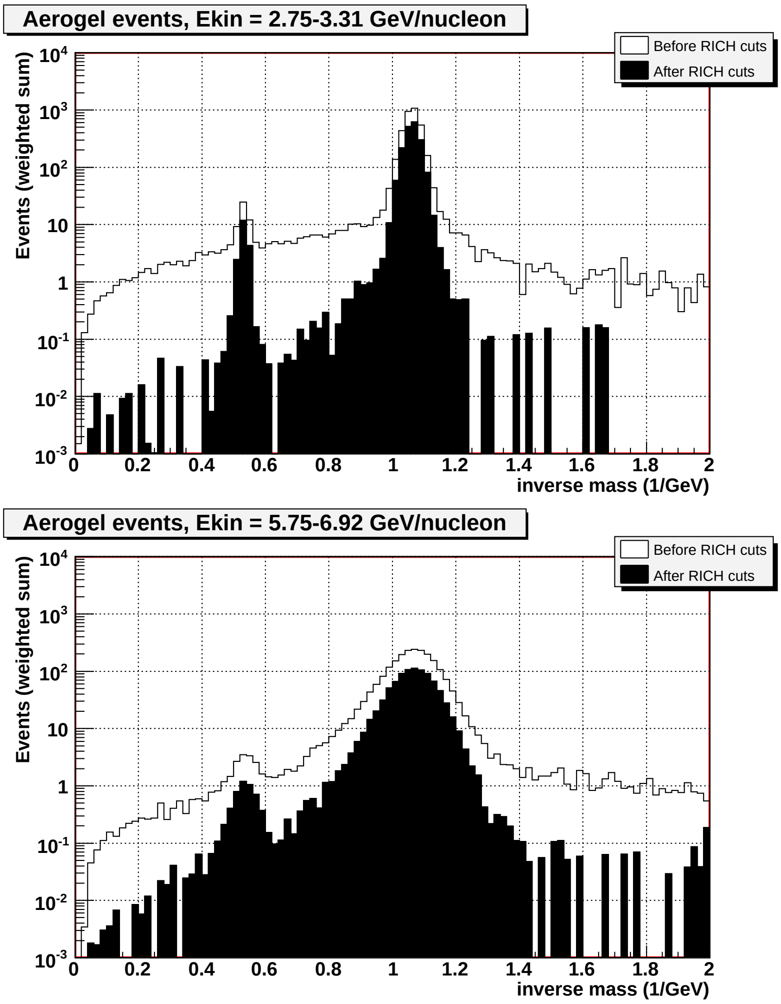

Figure 10.3: *D/p separation: examples of inverse mass distribution in aerogel events for two energy regions.*

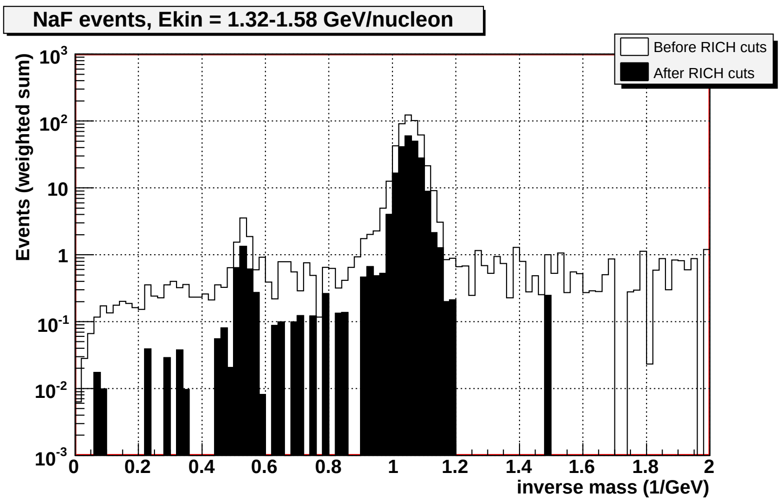

Figure 10.4: *D/p separation: example of inverse mass distribution in NaF events.*

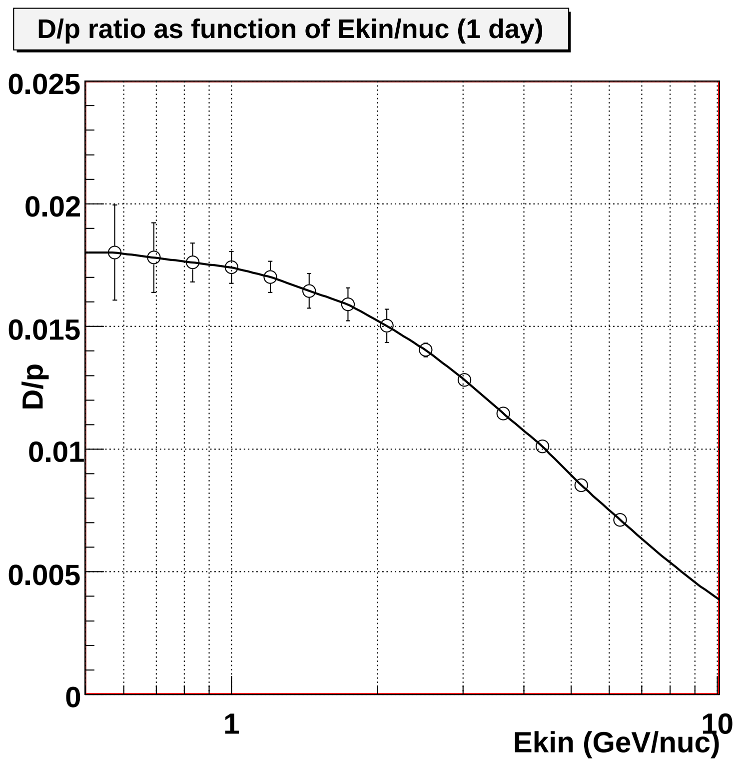

Figure 10.5: *Expected sensitivity of AMS for D/p ratio with one day of data. The solid curve (from Ref.* [146]*) corresponds to the expected ratio.*

Fig. 10.5 shows the expected sensitivity of AMS for the D/p ratio after one day of data taking. Results show that a single day of AMS-02 statistics will be sufficient to improve on the existing data for this ratio.

After all cuts, an acceptance of $\sim$ 0.07 m^2·sr was obtained for protons, and $\sim$ 0.05 m^2·sr for deuterons at $E_{kin} > 3$ GeV/nucleon (Fig. 10.6). The increase by a factor $\sim$ 10 in the acceptance above the aerogel threshold $E_{kin} = 2.1$ GeV/nucleon reflects the relative dimensions of the two radiators in the RICH detector.

The main background in the deuteron case comes from non-Gaussian tails of proton events with a bad velocity reconstruction. Errors in rigidity reconstruction ($\Delta R/R \sim 2\%$ in the GeV region) are not critical for this case.

The quality of D/p separation was evaluated by calculating the rejection factor obtained from the analysis procedure. The rejection factor Rej may be defined as the improvement that is obtained in the signal/background ratio in the selected event sample with respect to the original flux ratio, that is,

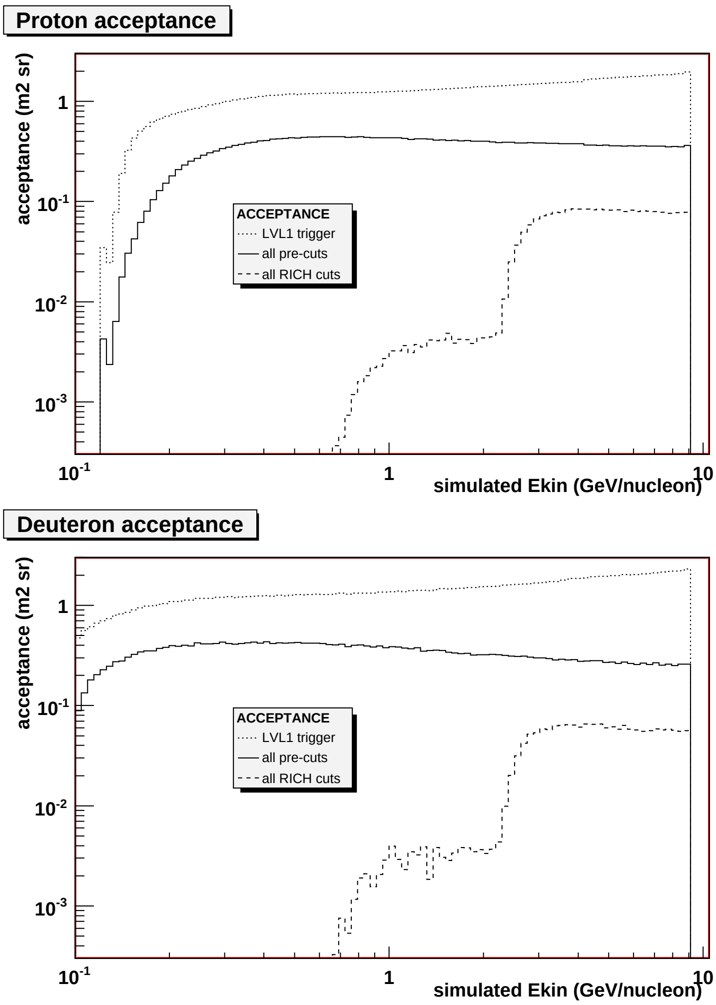

Figure 10.6: *Acceptance for protons (top) and deuterons (bottom) at different stages of event analysis. The lower line in each plot corresponds to the final acceptance.*

$$\frac{N_S}{N_B} = \frac{\Phi_{\mathrm{D}}}{\Phi_{\mathrm{p}}} Rej$$

where N_S is the number of deuterons correctly identified as such and N_B is the number of protons identified as deuterons, giving

$$Rej = \frac{N_S}{N_B} \frac{\Phi_{\mathrm{p}}}{\Phi_{\mathrm{D}}}$$

The final statistics N_S and N_B may be expressed, respectively, as

$$N_S = \Phi_{\mathrm{D}}\, Acc_{\mathrm{D}}\, \varepsilon_{\mathrm{D}\to\mathrm{D}}\, \Delta t$$
$$N_B = \Phi_{\mathrm{p}}\, Acc_{\mathrm{p}}\, \varepsilon_{\mathrm{p}\to\mathrm{D}}\, \Delta t$$

where Acc_{p} and Acc_{D} are the final detector acceptances (after all quality cuts are applied) for each particle type, and $\varepsilon_{\mathrm{D}\to\mathrm{D}}$ and $\varepsilon_{\mathrm{p}\to\mathrm{D}}$ are the probabilities of each kind of particle being classified (by reconstructed mass) as a deuteron.

The rejection factor may therefore be expressed as

$$Rej = \frac{Acc_{\mathrm{D}}}{Acc_{\mathrm{p}}} \frac{\varepsilon_{\mathrm{D}\to\mathrm{D}}}{\varepsilon_{\mathrm{p}\to\mathrm{D}}}$$

The results obtained for the rejection factor are presented in Fig. 10.7. In the optimal region immediately above the aerogel radiation threshold (corresponding to $E_{kin} < 5$ GeV/nucleon) rejection factors higher than 10^4 were attained. Only a lower bound could be given in this case, since no proton contamination was found in this region. The best relative mass resolutions for protons (Fig. 10.8) and deuterons are $\sim 2\%$ for both radiators in the regions above their respective thresholds.

The specific set of cuts shown here corresponds to an example of a selection procedure. Other variations are possible. In particular, rejection factors may be improved by applying stricter cuts, at the expense of a further acceptance reduction.

The results from the D/p separation study may be used to estimate the detector's ability to detect a significant antideuteron signal. We define the signal sensitivity $Sens$ for $\overline{\mathrm{D}}/\overline{\mathrm{p}}$ separation as

$$Sens = \frac{N_S}{\sqrt{N_B}} = \frac{\Phi_{\overline{\mathrm{D}}}\, Acc_{\overline{\mathrm{D}}}\, \varepsilon_{\overline{\mathrm{D}}\to\overline{\mathrm{D}}}}{\sqrt{\Phi_{\overline{\mathrm{p}}}\, Acc_{\overline{\mathrm{p}}}\, \varepsilon_{\overline{\mathrm{p}}\to\overline{\mathrm{D}}}}} \sqrt{\Delta t}$$

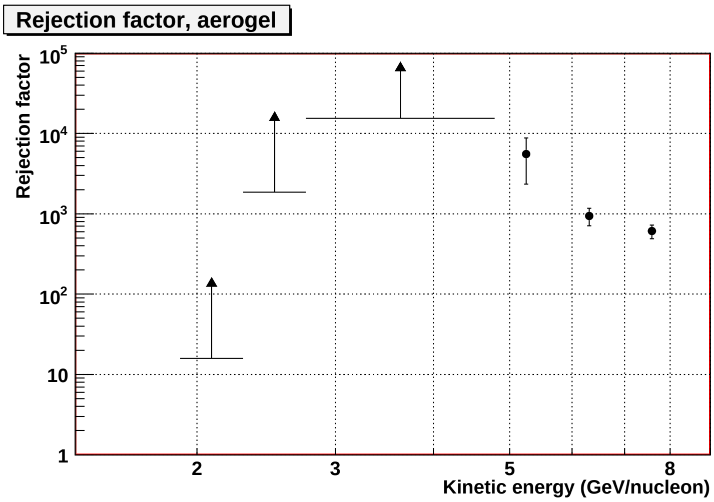

Figure 10.7: *Rejection factor for D/p separation in aerogel events.*

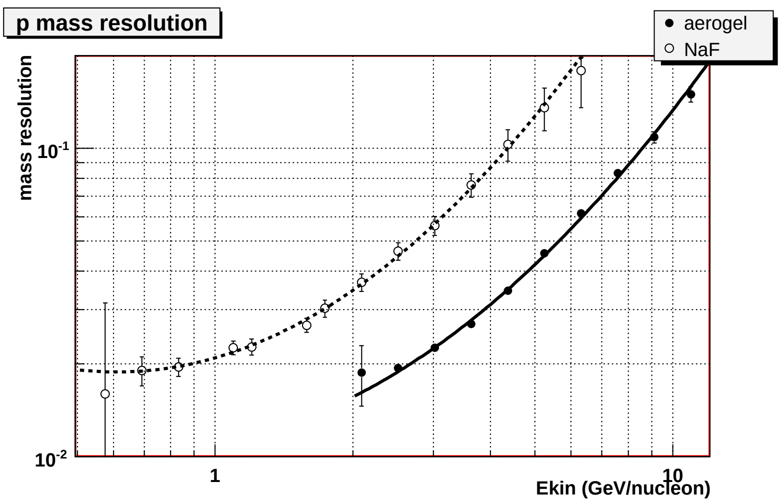

Figure 10.8: *Relative mass resolution for protons: NaF events (open dots) and aerogel events (filled dots).*

where in this case N_S is the number of antideuterons correctly identified as such and N_B is the number of antiprotons identified as antideuterons.

Such estimate was performed is the context of this work, assuming that the acceptance and rejection quality for $\overline{\text{D}}/\overline{\text{p}}$ are similar to those obtained for D/p, and that a significant detection requires a signal at the 3σ level, that is $Sens = 3$.

Unlike the rejection factor, the signal sensitivity is function of the time period considered ($Sens \propto \sqrt{\Delta t}$). A time period of 3 years (the minimum expected for AMS-02) was assumed for this calculation. The expected antiproton flux was taken from Ref. [63] and corresponds to a solar minimum.

The results obtained are shown in Fig. 10.9. The best results are obtained for the kinetic energy region between 2.8 and 4.8 GeV/nucleon, where the lower limit obtained for the rejection factor ($Rej > 1.6 \times 10^4$) corresponds to an upper limit on the minimum flux of 9×10^{-8} m^{-2} s^{-1} sr^{-1} (GeV/nuc)$^{-1}$. The remainder of the energy region of typical aerogel events, up to $\sim$ 8 GeV/nuc, has minimum fluxes between 10^{-7} and 10^{-6} m^{-2} s^{-1} sr^{-1} (GeV/nuc)$^{-1}$. A comparison of these results to those of the expected antideuteron fluxes presented in Fig. 10.1 shows that for the region between 2.8 and 4.8 GeV/nucleon it should be possible to detect the expected secondary antideuteron flux, which is approximately twice the upper limit obtained.

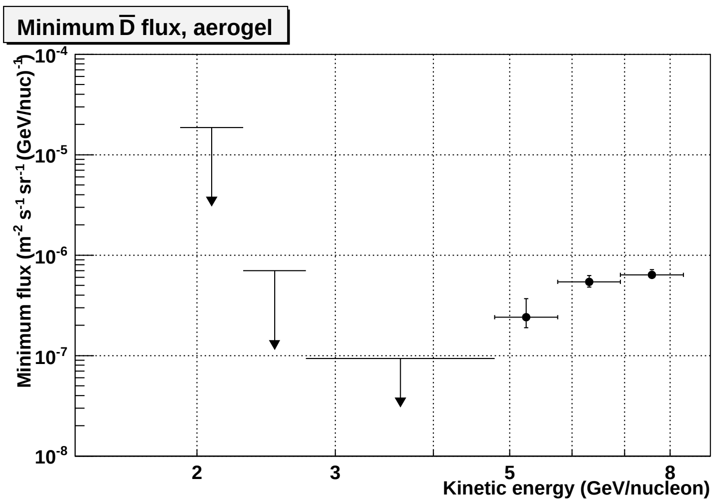

Figure 10.9: *Minimum antideuteron flux for a significant signal ($N_S/\sqrt{N_B} = 3$) to be obtained in $\overline{\text{D}}/\overline{\text{p}}$ separation in aerogel events with 3 years of data, as extrapolated from the rejection factor results of Fig. 10.7.*

10.3 ^{3}He/^{4}He and ^{10}Be/^{9}Be separation

Separation of light isotopes in AMS-02 was studied in the framework of the standalone RICH simulation using samples of simulated helium and beryllium events. Knowledge of isotopic ratios for these two elements has important implications on models of cosmic-ray production and propagation. In the case of helium, this happens because ^{4}He is a primary species, while ^{3}He is a secondary species produced in spallation reactions. In the case of beryllium, both isotopes ^{9}Be and ^{10}Be are secondaries but ^{9}Be is stable while ^{10}Be decays with a half-life $t_{1/2} = 1.51 \times 10^6$ years [145], which is of the order of galactic confinement times.

Only events above the geomagnetic cutoff were considered for simulation. The total number of events simulated was 2.0×10^6 in the case of helium, corresponding to one day of statistics, and 8.5×10^5 for beryllium, corresponding to the expected statistics for one year. Detailed statistics are presented in Table 10.2.

Element total	Isotope totals	
He : $\mathbf{2.02 \times 10^6}$	^{3}He : 3.39×10^5	^{4}He : 1.68×10^6
Be : $\mathbf{8.47 \times 10^5}$	^{9}Be : 6.97×10^5	^{10}Be : 1.49×10^5

Table 10.2: *Statistics for He and Be simulations used in mass separation study*

Figures 10.10 and 10.11 show the results obtained for isotopic ratios compared with the simulated distributions. Data from previous experiments are also shown for comparison. Satisfactory fits were obtained for the kinetic energy regions from the Čerenkov thresholds of each radiator up to ~ 3 GeV/nucleon (NaF) and ~ 10 GeV/nucleon (aerogel). These figures clearly show that even a small fraction of the expected AMS statistics will represent a major improvement on existing results for both elements.

10.4 Mass resolution and separation power

The studies described in the previous section led to the determination of mass resolution and separation power for different energies from fit results. In addition, a similar study was performed for D/p separation power in the RICH simulation,

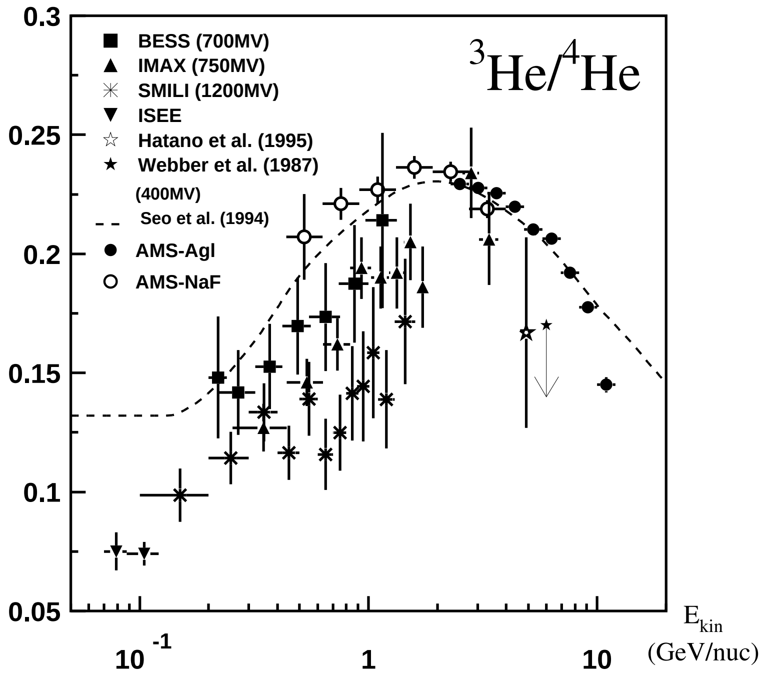

Figure 10.10: *Reconstruction of simulated ^{3}He/^{4}He ratio in AMS compared with data from other experiments* [148, 149, 150, 151, 152, 153]. *The simulated curve is from Ref.* [154].

providing a cross-check for the AMS simulation results described in Section 10.2. A total of 1.61×10^7 proton and 1.39×10^5 deuteron events, corresponding to one day of statistics, was used for aerogel studies, while the NaF response was evaluated using 1.52×10^7 proton and 1.31×10^5 deuteron events, corresponding to approximately one week of data.

Separation power was defined as the ratio $\frac{\Delta m}{\sigma_m}$. Figure 10.12 shows the results obtained for mass resolution and separation power as functions of kinetic energy for both radiators. Optimal mass resolutions were reached around 1 GeV/nucleon in NaF and 3 GeV/nucleon in aerogel. D/p results were similar to those obtained with the full AMS simulation.

Separation power is higher for lighter elements, suggesting isotope separation should be possible up to higher energies in the D/p case. However, the greater difference between proton and deuteron statistics (D/p $\sim 10^{-2}$) compared to the cases of He and Be isotopes eventually leads to the separation also being limited to

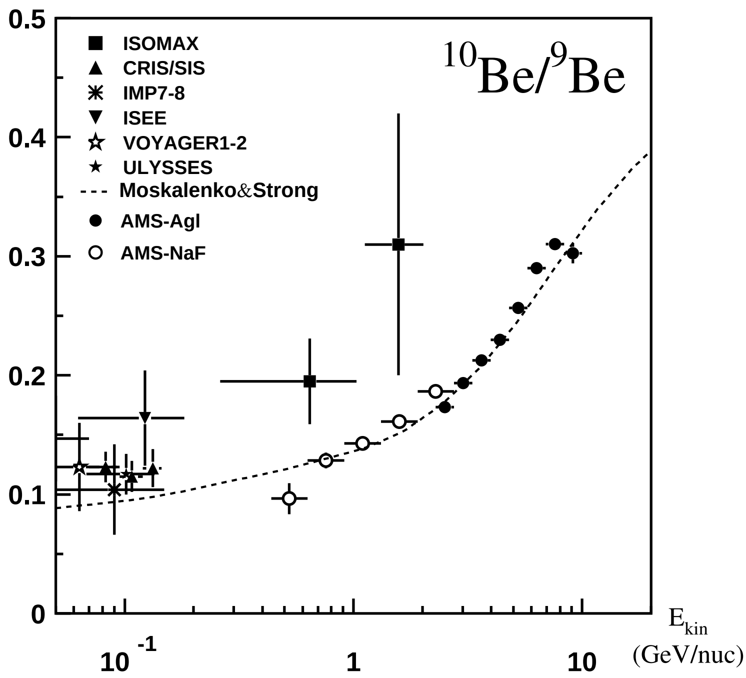

Figure 10.11: *Reconstruction of simulated $^{10}Be/^{9}Be$ ratio in AMS compared with data from other experiments* [155, 156, 157, 158, 159, 160]. *The simulated curve is from Ref.* [161].

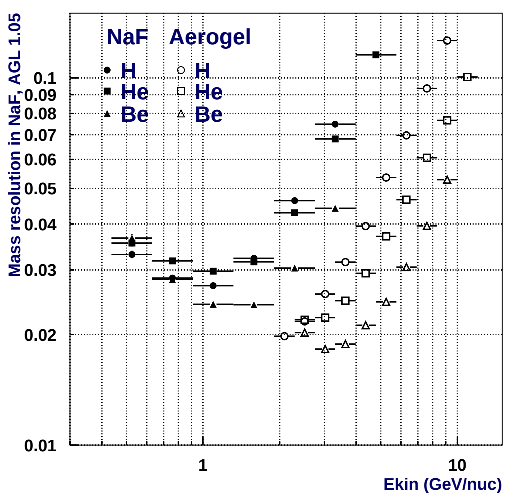

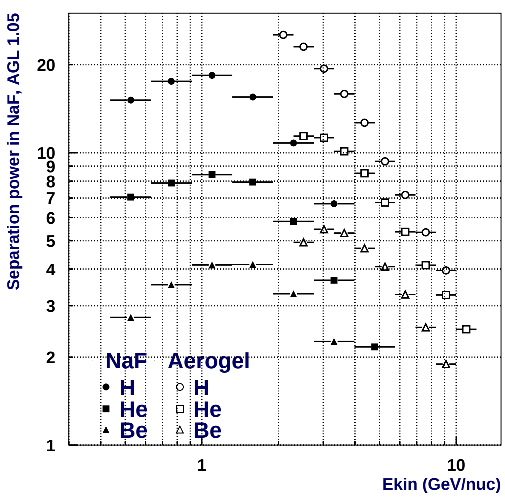

Figure 10.12: *Simulation results for mass resolution* (left) *and separation power* (right).

$\sim$ 10 GeV/nucleon like in heavier elements.

10.5 Conclusions

AMS-02 will provide a major improvement on the current knowledge of cosmic rays. Detailed simulations have been performed (using the detector configuration with a superconducting magnet) to evaluate the detector's particle identification capabilities, in particular those of the RICH, at the level of mass separation. These results may change as a consequence of the detector's new configuration with a permanent magnet decided in April 2010.

Simulation results show that the separation of light isotopes is feasible. Using a set of simple cuts based on event data, relative mass resolutions of $\sim$ 2% and rejection factors higher than 10^4 have been attained in D/p separation at kinetic energies of a few GeV/nucleon. The separation procedure presented here might be crucial for the identification of an antideuteron flux. An estimate derived from the D/p rejection factors indicates that for the detection of antideuterons in the region between 2.8 and 4.8 GeV/nucleon after 3 years of data taking a minimum flux no higher than 9×10^{-8} m^{-2} s^{-1} sr^{-1} (GeV/nuc)$^{-1}$ is needed, which is already lower than the estimated secondary antideuteron flux in that region. In the case of deuterons, their identification against the proton background is possible up to $\sim$ 8 GeV/nucleon. Results obtained for mass separation were confirmed by two independent simulations (full AMS simulation and RICH standalone simulation).

The separation of another two light elements, He and Be, was also studied. Simulation results show that ^{3}He/^{4}He and ^{10}Be/^{9}Be separation up to $\sim$ 10 GeV/nucleon is feasible. The most favourable mass resolutions obtained were similar to those in the D/p case, that is, $\sim$ 2%. Results from AMS on light isotope separation will provide new insights on the production and propagation of cosmic rays.

Conclusions

The research effort of the AMS collaboration leading to the construction of the final AMS-02 detector included the construction of a preliminary detector AMS-01, flown aboard the Space Shuttle in 1998, and detailed studies using ground-based prototypes, as well as the development of realistic detector simulations. A number of studies performed as part of this effort were described in the present document.

A method for charge reconstruction using scintillators in a high-momentum beam test was developed for application to data collected in the October 2003 RICH prototype test. Charge separation was proven to be feasible up to $Z \simeq 30$, with a charge resolution ranging from ~ 0.15 charge units for the lightest elements to ~ 0.35 for iron. Such results provided an independent charge measurement that was subsequently used to validate RICH charge measurements.

The light yield of seven aerogel samples tested with the RICH prototype in 2002 and 2003 was evaluated, using a detailed procedure that corrected for several systematic effects involved. The final results of this study indicated that one aerogel sample with $n = 1.05$, supplied by the Boreskov Institute of Catalysis in Novosibirsk, had the highest light yield by a wide margin, and led to the choice of the aforementioned aerogel material for the AMS-02 RICH detector.

A study of aerogel light yield was also performed for the AMS-02 RICH, using cosmic-ray data collected after the AMS-02 detector's first assembly in 2008. The same study was made for data coming from two independent detector simulations. A result of 9.0 photoelectrons was obtained from cosmics for the expected light yield in a fully-contained Čerenkov ring generated from a singly-charged particle with perpendicular incidence. This result was clearly lower than the ones obtained with simulations (11.2 and 10.5 p.e.) and also lower than the result obtained from a detailed extrapolation of RICH prototype data taking detector differences into account (12.2 p.e.), giving a possible indication of insufficient knowledge of the AMS-02 RICH detector. Data from the 2008 cosmic-ray test were also used to detect a displacement of the RICH detector with respect to the expected track position of the order of 1 mm in both x and y. In addition, the stability of measurements was tested by comparing light yield results from 98 data runs. Fluctuations at the level of 1% were observed.

Novel methods for the reconstruction of particle trajectory and Čerenkov angle without information from the Tracker were developed and applied to simulated single-charged events and also to cosmic data collected at ground level in 2008. Poor results were obtained in the context of a standalone reconstruction based solely on information from the RICH. Some success was achieved in the case of the Čerenkov angle, where an accuracy better than 2° for simulated events and 3° for cosmic data was obtained, but track reconstruction proved extremely difficult, with RICH entry points having an uncertainty of $\sim$ 10-15 cm. This study also included a calculation of the effective depth of the signal produced by a charged particle crossing the AMS-02 detector, which was evaluated at 1.8 cm. Better results were obtained for a family of algorithms combining RICH and TOF data, with information TOF planes used to obtain a rough estimate for the particle's trajectory. Precisions of $\sim 2°$ for the particle track, 1-2 cm for crossing positions at the radiator and detection matrix and $\sim 0.5°$ for the Čerenkov angle were obtained in the case of simulated aerogel events. However, these promising results could not be reproduced with similar quality in the case of real data, indicating that the detector's data acquisition needs to be improved to correspond to the design goals.

Simulation studies were performed on the capabilities of the AMS-02 RICH for mass separation in the case of light isotopes (D/p, ^{3}He/^{4}He, and ^{10}Be/^{9}Be), the techniques developed for D/p being extensible to the similar case of antideuteron identification ($\overline{\mathrm{D}}/\overline{\mathrm{p}}$). The separation of light isotopes proved feasible up to kinetic energies of $\sim$ 8 GeV/nucleon in the D/p case and $\sim$ 10 GeV/nucleon in the He and Be cases. Relative mass reslutions of $\sim$ 2% were attained in all cases. A lower limit higher than 10^4 was placed on the rejection factor for the best region in the D/p case, leading to the possibility of detecting the expected flux of secondary antideuterons with kinetic energies of a few GeV/nucleon and suggesting that AMS may be able to reach the level of $\overline{\mathrm{D}}/\overline{\mathrm{p}}$ separation ($\sim 10^5$) needed for the identification of a possible dark matter signal in the antideuteron channel. It should be noted, however, that these simulation studies were performed before changes in the final AMS-02 configuration were decided in April 2010, among those the inclusion of the permanent magnet instead of the superconducting magnet. The impact of these detector changes on mass separation is still to be evaluated.

The assembly and testing of the AMS-02 detector at CERN is finished. The detector will now be sent to Kennedy Space Center where it will be mounted on the Space Shuttle and fly to the International Space Station in February 2011. Once installed on the ISS, AMS-02 will acquire data for a minimum of three years. A total statistics of more than 10^{10} events will be collected, providing a major improvement on the current knowledge of cosmic rays and giving new insights on the detection of dark matter and the existence of cosmological antimatter.

Appendix A

Scintillator calibration tables for the 2003 beam test

Calibration results for Scintillator 1 (page 1/4: runs 506-525)

X_Z^a for each run

Z	506	510	511	513	514	515	516	517	518	519	520	525
0	374	374	374	374	374	374	374	374	374	374	374	374
1	385	385	385	385	385	385	385	385	385	385	385	385
2	418	418	418	418	418	418	418	418	416	418	418	418
3	473	473	477	473	473	473	473	473	473	473	473	477
4	546	550	550	546	546	546	550	550	542	550	546	550
5	637	652	652	637	637	637	652	652	637	647	642	652
6	740	762	762	746	740	746	757	762	740	751	746	768
7	852	874	874	846	852	852	857	868	846	863	852	880
8	959	995	989	959	959	959	971	983	959	977	965	995
9	1072	1114	1108	1072	1072	1072	1090	1102	1067	1096	1078	1114
10	1184	1230	1230	1184	1184	1184	1207	1224	1183	1207	1195	1236
11	1298	1343	1337	1298	1292	1292	1315	1332	1293	1320	1303	1349
12	1406	1457	1451	1400	1406	1406	1429	1446	1401	1429	1411	1463
13	1515	1572	1572	1509	1509	1515	1538	1555	1504	1543	1520	1583
14	1621	1680	1680	1615	1615	1615	1648	1669	1610	1648	1626	1691
15	1730	1790	1790	1719	1719	1719	1746	1774	1704	1757	1730	1796
16	1829	1902	1902	1818	1824	1829	1852	1880	1814	1863	1835	1902
17	1926	1997	1997	1921	1921	1931	1954	1978	1911	1964	1935	2007
18	2023	2101	2096	2013	2018	2028	2054	2080	2008	2059	2028	2106
19	2117	2206	2196	2112	2117	2117	2154	2175	2107	2159	2127	2206
20	2211	2297	2288	2206	2215	2215	2247	2270	2201	2247	2220	2302
21	2302	2388	2379	2292	2292	2297	2329	2365	2297	2347	2315	2379
22	2392	2470	2462	2380	2380	2392	2425	2450	2375	2429	2400	2466
23	2474	2552	2540	2466	2462	2474	2495	2527	2458	2507	2478	2552
24	2552	2635	2639	2544	2544	2548	2585	2614	2536	2598	2564	2631
25	2631	2712	2708	2627	2627	2623	2670	2697	2612	2670	2639	2724
26	2708	2789	2789	2700	2704	2700	2735	2770	2689	2739	2712	2797
27	2785	2866	2858	2777	2774	2777	2812	2847	2765	2816	2789	2874
28	2854	2943	2931	2854	2851	2847	2889	2924	2842	2893	2854	2951
29	2931	3020	3005	2931	2924	2924	2966	3001	2919	2970	2912	3028
30	3008	3097	3082	3008	3001	3001	3043	3078	2996	3047	2989	3105

Calibration results for Scintillator 1 (page 2/4: runs 526-543)

X_Z^a for each run

Z	**526**	**527**	**529**	**530**	**531**	**532**	**533**	**538**	**539**	**540**	**542**	**543**
0	374	374	374	374	374	374	374	370	370	370	370	370
1	385	385	385	385	385	385	385	382	382	382	382	382
2	418	418	418	418	418	418	418	417	417	417	417	417
3	477	477	477	477	477	473	473	472	472	472	472	472
4	550	550	550	550	550	550	550	548	548	548	548	548
5	647	647	647	652	647	647	647	644	644	644	644	634
6	762	757	757	757	757	757	757	747	747	747	758	732
7	874	874	868	868	868	868	868	852	852	852	864	842
8	989	989	983	989	983	983	983	970	970	970	982	946
9	1102	1102	1096	1108	1108	1096	1102	1085	1085	1085	1102	1062
10	1224	1224	1218	1224	1224	1218	1218	1198	1198	1198	1220	1175
11	1332	1332	1332	1332	1332	1326	1326	1308	1308	1308	1331	1281
12	1446	1451	1440	1446	1451	1446	1440	1421	1421	1421	1441	1387
13	1561	1566	1549	1561	1566	1549	1555	1523	1523	1523	1555	1487
14	1669	1675	1664	1675	1675	1658	1658	1628	1628	1639	1662	1597
15	1774	1779	1774	1779	1785	1774	1774	1742	1742	1742	1770	1702
16	1891	1885	1885	1885	1885	1880	1880	1835	1835	1845	1874	1802
17	1983	1988	1978	1983	1988	1983	1978	1932	1942	1952	1972	1893
18	2085	2085	2080	2080	2091	2070	2075	2032	2032	2051	2079	1992
19	2180	2180	2169	2180	2190	2169	2164	2125	2125	2145	2170	2079
20	2274	2279	2270	2270	2274	2261	2265	2225	2225	2234	2266	2175
21	2365	2365	2361	2365	2365	2356	2356	2315	2306	2315	2350	2270
22	2450	2454	2437	2441	2454	2441	2441	2392	2392	2400	2434	2350
23	2532	2540	2523	2527	2536	2523	2515	2468	2477	2477	2504	2426
24	2610	2618	2610	2618	2618	2594	2594	2558	2549	2566	2590	2518
25	2681	2700	2677	2689	2697	2677	2685	2639	2639	2645	2664	2590
26	2766	2774	2751	2762	2774	2754	2762	2702	2696	2709	2730	2661
27	2847	2858	2828	2835	2851	2835	2839	2772	2772	2772	2800	2727
28	2924	2935	2905	2908	2928	2912	2916	2842	2842	2842	2870	2797
29	3001	3012	2982	2985	3005	2989	2993	2912	2912	2912	2940	2867
30	3078	3089	3059	3062	3082	3066	3070	2982	2982	2982	3010	2937

Calibration results for Scintillator 1 (page 3/4: runs 544-587)

X_Z^a for each run

Z	**544**	**545**	**546**	**575**	**579**	**580**	**581**	**583**	**584**	**585**	**586**	**587**
0	370	370	370	370	364	364	364	364	364	364	364	364
1	382	382	382	382	397	402	402	402	402	402	402	402
2	417	417	417	416	504	504	504	504	504	512	512	512
3	472	472	472	474	666	676	676	676	676	676	676	687
4	548	548	548	550	874	887	874	887	887	887	887	901
5	644	644	644	649	1143	1155	1143	1155	1155	1168	1168	1168
6	752	747	758	756	1388	1399	1388	1410	1399	1432	1421	1421
7	858	858	864	869	1607	1617	1607	1627	1617	1656	1636	1636
8	970	976	982	986	1803	1821	1803	1830	1821	1858	1840	1840
9	1091	1091	1096	1102	1986	2003	1986	2003	2003	2037	2037	2020
10	1209	1209	1209	1217	2155	2179	2171	2187	2179	2218	2202	2195
11	1319	1319	1319	1335	2313	2328	2313	2342	2328	2378	2364	2349
12	1431	1431	1431	1440	2458	2483	2458	2496	2483	2521	2508	2502
13	1544	1539	1544	1562	2583	2617	2597	2624	2610	2651	2644	2630
14	1651	1651	1651	1670	2718	2741	2724	2741	2741	2786	2769	2764
15	1756	1756	1761	1779	2832	2861	2838	2866	2855	2900	2895	2878
16	1859	1859	1864	1877	2946	2969	2946	2986	2957	3026	2997	2997
17	1957	1957	1962	1994	3060	3096	3065	3091	3070	3147	3106	3101
18	2060	2051	2069	2086	3162	3189	3167	3189	3176	3244	3208	3212
19	2145	2150	2165	2182	3253	3284	3263	3294	3279	3345	3309	3314
20	2243	2248	2252	2268	3355	3384	3350	3388	3374	3441	3412	3398
21	2330	2334	2346	2353	3450	3474	3445	3474	3465	3537	3499	3503
22	2419	2419	2422	2438	3547	3564	3547	3568	3564	3619	3590	3607
23	2495	2504	2504	2521	3632	3661	3632	3661	3656	3718	3680	3684
24	2574	2578	2590	2599	3727	3756	3718	3737	3746	3813	3775	3780
25	2658	2655	2658	2683	3823	3837	3813	3833	3842	3909	3871	3876
26	2727	2720	2730	2760	3919	3933	3909	3929	3938	4005	3967	3972
27	2797	2790	2807	2829	4015	4029	4005	4025	4034	4101	4063	4068
28	2867	2860	2870	2901	4111	4125	4101	4121	4130	4197	4159	4164
29	2937	2930	2947	2973	4207	4221	4197	4217	4226	4293	4255	4260
30	3007	3000	3010	3045	4303	4317	4293	4313	4322	4389	4351	4356

Calibration results for Scintillator 1 (page 4/4: runs 588-614)

X_Z^a for each run

Z	588	589	590	591	599	607	612	613	614
0	364	364	364	364	368	370	366	366	366
1	408	408	408	408	402	385	374	374	374
2	512	512	512	512	512	399	399	399	399
3	687	676	687	687	685	440	438	438	438
4	901	901	901	901	890	493	488	488	490
5	1180	1180	1180	1180	1163	559	552	552	552
6	1432	1432	1432	1432	1415	631	620	624	624
7	1646	1646	1656	1656	1636	706	695	695	699
8	1849	1858	1849	1858	1834	785	773	773	777
9	2037	2037	2037	2045	2019	867	851	851	851
10	2218	2218	2218	2226	2192	942	927	927	931
11	2371	2378	2371	2386	2346	1021	1005	1001	1005
12	2521	2527	2514	2521	2490	1091	1077	1074	1081
13	2651	2664	2657	2657	2631	1174	1145	1153	1153
14	2781	2786	2792	2786	2752	1249	1230	1227	1238
15	2900	2906	2906	2912	2867	1315	1295	1295	1302
16	3020	3014	3026	3020	2978	1387	1358	1373	1373
17	3126	3126	3126	3137	3091	1461	1431	1443	1439
18	3230	3226	3235	3235	3195	1526	1500	1503	1500
19	3330	3335	3335	3335	3285	1591	1572	1568	1559
20	3431	3441	3436	3431	3390	1656	1637	1633	1633
21	3518	3532	3528	3532	3485	1725	1704	1697	1691
22	3607	3619	3615	3619	3570	1786	1768	1762	1752
23	3708	3713	3718	3718	3660	1851	1832	1825	1812
24	3804	3809	3813	3813	3750	1916	1897	1890	1874
25	3900	3905	3909	3909	3840	1981	1962	1955	1939
26	3996	4001	4005	4005	3930	2046	2027	2020	2004
27	4092	4097	4101	4101	4020	2111	2092	2085	2069
28	4188	4193	4197	4197	4110	2176	2157	2150	2134
29	4284	4289	4293	4293	4200	2241	2222	2215	2199
30	4380	4385	4389	4389	4290	2306	2287	2280	2264

Calibration results for Scintillator 2 (page 1/4: runs 506-525)

X_Z^b for each run

Z	506	510	511	513	514	515	516	517	518	519	520	525
0	283	283	283	283	283	283	283	283	283	283	283	283
1	299	299	299	299	299	299	299	299	299	299	299	299
2	372	372	372	372	372	372	372	372	368	372	372	372
3	494	494	496	494	494	494	494	494	494	494	494	496
4	674	661	653	663	674	674	661	661	664	661	663	653
5	876	878	878	865	876	876	878	878	876	878	876	867
6	1090	1091	1091	1090	1081	1092	1091	1091	1090	1091	1090	1091
7	1319	1312	1312	1297	1308	1308	1298	1301	1308	1311	1308	1312
8	1520	1524	1522	1504	1510	1510	1507	1503	1522	1511	1515	1513
9	1702	1701	1700	1686	1694	1694	1690	1683	1693	1698	1695	1692
10	1863	1862	1862	1844	1852	1852	1853	1846	1856	1853	1860	1861
11	2014	2013	2005	1993	1990	1993	1995	1990	2004	2003	2001	2004
12	2140	2140	2134	2116	2122	2125	2126	2121	2134	2126	2125	2127
13	2261	2255	2255	2234	2234	2240	2238	2237	2244	2247	2240	2249
14	2372	2367	2361	2346	2346	2346	2354	2350	2356	2355	2352	2361
15	2481	2475	2470	2452	2452	2452	2453	2449	2454	2463	2457	2464
16	2577	2575	2570	2545	2550	2555	2550	2541	2555	2560	2555	2560
17	2670	2675	2670	2640	2640	2650	2649	2640	2646	2659	2649	2669
18	2768	2765	2760	2734	2739	2749	2745	2734	2747	2750	2741	2757
19	2856	2855	2846	2824	2829	2829	2834	2818	2838	2839	2833	2842
20	2938	2938	2930	2905	2914	2914	2919	2905	2918	2919	2913	2934
21	3025	3021	3013	2988	2991	2996	2996	2992	3008	3013	3000	3008
22	3107	3103	3098	3070	3079	3087	3084	3075	3083	3090	3079	3091
23	3188	3180	3172	3157	3157	3165	3149	3149	3164	3165	3161	3168
24	3265	3257	3261	3230	3234	3234	3234	3230	3245	3247	3246	3241
25	3342	3334	3330	3307	3311	3303	3315	3311	3319	3315	3319	3333
26	3419	3411	3411	3384	3389	3384	3379	3384	3396	3385	3392	3403
27	3495	3488	3480	3465	3455	3465	3452	3461	3473	3464	3465	3476
28	3563	3560	3546	3538	3523	3530	3523	3535	3545	3539	3527	3550
29	3640	3637	3618	3613	3595	3605	3594	3610	3625	3614	3583	3626
30	3721	3714	3695	3690	3672	3687	3668	3687	3705	3691	3660	3703

Calibration results for Scintillator 2 (page 2/4: runs 526-543)

X_Z^b for each run

Z	**526**	**527**	**529**	**530**	**531**	**532**	**533**	**538**	**539**	**540**	**542**	**543**
0	283	283	283	283	283	283	283	272	272	272	272	272
1	299	299	299	299	299	299	299	294	294	294	294	294
2	372	372	372	372	372	372	372	365	365	365	365	365
3	496	496	497	496	496	488	488	487	487	487	487	487
4	653	653	661	653	653	653	653	646	646	646	646	668
5	867	867	867	878	867	867	867	861	861	861	861	871
6	1091	1080	1080	1080	1080	1080	1080	1079	1079	1079	1088	1078
7	1312	1301	1301	1301	1301	1301	1301	1290	1290	1290	1290	1310
8	1513	1502	1511	1513	1503	1503	1511	1501	1501	1501	1498	1504
9	1683	1682	1683	1692	1692	1674	1691	1683	1683	1683	1679	1687
10	1854	1846	1847	1854	1846	1846	1847	1839	1839	1831	1836	1845
11	1998	1984	1998	1991	1984	1984	1984	1987	1987	1972	1974	1983
12	2127	2121	2121	2121	2115	2115	2115	2112	2112	2100	2091	2109
13	2244	2238	2232	2238	2232	2221	2232	2233	2233	2221	2219	2225
14	2356	2350	2345	2351	2344	2334	2339	2331	2331	2332	2331	2339
15	2459	2453	2454	2453	2454	2444	2449	2442	2442	2431	2436	2438
16	2561	2550	2551	2550	2545	2536	2541	2537	2532	2527	2534	2538
17	2655	2655	2645	2650	2646	2636	2636	2636	2634	2623	2623	2630
18	2751	2747	2742	2738	2738	2721	2728	2717	2709	2712	2723	2725
19	2836	2832	2820	2824	2828	2813	2811	2820	2810	2807	2810	2810
20	2921	2921	2912	2908	2908	2896	2908	2900	2892	2889	2896	2896
21	3004	3000	2999	2999	2992	2984	2992	2990	2972	2972	2977	2981
22	3087	3080	3072	3074	3079	3066	3072	3067	3055	3055	3063	3059
23	3168	3157	3150	3157	3157	3145	3139	3143	3137	3128	3127	3135
24	3245	3227	3233	3242	3234	3211	3213	3226	3205	3205	3203	3221
25	3315	3307	3302	3311	3314	3291	3303	3304	3296	3281	3276	3287
26	3400	3383	3377	3384	3395	3366	3377	3367	3355	3356	3340	3358
27	3477	3472	3454	3455	3476	3443	3450	3437	3430	3423	3404	3432
28	3550	3552	3526	3524	3550	3517	3523	3507	3504	3493	3477	3504
29	3626	3637	3597	3598	3626	3593	3598	3577	3577	3563	3549	3574
30	3703	3714	3672	3675	3703	3671	3675	3647	3647	3633	3619	3644

Calibration results for Scintillator 2 (page 3/4: runs 544-587)

X_Z^b for each run

Z	**544**	**545**	**546**	**575**	**579**	**580**	**581**	**583**	**584**	**585**	**586**	**587**
0	272	272	272	-52	287	287	287	287	287	287	287	287
1	294	294	294	-34	315	319	320	320	320	319	319	319
2	365	365	365	18	406	404	406	406	406	411	411	411
3	487	487	487	134	549	558	559	558	559	558	558	568
4	646	646	646	289	742	749	742	749	755	744	749	761
5	861	861	861	491	994	994	994	994	1007	994	1007	1007
6	1079	1079	1088	708	1257	1250	1257	1270	1263	1268	1276	1276
7	1290	1289	1290	921	1520	1506	1520	1531	1519	1528	1529	1530
8	1490	1489	1499	1122	1766	1757	1760	1781	1777	1778	1772	1779
9	1673	1673	1680	1305	1991	1976	1980	1987	1999	1991	2004	1995
10	1830	1837	1830	1462	2175	2170	2179	2188	2194	2190	2193	2193
11	1969	1977	1969	1610	2359	2337	2341	2361	2364	2363	2373	2367
12	2093	2093	2093	1735	2498	2495	2484	2526	2520	2516	2523	2524
13	2218	2213	2218	1851	2645	2640	2643	2668	2664	2654	2667	2663
14	2323	2324	2323	1955	2771	2760	2768	2782	2793	2795	2795	2799
15	2423	2428	2428	2060	2892	2887	2892	2916	2917	2912	2928	2921
16	2522	2532	2532	2168	3012	3002	3006	3039	3029	3034	3032	3040
17	2614	2623	2622	2266	3121	3134	3122	3145	3145	3154	3144	3145
18	2709	2708	2716	2352	3241	3239	3237	3256	3264	3261	3256	3270
19	2791	2805	2805	2445	3341	3342	3342	3369	3372	3366	3364	3378
20	2876	2889	2886	2523	3442	3443	3432	3469	3468	3469	3471	3463
21	2957	2971	2977	2607	3534	3535	3529	3560	3559	3560	3560	3569
22	3047	3058	3054	2684	3634	3626	3632	3664	3663	3649	3657	3677
23	3116	3137	3127	2763	3729	3730	3724	3768	3763	3749	3754	3758
24	3184	3205	3203	2836	3826	3826	3811	3846	3855	3845	3851	3855
25	3268	3283	3270	2917	3923	3909	3908	3943	3952	3942	3948	3952
26	3343	3353	3344	2984	4020	4006	4005	4040	4049	4039	4045	4049
27	3408	3420	3416	3045	4117	4103	4102	4137	4146	4136	4142	4146
28	3476	3490	3479	3118	4214	4200	4199	4234	4243	4233	4239	4243
29	3546	3560	3556	3191	4311	4297	4296	4331	4340	4330	4336	4340
30	3616	3630	3619	3264	4408	4394	4393	4428	4437	4427	4433	4437

Calibration results for Scintillator 2 (page 4/4: runs 588-614)

X_Z^b for each run

Z	588	589	590	591	599	607	612	613	614
0	287	287	287	287	290	288	288	288	288
1	323	323	323	323	318	306	306	306	306
2	411	411	411	411	410	361	361	361	361
3	567	558	567	567	559	457	459	452	452
4	756	756	756	756	745	588	590	582	589
5	1007	1007	1007	1007	998	749	751	750	742
6	1275	1275	1275	1275	1260	928	920	929	920
7	1529	1529	1540	1540	1516	1118	1109	1109	1108
8	1779	1790	1772	1782	1775	1304	1304	1295	1295
9	2001	2001	1992	2001	1987	1494	1483	1473	1465
10	2199	2199	2196	2205	2191	1668	1652	1650	1650
11	2364	2369	2364	2379	2358	1834	1816	1808	1809
12	2524	2524	2516	2524	2504	1988	1976	1963	1972
13	2661	2667	2666	2669	2650	2122	2099	2102	2095
14	2795	2795	2802	2806	2781	2250	2241	2223	2232
15	2920	2926	2922	2938	2901	2360	2348	2337	2338
16	3039	3041	3043	3045	3021	2464	2443	2458	2452
17	3147	3158	3149	3163	3141	2569	2547	2557	2554
18	3261	3266	3270	3271	3245	2662	2650	2644	2644
19	3363	3374	3373	3377	3350	2762	2764	2741	2732
20	3468	3479	3478	3481	3455	2855	2857	2833	2838
21	3559	3574	3572	3583	3550	2949	2947	2917	2914
22	3660	3676	3671	3677	3645	3035	3039	3005	2999
23	3768	3773	3777	3777	3740	3125	3133	3096	3089
24	3865	3869	3874	3874	3845	3216	3230	3192	3180
25	3962	3966	3971	3971	3950	3311	3330	3291	3274
26	4059	4063	4068	4068	4055	3409	3428	3386	3370
27	4156	4160	4165	4165	4160	3504	3523	3480	3468
28	4253	4257	4262	4262	4265	3597	3618	3576	3564
29	4350	4354	4359	4359	4370	3687	3713	3672	3656
30	4447	4451	4456	4456	4475	3777	3804	3764	3746

Appendix B

Runs from cosmic-ray tests used in AMS-02 RICH studies

2008 test (98 runs)

Run order	**Run number**	**Date and time (UTC)**	**Run order**	**Run number**	**Date and time (UTC)**
1	1210152559	May 7, 09:29:19	21	1210340961	May 9, 13:49:21
2	1210152796	May 7, 09:33:16	22	1210346247	May 9, 15:17:27
3	1210153173	May 7, 09:39:33	23	1210349830	May 9, 16:17:10
4	1210235279	May 8, 08:27:59	24	1210678767	May 13, 11:39:27
5	1210237802	May 8, 09:10:02	25	1210682044	May 13, 12:34:04
6	1210239365	May 8, 09:36:05	26	1210685365	May 13, 13:29:25
7	1210242191	May 8, 10:23:11	27	1210688858	May 13, 14:27:38
8	1210242960	May 8, 10:36:00	28	1210692620	May 13, 15:30:20
9	1210257688	May 8, 14:41:28	29	1210695883	May 13, 16:24:43
10	1210259173	May 8, 15:06:13	30	1210755853	May 14, 09:04:13
11	1210259943	May 8, 15:19:03	31	1210760166	May 14, 10:16:06
12	1210264243	May 8, 16:30:43	32	1210763310	May 14, 11:08:30
13	1210321432	May 9, 08:23:52	33	1210767397	May 14, 12:16:37
14	1210322141	May 9, 08:35:41	34	1210770070	May 14, 13:01:10
15	1210325730	May 9, 09:35:30	35	1210773344	May 14, 13:55:44
16	1210327004	May 9, 09:56:44	36	1210777746	May 14, 15:09:06
17	1210328015	May 9, 10:13:35	37	1210837302	May 15, 07:41:42
18	1210329213	May 9, 10:33:33	38	1210841169	May 15, 08:46:09
19	1210337886	May 9, 12:58:06	39	1210846309	May 15, 10:11:49
20	1210338993	May 9, 13:16:33	40	1210850475	May 15, 11:21:15

continues on next page

continued from previous page

Run order	Run number	Date and time (UTC)	Run order	Run number	Date and time (UTC)
41	1210851016	May 15, 11:30:16	70	1211535240	May 23, 09:34:00
42	1210855348	May 15, 12:42:28	71	1211541514	May 23, 11:18:34
43	1210859181	May 15, 13:46:21	72	1211546717	May 23, 12:45:17
44	1210861796	May 15, 14:29:56	73	1211902994	May 27, 15:43:14
45	1210862656	May 15, 14:44:16	74	1211903814	May 27, 15:56:54
46	1210924918	May 16, 08:01:58	75	1211962811	May 28, 08:20:11
47	1210929142	May 16, 09:12:22	76	1211963357	May 28, 08:29:17
48	1210932905	May 16, 10:15:05	77	1212479283	June 3, 07:48:03
49	1210935256	May 16, 10:54:16	78	1212482890	June 3, 08:48:10
50	1210936492	May 16, 11:14:52	79	1212485738	June 3, 09:35:38
51	1211202104	May 19, 13:01:44	80	1212487970	June 3, 10:12:50
52	1211204718	May 19, 13:45:18	81	1212497157	June 3, 12:45:57
53	1211209297	May 19, 15:01:37	82	1212499068	June 3, 13:17:48
54	1211268924	May 20, 07:35:24	83	1212500130	June 3, 13:35:30
55	1211271376	May 20, 08:16:16	84	1212500400	June 3, 13:40:00
56	1211279021	May 20, 10:23:41	85	1212502499	June 3, 14:14:59
57	1211281154	May 20, 10:59:14	86	1212505913	June 3, 15:11:53
58	1211284430	May 20, 11:53:50	87	1212565573	June 4, 07:46:13
59	1211294950	May 20, 14:49:10	88	1212569569	June 4, 08:52:49
60	1211297915	May 20, 15:38:35	89	1212572935	June 4, 09:48:55
61	1211301124	May 20, 16:32:04	90	1212576870	June 4, 10:54:30
62	1211452501	May 22, 10:35:01	91	1212581115	June 4, 12:05:15
63	1211457638	May 22, 12:00:38	92	1212659144	June 5, 09:45:44
64	1211461525	May 22, 13:05:25	93	1212662090	June 5, 10:34:50
65	1211465092	May 22, 14:04:52	94	1212669748	June 5, 12:42:28
66	1211468400	May 22, 15:00:00	95	1212671021	June 5, 13:03:41
67	1211472211	May 22, 16:03:31	96	1212672689	June 5, 13:31:29
68	1211475797	May 22, 17:03:17	97	1212674609	June 5, 14:03:29
69	1211531761	May 23, 08:36:01	98	1212675762	June 5, 14:22:42

2009 test (52 runs)

Run order	Run number	Date and time (UTC)	Run order	Run number	Date and time (UTC)
1	1261312836	December 20, 12:40:36	27	1261377214	December 21, 06:33:34
2	1261313895	December 20, 12:58:15	28	1261483931	December 22, 12:12:11
3	1261314650	December 20, 13:10:50	29	1261488059	December 22, 13:20:59
4	1261317314	December 20, 13:55:14	30	1261491917	December 22, 14:25:17
5	1261327602	December 20, 16:46:42	31	1261495990	December 22, 15:33:10
6	1261329546	December 20, 17:19:06	32	1261496618	December 22, 15:43:38
7	1261329735	December 20, 17:22:15	33	1261500791	December 22, 16:53:11
8	1261330025	December 20, 17:27:05	34	1261505015	December 22, 18:03:35
9	1261332091	December 20, 18:01:31	35	1261509032	December 22, 19:10:32
10	1261334141	December 20, 18:35:41	36	1261512851	December 22, 20:14:11
11	1261336353	December 20, 19:12:33	37	1261516375	December 22, 21:12:55
12	1261338441	December 20, 19:47:21	38	1261520220	December 22, 22:17:00
13	1261340605	December 20, 20:23:25	39	1261523725	December 22, 23:15:25
14	1261342756	December 20, 20:59:16	40	1261527328	December 23, 00:15:28
15	1261344615	December 20, 21:30:15	41	1261530902	December 23, 01:15:02
16	1261344966	December 20, 21:36:06	42	1261534512	December 23, 02:15:12
17	1261347127	December 20, 22:12:07	43	1261538095	December 23, 03:14:55
18	1261349201	December 20, 22:46:41	44	1261541623	December 23, 04:13:43
19	1261351343	December 20, 23:22:23	45	1261541711	December 23, 04:15:11
20	1261353402	December 20, 23:56:42	46	1261545299	December 23, 05:14:59
21	1261357242	December 21, 01:00:42	47	1261548911	December 23, 06:15:11
22	1261361156	December 21, 02:05:56	48	1261552897	December 23, 07:21:37
23	1261363218	December 21, 02:40:18	49	1261556194	December 23, 08:16:34
24	1261365727	December 21, 03:22:07	50	1261560919	December 23, 09:35:19
25	1261369461	December 21, 04:24:21	51	1261564202	December 23, 10:30:02
26	1261373578	December 21, 05:32:58	52	1261567088	December 23, 11:18:08

Bibliography

[1] A. Einstein. Über die von der molekularkinetischen Theorie der Wärme geforderte Bewegung von in ruhenden Flüssigkeiten suspendierten Teilchen. *Annalen der Physik*, 322(8):549–560, 1905.

[2] R. Brown. A brief account of microscopical observations made in the months of June, July and August, 1827, on the particles contained in the pollen of plants; and on the general existence of active molecules in organic and inorganic bodies. *Phil. Mag.*, 4:161–173, 1828.

[3] W. C. Röntgen. Über eine neue Art von Strahlen. *Aus den Sitzungsberichten der Würzburger Physik.-medic. Gesellschaft Würzburg*, pages 137–147, 1895.

[4] H. Becquerel. Sur les radiations émises par phosphorescence. *Comptes Rendus*, 122:420–421, 1896.

[5] J. J. Thomson. Cathode Rays. *Phil. Mag.*, 44:293, 1897.

[6] V. F. Hess. Über Beobachtungen der durchdringenden Strahlung bei sieben Freiballonfahrten. *Physikalische Zeitschrift*, 13:1084–1091, 1912.

[7] http://lpnp90.in2p3.fr/HESS/sections/public_section/astronomie_gamma/pictures/victor-hess.

[8] V. Ginzburg. Cosmic ray astrophysics (history and general review). *Physics-Uspekhi*, 39:155–168, 1996.

[9] R. A. Millikan and G. H. Cameron. High frequency rays of cosmic origin III. measurements in snow-fed lakes at high altitudes. *Phys. Rev.*, 28(5):851–868, 1926.

[10] W. Bothe and W. Kolhörster. Das Wesen der Höhenstrahlung. *Physikalische Zeitschrift*, 56:751–777, 1929.

[11] C. D. Anderson. The apparent existence of easily deflectable positives. *Science*, 76(1967):238–239, 1932.

[12] C. D. Anderson. The Positive Electron. *Phys. Rev.*, 43:491–494, 1933.

[13] T. H. Johnson. Cosmic-Ray Intensity and Geomagnetic Effects. *Rev. Mod. Phys.*, 10:193–244, 1938.

[14] M. Schein *et al.* The Nature of the Primary Cosmic Radiation and the Origin of the Mesotron. *Phys. Rev.*, 59:615–615, 1941.

[15] C. B. Ramsey. Radiocarbon dating: revolutions in understanding. *Archaeometry*, 50(2):249–275, 2008.

[16] F. A. Cuccinotta and M. Durante. Cancer risk from exposure to galactic cosmic rays: implications for space exploration by human beings. *Lancet Oncology*, 7:431–435, 2006.

[17] P. Spillantini *et al.* Shielding from cosmic radiation for interplanetary missions: Active and passive methods. *Radiation Measurements*, 42:14–23, 2007.

[18] D. T. Welling. The long-term effects of space weather on satellite operations. *Ann. Geophys.*, 28:1361–1367, 2010.

[19] F. Wang and V. D. Agrawal. Single Event Upset: An Embedded Tutorial. In *Proc. 21st Int. Conf. on VLSI Design*, pages 429–434, 2008.

[20] J. Kirkby. Cosmic rays and climate. *Surv. Geophys.*, 28:333–375, 2007.

[21] http://cdsweb.cern.ch/journal/cernbulletin/2010/12/news%20articles/1249542?ln=en.

[22] http://cerncourier.com/cws/article/cern/41712.

[23] http://astroparticle.uchicago.edu/cosmic_ray_spectrum_picture.htm.

[24] C. Amsler *et al.* (Particle Data Group). Review of Particle Physics. *Phys. Lett. B*, 667:1, 2008.

[25] K. Greisen. End to the Cosmic-Ray Spectrum? *Phys. Rev. Lett.*, 16:748–750, 1966.

[26] G. T. Zatsepin and V. A. Kuz'min. Upper Limit of the Spectrum of Cosmic Rays. *J. Exp. Th. Phys. Lett.*, 4:78–80, 1966.

[27] M. Takeda *et al.* Energy determination in the Akeno Giant Air Shower Array experiment. *Astropart. Phys.*, 19:447–462, 2003.

[28] R. Abbasi *et al.* Observation of the ankle and evidence for a high-energy break in the cosmic ray spectrum. *Phys. Lett. B*, 619:271–280, 2005.

[29] R. Abbasi *et al.* First Observation of the Greisen-Zatsepin-Kuzmin Suppression. *Phys. Rev. Lett.*, 100:101101, 2008.

[30] M. Roth *et al.* (Auger Collaboration). Measurement of the UHECR energy spectrum using data from the Surface Detector of the Pierre Auger Observatory. In *Proc. 30th Int. Cosmic Ray Conf. (Merida)*, 2007. paper 0313, arXiv:0709.2096 (astro-ph).

[31] L. Perrone *et al.* (Auger Collaboration). Measurement of the UHECR energy spectrum from hybrid data of the Pierre Auger Observatory. In *Proc. 30th Int. Cosmic Ray Conf. (Merida)*, 2007. paper 0316, arXiv:0709.2643 (astro-ph).

[32] A. M. Hillas. Cosmic Rays: Recent Progress and some Current Questions. In H.-R. Klöckner, S. Rawlings, M. Jarvis, A. Taylor (eds.), *Cosmology, Galaxy Formation and Astroparticle Physics on the pathway to the SKA — Proceedings of the conference held in Oxford on the 10, 11 & 12 of April 2006.* Astron, 2006. arXiv:astro-ph/0607109v2.

[33] J. A. Simpson. Elemental and isotopic composition of galactic cosmic rays. *Ann. Rev. Nucl. Part. Sci.*, 33:323–381, 1983.

[34] M. Garcia-Munoz and J. A. Simpson. The elemental abundances of hydrogen through nickel in the low energy cosmic rays. In *Proc. 16th Int. Cosmic Ray Conf. (Kyoto)*, volume 1, pages 270–275, 1979.

[35] R. Schwenn. Space Weather: The Solar Perspective. *Living Rev. Solar Phys.*, 3, 2006. Online article, accessed July 22, 2010.

[36] L. J. Gleeson and W. I. Axford. Cosmic rays in the interplanetary medium. *Astrophys. J.*, 149:L115–L118, 1967.

[37] L. J. Gleeson and W. I. Axford. Solar modulation of galactic cosmic rays. *Astrophys. J.*, 154:1011–1026, 1968.

[38] I. G. Usoskin and K. Mursula. Long-term solar cycle evolution: review of recent developments. *Solar Physics*, 218:319–343, 2003.

[39] A. Balogh and M. J. Thompson. Introduction to Solar Magnetism: The Early Years. *Space Sci. Rev.*, 144:1–14, 2009.

[40] http://science.nasa.gov/newhome/pad/sun_today.htm.

[41] J. A. Eddy. The Maunder Minimum. *Science*, 192(4245):1189–1202, 1976.

[42] F. Steinhilber *et al.* Solar modulation during the Holocene. *Astrophys. Space Sci. Trans.*, 4:1–6, 2008.

[43] http://solarscience.msfc.nasa.gov/predict.shtml.

[44] http://www.ngdc.noaa.gov/iaga/vmod/.

[45] M. A. Shea and D. F. Smart. Geomagnetic cutoff rigidities and geomagnetic coordinates appropriate for the Carrington flare Epoch. *Adv. Space Research*, 38:209–214, 2006.

[46] D. F. Smart and M. A. Shea. Fifty years of progress in geomagnetic cutoff rigidity determinations. *Adv. Space Research*, 44:1107–1123, 2009.

[47] K. Greisen. Cosmic ray showers. *Ann. Rev. Nucl. Part. Sci.*, 10:63–108, 1960.

[48] http://www-ik.fzk.de/corsika/.

[49] F. Schmidt. CORSIKA shower images. http://www.ast.leeds.ac.uk/∼fs/showerimages.html.

[50] T. D. Lee. A brief history of the muon. *Hyperfine Interactions*, 86:439–453, 1994.

[51] S. H. Neddermeyer and C. D. Anderson. Note on the Nature of Cosmic-Ray Particles. *Phys. Rev.*, 51:884–886, 1937.

[52] J. C. Street and E. C. Stevenson. New Evidence for the Existence of a Particle of Mass Intermediate Between the Proton and Electron. *Phys. Rev.*, 52:1003–1004, 1937.

[53] S. H. Neddermeyer and C. D. Anderson. Cosmic-Ray Particles of Intermediate Mass. *Phys. Rev.*, 54:88–89, 1938.

[54] C. M. G. Lattes *et al.* Processes involving charged mesons. *Nature*, 159:694–697, 1947.

[55] G. D. Rochester and C. C. Butler. Evidence for the existence of new unstable elementary particles. *Nature*, 160:855–857, 1947.

[56] J. Abraham *et al.* (Auger Collaboration). Properties and performance of the prototype instrument for the Pierre Auger Observatory. *Nucl. Instrum. Meth. A*, 523:50–95, 2004.

[57] K. Yoshimura *et al.* BESS-Polar experiment: Progress and future prospects. *Adv. Space Res.*, 42:1664–1669, 2008.

[58] J. R. Hörandel. Cosmic-ray composition and its relation to shock acceleration by supernova remnants. *Adv. Space Res.*, 41:442–463, 2008.

[59] E. Fermi. On the Origin of the Cosmic Radiation. *Phys. Rev.*, 75:1169–1174, 1949.

[60] The Pierre Auger Collaboration. Correlation of the Highest-Energy Cosmic Rays with Nearby Extragalactic Objects. *Science*, 318(5852):938–943, 2007.

[61] The Pierre Auger Collaboration. Astrophysical Sources of Cosmic Rays and Related Measurements with the Pierre Auger Observatory. In *Proc. 31st Int. Cosmic Ray Conf. (Lodz)*, 2009. arXiv:0906.2347v2 (astro-ph).

[62] J. Einasto. Dark Matter. 2009. arXiv:0901.0632 (astro-ph.CO).

[63] F. Donato *et al.* Antiprotons from spallations of cosmic rays on interstellar matter. *Astrophys. J.*, 563:172–184, 2001.

[64] F. Donato *et al.* Antideuterons from supersymmetric dark matter. In *Proc. 30th Int. Cosmic Ray Conf. (Merida)*, 2007. paper 0519, arXiv:0709.2098v1 (astro-ph).

[65] A. W. Strong *et al.* Cosmic-ray propagation and interactions in the Galaxy. 2007. arXiv:astro-ph/0701517v1.

[66] J. R. Hörandel. On the knee of the energy spectrum of cosmic rays. *Astropart. Phys.*, 19:193–220, 2003.

[67] S. Webb. *Measuring the Universe: The Cosmological Distance Ladder*. Springer, 1999.

[68] B. F. Schutz. *Gravity from the Ground Up: An Introductory Guide to Gravity and General Relativity*. Cambridge University Press, 2003.

[69] E. Hubble. A relation between distance and radial velocity among extra-galactic nebulae. *Proc. Natl. Acad. Sci.*, 15:168–173, 1929.

[70] A. Einstein. Die Grundlage der allgemeinen Relativitätstheorie. *Annalen der Physik*, 49:769–822, 1916.

[71] A. Einstein. Kosmologische betrachtungen zur allgemeinen relativitätstheorie. *Sitzungsberichte der Königlich Preussischen Akademie der Wissenschaften*, pages 142–152, 1917 (part 1).

[72] N. Straumann. The history of the cosmological constant problem. 2002. arXiv:gr-qc/0208027v1.

[73] S. Burles *et al.* Big-Bang Nucleosynthesis: Linking Inner Space and outer Space. 1999. arXiv:astro-ph/9903300v1.

[74] A. A. Penzias and R. W. Wilson. A measurement of excess antenna temperature at 4080 Mc/s. *Astrophys. J.*, 142:419–421, 1965.

[75] F. Zwicky. Die Rotverschiebung von extragalaktischen Nebeln. *Helvetica Physica Acta*, 6:110–127, 1933.

[76] F. Zwicky. On the Masses of Nebulae and of Clusters of Nebulae. *Astrophys. J.*, 86:217, 1937.

[77] H. W. Babcock. The Rotation of the Andromeda Nebula. *Lick Obs. Bull.*, 498:41–51, 1939.

[78] V. C. Rubin. A brief history of dark matter. In *The Dark Universe: Matter, Energy and Gravity*, pages 1–13. Cambridge University Press, 2003.

[79] S. van den Bergh. The Early History of Dark Matter. *Publ. Astron. Soc. Pac.*, 111:657–660, 1999.

[80] S. M. Faber and J. S. Gallagher. Masses and mass-to-light ratios of galaxies. *Ann. Rev. Astron. Astrophys.*, 17:135–187, 1979.

[81] A. Linde. Inflationary Cosmology. 2007. arXiv:0705.0164v2 (hep-th).

[82] W. L. Freedman. Determination of Cosmological Parameters. 1999. arXiv:astro-ph/9905222.

[83] R. H. Sanders and S. S. McGaugh. Modified Newtonian Dynamics as an Alternative to Dark Matter. *Ann. Rev. Astron. Astrophys.*, 40:263–317, 2002.

[84] B. Carr. Baryonic dark matter. *Ann. Rev. Astron. Astrophys.*, 32:531–590, 1994.

[85] B. Carr. Baryonic and Non-Baryonic Dark Matter. 2000. arXiv:gr-qc/0008005.

[86] S. Perlmutter *et al.* Discovery of a supernova explosion at half the age of the Universe. *Nature*, 391:51–54, 1998.

[87] A. G. Riess *et al.* Observational Evidence from Supernovae for an Accelerating Universe and a Cosmological Constant. *Astron. J.*, 116:1009–1038, 1998.

[88] S. Perlmutter *et al.* Measurements of the cosmological parameters Ω and Λ from 42 high-redshift supernovae. *Astrophys. J.*, 517:565–586, 1999.

[89] M. S. Turner. Dark Matter and Dark Energy in the Universe. In B. K. Gibson, R. S. Axelrod, M. E. Putman (eds.), *The Third Stromlo Symposium: The Galactic Halo (ASP Conference Series, 165)*, pages 431–452.

[90] P. J. E. Peebles and B. Ratra. The Cosmological Constant and Dark Energy. 2002. arXiv:astro-ph/0207347v2.

[91] http://map.gsfc.nasa.gov/.

[92] C. L. Bennett *et al.* Scientific results from the Cosmic Background Explorer (COBE) (microwave/infrared). *Proc. Natl. Acad. Sci.*, 90(11):4766–4773, 1993.

[93] M. Kowalski *et al.* Improved cosmological constraints from new, old, and combined supernova data sets. *Astrophys. J.*, 686:749–778, 2008.

[94] W. J. Percival *et al.* Measuring the Baryon Acoustic Oscillation scale using the SDSS and 2dFGRS. *Mon. Not. R. Astron. Soc.*, 381:1053–1066, 2007.

[95] E. Komatsu *et al.* Seven-year Wilkinson Microwave Anisotropy Probe (WMAP) Observations: Cosmological Interpretation. 2010. arXiv:1001.4538v2 (astro-ph.CO).

[96] R. Rebolo. Baryonic Dark Matter. *Nucl. Phys. B (Proc. Suppl.)*, 110:16–25, 2002.

[97] E. Komatsu *et al.* Five-year Wilkinson Microwave Anisotropy Probe observations: cosmological interpretation. *Astrophys. J., Suppl. Series*, 180:330–376, February 2009.

[98] E. W. Otten and C. Weinheimer. Neutrino mass limit from tritium β decay. *Rep. Prog. Phys.*, 71:086201, 2008.

[99] M. Beck for the KATRIN collaboration. The KATRIN experiment. 2009. arXiv:0910.4862v2 (nucl-ex).

[100] K. Freese. Review of observational evidence for dark matter in the Universe and in upcoming searches for dark stars. 2008. arXiv:0812.4005v1 (astro-ph).

[101] R. Bernabei *et al.* First results from DAMA/LIBRA and the combined results with DAMA/NaI. *Eur. Phys. J. C*, 56:333–355, 2008.

[102] D. S. Akerib. The Search for Dark Matter. *Nucl. Phys. A*, 827:34c–41c, 2009.

[103] http://www.fnal.gov/pub/presspass/press_releases/higgs-mass-constraints-20100726.html.

[104] S. P. Martin. A Supersymmetry Primer. 2008. arXiv:hep-ph/9709356v5.

[105] A. Djouadi. The anatomy of electroweak symmetry breaking Tome II: The Higgs bosons in the Minimal Supersymmetric Model. *Phys. Rep.*, 459:1–241, 2008.

[106] F. D. Steffen. Supersymmetric Dark Matter Candidates. 2007. arXiv:0711.1240v2 (hep-ph).

[107] J. L. Feng *et al.* Searches for Supersymmetry at High-Energy Colliders. 2009. arXiv:0903.0046v2 (hep-ex).

[108] http://pamela.roma2.infn.it/index.php.

[109] NASA AMS webpage (http://ams-02project.jsc.nasa.gov/index.htm).

[110] V. M. Balebanov et al. Alpha Magnetic Spectrometer (AMS) for Extraterrestrial Study of Antimatter, Matter and Missing Matter on The International Space Station Alpha — Proposal to the United States Department of Energy, approved April 1995.

[111] AMS on ISS — Construction of a particle physics detector on the International Space Station. Internal AMS document.

[112] http://science.ksc.nasa.gov/shuttle/missions/sts-91/mission-sts-91.html.

[113] NASA Image eXchange (http://nix.nasa.org).

[114] M. Aguilar *et al.* (AMS Collaboration). The Alpha Magnetic Spectrometer (AMS) on the International Space Station: Part I — results from the test flight on the space shuttle. *Phys. Rep.*, 366:331–405, 2002.

[115] J. Alcaraz *et al.* (AMS collaboration). Search for Antihelium in Cosmic Rays. *Phys. Lett. B*, (461):387–396, 1999.

[116] J. Alcaraz *et al.* (AMS collaboration). Helium in Near Earth Orbit. *Phys. Lett. B*, (494):193–202, 2000.

[117] J. Alcaraz *et al.* (AMS collaboration). Cosmic Protons. *Phys. Lett. B*, (490):27–35, 2000.

[118] J. Alcaraz *et al.* (AMS collaboration). Leptons in Near Earth Orbit. *Phys. Lett. B*, (484):10–22, 2000.

[119] J. Alcaraz *et al.* (AMS collaboration). Protons in Near Earth Orbit. *Phys. Lett. B*, (472):215–226, 2000.

[120] M. Aguilar *et al.* A study of cosmic ray secondaries induced by the *Mir* space station using AMS-01. *Nucl. Instrum. Meth. B*, 234:321–332, 2005.

[121] M. Aguilar *et al.* (AMS-01 Collaboration). Cosmic-ray positron fraction measurement from 1 to 30 GeV with AMS 01. *Phys. Lett. B*, 646:145–153, 2007.

[122] NASA Consolidated Launch Manifest — Space Shuttle Flights and ISS Assembly Sequence (http://www.nasa.gov/mission_pages/station/structure/iss_manifest.html).

[123] The Alpha Magnetic Spectrometer Experiment (http://www.ams02.org).

[124] The Alpha Magnetic Spectrometer Home Page (http://ams.cern.ch).

[125] LIP AMS webpage (http://www.lip.pt/~amswww).

[126] CERN Document Server (http://cdsweb.cern.ch).

[127] *GEANT—Detector description and simulation tool — CERN Program Library Long Write-up W5013*. CERN, 1993.

[128] S. Agostinelli *et al.* (Geant4 Collaboration). Geant4—a simulation toolkit. *Nucl. Instrum. Meth. A*, 506:250–303, 2003.

[129] J. Allison *et al.* Geant4 Developments and Applications. *IEEE Trans. Nucl. Sci.*, 53(1):270–278, 2006.

[130] http://root.cern.ch.

[131] M. L. Arruda. *Charge and velocity reconstruction with the RICH detector of the AMS experiment — Analysis of the RICH prototype data*. PhD thesis, Instituto Superior Técnico, Technical University of Lisbon, January 2008.

[132] J. Séguinot and T. Ypsilantis. Photo-ionization and Cherenkov ring imaging. *Nucl. Instrum. Meth.*, 142:377–391, 1977.

[133] http://www.catalysis.nsk.su/.

[134] http://lpsc.in2p3.fr/cream/ancien_site_2007/ams-eng/lgpt2.html.

[135] http://panasonic-electric-works.net/.

[136] P. Aguayo *et al.* Prototype study of the Cherenkov imager of the AMS experiment. *Nucl. Instrum. Meth. A*, 560(2):291–302, May 2006.

[137] B. Alpat *et al.* Charge determination of nuclei with the AMS-02 silicon tracker. *Nucl. Instrum. Meth. A*, 540(1):121–130, March 2005.

[138] L. Amati *et al.* The TOF counters of the AMS-02 experiment: space qualification tests and beam test results. *Nucl. Phys. B (Proc. Suppl.)*, 150:276–280, 2006. Proceedings of the 9th Topical Seminar on Innovative Particle and Radiation Detectors.

[139] J. B. Birks. Scintillators from organic crystals: Specific fluorescence and relative response to different radiations. *Proc. Phys. Soc. A*, 64:874–877, 1951.

[140] C. N. Chou. The nature of the saturation effect of fluorescent scintillators. *Phys. Rev.*, 87:904–905, 1952.

[141] V. Choutko, private communication.

[142] M. L. Arruda. *Čerenkov Ring Acceptance in the RICH Detector of the AMS experiment — Optimization of a Dual Radiator Configuration.* Master's thesis, Instituto Superior Técnico, Technical University of Lisbon, June 2003.

[143] E. Lanciotti. *Estudio de las capacidades del detector RICH de AMS mediante el análisis de los datos de un prototipo en un haz de iones.* PhD thesis, Universidad Complutense de Madrid, 2006.

[144] W. H. Press *et al.* *Numerical Recipes: The Art of Scientific Computing (FORTRAN Version).* Cambridge University Press, 2$^{\text{nd}}$ edition, 1989.

[145] National Nuclear Data Center — Chart of Nuclides (http://www.nndc.bnl.gov/chart/).

[146] E. S. Seo *et al.* Study of cosmic-ray H and He isotopes at 23 AU. *Astrophys. J.*, 432:656–664, 1994.

[147] C. J. Delgado Méndez. *Medida de la velocidad de mounes y nucleos ligeros con un prototipo del contador RICH del experimento AMS.* PhD thesis, Universidad Autonoma de Madrid, 2003.

[148] J. Z. Wang *et al.* Measurement of cosmic-ray hydrogen and helium and their isotopic composition with the BESS experiment. *Astrophys. J.*, 564:244–259, 2002.

[149] O. Reimer *et al.* The cosmic-ray ^{3}He/^{4}He ratio from 200 MeV per nucleon^{-1} to 3.7 GeV per nucleon^{-1}. *Astrophys. J.*, 496:490–502, 1998.

[150] J. J. Beatty *et al.* The cosmic-ray ^{3}He/^{4}He ratio from 100 to 1600 MeV amu^{-1}. *Astrophys. J.*, 413:268–280, 1993.

[151] R. Kroeger. Measurements of hydrogen and helium isotopes in Galactic cosmic rays from 1978 through 1984. *Astrophys. J.*, 303:816–828, 1986.

[152] Y. Hatano *et al.* Relative abundance of ^{3}He and ^{4}He in cosmic rays near 10 GV. *Phys. Rev. D*, 52(11):6219–6223, 1995.

[153] W. R. Webber *et al.* A reexamination of the cosmic-ray helium spectrum and the ^{3}He/^{4}He ratio at high energies. *Astrophys. J.*, 312:178–182, 1987.

[154] E. S. Seo and V. S. Ptuskin. Stochastic reacceleration of cosmic rays in the interstellar medium. *Astrophys. J.*, 431:705–714, 1994.

[155] T. Hams *et al.* ^{10}Be/^{9}Be ratio up to 1.0 GeV/nucleon measured in the ISOMAX 98 balloon flight. In *Proc. 27th Int. Cosmic Ray Conf. (Hamburg)*, pages 1655–1658, 2001.

[156] G. A. de Nolfo *et al.* A measurement of the ^{10}Be/^{9}Be ratio up above 1.0 GeV/nucleon: Results from the 1998 flight of ISOMAX. In *Proc. 27th Int. Cosmic Ray Conf. (Hamburg)*, pages 1659–1662, 2001.

[157] N. E. Yanasak *et al.* Implications for Cosmic Ray Propagation from ACE Measurements of Radioactive Clock Isotope Abundances. In *Proc. 26th Int. Cosmic Ray Conf. (Salt Lake City)*, volume 3, pages 9–12, 1999.

[158] J. A. Simpson and M. Garcia-Munoz. Cosmic-ray lifetime in the galaxy: experimental results and models. *Space Sci. Rev.*, 46:205–224, 1988.

[159] A. Lukasiak *et al.* The isotopic composition of cosmic-ray beryllium and its implication for the cosmic ray's age. *Astrophys. J.*, 423:426–431, 1994.

[160] J. J. Connell. Galactic cosmic-ray confinement time: *Ulysses* high energy telescope measurements of the secondary radionuclide ^{10}Be. *Astrophys. J.*, 501:L59–L62, 1998.

[161] A. W. Strong and I. V. Moskalenko. Models for galactic cosmic-ray propagation. *Adv. Space Res.*, 27(4):717–726, 2001.